

Rashid A. Ganeev

Frequency Conversion of Ultrashort Pulses in Extended Laser- Produced Plasmas

Springer Series on Atomic, Optical, and Plasma Physics

Volume 89

Editor-in-chief

Gordon W.F. Drake, Windsor, Canada

Series editors

James Babb, Cambridge, USA

Andre D. Bandrauk, Sherbrooke, Canada

Klaus Bartschat, Des Moines, USA

Philip George Burke, Belfast, UK

Robert N. Compton, Knoxville, USA

Tom Gallagher, Charlottesville, USA

Charles J. Joachain, Bruxelles, Belgium

Peter Lambropoulos, Iraklion, Greece

Gerd Leuchs, Erlangen, Germany

Pierre Meystre, Tucson, USA

The Springer Series on Atomic, Optical, and Plasma Physics covers in a comprehensive manner theory and experiment in the entire field of atoms and molecules and their interaction with electromagnetic radiation. Books in the series provide a rich source of new ideas and techniques with wide applications in fields such as chemistry, materials science, astrophysics, surface science, plasma technology, advanced optics, aeronomy, and engineering. Laser physics is a particular connecting theme that has provided much of the continuing impetus for new developments in the field, such as quantum computation and Bose-Einstein condensation. The purpose of the series is to cover the gap between standard undergraduate textbooks and the research literature with emphasis on the fundamental ideas, methods, techniques, and results in the field.

More information about this series at <http://www.springer.com/series/411>

Rashid A. Ganeev

Frequency Conversion of Ultrashort Pulses in Extended Laser-Produced Plasmas

 Springer

Rashid A. Ganeev
Ophthalmology and Advanced Laser
Medical Center
Saitama Medical University
Moroyama
Japan

ISSN 1615-5653 ISSN 2197-6791 (electronic)
Springer Series on Atomic, Optical, and Plasma Physics
ISBN 978-981-10-0193-2 ISBN 978-981-10-0194-9 (eBook)
DOI 10.1007/978-981-10-0194-9

Library of Congress Control Number: 2015960774

© Springer Science+Business Media Singapore 2016

This work is subject to copyright. All rights are reserved by the Publisher, whether the whole or part of the material is concerned, specifically the rights of translation, reprinting, reuse of illustrations, recitation, broadcasting, reproduction on microfilms or in any other physical way, and transmission or information storage and retrieval, electronic adaptation, computer software, or by similar or dissimilar methodology now known or hereafter developed.

The use of general descriptive names, registered names, trademarks, service marks, etc. in this publication does not imply, even in the absence of a specific statement, that such names are exempt from the relevant protective laws and regulations and therefore free for general use.

The publisher, the authors and the editors are safe to assume that the advice and information in this book are believed to be true and accurate at the date of publication. Neither the publisher nor the authors or the editors give a warranty, express or implied, with respect to the material contained herein or for any errors or omissions that may have been made.

Printed on acid-free paper

This Springer imprint is published by SpringerNature
The registered company is Springer Science+Business Media Singapore Pte Ltd.

To my parents, wife, son, and daughter

Preface

The goal of this book is to show the most recent findings of newly emerged field of high-order harmonic generation (HHG) of laser radiation in the extended laser-produced plasma plumes. Ablation targets for HHG differ from the conventional gas targets used for harmonic generation in a number of ways. They are usually preformed plasmas with a density distribution that is determined by the ablation dynamics and subsequent evolution of plasma, which depend on the target composition and ablation pulse parameters in a complex way. In this connection, I would like to say a few words about different methods of generation of the coherent short-wavelength radiation using HHG approach.

The HHG in gases was for the first time observed in the second half of the 1980s using picosecond Nd:YAG lasers (as well as an excimer laser at 248 nm). The harmonics from different gases up to the 21st and 33rd orders of 1064 nm radiation were reported at an intensity of $3 \times 10^{13} \text{ W cm}^{-2}$, which led to an enormous growth of interest in this area of nonlinear optics. Those studies have demonstrated that the application of gases as nonlinear media can be used as an advanced method for generation of coherent extreme ultraviolet (XUV) radiation using picosecond driving pulses. Those early developments were further transformed in the field of gas HHG spectroscopy when new, predominantly femtosecond, lasers became involved in this field of study. Currently, harmonics up to the 5000th orders have been reported, although most recent studies are related with the development of the attosecond sources of laser radiation based on the gas HHG. Other applications include the analysis of the orientational features of some gaseous molecules through the study of variable harmonic spectra from these species, as well as the applications of gas harmonics for surface science, biology, medicine, and different branches of physics and chemistry. The attractiveness of this method is based on the availability of moderate-level femtosecond lasers in many laboratories worldwide and the simplicity of handling the gas-jet technique.

Another method, harmonic generation from the surfaces, which is based on completely different physical principles than HHG in gases, is less popular due to the sophisticated equipment required for its implementation. However, this method

is well elaborated and used in advanced laboratories. Very high fluences and intensities (of the order of 10^{18} W cm⁻² or higher) and, most importantly, very high contrast ratios between the driving pulse and the prepulse already existing in any laser system are the main requirements for this technique. Not many laboratories can afford these conditions for surface HHG. Nevertheless, high cutoffs (up to the 2000th harmonics) and high conversion efficiencies for the lowest orders of harmonics were reported using this technique. Two distinct generation mechanisms have been identified to contribute to surface HHG: the coherent wake emission and the relativistic oscillating mirror process. Both mechanisms emit coherent XUV radiation in the reflected direction through nonlinear conversion processes at the plasma front surfaces.

One has to note that there are many good publications showing a whole picture of developments of the HHG in gases. The mechanisms of odd and even harmonic generation in the reflection of laser radiation from the surfaces are also frequently discussed in the literature. These HHG techniques are beyond the scope of this book. My aim is to familiarize the reader with the most recent approaches of harmonic generation in the XUV range with the use of the extended plasma plumes, which have never been used and are different from commonly used gas-jet sources.

Two monographs on the history of harmonic generation in the narrow plasmas and the achievements using new approaches that emerged between 2005 and 2013 have already been published (R.A. Ganeev, *High-Order Harmonic Generation in Laser Plasma Plumes*, Imperial College Press, 2012; R.A. Ganeev, *Plasma Harmonics*, Pan Stanford Publishing, 2014). Meanwhile, the developments in this field have shown new opportunities in further amendments of this technique. I will discuss some of these new findings appeared during HHG experiments in the narrow plasma plumes, while mostly concentrate on the studies using the extended plasmas.

What differs this book from my above-mentioned publications? The main difference is related to the application of the long plasma medium for HHG, instead of short one, to demonstrate the attractive properties of extended laser-produced plasmas from the point of view of the high-order nonlinear optical properties of various materials. Particularly, the quasi-phase matching in modulated plasmas demonstrated in a few recent studies has revealed the opportunity to tune the groups of enhanced harmonics along the XUV by different means. Another interesting finding is related with the opportunity to analyze the electron density of extended modulated plasmas. Other developments are related to the new advanced methods of harmonic generation emerged during recent time. Those methods include the application of double-pulse scheme for the analysis of the nonlinear optical properties of extended targets without the preliminary ablation by the picosecond heating pulses. The application of extended nonmetal targets (semiconductors, crystals, clustered carbon structures, etc.) allows the analysis of the relation between the excited ionic species emitting incoherent light and the harmonics coinciding with these ionic transitions. The studies of resonance enhancement in the nonmetal ablations reveal new opportunities to move farther toward the shortest wavelengths. A search of the enhanced response of carbon-contained clusters, study of the

morphology of nanoparticle deposits from the ablated long targets, applications of the graphene-wrapped sheets for HHG, amendments of the two-color pump of plasmas caused by the positive dispersion of the extended medium allowing better overlap of the fundamental and second-harmonic orthogonal fields, etc., are among other distinctive moments differing this book from the two previous monographs.

All these amendments of plasma harmonics could not be realized without the collaboration between various research groups involved in the studies of the nonlinear optical properties of ablated species. Among numerous colleagues, I met and had the privilege to collaborate, I would like to thank H. Kuroda, M. Suzuki, S. Yoneya, M. Baba, and F. Mitani (Saitama Medical University, Japan); T. Ozaki, L. B. Elouga Bom, J. Abdul-Haji, and F. Vidal (Institut National de la Recherche Scientifique, Canada); P.D. Gupta, P.A. Naik, H. Singhal, J.A. Chakera, R.A. Khan, U. Chakravarty, M. Raghuramaiah, V. Arora, M. Kumar, and M. Tayyab (Raja Ramanna Centre for Advanced Technology, India); J.P. Marangos, J.W.G. Tisch, C. Hutchison, T. Witting, F. Frank, T. Siegel, A. Zaïr, Z. Abdelrahman, and D.Y. Lei (Imperial College, United Kingdom); M. Castillejo, M. Oujja, M. Sanz, I. López-Quintás, and M. Martín (Instituto de Química Física Rocasolano, Spain); H. Zacharias, J. Zheng, M. Wöstmann, and H. Witte (Westfälische Wilhelms-Universität, Germany); T. Usmanov, G.S. Boltaev, I.A. Kulagin, V.I. Redkorechev, V.V. Gorbushin, R.I. Tugushev, and N.K. Satlikov (Institute of Ion-Plasma and Laser Technologies, Uzbekistan); M.B. Danailov (Sincrotrone Trieste, Italy); B.A. Zon and M.V. Frolov (Voronezh State University, Russia); D.B. Milošević (University of Sarajevo, Bosnia and Herzegovina); M. Lein and M. Tudorovskaya (Leibniz Universität Hannover, Germany); E. Fiordilino (Università degli Studi Palermo, Italy); V. Toşa and K. Kovács (National Institute of R&D Isotropic and Molecular Technologies, Romania); V.V. Strelkov and M.A. Khokhlova (General Physics Institute, Russia); M.K. Kodirov and P.V. Redkin (Samarkand State University, Uzbekistan); A.V. Andreev, S.Y. Stremoukhov and O.A. Shoutova (Moscow State University, Russia) for their activity in the development of this relatively new field of nonlinear optics. Among them, I would like to underline the role of Prof. H. Kuroda who actively pursued the field of plasma harmonics starting from the very beginning of these studies in 2005. Professor Kuroda has supported my proposal to initiate the studies of the extended plasma media for the HHG. His invitation to carry out these studies in Saitama Medical University, Japan, played a crucial role in the developments of this field.

My wife Lidiya, son Timur, and daughter Dina are the main inspirations of all my activity. Now, becoming a grandfather, I would like to include Timur's wife Anya and our beloved grandson Timofey in the list of most important people, who help me to overcome various obstacles of the life of scientific tramp.

This book is organized as follows. Theoretical and experimental aspects of HHG are considered in the Introduction section. In Chap. 2, a review of most important results of the HHG in narrow plasmas is presented. Here, I also show recent studies of the small-sized plasma plumes as the emitters of high-order harmonics. In Chap. 3, various findings during application of extended plasmas for harmonic generation are analyzed. One of the most important applications of extended plasmas, the

quasi-phase matching of generated harmonics, is demonstrated in Chap. 4. Here, I show various approaches in modification of perforated plasma plumes. Chapter 5 depicts the nonlinear optical features of the extended plasmas produced on the surfaces of different nonmetal materials. Chapter 6 is dedicated to the analysis of the new opportunities of extended plasma-induced HHG. The advantages of application of the long plasma plumes for HHG, such as resonance enhancement and double-pulse method, are discussed in Chap. 7. Finally, I summarize all these findings and discuss the perspectives of extended plasma formations for efficient HHG and nonlinear optical plasma spectroscopy.

Moroyama, Japan
January 2016

Rashid A. Ganeev

Contents

1 Introduction. Theory and Experiment of High-Order Harmonic Generation in Narrow and Extended Media	1
1.1 High-Order Harmonic Generation in Isotropic Medium: Three-Step Model and Macroscopic Consideration of Frequency Conversion	1
1.2 Overview of the Applications of Long Gaseous Media for the HHG	4
References	6
2 HHG in Short-Length Plasmas	9
2.1 Modern History and Perspectives of Harmonic Generation in Narrow Plasma Plumes	9
2.2 Spatial Coherence Measurements of Non-resonant and Resonant High-Order Harmonics Generated in Narrow Laser Ablation Plumes	14
2.3 Resonance Processes in the Plasma Plumes	21
2.3.1 Resonant and Non-resonant High-Order Harmonic Generation in the Plasmas Produced by Picosecond and Femtosecond Pulses	21
2.3.2 Resonance Enhancement of the 11th Harmonic of 1064 nm Picosecond Radiation Generated in Lead Plasma	28
2.4 Peculiarities of the High-Order Harmonics from Different Narrow Plasmas Generating at 1 kHz Repetition Rate	37
2.5 Concluding Comments	45
References	46
3 HHG in Extended Plasmas	51
3.1 Advanced Properties of Extended Plasmas for Efficient High-Order Harmonic Generation	51

3.2	Enhanced Harmonic Generation Using Different Second-Harmonic Sources for the Two-Color Pump of Extended Laser-Produced Plasmas	57
3.3	Modification of Modulated Plasma Plumes	67
3.4	Characterization of the High-Order Harmonics of 64 fs Pulses Generated in Extended Plasma Plumes	73
3.5	Concluding Comments	80
	References	81
4	Quasi-Phase-Matching of Harmonics in Laser-Produced Plasmas	85
4.1	Perforated Target Ablation for the Formation of the Modulated Plasma for Quasi-Phase-Matched Harmonic Generation	87
4.2	Quasi-Phase-Matching of Harmonics Using the Variable Multi-jet Plasmas	92
4.3	QPM-Induced Enhancement of HHG During Two-Color Pump of Multi-jet Plasmas	98
4.4	Peculiarities of QPM Harmonics Using Different Targets and Pump Schemes	103
4.5	Influence of Plasma Jet Sizes and Pulse Energies on the Characteristics of QPM Harmonics	108
4.6	Concluding Comments	116
	References	117
5	Peculiarities of the HHG in the Extended Plasmas Produced on the Surfaces of Different Materials	119
5.1	Harmonic Generation in the Plasmas Produced on the 5-mm-Long Crystal Surfaces	121
5.2	Application of the Laser Plasmas Produced on the Extended Surfaces of Elemental Semiconductors	127
5.3	Application of Carbon Cluster-Contained Extended Plasmas for the High-Order Harmonic Generation of Ultrashort Pulses	133
5.4	Morphology of Laser-Produced Carbon Nanoparticle Plasmas and High-Order Harmonic Generation of Ultrashort Pulses in Extended Clustered Media	139
5.5	Graphene-Contained Extended Plasma: A Medium for the Coherent Extreme Ultraviolet Light Generation	150
5.6	Concluding Comments	153
	References	155
6	New Opportunities of Extended Plasma Induced Harmonic Generation	161
6.1	Third and Fourth Harmonics Generation in Laser-Induced Periodic Plasmas	162

- 6.2 Resonance-Enhanced Harmonics Generated in Nanoparticle and Monomer Plasmas 170
- 6.3 Electron Density Measurements in Laser-Produced Plasma Using the Nonlinear Optical Method 178
- 6.4 Concluding Comments 185
- References 187
- 7 Harmonic Characterization Using Different HHG Schemes in the Extended Plasmas 189**
 - 7.1 Low- and High-Order Harmonic Generation in the Extended Plasmas Produced by Laser Ablation of Zinc and Manganese Targets 190
 - 7.2 Application of Double Femtosecond Pulses for Plasma Harmonic Generation 200
 - 7.3 Concluding Comments 207
 - References 207
- 8 Summary: Achievements and Perspectives 209**
 - References 216
- Index 219**

Chapter 1

Introduction. Theory and Experiment of High-Order Harmonic Generation in Narrow and Extended Media

High-order harmonic generation (HHG) is a technique for producing spatially and temporally coherent extreme ultraviolet (XUV) light. HHG in isotropic media occurs when an intense pulsed laser beam is focused into a gas jet or plasma. The intensity of the laser light is chosen such that its electric field amplitude is comparable to the electric field in atoms and ions. Such fields are able to detach electrons from above species by tunnel ionization, as opposed to photo-ionization by a weak field with high enough photon energy. The detached electron is accelerated in the field and under certain conditions has significant probability to hit the ion left behind upon return. The “collision” results in the emission of high energy photons. This description is called three-step model. The details of this process will be discussed below.

The use of extended media may offer new opportunities in application of XUV radiation for various needs. In Introduction, we discuss the use of extended gaseous media for HHG and show the advantages of this approach, which has prompted the use of long medium for the studies of the high-order nonlinear optical properties of various materials through the plasma harmonic approach.

1.1 High-Order Harmonic Generation in Isotropic Medium: Three-Step Model and Macroscopic Consideration of Frequency Conversion

When a high-intensity laser pulse passes through a gaseous or plasma medium, its atoms and ions emit odd harmonics. For a laser radiation wavelength λ , a superposition of the components λ , $\lambda/3$, $\lambda/5$, $\lambda/7$, etc. is observed at the output of the nonlinear medium. The harmonics of laser radiation result from a three-stage process [1–3] that comprises the ionization of an atom (or ion), the electron acceleration in the electromagnetic field, and the subsequent recombination with parent particle and emission of harmonics. This process is periodically repeated every half cycle of the electromagnetic wave. The highest-order harmonics are due to the electron acceleration at the instant of ionization at the peak intensity of the

laser pulse. Therefore, the generation of highest-order harmonics in isotropic media results from the interaction of a high-intensity light field with atoms [4–6], atomic clusters [7, 8], molecules [9, 10], and ions [11–16].

A characteristic feature of the three-stage HHG is a rapid decrease in the intensity of low-order harmonics followed by a long plateau where the intensities of high-order harmonics differ only slightly from one another, and an abrupt decrease in the intensity of the highest-order harmonics generated (the so-called harmonic cut-off H_c). The position of H_c is determined by the ionization potential I_i of the particles participating in harmonic generation (of atoms in the case of HHG in gases and of ions in the case of HHG in a plasma) and by the ponderomotive potential, which defines the accelerated electron energy and depends on the intensity of femtosecond radiation and its wavelength ($U_p \approx 9.3 \times 10^{-14} I_p [\text{W cm}^{-2}] \lambda^2 [\mu\text{m}^2]$). The highest photon energy of the harmonics generated is defined by the relation $E_c \approx I_i + 3.17U_p$.

The main HHG properties may be characterized with the aid of a semiclassical model [1–3], although a more accurate description calls for a consistent quantum mechanical treatment. In the semiclassical model, an electron detached from an atom is considered a free particle, and the effect of all bound states, with the exception of the ground state, is assumed to be negligible. These assumptions are satisfied in the tunnel ionization regime, which is characterized by the inequality $\gamma < 1$ for the Keldysh parameter $\gamma = \omega_L(2I_i)^{0.5}E^{-1}$ where ω_L is the laser radiation frequency and E is the magnitude of the electric vector of the electromagnetic wave. High-power ultrashort laser pulses are best suited for the fulfillment of these conditions.

Along with the microscopic consideration of the processes occurring in the interaction of high-power ultrashort laser pulses with atoms and ions, account should also be taken of macroscopic processes such as the effect of transmission through a medium and group effects. These effects primarily include dephasing, absorption, and defocusing. These processes are analyzed in [17].

The cut-off law clarifies that the maximum harmonic frequency achievable from the HHG process is strongly linked to the ponderomotive potential U_p and thus to the field amplitude and the wavelength of the fundamental laser light. The maximum applicable field amplitude is limited, because, for very high intensities of the driving laser well above $10^{16} \text{ W cm}^{-2}$, the magnetic component of the laser field becomes strong enough to induce a lateral acceleration, hence deflecting the electron, reducing the overlap between the electronic and the nuclear wave packets and thus preventing efficient harmonic generation. However, the cut-off law states that the maximum harmonic frequency in the HHG spectra will increase for longer wavelengths of the driving laser field. A shift of the cut-off frequency towards the water window, or even the keV range of photon energy, by using driving lasers in the few μm range was demonstrated at experimentally relevant harmonic flux in [18, 19].

Note that not only the cut-off law, but also some other interesting limits on the HHG process are explained by the above model. For instance, HHG will only occur if the driving laser field is linearly polarized. Electrons in an elliptically polarized

laser field fly in spirals and therefore miss the parent nucleus. In terms of quantum mechanics, the overlap of the nuclear and the electron wave packets is reduced upon return. This has been observed in experiments, where the intensity of harmonics has decreased rapidly with increasing ellipticity [20]. However, it is possible to generate elliptically polarized harmonics with linearly polarized driving laser fields by using aligned molecules as non-linear media for harmonic generation, for example laser aligned N_2 molecules as demonstrated in [21].

The conclusions on the coherence properties of the HHG radiation can also be drawn from the above model. The electron has to be considered as a quantum mechanical wave packet, which undergoes a transition from a bound state to a continuum state at a certain time t_i , evolves in the laser field and finally descends to the bound state again under radiation of the kinetic energy gained while propagating through the continuum. This quantum wave packet oscillates with its own frequency, however the total phase of the electron at recombination and therefore the phase of the occurring XUV radiation is strongly linked to the time of ionization and to the strength of the fundamental laser. Thus the phase of the electronic wave packet at recombination and therefore the phase of the XUV light are locked to the phase and amplitude of the fundamental laser beam. This influences the collective behavior in the spatial domain, since coherence properties of the irradiating laser are transferred to the harmonic emission, hence forth HHG is a spatially coherent process.

The total emitted field in a macroscopic medium is given by a sum over the emissions from many atoms. Thus not only the single atom response, but also collective effects as phase matching or re-absorption of the XUV light determine the intensity of the generated harmonics. Phase matching is given, if the radiation generated by different atoms at different positions in the medium interferes constructively at the exit of the medium. For a perfect match of phases, this condition can be presented as

$$\Delta k = k_q - qk_0 = 0, \quad (1.1)$$

where Δk denotes the mismatch between the wave vectors k_q of harmonic q and k_0 of the fundamental. Approximate phase matching is achieved for

$$\Delta k L_{\text{med}} < \pi, \quad (1.2)$$

where L_{med} describes length of the medium. The dependence of the harmonic phase φ_q on the laser intensity at the position of emission can be written as $\varphi_q = \alpha_q I$, where α_q is linked to the q th Fourier component of the atomic polarization and proportional to the atomic dipole moment and density. An additional wave vector $k_1 = -\nabla \varphi_q$ enters the phase mismatch, leading to a generalized phase matching condition for HHG [22, 23]:

$$\Delta k = k_q - qk_0 + k_1. \quad (1.3)$$

The transversal intensity profile and wavefront shape play an important role for optimizing the HHG yield. Here we consider the case when the Gouy phase shift becomes insignificant during propagation of the loosely focused fundamental radiation through the extended medium. The condition for this consideration is related with the relation

$$L_{\text{med}} < b. \quad (1.4)$$

Here b denotes the confocal parameter of the focused radiation. This relation indicates that the focused radiation propagates through the medium at the conditions of plane wave when the phase of wave front becomes unchanged along the beamwaist. More details on the phase matching conditions will be discussed in Chap. 4.

1.2 Overview of the Applications of Long Gaseous Media for the HHG

The most common experimental setup of HHG comprises (apart from laser system and diagnostic apparatus) a gas puff target. Such a target is basically a gas valve injecting a portion of a gas at desired pressure. The valve is repetitively opens and the laser pulses interact with gas in proximity of valve exhaust. Typical repetition rate of the gas puffs is <100 Hz. The valves may have either circular symmetry or could be elongated. Elongated valves provide higher XUV beam outputs but limiting factor is re-absorption in a gas. Thus long valves are used for wavelengths >20 nm (also because of the longer coherence length for longer wavelengths). On the other hand, circular (e.g. 0.5 mm diameter) gas puff valves are used in shorter-wavelength HHG.

High-order harmonics are also generated in extended gas cells. A gas cell is a simple container filled with a noble gas at moderate pressure (few tens of mbar). Arrangements with gas cells are very comfortable to work with because, compared to the gas puff targets, there are fewer parameters to optimize to maintain the phase matching. In this case the phase matching is obtained by tuning only longitudinal position of a cell and gas pressure in it. The gas cells can be as long as desired (due to technical ease of construction compared to gas puff valves). This setup is also favorable when maximization of interaction length is wanted.

Another possible geometry of HHG involves hollow fibers filled with a conversion gas. In such a fiber laser pulses are propagating even meters long resulting in efficient transfer of driving field energy into XUV beam. This geometry is also popular due to ease of control of phase-matching by the fiber parameters.

Below we briefly review the advantages of long media over the narrow ones in the case of the HHG in gases. Initially, HHG was studied using the narrow gas jets, with the sizes of the active medium of the order of 0.3–0.5 mm to decrease the residual pressure in the XUV spectrometers. The gradual increase of the sizes of

gaseous medium led to the growth of harmonic yield and cut-off, as well as appearance of new features of this process. Previous studies have revealed various peculiarities of extended gaseous media. Below we present a short overview of the experiments related with the application of such elongated species for HHG.

The efficient high-order harmonic generation in a two-color laser field using a long gas jet of He was reported in [24]. With the optimization of laser parameters and target conditions, strong harmonics were produced at $2(2n + 1)$ th orders in an orthogonally polarized two-color field. The strongest harmonic at the 38th order (21.6 nm) reached the energy of 0.6 μJ with a 6 mm gas jet, giving a conversion efficiency as high as 2×10^{-4} .

The generation of high-order harmonics in a 4-mm-long gas cell was reported in [25] using mid-infrared femtosecond pulses at various wavelengths (1240, 1500, and 1800 nm). It was observed that the yield and cut-off energy of the generated high-order harmonics critically depend on focal position, gas pressure, and size of the input beam which can be controlled by an aperture placed in front of the focal lens. By optimizing the experimental parameters, a cutoff energy at ~ 190 eV was achieved with the 1500 nm driving pulses, which is the highest for the three wavelengths chosen in those experiment.

The generation of intense XUV supercontinuum with photon energies spanning from 35 to 50 eV (i.e., supporting an isolated attosecond pulse with a duration of ~ 271 as) by loosely focusing the 35 fs, 11 mJ pulses from a femtosecond laser amplifier into a 10-mm long gas cell filled with krypton gas was analyzed in [26]. The dramatic change of spectral and temporal properties of the driver pulses after passing through the gas cell indicates that propagation effects play a significant role in promoting the generation of the XUV supercontinuum.

A simple and robust, yet powerful enhancement scheme based on a dual gas-cell setup was reported in [27]. HHG in neon using a high-energy (20 mJ), near-infrared fundamental field, loosely focused in a long gas cell, resulting in high-order harmonics in the 40–100 eV range, with a typical energy of 10 nJ per harmonic order was observed. The addition of a high-pressure Ar gas cell before the generation cell produces a large enhancement of the harmonics generated in the Ne-filled cell. It was shown both experimentally and theoretically that the observed enhancement is due to below-threshold, low-order harmonics, which modify the fundamental field in such a way that the contribution of the short trajectories is increased. This effect of seeding HHG using harmonics generated in a separate gas cell has shown that low-order harmonics are responsible for the resulting enhancement. The combined electric field preferentially enhances the short trajectories while suppressing depletion and plasma dispersion effects. The required phase difference between the fundamental and the low-order harmonics is obtained by adjusting the pressure in the seeding cell, thus modifying the free-electron dispersion.

A high intensity soft X-ray coherent beam could be obtained using a loose focusing geometry in the extended medium, which allows coupling a significant amount of laser energy in the HHG process [28–30]. At a given laser intensity, the increased number of ‘atomic harmonic converters’ takes part in frequency conversion under improved phase matching conditions. Using a long gas cell and a

long focal length lens (7.5 m), the emitting volume can be increased by orders of magnitude as compared to standard HHG setups. This approach allows reaching more than 10 μJ per shot in the whole harmonic frequency comb and up to 1 μJ (1.6×10^{11} photons) for the 25th ($\lambda = 32$ nm) harmonic [31].

The increase of medium length allows compensating the decrease of harmonic yield using the mid-infrared lasers [32]. In that case the phase-matching coherence process can be extended in part because the gas becomes increasingly transparent at photon energies approaching the kilo-electron volt region. Another possible geometry of HHG involves hollow fibers filled with a conversion gas [33]. The low single-atom yield can be compensated by coherently combining HHG from a large number of emitters.

Since the discovery of the HHG process in gases over two decades ago [34, 35], its conversion efficiency has been progressively improved by optimizing the macroscopic phase-matching conditions and the microscopic single atom response [36]. High-order harmonic generation using isotropic media has been carried out in different conditions, such as high-pressure jets [37], gas cells [38], semi-infinite media, and capillaries [18]. Phase-matching optimization using loosely focused (possibly self-guided) fundamental fields has led to conversion efficiencies of $\sim 10^{-7}$ in neon [38], $\sim 10^{-5}$ in argon [30], and slightly below 10^{-4} in xenon [28, 29].

This brief review of previous studies of the HHG in extended gases suggests that similar approach could be successfully applied in other medium, laser-produced extended plasmas. In the following chapters, we analyze the difference in the harmonic characteristics in the case of application of narrow (Chap. 2) and extended (Chaps. 3–7) plasmas.

References

1. J.L. Krause, K.J. Schafer, K.C. Kulander, *Phys. Rev. Lett.* **168**, 3535 (1992)
2. P.B. Corkum, *Phys. Rev. Lett.* **71**, 1994 (1993)
3. M. Lewenstein, P. Balcou, M.Y. Ivanov, A. L’Huillier, P.B. Corkum, *Phys. Rev. A* **49**, 2117 (1994)
4. K. Miyazaki, H. Takada, *Phys. Rev. A* **52**, 3007 (1995)
5. P. Christov, M.M. Murnane, H.C. Kapteyn, *Phys. Rev. Lett.* **78**, 1251 (1997)
6. G. Tempea, M. Geissler, M. Schnürer, T. Brabec, *Phys. Rev. Lett.* **84**, 4329 (2000)
7. T.D. Donnelly, T. Ditmire, K. Neuman, M.D. Pery, R.W. Falcone, *Phys. Rev. Lett.* **76**, 2472 (1996)
8. S.X. Hu, Z.Z. Xu, *Appl. Phys. Lett.* **71**, 2605 (1997)
9. M.Y. Ivanov, P.B. Corkum, *Phys. Rev. A* **48**, 580 (1993)
10. Y. Liang, S. Augst, S.L. Chin, Y. Beaudoin, M. Chaker, *J. Phys. B: At. Mol. Opt. Phys.* **27**, 5119 (1994)
11. Y. Akiyama, K. Midorikawa, Y. Matsunawa, Y. Nagata, M. Obara, H. Tashiro, K. Toyoda, *Phys. Rev. Lett.* **69**, 2176 (1992)
12. C.-G. Wahlström, S. Borgström, J. Larsson, S.-G. Pettersson, *Phys. Rev. A* **51**, 585 (1995)
13. R.A. Ganeev, V.I. Redkorechev, T. Usmanov, *Opt. Commun.* **135**, 251 (1997)
14. K. Krushelnick, W. Tighe, S. Suckewer, *J. Opt. Soc. Am. B* **14**, 1687 (1997)

15. R.A. Ganeev, L.B. Elouga Bom, T. Ozaki, Appl. Phys. Lett. **91**, 131104 (2007)
16. R.A. Ganeev, L.B. Elouga Bom, T. Ozaki, J. Appl. Phys. **102**, 073105 (2007)
17. D.B. Milošević, J. Opt. Soc. Am. B **23**, 308 (2006)
18. T. Popmintchev, M.-C. Chen, P. Arpin, M.M. Murnane, H.C. Kapteyn, Nature Photon. **4**, 822 (2010)
19. M.-C. Chen, P. Arpin, T. Popmintchev, M. Gerrity, B. Zhang, M. Seaberg, D. Popmintchev, M.M. Murnane, H.C. Kapteyn, Phys. Rev. Lett. **105**, 173901 (2010)
20. K. Budil, P. Salieres, M. Perry, A. L'Huillier, Phys. Rev. A **48**, 3437 (1993)
21. X. Zhou, R. Lock, N. Wagner, W. Li, H.C. Kapteyn, M.M. Murnane, Phys. Rev. Lett. **102**, 073902 (2009)
22. E. Constant, E. Mével, Attosecond Pulses, in *Femtosecond Laser Pulses: Principles and Experiments*, ed. by C. Rullière Chapter 12, 395 (Springer, Berlin, 2005)
23. P. Balcou, P. Salières, A. L'Huillier, M. Lewenstein, Phys. Rev. A **55**, 3204 (1997)
24. I.J. Kim, G.H. Lee, S.B. Park, Y.S. Lee, T.K. Kim, C.H. Nam, T. Mocek, K. Jakubczak, Appl. Phys. Lett. **92**, 021125 (2008)
25. Y. Fu, H. Xiong, H. Xu, J. Yao, Y. Yu, B. Zeng, W. Chu, X. Liu, J. Chen, Y. Cheng, Z. Xu, Phys. Rev. A **79**, 013802 (2009)
26. B. Zeng, W. Chu, G. Li, J. Yao, J. Ni, H. Zhang, Y. Cheng, Z. Xu, Y. Wu, Z. Chang, Phys. Rev. A **85**, 033839 (2012)
27. F. Brizuela, C.M. Heyl, P. Rudawski, D. Kroon, L. Rading, J.M. Dahlström, J. Mauritsson, P. Johnsson, C.L. Arnold, A. L'Huillier, Scient. Reports **3**, 1410 (2013)
28. J.-F. Hergott, M. Kovacev, H. Merdji, C. Hubert, Y. Mairesse, E. Jean, P. Breger, P. Agostini, B. Carré, P. Salières, Phys. Rev. A **66**, 021801 (2002)
29. E. Takahashi, Y. Nabekawa, K. Midorikawa, Opt. Lett. **27**, 1920 (2002)
30. E. Takahashi, Y. Nabekawa, T. Otsuka, M. Obara, K. Midorikawa, Phys. Rev. A **66**, 021802 (2002)
31. A. Ravasio, D. Gauthier, F.R.N.C. Maia, M. Billon, J.-P. Caumes, D. Garzella, M. Géléoc, O. Gobert, J.-F. Hergott, A.-M. Pena, H. Perez, B. Carré, E. Bourhis, J. Gierak, A. Madouri, D. Maily, B. Schiedt, M. Fajardo, J. Gautier, P. Zeitoun, P.H. Bucksbaum, J. Hajdu, H. Merdji, Phys. Rev. Lett. **103**, 028104 (2009)
32. T. Popmintchev, M.-C. Chen, D. Popmintchev, P. Arpin, S. Brown, S. Ališauskas, G. Andriukaitis, T. Balčiunas, O.D. Mücke, A. Pugzlys, A. Baltuška, B. Shim, S.E. Schrauth, A. Gaeta, C. Hernández-García, L. Plaja, A. Becker, A. Jaron-Becker, M.M. Murnane, H.C. Kapteyn, Science **336**, 1287 (2012)
33. A. Rundquist, C.G. Durfee, Z. Chang, C. Herne, S. Backus, M.M. Murnane, H.C. Kapteyn, Science **280**, 1412 (1998)
34. M. Ferray, A. L'Huillier, X.F. Li, G. Mainfray, C. Manus, J. Phys. B: At. Mol. Opt. Phys. **21**, L31 (1988)
35. A. McPherson, G. Gibson, H. Jara, U. Johann, T.S. Luk, I.A. McIntyre, K. Boyer, C.K. Rhodes, J. Opt. Soc. Am. B **4**, 595 (1987)
36. P. Rudawski, C.M. Heyl, F. Brizuela, J. Schwenke, A. Persson, E. Mansten, R. Rakowski, L. Rading, F. Campi, B. Kim, P. Johnsson, A. L'Huillier, Rev. Sci. Instrum. **84**, 073103 (2013)
37. T. Brabec, F. Krausz, Rev. Mod. Phys. **72**, 545 (2000)
38. E.J. Takahashi, Y. Nabekawa, K. Midorikawa, Appl. Phys. Lett. **84**, 4 (2004)

Chapter 2

HHG in Short-Length Plasmas

Here we discuss some most recent advantages in the developments of the HHG in the narrow (0.3–0.5 mm) plasmas. Among them are the spatial coherence measurements of non-resonant and resonant high-order harmonics generated in narrow laser ablation plumes, resonance processes in plasma plumes, and peculiarities of the high-order harmonics from different narrow plasmas generating at 1 kHz repetition rate.

2.1 Modern History and Perspectives of Harmonic Generation in Narrow Plasma Plumes

A search for the ways for increasing the notoriously low HHG efficiency in the extreme ultraviolet region has long been (and still is) among the most topical problems of nonlinear optics. In the majority of cases, the conversion efficiency of the high-order harmonics generating in the gaseous and plasma media turns out to be insufficient for using them as the reliable coherent short-wavelength radiation sources in biology, plasma diagnostics, medicine, microscopy, photolithography, XUV coherent diffraction imaging, and time-resolved measurements, to mention few of them.

First experiments using narrow over-excited plasma plumes were carried out in 1990s [1–6] and have shown the frustrating results. Nevertheless, there was a reason to hope that harmonic intensities may be substantially increased and efficient shorter-wavelength coherent radiation could be achieved using properly produced plasmas. There are no fundamental limitations here; it only remained finding the “optimal” conditions for formation of a plasma plume to serve as the efficient medium for the HHG. Laser-produced plasma may be validly used for this process if the effects of the limiting factors (self-defocusing, self-phase modulation, and wave phase mismatch of the harmonics and the radiation being converted) are minimized, as it was underlined in early studies of plasma HHG [1, 3, 5].

Among the special features of HHG in laser-produced plasmas, one can note a wide range of medium characteristics, which can be tuned by varying the conditions

of ablation on the surface of a solid. This applies to such parameters as plasma length, density of ions, electrons, and neutral particles, and degree of their excitation. The use of any elements of the periodic table (Fig. 2.1) [7], as well as thousands of complex samples that exist as solids, may largely extend the range of materials employed, whereas only a few noble gases are typically available for the gas HHG. Thus the exploration of practically any solid-state material through the nonlinear spectroscopy comprising laser ablation and harmonic generation can be considered as a new tool for material science.

In several cases, this method furnishes an opportunity to realize the quasi-resonance conditions and increase the efficiency of single harmonic generation due to the effect of ion transitions on the nonlinear response in different spectral regions, thus allowing the studies of those transitions possessing large oscillator strengths. This effect (Fig. 2.2a) [8] could be hardly observed in the gas HHG because of a low probability for the coincidence of the atomic transition frequencies of a few gases and the frequencies of the single harmonics of laser sources. In the meantime, studies of resonance-induced modification of the harmonic spectra generated in gases have demonstrated the enhancement of the narrow parts of harmonics due to the influence of Fano resonances and Stark shift [9].

The modern history of harmonic studies using narrow plasmas has started in 2005 [10]. A substantial increase in the highest order of generating harmonics, observation of a long plateau and emergence of a second plateau in the energy distribution of highest-order harmonics, high efficiencies obtained with several plasma formations, realization of the resonance enhancement of individual harmonics, efficient harmonic enhancement from the plasma plumes containing clusters of different materials, and other properties revealed in [11–16] have demonstrated the advantages of using optimally prepared laser-produced plasmas for the HHG. The orders of harmonics obtained in plasma media to date range into the sixties and seventies [17, 18]. The harmonics up to the 101st order have been

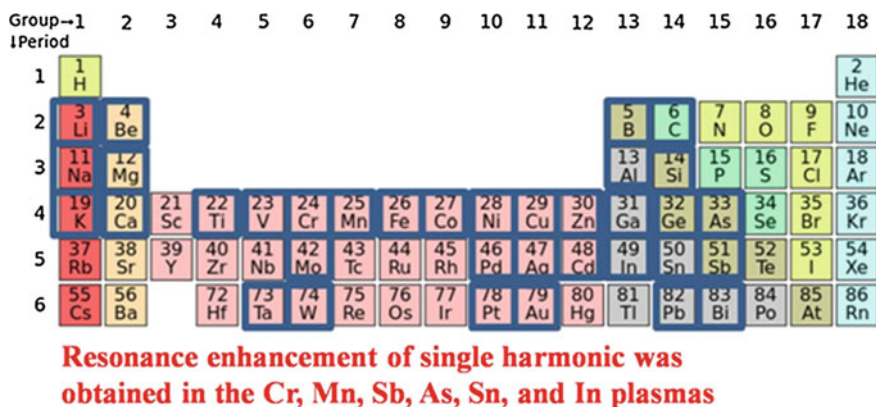


Fig. 2.1 The elements of periodic table (in *thick squares*), which were studied for the HHG in the ablation plumes. Reproduced from [7] with permission from Optical Society of America

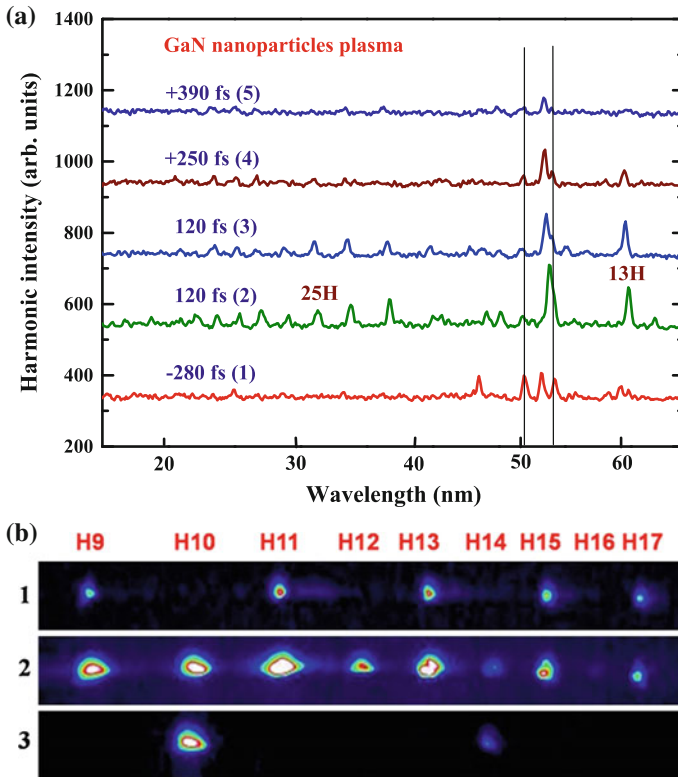
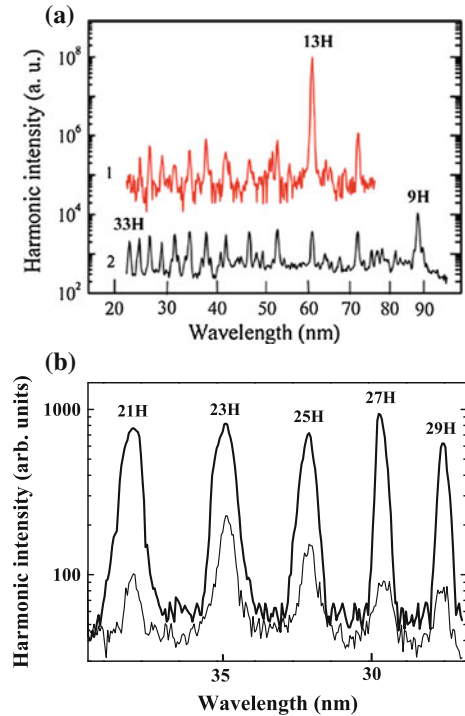


Fig. 2.2 **a** Harmonic spectra obtained from the GaN nanoparticles-contained plasma using the pulses of different chirp and duration. Reproduced from [8] with permission from American Physical Society. **b** CCD images of the harmonic spectra between the 9th and 17th orders generated in the C_{60} plasma in the cases of (1) single-color fundamental pump (800 nm), (2) two-color pump (800 + 400 nm), and (3) single-color second harmonic pump (400 nm). The data were collected under similar experimental conditions. Adapted from [23] with permission from American Physical Society. Copyright 2009

demonstrated during generation in the thin manganese plasma [19] and currently can be routinely achieved using the moderate level (60 fs, 3 mJ) laser pulses. The plasma HHG conversion efficiency in the plateau region amounted to 10^{-5} was demonstrated in the case of the laser ablation of silver targets [20–22]. Application of two-color pump led to enhancement of the odd harmonics, as well as to the appearance of strong even orders (Fig. 2.2b) [23]. In addition to that, the conversion efficiency towards a resonantly enhanced high-order harmonic was almost two orders stronger compared with the neighboring harmonics (Fig. 2.3a) [24].

The quest for new plasma media that would favor the enhancement of an individual harmonic allows further improvement of harmonic conversion efficiency. The production of a single high-intensity harmonic (rather than a group of harmonics of equal intensity in the plateau region) would open up the way to the

Fig. 2.3 a HHG spectra obtained from the (1) indium and (2) silver plasmas. Reproduced from [24] with permission from Optical Society of America.
b Harmonic distribution in the mid-plateau region in the cases of the plasma produced on the surface of bulk Ag target (*thin line-out*) and the Ag nanoparticles-contained plasma (*thick line-out*). Reproduced from [28] with permission from IOP Publishing. All rights reserved



practical application of these coherent short-wavelength sources. Resonantly enhanced harmonics observed in several plasma media allowed expecting that similar conditions will be discovered using other plasma formations. The generated harmonic wavelength may then be tuned to the transitions with high oscillator strength by wavelength tuning of the driving laser [14], as well as by varying the chirp of laser radiation [11, 13, 16]. Many new features of plasma harmonics, which were emerged during last time, allow expecting further extension of our knowledge of the material properties using this new tool of nonlinear spectroscopy. The advantages of harmonic studies in the thin plasma plumes were summarized in the monographs [25–27].

Among the achievements emerged during following years one can admit the application of the ablated nanoparticles and clusters (Fig. 2.3b) [28], definition of the high-order nonlinearities of fullerenes [29], single sub-femtosecond harmonic generation in manganese plasma using few-cycle pulses (Fig. 2.4a) [30], comparative research of plasma and gas media for efficient HHG [31], temporal characterization of plasma harmonics [32, 33], generation of continuum plasma harmonics [34], stabilization of harmonic yield over one million laser shots on the rotating targets [35], generation of high-order harmonics using picosecond driving pulses [36], various applications of 1 kHz lasers for plasma HHG to increase the average power of converted radiation [37, 38], demonstration of the quantum path

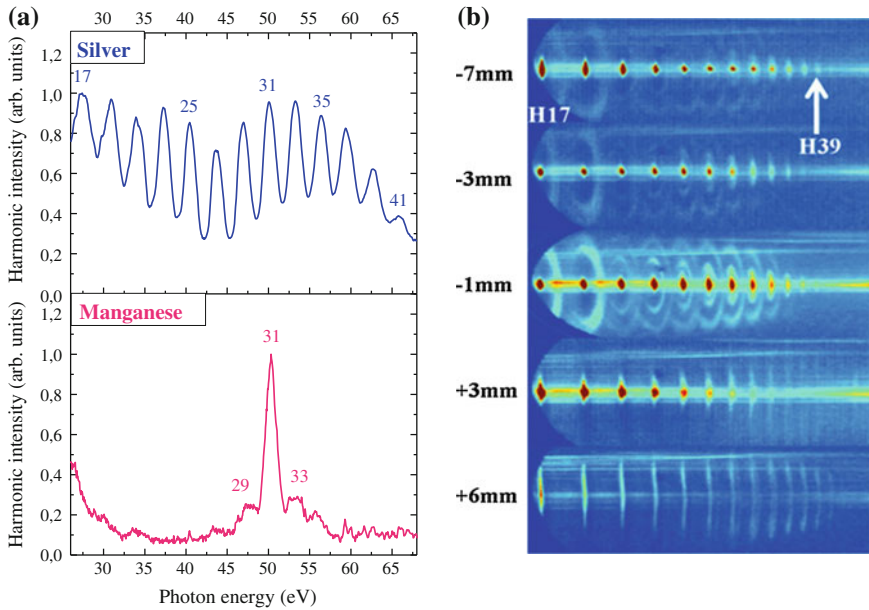


Fig. 2.4 **a** Harmonic spectra from the silver plasma (*upper curve*) and manganese plasma (*bottom curve*). Reproduced from [30] with permission from Optical Society of America. **b** Dependence of harmonic spectra on the position of aluminum plasma with respect to the focus of femtosecond radiation (negative values on the pictures correspond to focusing after plasma plume). Reproduced from [39] with permission from American Physical Society. Copyright 2011

interference of the long and short trajectories of electrons in plasma HHG experiments (Fig. 2.4b) [39], etc. All those findings substantially pushed ahead our knowledge of the peculiarities of plasma media through the analysis of their high-order nonlinear optical characteristics.

It follows from the above that investigations in this area of nonlinear optics are making rapid strides and may bring new success in the nearest future. Plasma harmonics became an important part of the studies carrying out in various laboratories worldwide [32–34, 40–46]. The achievements of present-day plasma harmonic studies motivate for further development of this technique. Recent reviews of various aspects of plasma harmonics [7, 22] made it clear that this field of nonlinear optics rapidly develops towards the applications of plasma harmonic spectroscopy, as well as further amendments of harmonic yield.

I hope that, with this short review, I convinced the reader that the plasma HHG is not simply another method for generation of coherent XUV light but rather a new technique for the analysis of various features of the harmonic emitters appearing in the plasma plumes during laser ablation of solids. In the following sections of this chapter we will discuss some most recent advantages in the developments of the HHG in the narrow (0.3–0.5 mm) plasmas.

2.2 Spatial Coherence Measurements of Non-resonant and Resonant High-Order Harmonics Generated in Narrow Laser Ablation Plumes

The high coherence of the drive laser beam can be transferred to the harmonic radiation, which can thus exhibit near full spatial coherence [47]. This makes high-order harmonics an attractive table-top, short-wavelength source for applications, such as diffraction imaging [48], holography [49, 50], and, more generally, for short-wavelength interferometry using wavefront division [51].

Studies of the spatial coherence of harmonic radiation have proved useful in helping to elucidate the underlying physics of the HHG process [52], particularly in identifying mechanisms that can degrade the coherence. Previous measurements in gas targets showed that, for laser intensities high enough to cause significant ionization of the neutral medium, the rapid production of free electrons can degrade the coherence [53–55]. The refractive index of the free electrons imparts a rapidly varying phase on the harmonic. This can lower its spatial coherence if the rate of formation of free electrons varies at different points across the focused beam [54], leading to decorrelation of the time-dependent fields. This can be caused by density or laser-intensity variations across the laser focus.

Ablation targets for HHG differ from conventional (neutral) gas targets in a number of ways. Firstly, they are usually preformed plasmas with a density distribution that is determined by the ablation dynamics and subsequent evolution of the plasma, which depend on the target composition and ablation pulse parameters in a complex way. Secondly, the HHG process can be resonantly enhanced in the plasma [24]. In the four-step model of the resonant enhancement [56], the third step (recombination) of the conventional three-step model of HHG is partitioned into two steps: the capture of a laser-accelerated electron into an autoionizing state of the parent ion followed by the radiative relaxation to the ground state with emission of the harmonic photon. For HHG in gas targets, the harmonic phase is largely determined by the phase accumulated by the electron wavepacket during its quasi-free motion in the laser field (step 2), which is the same in both the three-step and four-step models. However, in the four-step model, the phase added during the fourth step (radiative relaxation) is not negligible and can be very sensitive to the detuning from the resonance. Recently, phase distortion of resonantly enhanced harmonics in Sn ablation plumes has been investigated using the RABBIT technique for different amounts of detuning of the 17th harmonic radiation from the Sn II plasma transition at 26.27 eV [33].

These differences between ablation and conventional gas target for HHG raise interesting questions about the degree of spatial coherence of high harmonics from ablation plumes. First study of the spatial coherence of the high order harmonic radiation generated by the interaction of 45 fs Ti:sapphire laser beam with carbon (graphite) plasma plume has been reported in [45]. It was observed that the spatial coherence varies with harmonic order, laser focal spot size in plasma plume, and peaks at an optimal spot size. It has also been reported that the spatial coherence is

higher when the laser pulse is focused before the plasma plume than when focused after the plume, and it decreases with increase in the harmonic order. The optimum laser parameters and the focusing conditions to achieve good spatial coherence with high harmonic conversion have been identified, which is desirable for practical applications of the harmonic radiation.

It is known that these harmonics are emitted as low divergence, near Gaussian beams [around 2 mrad full-width-at-half-maximum (FWHM)]. Below we discuss direct measurement of their spatial coherence [57]. The reviewed studies have shown that the spatial coherence of both non-resonant and resonant harmonics from carbon, zinc, and indium ablation targets generated with few-cycle pulses is reasonably high (in the range of 0.6–0.75) and somewhat higher than for harmonics generated in argon gas under similar experimental conditions. This finding confirms that high-order harmonics from ablation plumes can be used in applications requiring high spatial coherence. For such applications, other features of the harmonic radiation from ablation targets may be useful, such as the resonant enhancement of particular harmonic orders that give rise to quasi-monochromatization of the radiation, thus reducing the requirements for spectral filtering.

The experimental set-up for the measurements of the coherence of plasma harmonics is shown in Fig. 2.5. A Ti:sapphire laser was used in these experiments and provided pulses of 30 fs duration and energies of up to 2.5 mJ at a repetition rate of 1 kHz. These pulses were focused into a 1-m-long differentially pumped hollow core fiber (250 μm inner core diameter) filled with neon [58]. The spectrally

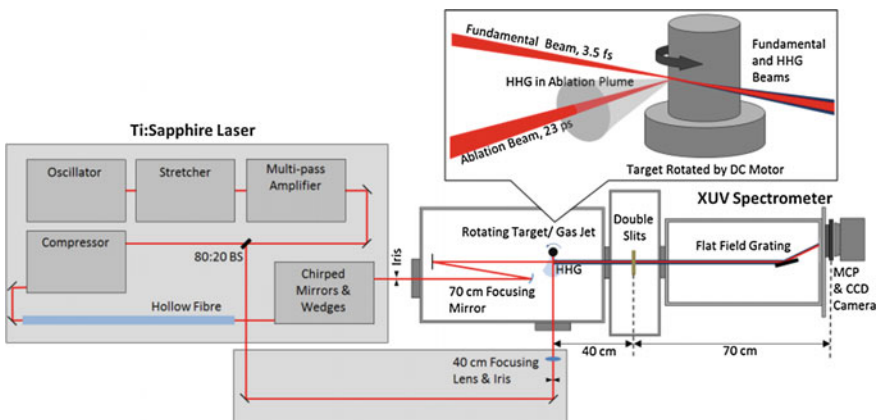


Fig. 2.5 Experimental setup for measuring the spatial coherence of the harmonics generated in ablation plasma plumes and gas targets. A chirped pulse amplification system with a hollow fiber pulse compressor was used to produce the few-cycle pulses to drive HHG. A beam-splitter was used to pick off part of the stretched laser pulse for ablation. A rotating target set-up allowed operation at 1 kHz pulse repetition rate. The harmonics were analyzed using a spatially-resolving XUV spectrometer with micro-channel plate detector. Double slits could be introduced into the harmonic beam to produce an interference pattern on the detector, from which the coherence of the radiation could be determined. Reproduced from [57]. Copyright 2014. AIP Publishing LLC

broadened pulses at the output of the fiber system were compressed by 10 chirped mirrors. High-intensity few cycle pulses (775 nm central wavelength, 0.5 mJ, 4 fs) were typically obtained. The compressed pulses were characterized spatially and temporally with a spatially encoded arrangement for spectral shearing interferometry for direct electric field reconstruction [59]. A part of the uncompressed beam of the chirped pulse amplification Ti:sapphire laser (central wavelength 800 nm, pulse energy 120 μ J, pulse duration 23 ps, pulse repetition rate 1 kHz) was split from the beam line prior to the laser compressor stage and was directed into the vacuum chamber to create an ablation plume from the target. The picosecond pulses were focused by a 400 mm focal length spherical lens to the intensity on the target surface of $I_{\text{ps}} = 8 \times 10^9 \text{ W cm}^{-2}$. Ablation plumes from carbon, zinc, and indium were produced in these experiments. The 15 mm diameter rods of these materials rotated at 30 rpm, which allowed a considerable improvement of the stability of harmonics compared with fixed targets in the case of high pulse repetition rate (1 kHz). In particular, it was shown that once the target rotation is stopped, the harmonic efficiency from the plasmas decreased by more than one order of magnitude within 1–2 s [35]. Harmonics were generated with 4 fs laser pulses, which were focused into the ablation plumes using a 700 mm focal length spherical mirror. The delay between the picosecond and the femtosecond pulses was set to 33 ns. The focal position of the femtosecond pulse with respect to the ablation plume was chosen to maximize the harmonic signal, and the intensity in the ablation plume was estimated to be $I_{\text{fs}} = 3 \times 10^{14} \text{ W cm}^{-2}$. This estimate was consistent with the 70 eV high-order harmonic cut-off that was observed in neon. Neon provides a more reliable corroboration of intensity than the HHG cut-off in argon due to the Cooper minimum in argon at 48 eV that masks the real cut-off position.

The harmonics were analyzed using an XUV spectrometer with a grazing incidence flat-field grating and an imaging micro-channel plate (MCP) detector coupled to a phosphor screen [60]. The spatially resolved spectra of the generated harmonics on the phosphor screen were recorded with a CCD camera. The experimental setup allowed the removal of the ablation target and generation of harmonics in a gas target (Ar or Ne, density $\sim 10^{18} \text{ cm}^{-3}$, target length $L = 1.5 \text{ mm}$) placed at the same position. Under these conditions, the spatially resolved HHG spectra are dominated by the low-divergence short trajectory contribution.

The spatial coherence of the harmonics was measured using double slit interference. A pair of slits was mounted on a translation stage and placed 40 cm from the targets and 70 cm from the MCP. The slits were made in a tungsten foil and had 50 μm spacing, 6 μm width, and were 10 mm long. Each interference pattern (“frame”), measured in this experiment, was integrated over 1000 laser shots. A series of measurements were made for different targets (laser-produced plasmas and Ar gas) in the following energy ranges: 15–30 eV for C, Zn, and In and 15–40 eV for Ar. The relatively low cut-off observed for C is in agreement with earlier work [44]. For each fringe pattern, the fringe visibility was determined through the relation $V = (I_{\text{max}} - I_{\text{min}})/(I_{\text{max}} + I_{\text{min}})$, where I_{max} and I_{min} are the maximum and minimum intensities of the interference pattern. With equal intensity at both slits, as

was the case in those measurements, the fringe visibility at the centre of the fringe pattern was equal to the modulus of the complex coherence factor.

Figures 2.6, 2.7, 2.8 and 2.9 show the double-slit interference data for harmonics from C, Zn, and In plasmas, and from Ar gas targets, respectively. In each figure, the spatially resolved HHG spectrum is shown in part (a), the spatially integrated spectrum is shown in part (b), and a spatial lineout of a single harmonic (interference pattern) is shown in part (c). Taking an average of the visibility at the centre of the fringe pattern over 20 frames, the measured visibilities for the different targets and harmonic orders are as follows: $V = 0.63$ for C_{H13} (i.e. 13th harmonic generated in the carbon plasma); $V = 0.66$ for In_{H13} ; $V = 0.74$ for Zn_{H11} ; and $V = 0.47$ for Ar_{H15} . The HHG spectra from Zn and In have shown resonantly enhanced harmonics due to the overlap of harmonic radiation with plasma resonance lines. In the case of Zn (Fig. 2.7), the emission spectrum was dominated by a peak at ~ 18 eV, which was identified as the partial overlap of H11 (photon energy ~ 17 eV, FWHM bandwidth ~ 1 eV) with the 18.3 eV transition $3d^{10}-3d^9(^2D)4p$ of Zn III, which has an oscillator strength significantly greater than other lines in

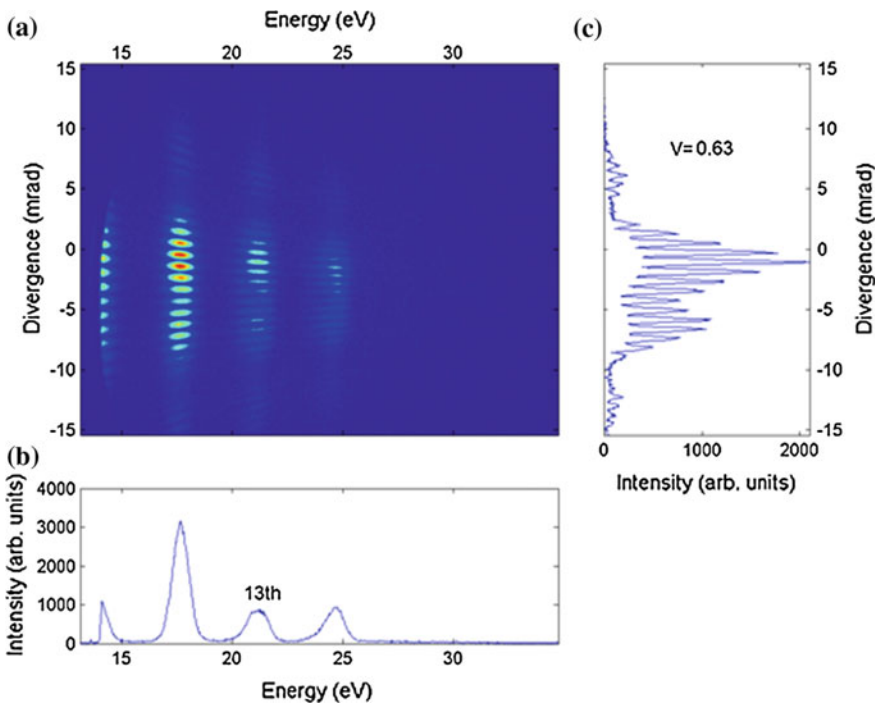


Fig. 2.6 Non-resonant harmonics generated in a carbon plasma plume. **a** Spatially resolved HHG spectrum showing interference fringes from the double slits, **b** spectral line-out, **c** spatial line-out of the interference pattern for the 13th harmonic. The average visibility of fringes near the centre of the pattern was $V = 0.63$. Reproduced from [57]. Copyright 2014. AIP Publishing LLC

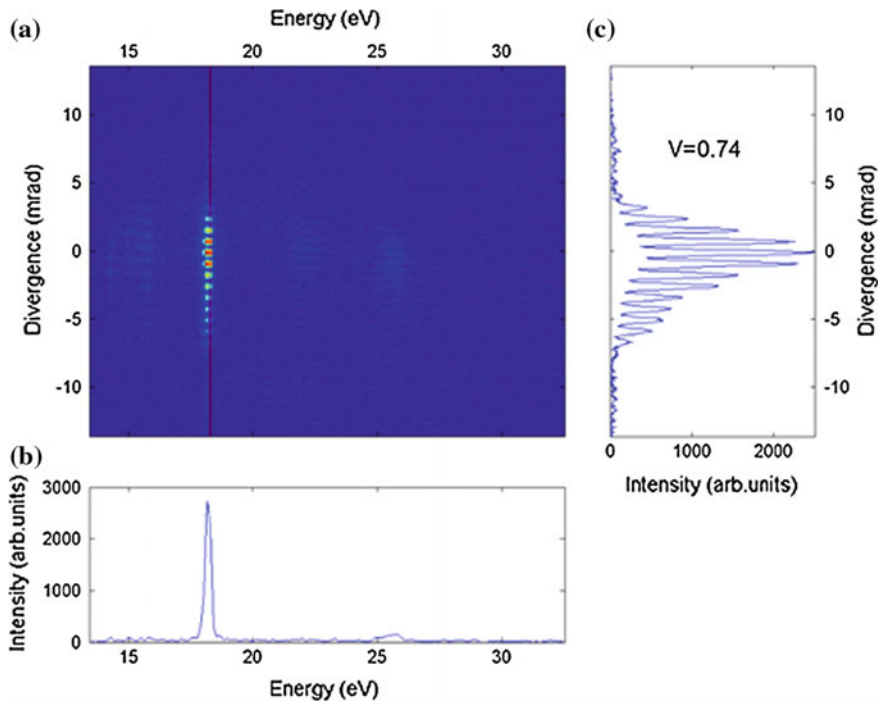


Fig. 2.7 Resonantly enhanced harmonics generated in a zinc plasma plume. **a** Spatially resolved HHG spectrum showing interference fringes from the double slits, **b** spectral line-out showing enhancement of the 11th harmonic due to its overlap with a plasma transition line in Zn^+ at 18.3 eV, **c** spatial line-out of the resonant harmonic. The average visibility of fringes near the centre of the pattern was $V = 0.74$. Reproduced from [57]. Copyright 2014. AIP Publishing LLC

this spectral region [61]. For In (Fig. 2.8), an enhanced feature at ~ 20 eV was observed and attributed to the overlap of H13 (photon energy ~ 20 eV, FWHM bandwidth ~ 1 eV) with the 19.9 eV ground to autoionizing state transition $4d^{10}5s^21S_0-4d^95s^25p(^2D)1P_1$ in In II, which has an oscillator strength (gf) $\sim 10 \times$ larger than other transitions [62]. The variation of HHG conversion efficiency in the vicinity of resonance lines of indium has been reported in [24].

Attempts were made to calculate the visibility of the nonresonant harmonics of Zn and In; however, the signal to noise ratio was too low to accurately analyze the fringe patterns. The maximum visibility measured in those experiments ($V = 0.74$ for the Zn target) was lower than reported visibilities of gases in some earlier work [47] but is consistent with a small departure from full spatial coherence for the driving laser field. In the absence of other effects that can degrade the coherence, the visibility of the fringe pattern for the q th harmonic is approximately given by $V_q \approx 1 - q(1 - V_1)$, where V_1 is the visibility for the driving laser field [54]. Hence, a value of $V_1 = 0.98$ for the laser beam would already completely account for the visibility $V_{\text{H11}} = 0.74$ measured for the 11th harmonic from the Zn target. Though

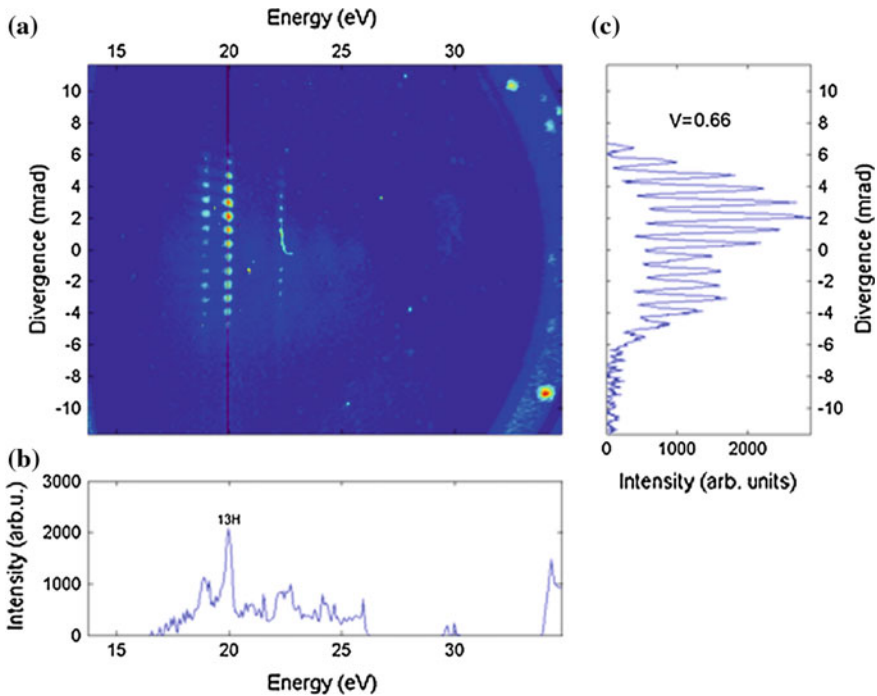


Fig. 2.8 Resonantly enhanced harmonics generated in an indium plasma plume. **a** Spatially resolved HHG spectrum showing interference fringes from the double slits, **b** spectral line-out showing enhancement of the 13th harmonic due to its overlap with a plasma transition line in In^+ at 19.9 eV, **c** spatial line-out of the resonant harmonic. The average visibility of fringes near the centre of the pattern was $V = 0.66$. Reproduced from [57]. Copyright 2014. AIP Publishing LLC

the femtosecond laser beam exhibited essentially full spatial coherence, one cannot rule out such a small decrease in coherence of the radiation delivered to the target, for example, due to nonlinear propagation effects in air and the vacuum chamber window coupled with a small intensity asymmetry of the transverse beam profile.

The significantly lower visibility ($V = 0.47$) observed for harmonics from Ar gas, compared to the plasma targets (average visibility 0.68), was attributed to increased free electron production during the propagation of laser pulse through the Ar gas compared to the other targets. One should note that only rapid variation of the free electron density during the HHG process can degrade the harmonic spatial coherence. Pre-existing free electrons in the ablation plumes should not degrade the coherence, since their density is effectively static on the timescale of the few-cycle pulse.

The tunnel ionization of the targets by a 4 fs laser pulse was simulated using ionization rates from Ammosov-Delone-Krainov (ADK) theory [63]. In the absence of details of the ionic composition of the ablation plasmas, it was assumed that the plasma targets are fully singly ionized. ADK rates are known to be reasonably accurate for rare gases such as Ar, but for multielectron atoms they significantly

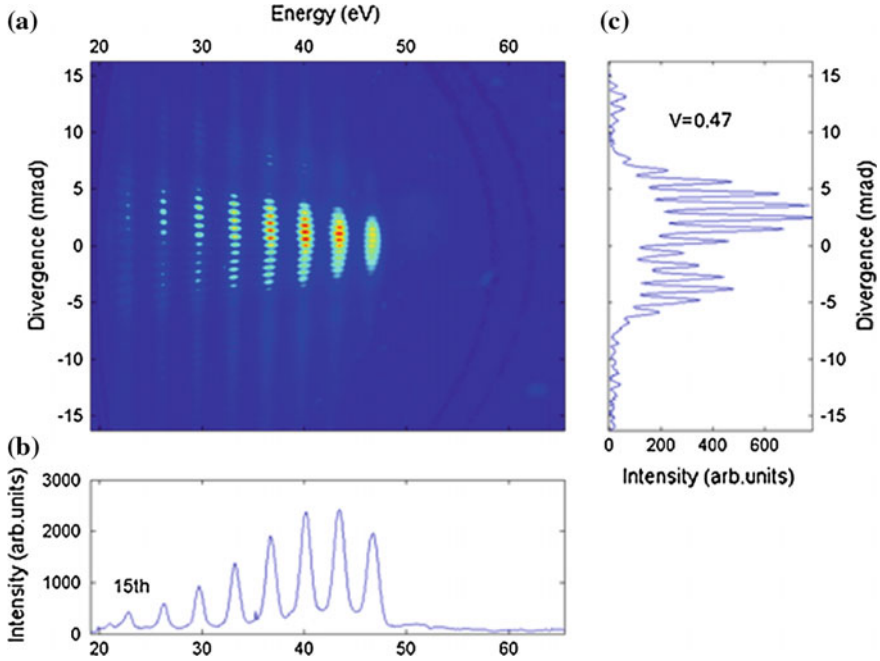


Fig. 2.9 High-order harmonics generated in argon gas. **a** Spatially resolved HHG spectrum showing interference fringes from the double slits, **b** spectral line-out, **c** spatial line-out of the 15th harmonic. The average visibility of fringes near the centre of the pattern was $V = 0.47$. Reproduced from [57]. Copyright 2014. AIP Publishing LLC

overestimate the ionization rate [64]. Therefore, the calculations for C, Zn, and In provide an upper limit for the ionization fraction in those atoms. For a peak intensity of $3 \times 10^{14} \text{ W cm}^{-2}$, the ionization fraction at the peak of the pulse was calculated to be ~ 0.1 for Ar ($I_p = 15.75 \text{ eV}$) compared with $\sim 10^{-5}$ for C II ($I_p = 24.4 \text{ eV}$), 0.004 for In II ($I_p = 18.87$), and ~ 0.01 for Zn II ($I_p = 17.96 \text{ eV}$). Using the target densities given earlier, this implies a free electron density of $\sim 10^{17} \text{ cm}^{-3}$ produced during HHG in the Ar target, which is at least 3 \times , 8 \times , and 3000 \times higher than for Zn, In, and C targets, respectively. The measured visibility for the case of Ar is consistent with earlier work in which free electron densities in the region of 10^{17} cm^{-3} produced during harmonic generation were shown to lead to a reduction in harmonic visibility to the range of 0.4–0.6 for similar harmonic orders [52, 55]. One can note that for carbon, an intensity of $3 \times 10^{14} \text{ W cm}^{-2}$ is close to the ionization saturation intensity. Therefore, a small fraction of neutral carbon atoms in the ablation plume ($I_p = 11.26 \text{ eV}$), as seen in earlier work [65], would increase the electron density significantly compared to the value calculated above. This could explain the lower visibility for harmonics generated in carbon compared to the other plasma targets.

2.3 Resonance Processes in the Plasma Plumes

2.3.1 *Resonant and Non-resonant High-Order Harmonic Generation in the Plasmas Produced by Picosecond and Femtosecond Pulses*

In order to increase the conversion efficiency into high-order harmonics at kHz repetition rate various routes can be followed. New methods of plasma formation could be an attractive way to improve the harmonic yield. A straightforward implementation is the replacement of the plasma generating laser beam with several tens to hundreds of picosecond duration by one which features only a few tens of femtosecond duration. Thereby, one can elucidate the importance of the laser intensity or the laser fluence for the formation of the plasma, which shows the optimal harmonic yield. Closely related is the investigation of an enhancement of specific harmonics in the spectral vicinity of ionic transitions of the plasma constituents [24, 38]. Below we analyze the results on the application of femtosecond and picosecond laser pulses for plasma formation on metal targets at 1 kHz repetition rate and particularly take attention to the resonance enhancement of single harmonics in these plasmas [66].

A chirped-pulse amplified Ti:sapphire laser with preamplifier and cryogenically cooled booster amplifier [67] delivering pulses with 40 fs duration at a central wavelength of 800 nm and at 1 kHz repetition rate was used as the main laser driving source. Part of the uncompressed radiation was split off from the beam line prior to the compressor stage (800 nm, 0.8 mJ, 12 ps) and used for ablation of the solid targets placed in a vacuum chamber (Fig. 2.10a). This beam was loosely focused onto the target with a spot size of about 300 μm diameter. The resulting intensity of the heating pulse on the target surface of up to $E_{\text{hp}} = 9 \times 10^{10} \text{ W cm}^{-2}$ created a weakly ionized plasma plume. After a variable optical delay in the range from 5 to 75 ns, required for formation and expansion of the plasma plume away from the target surface, the compressed driving laser pulse (800 nm, 0.6 mJ, 40 fs) was focused into the plasma by a 500 mm focal length lens to generate the high-order harmonics. Intensities up to $4 \times 10^{14} \text{ W cm}^{-2}$ have been employed. The position of the focus relative to the plume was chosen to maximize the harmonic output. HHG experiments were also performed using the femtosecond pulse with 40 fs duration as ablating pulse. In that case a beam splitter was placed outside the laser and divided the femtosecond beam into two parts of equal energy of 0.6 mJ for the heating and the harmonic driving pulses (Fig. 2.10a).

The harmonic emission was analyzed using an XUV spectrometer consisting of a flat field grating and MCP detector coupled to a phosphor screen. The images of harmonics were captured using a cooled CCD camera. The XUV spectrometer allowed the registration of the 11th to 23rd harmonics of 800 nm radiation. Various targets (Al, Cu, Ag, In, and Sn) prepared as 15 mm thick rods were used in these experiments. To minimize overheating and damage of the surface from repeated laser shots the rods rotated at slow revolutions, thus ensuring more stable ablation

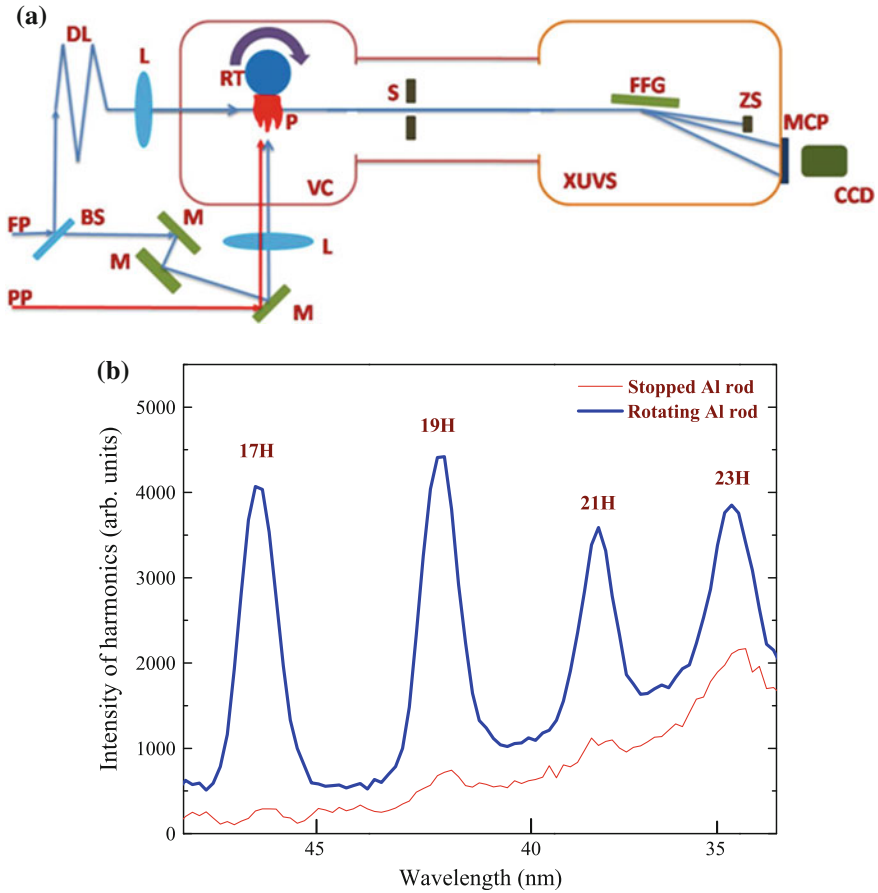


Fig. 2.10 **a** Experimental setup for plasma harmonic generation using picosecond and femtosecond heating pulses. PP, picosecond pulses; FP, femtosecond pulses; BS, beam splitter; M, mirrors; DL, delay line; L, focusing lenses; VC, vacuum chamber; RT, rotating target; P, plasma plume; S, slit; XUVS, extreme ultraviolet spectrometer; FFG, flat field grating; ZS, zero-order diffraction stop; MCP, micro-channel plate; CCD, CCD camera. **b** Harmonic yields from the plasma produced on the rotating (*thick blue curve*) and stopped (*thin red curve*) aluminum rods. Reproduced from [66] with kind permission of The European Physical Journal (EPJ)

conditions analogous to the technique of plasma harmonics stabilization [35]. After moving to a new spot, the previously irradiated target area cooled down and became available again (one rotation later) for further ablation with approximately the same harmonic yield.

The stability of the harmonics from plasma plumes is an important issue for any application of coherent short-wavelength radiation. The cylindrical metallic rods were rotated with different revolutions per minute. A variation from 10 to 300 rpm did not considerably influence the harmonic yield. At the given pumping laser spot

size a rotational speed of 50 revolutions per minute would yield a new surface area for each laser pulse. It seems that this is not necessary for a stable operation. Once the target rotation is stopped, the harmonic efficiency from the plasma plume was significantly decreased. Figure 2.10b shows the line-outs of the harmonic spectra generated from the plasmas produced during ablation of rotating (thick blue curve) and stopped (thin red curve) aluminum rods. One can see the drastic difference between these two spectra collected at identical experimental conditions of target ablation. The harmonics (17th–23rd orders) decreased by a factor of greater than 10 within a few seconds once the target stopped to rotate. The reason of such a drastic decrease is the melting of the surface of the fixed target, as has been reported in [35].

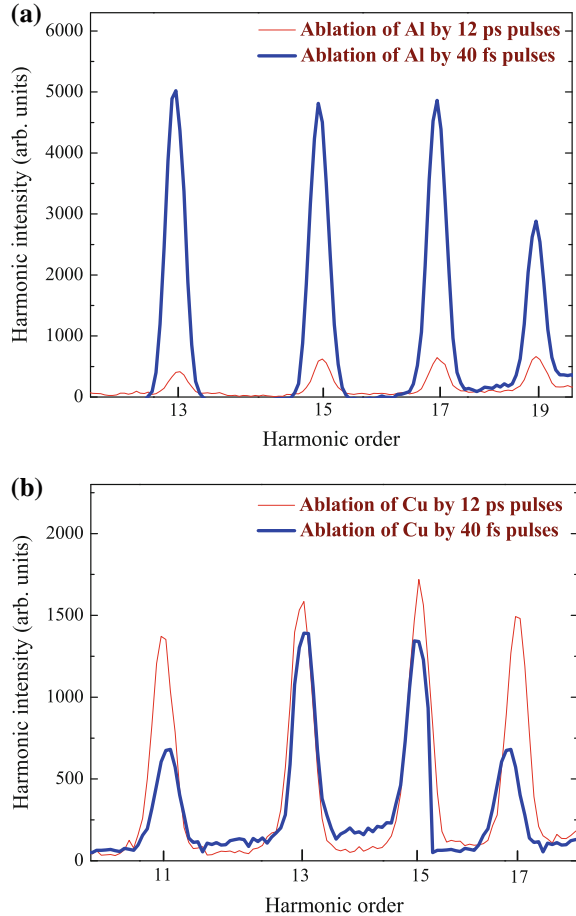
The conversion efficiency in the Al plasma in the range of 17th–23rd harmonics was estimated from the comparison with the harmonics generated in the silver plasma during a same set of experiments. The conversion efficiency from the latter medium at similar conditions of experiments has been reported in [20] to be 8×10^{-6} . One can point out the difficulty in carrying out the experiments at absolutely the same conditions. The efficiency of HHG depends on the density of the target, the laser pulse parameters (intensity, pulse duration, contrast, focusability, etc.), background ionization, composition of the medium, etc. These parameters cannot exactly be reproduced in different experimental setups with different driving laser sources. However, previous experiments show that the ratio between the harmonic yields from different plasmas remains approximately the same even when being studied in different laboratories. The density of the plasma was optimized in both cases to provide a maximum harmonic yield. The contrast does not play any role during plasma HHG. The same can be said about the pulse duration. The intensity defines the cut-off harmonic rather than the harmonic yield being in the saturation conditions. Focusability plays role in the case when the Rayleigh length becomes shorter than the size of nonlinear medium.

Background ionization was optimized in all plasma harmonic experiments prior to the measurements of the conversion efficiency. The composition of the medium was the same (neutrals and singly ionized particles of Al and Ag with approximately the same ionization rate). So, the optimization of HHG in both plasmas allows a rough estimation of the HHG efficiency. The efficiencies of harmonics from these two plasmas were rated as 1:4.

After achieving stable harmonic generation using picosecond ablating pulses, comparative studies were carried out on the plasma formation using pulses of different duration (12 ps and 40 fs). In these two cases approximately the same fluence of the heating pulses was maintained ($\sim 1 \text{ J cm}^{-2}$) by using the same focusing conditions and heating pulse energy, while the intensities of heating 12 ps and 40 fs pulses were 9×10^{10} and $2.5 \times 10^{13} \text{ W cm}^{-2}$. Note the ~ 300 times increase of the intensity of the heating pulse on the target surface in the case of femtosecond pulses compared to picosecond pulses.

One of the aims of these studies was to define which parameter, fluence or intensity of the heating pulse, plays the dominant role in the formation of the suitable plasma for efficient HHG. Figure 2.11 shows two examples of harmonic

Fig. 2.11 Harmonics from the **a** Al and **b** Cu plasmas produced by 12 ps (*thin red curves*) and 40 fs (*thick blue curves*) heating pulses. Reproduced from [66] with kind permission of The European Physical Journal (EPJ)



spectra obtained from (a) aluminum and (b) copper plasmas using the picosecond (thin red curves) and femtosecond (thick blue curves) pulses. One can notice comparable harmonic yields from the Cu plasmas in both regimes of plasma formation, while in the case of Al plasmas, in the fluence range investigated, some advantage of plasma formation using femtosecond pulses for efficient HHG was observed. The use of relatively long or short heating pulses may drastically change the dynamics of formation and spreading of the laser plasma. First attempt to address this issue in the case of plasma plumes was reported in [68].

The observed prevalence of femtosecond pulse produced plasma over picosecond pulse produced plasma could be related with the dynamics of the plasma formation on the aluminum surface. One can assume that, in the case of short pulses, the ablation of aluminum could lead to the formation of some amount of nanoparticles in the plasma plume. These particles may cause the enhancement of the harmonic yield compared with the neutrals. To prove this assumption one has to

analyze the morphology of debris from the ablation of the Al target by the femtosecond pulses as well as to use mass spectrometry of the plasma plume. Probably, the ablation of aluminum was carried out at the conditions when the “optimal” plasma formation coincided with the conditions for the formation of aluminum clusters. Another situation was in the case of other targets. The over-excitation of targets leading to the formation of nanoparticles caused the appearance of a significant amount of free electrons, which led to a phase mismatch of the interacting waves.

The most important parameter for plasma formation turned out to be the fluence rather than the intensity of the pumping radiation. When the fluence was maintained in the range of $0.8\text{--}1.2\text{ J cm}^{-2}$, the harmonics from the plasma showed a reasonably good stability using either picosecond or femtosecond heating pulses. An increase of this parameter to greater than 2.3 J cm^{-2} resulted in a disruption of the harmonic spectra, the appearance of strong ionic lines, and a phase-mismatch between driving and harmonic waves due to the presence of abundant free electrons. One may conclude from the above results that, at the used experimental conditions, laser ablation using pulses of different duration at optimal and equal fluences of the ablating radiation leads to the formation of comparable atom and ion concentrations in both plasmas. These plasma bursts reached the position of the femtosecond driving pulse at about the same time and contained approximately the same number of particles (ions and neutrals) per volume unit.

Below we discuss the resonant enhancement of some specific harmonics generated at different conditions of target ablation (i.e. picosecond and femtosecond pulse induced plasma formation). It has previously been shown that a resonance-induced enhancement of HHG can be achieved in various plasma media at specific single harmonics. Since the first observation of this phenomenon in indium plasma [24], some new media (GaAs [13], Sb [69], Cr [16]) were identified for the potential enhancement of single harmonics due to their spectral closeness with the ionic transitions possessing strong oscillator strengths. Analogous attempts for noble gases, both theoretical and experimental, were reported, which, however, were less successful to demonstrate, until recent time, a resonance enhancement of a single harmonic, even in cases where such an enhancement was expected [70–73]. This fact can be attributed to the availability of a much wider range of target materials for plasma HHG compared to the few commonly used gases, which increases the possibility of the resonance of an ionic transition in the plasma media matching one of the harmonic wavelengths.

The resonant enhancement of HHG was observed in the tin plasma using the picosecond heating pulses (Fig. 2.12a). A strong 17th harmonic ($h\nu = 26.35\text{ eV}$) was observed analogous to those reported in previous studies of this plasma medium [14, 38, 74]. However, in the present case a stronger enhancement of the 17th harmonic is observed, with an enhancement factor of about $10\times$ compared with neighboring harmonic orders. Further, the 13th harmonic ($h\nu = 20.15\text{ eV}$) generated in an indium plasma was studied at different ablation conditions. The experiments with indium plasma produced by laser ablation using picosecond pulses showed an about 70-fold enhancement of the 13th harmonic relative to the

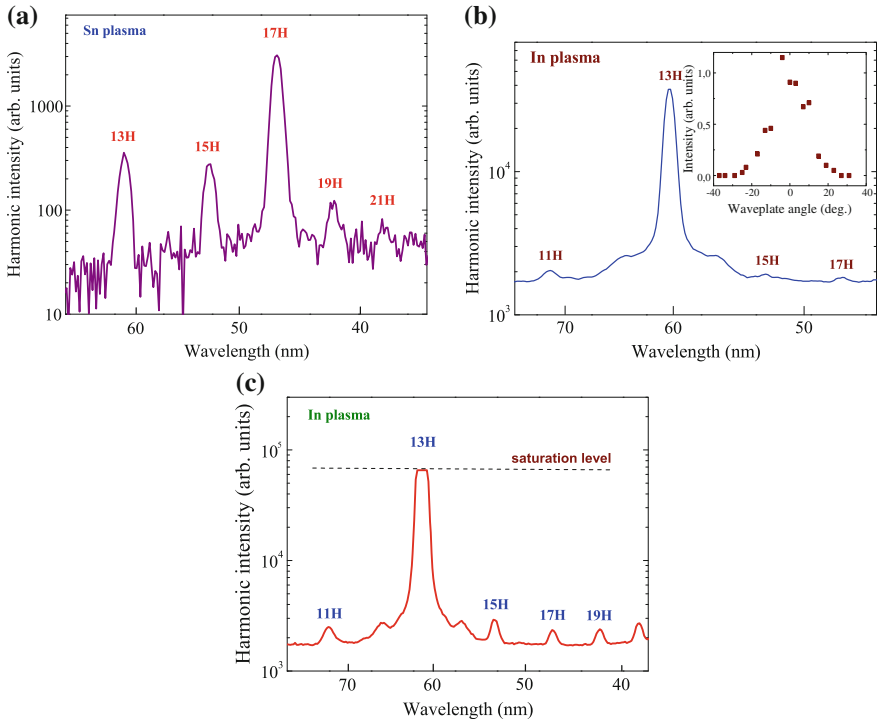


Fig. 2.12 **a** Harmonic spectrum from tin plasma. The resonant (17th) harmonic was ~ 10 times stronger than neighboring ones. **b** Indium harmonic spectrum in the case of plasma produced by 12 ps pulses. The ratio between the 13th and other harmonics in this region was ~ 70 . *Inset* Polarization dependence of the 13th harmonic yield. **c** Harmonic spectrum from the indium plasma produced by 40 fs pulses. The 13th harmonic was saturated. The enhancement of resonance harmonic over the plateau harmonics exceeded 10^2 . Reproduced from [66] with kind permission of The European Physical Journal (EPJ)

neighboring ones (Fig. 2.12b). Polarization measurements of the 13th harmonic yield showed the expected decrease of its intensity with the change of the polarization of the driving radiation from linear to elliptical and circular, which is a characteristic feature of this nonlinear optical process (see inset in Fig. 2.12b).

The application of femtosecond pulses for ablation of the rotating indium target showed an even stronger 13th harmonic generation, with pronounced neighboring harmonics (Fig. 2.12c). The saturated 13th harmonic is presented in this figure together with the 11th to 21st harmonics. In this case the enhancement exceeded a factor of $100\times$. Note the logarithmic scales of the harmonic intensities in Fig. 2.12. The two side lobes visible in the spectral vicinity of the 13th harmonic actually also belong to this harmonic and can be traced to the quantum path interference ring between the short and long trajectories of accelerated electrons. The intensity of this ring is comparable with those of neighboring harmonics, as the line-outs in Fig. 2.12b, c suggest.

Below we discuss the concentration properties of the plasmas produced by the pulses of different duration studied in [66]. The molecular dynamics based laser ablation simulation for Al and Cu targets was carried out using optimal experimental parameters of laser radiation by means of the code ITAP IMD [75]. One can take the advantage of short heating pulses (12 ps and 40 fs), which allowed a direct simulation of the ablation process at equal fluence (1 J cm^{-2}). However, the optimal delay between the beginning of ablation and the interaction of targets with the driving pulse is of the order of tens of nanoseconds, which cannot be easily simulated directly. In addition, little is known about the heating of already ablated particles. Therefore, for a correct treatment of the delay, which is an important optimization parameter, one should use the following calculation model. After leaving the surface of the sample all particles were considered as non-interacting with the field and were removed from further simulation time steps. For all particles, which left the surface after a given simulation time step, only those with kinetic energies sufficient to be in the interaction volume ($\sim 200 \text{ }\mu\text{m}$ above the surface) exactly after the supposed delay (5, 30, 40 and 75 ns) were chosen for calculation.

In order to calculate the relative concentration of neutrals and ions the single atom ionization probabilities were calculated by time-dependent density functional theory using the Octopus package [76, 77]. The ionization probability was computed as the occupation of all but the 10 lowest states. The simulations for the 40 fs ablating pulse were performed directly. For 12 ps ablation pulses a series of calculations over 50 fs with constant intensities was performed, which allowed the definition of ionization probability over the envelope of the ablating pulse, which is then approximated by a least-squares fit to yield a continuous time dependent function of the ionization probability. Then, at every time step of the molecular dynamics simulation, the number of particles with velocities sufficient to reach the interaction region after a given delay was multiplied by this ionization probability. This approach yielded the concentration of ionized particles in the interaction region with the fundamental HHG pulse. As a result, the relative number of ionized species was slightly different for different delays, however, the absolute difference was no larger than 5 %. Calculations were performed for Al and Cu for two ablating pulse durations. The concentrations of neutral and ionized particles obtained are presented in Table 2.1. The most important parameter for plasma concentration turned out to be the fluence rather than the intensity of the heating radiation.

One may see from the results presented in table that, at the used experimental conditions, all concentrations arising from ablation by the picosecond and femtosecond pulses of the same fluence are close to each other. It is seen that for Al the largest concentration of neutral particles was obtained for 30 ns delay for both heating pulses, while for Cu better results were found for 40 ns delay. One should note that, at given HHG conditions (driving pulse is not ultrashort, plasma is not very dense, no resonant absorption is present), the plasma concentration influences the HHG yield mainly in two ways. It increases the number of particles participating in HHG, and thus HHG intensity grows with the increase of the concentration, and further it increases the number of the free electrons, which influence HHG efficiency in a rather complicated way.

Table 2.1 Concentrations of neutral and ionized atoms in the interaction volume (in 10^{17} cm^{-3}) for two different durations of the ablation pulse on the Al and Cu targets and at different delays between heating and driving pulses

Delay (ns)	Al				Cu			
	40 fs		12 ps		40 fs		12 ps	
	Neutral	Ion	Neutral	Ion	Neutral	Ion	Neutral	Ion
5	1.53	0.24	1.67	0.11	1.51	0.26	1.43	0.12
30	3.47	0.21	2.79	0.15	2.77	0.23	2.65	0.14
40	2.58	0.26	2.61	0.13	3.15	0.31	2.88	0.16
75	1.73	0.27	1.45	0.10	1.61	0.24	1.51	0.11

Pulse energies of 0.6 and 0.8 mJ were assumed for 40 fs and 12 ps ablating pulses, respectively. Reproduced from [66] with kind permission of The European Physical Journal (EPJ)

2.3.2 Resonance Enhancement of the 11th Harmonic of 1064 nm Picosecond Radiation Generated in Lead Plasma

Here we analyze the results of studies of the HHG in a lead plasma using the relatively long (picosecond) driving pulses [78]. The two-stage amplification of a single pulse of Nd:YAG laser (wavelength 1064 nm, pulse duration 38 ps) was followed by splitting of this pulse into two parts, one (pump pulse) with the energy of 5 mJ, which was used for plasma formation on the target, and another (probe pulse) with the energy of up to 28 mJ, which was used, after some delay, for frequency conversion in the prepared plasma. The pump pulse was focused inside the vacuum chamber containing an ablating target to create the plasma plume. The intensity of the probe pulse at the focus was $4 \times 10^{13} \text{ W cm}^{-2}$. The delay between these two pulses during most of experiments was maintained at 50–70 ns, which is optimal for efficient harmonic generation in laser-produced plasmas. The pulse delay was changed by introducing variable path for the converting pulse. The harmonic radiation was analyzed using the vacuum monochromator and was detected using the luminescent absorber (sodium salicylate) and photomultiplier tube (PMT).

The Pb, Sn:Pb alloy, and Sn were used as the targets during these experiments. A three-coordinate manipulator made it possible to change the targets and to control the zone of interaction of the probe radiation with the plasma relative to the target surface. Various gases were inserted inside the vacuum chamber containing plasma plumes to analyze the influence of the dispersion properties of these gases on the variations of harmonic spectra. The chamber allowed the insertion of the gases and was connected to the vacuum monochromator, thus the gas was also inserted in this monochromator. The absorption of the resonance-enhanced 11th harmonic of 1064 nm radiation at the used densities of gases was insignificant.

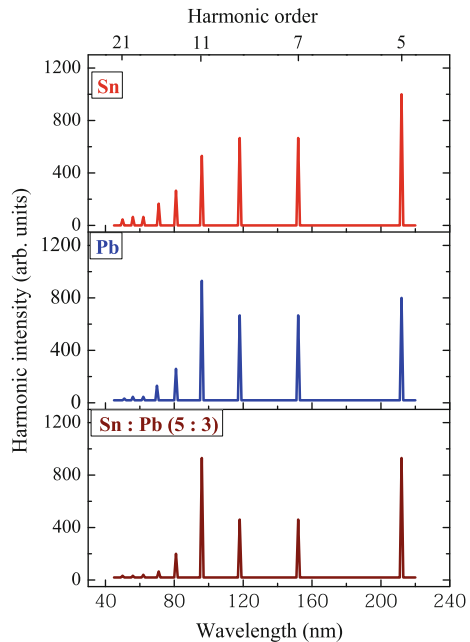
Below we present some specific features of lead and alloy plasmas as the media of HHG using the picosecond laser pulses. The goal of these studies was to define

whether the components of Pb-containing plasma influence the resonance-enhanced harmonic generation efficiency. Changing a composition of plasma from pure lead was accomplished using an alloy of this material, which consisted of tin and lead (at a volume ratio of $\sim 5:3$). Plasma harmonic spectra from pure lead and Pb:Sn alloy with those from pure tin were compared during these studies. To analyze the influence of the propagation effect the variations of harmonic spectra from lead plasma were studied while adding different gases in the vacuum chamber, thus changing the dispersion inside the plasma plume.

Figure 2.13 shows the HHG spectra obtained in the Sn, Pb, and Sn:Pb alloy plasma plumes. The harmonics from tin plasma (Fig. 2.13, upper panel) showed a gradual decrease of each next order, which is a common feature in the case of most of plasma HHG experiments [13]. Contrary to that, a lead plasma demonstrated the enhanced 11th harmonic (Fig. 2.13, middle panel), which was stronger than the lower orders. This peculiarity of lead harmonics was maintained at different conditions of experiments by varying the confocal parameter, plasma length, and so forth. The concentration of plasma ($\sim 2 \times 10^{17} \text{ cm}^{-3}$) was insufficient for the absorption of lower-order harmonics to create the conditions of the stronger 11th harmonic compared with lower ones.

The harmonics from the mixture of lead and tin plasmas comprised both harmonic spectra while maintaining the enhanced 11th harmonic (Fig. 2.13, bottom panel). It is seen that the role of other plasma components (i.e., the tin in the case of ablating Sn:Pb alloy) was insignificant and did not lead to the considerable variation of the envelope of harmonic spectra compared with the pure Pb plasma plume.

Fig. 2.13 Harmonic spectra from the Sn, Pb, and Sn:Pb alloy (5:3) plasmas. Reproduced from [78] with permission from Optical Society of America

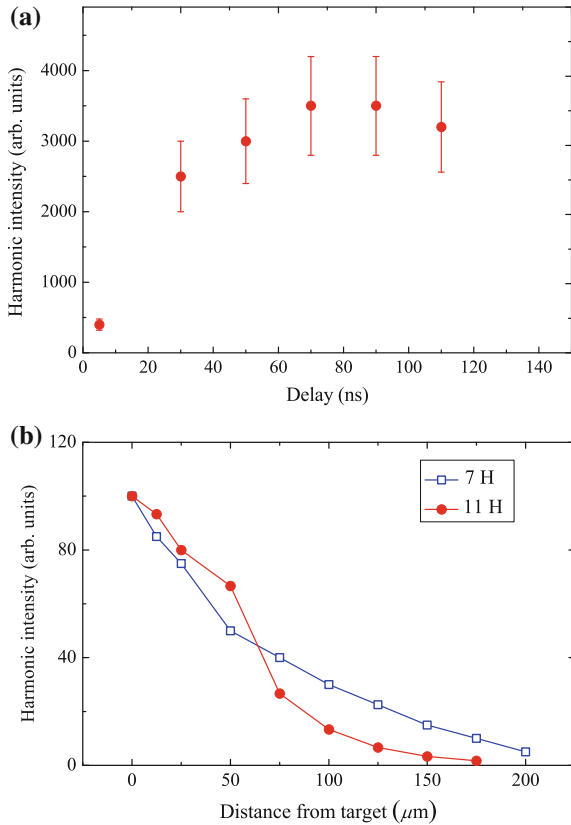


There are no specific reasons in different enhancement factors of the 11th harmonic in the pure Pb and Sn:Pb plasmas. The ratio I_{11H}/I_{5H} from shot to shot was close to 1, or slightly larger, while in both plasmas stronger 11th harmonic was observed with regard to the 9th and 7th orders. This observation points out the insignificant influence of the dispersion properties of additional plasma component on the relation between the phases of the 11th harmonic and 1064 nm radiation.

The comparative studies of harmonic generation efficiency were carried out by moving the translating stage up and down, thus allowing to measure the HHG conversion efficiency (in arbitrary units) in different plasmas without changing the conditions of experiments (delay between pulses, intensity of the heating and converting pulses, distance from the target to the axis of propagation of the converting radiation, confocal parameter of the radiation, and so forth). These studies allowed comparing the efficiencies of harmonics from various metal plasmas during one set of measurements just by changing the targets at similar conditions. The meaning of “arbitrary units” refers to the voltage signal measured from the PMT registering the luminescence from the sodium salicylate. No absolute measurements of HHG conversion efficiency were carried out for each set of studies, since it was unpractical due to necessity in the changes of the conditions of experiments. However, in some cases the absolute values of conversion efficiency were measured by using the technique described in [20]. The conversion efficiency of HHG was defined using the following procedure. At the first step, the fourth harmonic signal was measured using a “monochromator + sodium salicylate + PMT” detection system using the calibrated energy of the 4th harmonic of 1064 nm radiation generating in the nonlinear crystals. This allowed the calibration of monochromator and registration system at the wavelength of 266 nm. Since the quantum yield of sodium salicylate has the same value along a broad range between 30 and 350 nm, the calibration of the registration system at 266 nm allowed the calculation of the conversion efficiency along the whole spectral range of harmonic measurements.

The conversion efficiency of the 11th harmonic from the Pb plasma was measured to be 3×10^{-6} . The enhanced harmonic from lead plasma was analyzed at different experimental conditions. The delay between heating and converting pulses is crucial for optimization of the HHG. A typical dependence of the 11th harmonic intensity on the delay between pulses is presented in Fig. 2.14a. At the initial stages of plasma formation the concentration of particles (neutrals and singly charged ions) in the interaction area is insufficient, since the particles possessing the velocities of $\sim 5 \times 10^5 \text{ cm s}^{-1}$ do not reach the optical axis of probe beam propagation ($\sim 100 \text{ }\mu\text{m}$ above the target surface). The increase of delay allowed the appearance of plasma particles along the path of the probe pulse, which caused the growth of HHG efficiency. Further increase of delay led to saturation of the HHG at $\sim 70 \text{ ns}$ and gradual decrease of conversion efficiency at longer delays ($>110 \text{ ns}$). The influence of the distance between the target and the optical axis of propagation of the probe radiation at a fixed delay is shown in Fig. 2.14b. This distance was varied by a manipulator, which controlled the position of the target relative to the waist of the probe picosecond radiation.

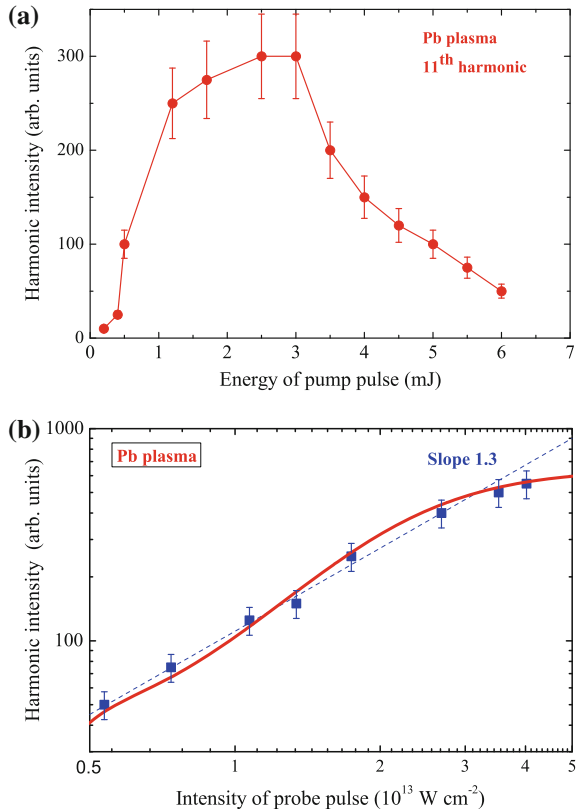
Fig. 2.14 **a** The dependence of the 11th harmonic intensity on the delay between the pump and probe pulses. **b** Harmonic intensity as a function of the distance between Pb target surface and probe beam axis for the 7th (*squares*) and 11th (*circles*) harmonics. Reproduced from [78] with permission from Optical Society of America



The common feature of these studies was an abrupt decrease of harmonics at the irradiation of targets above the optimal level. The term “optimal level” refers to the conditions of plasma ablation when the components of ablation do not cause the growth of the impeding processes, which restrict, or even entirely cancel, the harmonic generation. Those include (a) the excess of free electron concentration leading to strong variation of the dispersion properties of the nonlinear medium and to the phase mismatch between the interacting waves, (b) the excess in absorption of the XUV radiation, and (c) the intense emission from the plasma. The origin of these processes is related with the formation of highly ionized plasma, which leads to the appearance of the abundance of free electrons. The latter species cause a phase mismatch between the waves of probe and harmonic fields. This effect is especially important for the lower-order harmonics. One can note that a decrease of harmonic efficiency in highly ionized plasma has been reported for higher-order harmonics as well [1, 4, 5, 25], though this effect was less abrupt than that observed in the discussed studies. Figure 2.15a shows the influence of the energy of the heating pulse on the intensity of the 11th harmonic generating in the lead plasma.

Fig. 2.15 a The dependence of the harmonic intensity on the pump pulse energy for the 11th harmonic generating in the lead plasma.

b Comparison of experimental (squares, dashed curve) and calculated (solid curve) dependences of the 11th harmonic yield on the converting pulse intensity. Reproduced from [78] with permission from Optical Society of America



Harmonic intensity increased up to the heating pulse energy of 3 mJ. Further growth of the pulse energy led to a decrease of harmonic intensity.

Lead plasma is not the first plasma medium where the enhancement of some specific harmonic was reported. It is just a sample showing such feature while using the 1064 nm radiation. Mn, In, Te, As, Sn, and Cr were among the plasma plumes where the enhancements of single harmonic of 800 nm radiation of a Ti:sapphire laser were reported [79]. Notice that no enhancement of the single harmonic was observed from these metal plasmas using the Nd:YAG laser radiation, and vice versa, the 800 nm femtosecond lasers were not able to produce the enhanced single harmonic from the lead plasma. All previous studies point out a decisive role of the properties of the target material, such as the ionic resonances possessing large oscillation strengths, on the resonance enhancement of single harmonic. The closeness of the ionic transition possessing high gf and the enhanced harmonic has been clearly shown in the case of indium plasma, where the 13th harmonic of 800 nm radiation was considerably (up to a hundred times) stronger than all (even lower-order) neighboring harmonics [24] (see also previous section).

There are various theoretical studies offering the explanations of the resonance-induced enhancement of harmonics [56, 70–72, 80–86]. Particularly in [56], this process was described in the frames of the four-stage model. However, this model could be applied when the resonance level is an autoionizing state, which is not a case of the low-lying states of Pb ions presumably involved in the observed enhancement of 11th harmonic. Probably, the model developed in [71] is more suitable for the discussed conditions. Strongly coupled, low-lying states are a feature of many atomic and molecular systems with ionization potentials substantially lower than those of noble gases. Their calculations showed that the resonance width of the enhancement can be smaller than the laser bandwidth, which means that this is an explicitly multiphoton process. Note that the experimental evidence of resonantly induced single harmonic enhancement was mostly reported in the case of plasma HHG studies. It is obvious that the probability of such occasional coincidence of the wavelengths of ionic transition and harmonics is extremely small among a few used gases, while most of the materials exist in a solid state and thus could be ablated to produce a plasma plume.

The analysis of the influence of the probe intensity on the 11th-harmonic yield from the lead plasma was carried out as well (Fig. 2.15b). The slope of this dependence was close to 1.3 (dashed line). As the frequency shift from the 11th photon resonance between ground and excited states $6s^26p\ ^2P_{1/2}-6s^28d\ ^2D_{3/2}$ (96.72 nm) of Pb II was only 4.5 cm^{-1} , the analysis of harmonic yield was carried out using the resonant approach [87–89]. In this approach, the squared module of the off-diagonal elements of the density matrix defines the resonant harmonic intensity. The calculated $I_{11H}(I_{\text{probe}})$ dependence using the fittings of AC Stark shift, relaxation time, and generalized matrix elements is presented as the solid line in Fig. 2.15b. The influence of resonances in the enhancement of the single harmonic is defined by both the oscillator strength of the nearby transition and the detuning between the wavelengths of harmonic and transition. There is no need for exact coincidence of the resonance transition and harmonic. The optimal detuning defines how strong the nonlinear optical response is expected to be. Indeed, the coincidence of 11th harmonic ($\lambda = 96.73\text{ nm}$) and 96.72 nm transition may be the reason for the insignificant enhancement of this harmonic due to self-absorption, as was observed in those studies. Probably, another reason for a weak enhancement is a small gf of this transition. One can note that all previous observations of resonantly induced harmonic enhancement were obtained at different detuning of harmonics with regard to the exact positions of ionic transitions. Thus, the exact coincidence of these wavelengths may cause some restrictions in the harmonic enhancement due to the influence of self-absorption.

The role of atomic resonances in the growth of the laser radiation conversion efficiency has been actively discussed in the framework of the perturbation theory at the early stages of the study of low-order harmonic generation (see [88] and the references therein). In the case of HHG, the increase in the efficiency of generated harmonics due to resonance processes has come under consideration almost two decades ago, and this approach appears to have considerable promise with the use of ionic and, in some cases, atomic resonances.

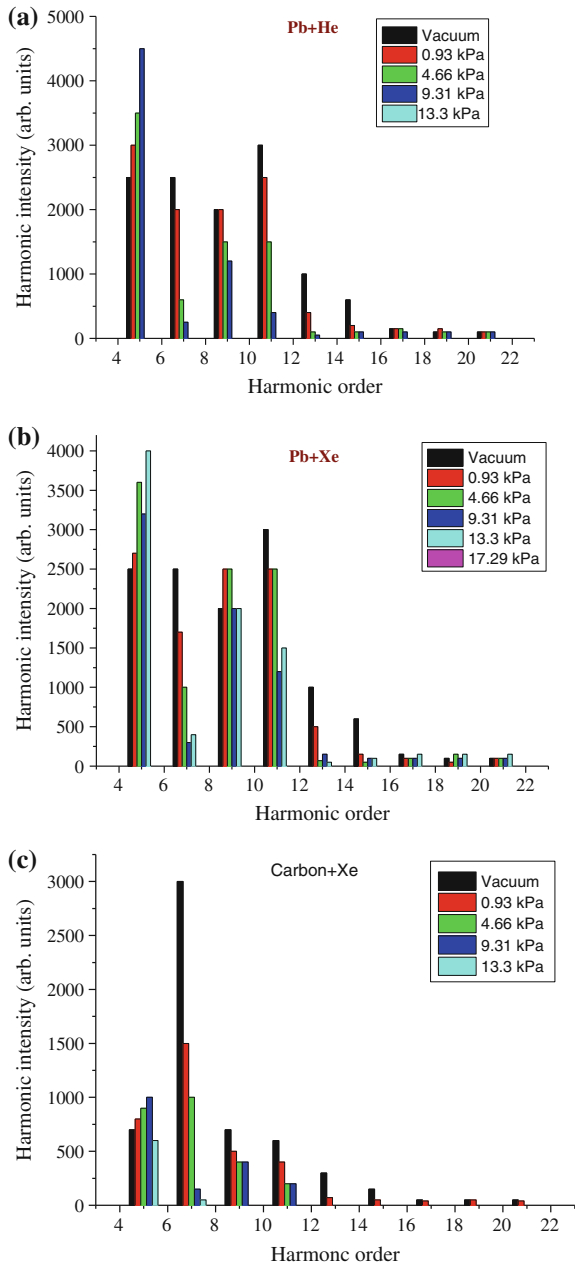
The resonance HHG studies comprised both the theoretical analysis of this process and the first attempts to form the resonance conditions in experiments. While theoretical estimates testified the possibility of an efficient enhancement of individual harmonics, experimental works revealed the difficulties encountered in gas harmonics. Therefore, the use of plasma media could largely facilitate the solution of the problem of resonance harmonic enhancement. Examining a large group of potential targets allowed identifying some of them as suited for demonstrating this process. The advantages of plasma HHG over gas HHG were amply manifested in this case because the number of possible media in the former case is far greater than in the latter case. The observation of enhanced harmonic in Pb plasma in the vicinity of singly charged ionic transition (96.72 nm) just another proof of the concept.

The role of resonances on the high-order nonlinear optical response of medium could be monitored by two methods: tuning of the driving radiation wavelength and changing the phase relations of the interacting waves. The former method was often used in the case of resonance-enhanced harmonics of the broadband Ti:sapphire lasers allowing both direct tuning of radiation wavelength and manipulation of the harmonic wavelength through the chirp variation. This approach cannot be applied in the case of the Nd:YAG laser, since it is impossible to tune the wavelength of this narrowband laser. The only clear proof for the involvement of the resonance on the yield of the 11th harmonic could be the variation of the phase mismatch between the two waves (1064 and 96 nm) in the vicinity of this ionic transition. Below we discuss the experiments allowing the variation of the refractive index of medium by adding different gases in the plasma. We would like to remind that this approach in the studies of the resonance enhancement is not new. It was used in the early stage of low-order harmonic and parametric generation in gases, which showed the attractiveness of the manipulation of the phase relations in the vicinity of resonances by introducing the variable ratios of positive and negative dispersions using different gases [88].

The insertion of gases in the vacuum chamber containing targets led to variations of harmonic spectra compared with the case of pure lead plasma. Four gases (He, Ar, Kr, Xe) possessing different dispersion, as well as different absorption, in the 50–250 nm region were used in the discussed studies. Figure 2.16a, b shows the Pb harmonic spectra in the presence of light (He) and heavy (Xe) gases. The former gas possesses weak absorption until 65 nm, and thus its influence on the variations of harmonic spectra could be attributed mostly to the optical dispersion properties of the gas changing the phase matching conditions for resonant and out-of-resonance harmonics.

The He pressure was varied up to 13.3 kPa, above which the optical breakdown of the gas (without ignition of the metal plasma) was observed. One can see the abrupt decrease of 11th harmonic with the increase of He pressure. Meanwhile, some harmonics, in particular the 9th one, showed less decrease, and the 5th harmonic became even stronger compared with the plasma formation at vacuum conditions. Approximately same features were observed in the case of insertion of the xenon gas, though a decrease of the 11th harmonic was not so pronounced.

Fig. 2.16 Variations of plasma harmonic spectra generated at different pressures of the gases inserted in the target chamber. **a** Pb plasma, He gas, **b** Pb plasma, Xe gas, **c** carbon plasma, Xe gas. Reproduced from [78] with permission from Optical Society of America



The influence of different gases on the harmonic spectra from the plasma media showing the enhancement of specific orders was compared. Recently, the plasma harmonics from graphite ablation using 1064 nm radiation were studied and a

strong 7th harmonic of Nd:YAG laser radiation (152 nm) was observed [90]. The enhancement of this harmonic was attributed to the closeness with the ionic transition of carbon, which led to the formation of phase-matching conditions in this particular case. Figure 2.16c shows the spectra of carbon harmonics at different pressures of xenon. One can see that a decrease of the strong 7th harmonic with the growth of gas pressure resembles the one shown in the case of the 11th harmonic generating in the lead plasma (Fig. 2.16a). The comparable variations of Pb and C harmonic spectra may lead to the following conclusions. The enhancement of harmonics at purely plasma conditions (i.e., without insertion of the gases) in both these cases was originated from better phase matching of the converting and harmonic waves (11th and 7th harmonics from the lead and carbon plasmas, respectively). The addition of the medium possessing positive dispersion worsens the phase matching between the waves and correspondingly decreases the intensities of those harmonics. The role of the gas on other harmonics is also defined by the positive addition to the refractive index of the plasma–gas mixture. However, in that case the dispersion properties of the gas play a less decisive role compared with the resonance-enhanced harmonics.

The role of gas absorption on the observed properties of the resonant harmonic was also analyzed in those studies. At the most unfavorable conditions (2-m-long optical path inside the monochromator, He gas pressure 7 kPa) the absorption starts at 23 eV [91], which corresponds to the 19th harmonic of 1064 nm radiation, while the transmittance for lower-order harmonics was equal to 1 (1.17 eV corresponds to the energy of 1064 nm probe photons). No significant absorption of the 11th harmonic in Ar and Ne was observed at these experimental conditions. In the cases of Ne and Ar the absorption starts at 19 and 14.5 eV, respectively, which should lead to the suppression of the 17th and 13th harmonics but not the 11th one ($E_{11H} = 12.9$ eV). The insertion of Xe led to the 30 % absorption of the 11th harmonic [91], since the transmission in this gas started to decrease at ~ 12 eV (for Kr this value is 13.8 eV, and this gas does not absorb the 11th harmonic).

The reviewed studies showed that the insertion of gas led to the change of the influence of the propagation effect on the harmonic generation. Probably, the combination of micro-processes (i.e., closeness of harmonic wavelength and ionic transition, absorption processes) and macro-processes (propagation effect comprising the joint influence of Gouy phase, dispersion of plasma close to the resonant transitions, and dispersion of neutral gas) cause the observed variations of harmonic spectra from the plasma plume at different gas pressures.

The concentration of lead particles in the area of interaction with the probe pulse ($\sim 2 \times 10^{17} \text{ cm}^{-3}$) becomes comparable with the one of gases $[(1-10) \times 10^{17} \text{ cm}^{-3}]$ inside the plasma volume. At the early stages of gas harmonic studies, the inclusion of an additional gaseous component allowed the enhancement (or decrease) of generating harmonics in the gas mixtures in the vacuum ultraviolet range due to achievement of the phase matching conditions between the interacting waves [92–94].

2.4 Peculiarities of the High-Order Harmonics from Different Narrow Plasmas Generating at 1 kHz Repetition Rate

Each plasma component can cause constructive or destructive action on the overall nonlinear optical response of a whole ensemble of plasma particles. Some components, e.g., free electrons, large nanoparticles or aggregates and microparticles, generally cause a decrease of the HHG conversion efficiency due to some impeding processes originating from the nature of these particles. Free electrons, for instance, enhance the phase-mismatch between driving and harmonic fields, which has a negative influence on the conditions of efficient HHG. Their negative impact on HHG has long been known starting from the very beginning of the studies of gas harmonics [95–97]. To minimize their influence on HHG the intensity of laser radiation is maintained at conditions where multi-photon and tunneling ionization do not create large amount of free electrons.

The presence of free electrons in plasma plumes is unavoidable due to the nature of laser-induced ablation of solid targets. However, even in that case one can limit their influence so that HHG does not suffer greatly from the difference between the phases of interacting waves. Singly charged ions are the main emitters, which are responsible for achieving extended spectral cut-offs and relatively high efficiencies of the HHG process [25]. Neutral atoms also generate strong harmonics; however, in that case the cut-off occurs at lower photon energies than in the case of ions. Small nanoparticles may considerably enhance the intensities in HHG [26]. Their properties as efficient emitters of harmonics were analyzed during both gas [98–101] and plasma [102–106] HHG studies. Theoretical simulations predicted a considerable increase of the harmonic conversion efficiency compared to the corresponding monoatomic media [107–110].

The HHG conversion efficiency considerably depends on the relative phases of harmonics from different emitters within the plasma plumes, realized as constructive or destructive interference. A few studies were reported on the interference of the HHG emitted by successive sources or mixtures of different gases [111–114]. A suppression of harmonic efficiency in a mixture of Ag and Au nanoparticles compared with the separated ingredients was reported in [115]. Modifications of harmonic spectra were also observed for separated boron and carbon targets in comparison with their mixtures. In that case a destructive interference was observed, too, similar to the mixtures of Ag and Au nanoparticles. The HHG efficiency considerably decreased for both higher and lower harmonics compared with the case of separately ablated boron and graphite targets [115].

Another interesting issue is a comparative analysis of harmonic generation from gases and plasmas. Recent studies have demonstrated superior properties of the carbon plasma, which allowed the generation of lower-order harmonics with reported five [116] and ten [34] times higher efficiency than in the case of an argon gas medium. A morphological analysis of the carbon plasma debris revealed an abundance of carbon nanoparticles in the plasma. The increase in harmonic yield

was attributed to the presence of those carbon nanoparticles in the ablation plume which can enhance the nonlinear optical response of the medium. Those studies were carried out using a few-cycle pulses of 3.5 and 8 fs duration, respectively. For a more general application of plasma harmonics it is interesting to generate carbon plasma harmonics and compare their yield with argon gas harmonics using longer driving pulses as well.

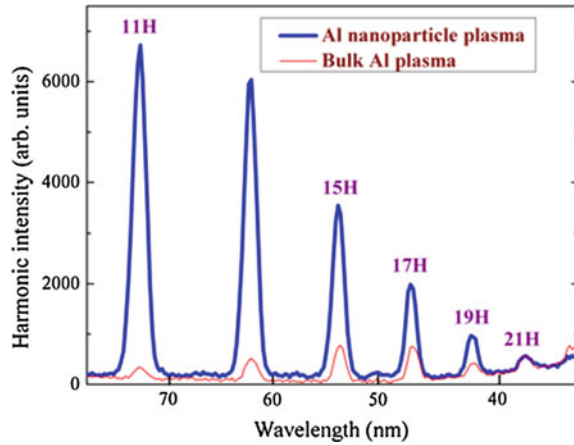
Here we discuss the above issues, which were studied using a femtosecond laser operated with the pulse duration of 40 fs. We analyze the reported results of harmonic generation from mono- and nanoparticle- containing plasma plumes, compare the harmonic yields from Zn, Cu, and brass alloy to address the issue of interference of harmonic generation from species of different origin, and finally compare the HHG efficiencies from gaseous (argon) and plasma (carbon) media at comparable conditions [117].

A 1 kHz repetition rate chirped pulse amplification Ti:sapphire laser was used as the laser driving source. The scheme of HHG was similar to the one described in Sect. 2.3.1. The delay between heating and driving pulses could be variably adjusted with respect to each other between $\Delta t = 0$ and 100 ns to allow for the formation and expansion of the plasma plume away from the surface of the target before propagation of the driving pulse. It should be noted that for an increasing delay the optical pathway of the femtosecond pulse had to be increased up to 30 m. Therefore, for each delay setting the dispersion in air had to be pre-compensated, and the other beam parameters had to be kept constant. For lighter atoms a short delay of, e.g. $\Delta t = 25$ ns for C, and for heavier atoms a longer delay, e.g. $\Delta t = 70$ ns for Ag proved to be optimal.

Various targets (Al, Cu, Zn, brass, graphite, and Ag) as well as nanoparticles were used for these experiments. For a comparison of the conversion efficiency into harmonic radiation the solid target could be replaced by a gas cell (length $L = 0.7$ mm) operated with a continuous Ar flow at an optimal pressure of 100 mbar for gas HHG [118, 119] without changing other experimental parameters, in particular the laser properties.

In Fig. 2.17 the HHG spectra recorded for the 11th to 23rd harmonics generated in the plasmas produced on bulk and nanoparticle aluminum targets are presented. The ablation conditions with respect to pulse energy and fluence of the ablation pulse, as well as of the driving pulse, remained identical for these two samples. The same holds for other parameters of the experiment, like the distance between the target surface and the driving beam (~ 100 μm), the pulse duration of the ablation pulse (12 ps), and the delay between the ablation and driving pulses ($\Delta t = 30$ ns). Figure 2.17 shows the line-outs of the harmonic spectra generated in the spectral range between $\lambda = 35$ and 80 nm for nanoparticle (thick blue line) and bulk (thin red line) Al targets. For the two lowest orders (11th and 13th) of the displayed harmonics, the intensity ratio $I_{\text{nano}}/I_{\text{bulk}}$ was found to be approximately 30 and 15, respectively. This ratio decreases for higher harmonics until above the 23rd order when the harmonics from the nanoparticle target entirely disappear, while the harmonics from the bulk Al target show similar intensities over the whole spectrum. This observation is a clear experimental evidence for the low degree of ionization of

Fig. 2.17 Harmonic spectra from plasmas produced on the bulk Al (*thin curve*) and Al nanoparticles contained targets (*thick curve*). Reproduced from [117] with permission from Springer Science+Business Media



the plasma obtained from glued nanoparticles, because the harmonics, which can be generated from ions only, are suppressed. The harmonic cut-off in the spectra from bulk Al was beyond the short-wavelength limit of XUV spectrometer ($\lambda = 35$ nm), while in accordance with earlier observations it should be in the region of 20 nm (41st harmonic, [120]). Further, the ablation of the pure glue alone, without nanoparticles, did not lead to harmonic generation, which confirms that the emitters of harmonics were associated with the aluminum nanoparticles. The harmonics generated from the nanoparticle plasma target showed a larger divergence than those from the bulk target. This larger divergence could arise from a stronger influence of the long trajectories of accelerated electrons on the yield of the harmonic radiation. This observation can also be related to a growth of the recombination cross section when returning electrons moving on the long trajectory have a higher probability to recombine with larger particles. The observation of only relatively low-order harmonics from the Al nanoparticle-containing plasma could be related with the origin of nanoparticle-induced HHG, which is assumed to occur from neutral particles. Additionally the ionization potential of Al clusters containing more than about 15 atoms falls below the ionization potential of a single neutral Al atom (5.98 eV) and further decreases with increasing particle number (~ 5.2 eV for $n = 50$) [121]. This also leads to a lower cut-off in the harmonic spectra.

In a molecular dynamics simulation the evolution of the kinetic energy of ablated Al atoms from bulk and nanoparticle targets was studied based on the ITAP IMD molecular dynamics code. The calculations were performed for two different durations of the ablating pulse (12 and 28 ps). When comparing the two targets it is evident that in the case of a nanoparticle target (Fig. 2.18; blue triangles and black squares) the ablated atoms have an average kinetic energy, which is lower by a factor of two compared to atoms ablated from the corresponding bulk target (pink triangles and red dots) over the entire pulse duration of the ablating pulse. In order to gain further insight from these results one may consider two scenarios. If an atom is ablated instantly from the target, then its kinetic energy will be relatively

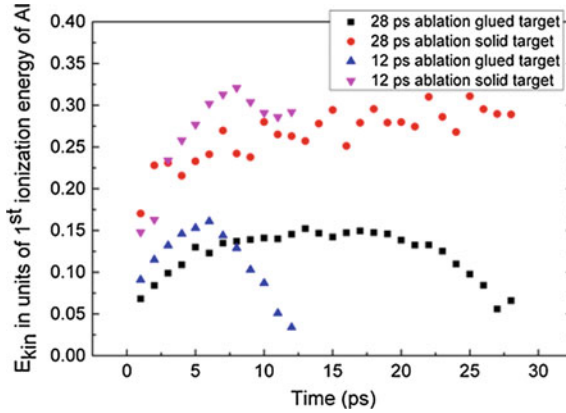


Fig. 2.18 Molecular dynamics simulation of the average kinetic energy of aluminum atoms ablated from $5 \times 5 \times 5 \text{ nm}^3$ Al nanoparticles (blue triangles and black squares) and a solid Al target (pink triangles and red dots). Two different durations of the ablating laser pulse of 12 and 28 ps have been assumed in the simulation. The energy scale is normalized to the first ionization potential of aluminum (5.98 eV). Reproduced from [117] with permission from Springer Science +Business Media

high. However, if an atom gains the energy sufficient to break a bulk bond via energy exchange with neighboring atoms, its kinetic energy will be low and very unlikely exceed the doubled value of the binding energy. The kinetic energy of the ablated atoms is thus a good indicator of the nature of the ablation process. In the discussed case the significantly larger kinetic energy of ablated atoms from the solid target have shown that the ablation process occurs instantly for atoms near the surface and becomes more stable with surface melting. In the case of nanoparticle ablation the process is different. The strong decrease of the kinetic energy near the end of the pulse indicates that the nanoparticle is completely ablated. Otherwise the energy exchange between neighboring atoms would lead to a stable average kinetic energy. The simulations together with these considerations lead thus to the conclusion that the nanoparticles are evaporated more uniformly and are ablated completely before the pulse ends.

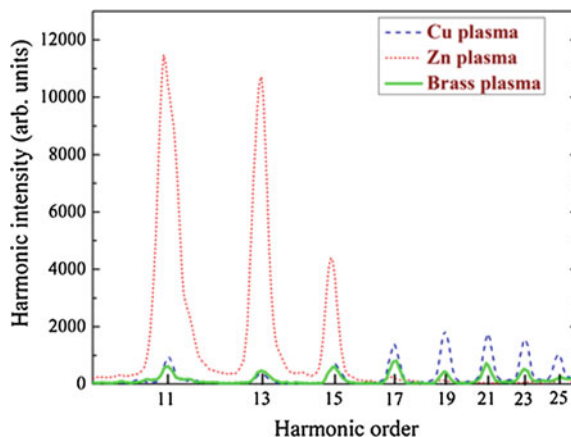
Below we discuss the case when the mixed materials participate in HHG. The influence of two sources of emission on the intensities of HHG is a rather complicated phenomenon. HHG in mixed gases has been reported in several studies [11, 114, 122, 123] in which a suppression of the harmonics above the cut-off of one of the gases was observed. Constructive interference due to quasi-phase matching can be achieved when these gas sources are located at appropriate distances from each other [112, 124–126]. Analogous features were reported for mixed boron and carbon plasmas, which separately showed considerably different cut-offs [115]. Also in that case a destructive interference occurred over the whole observed spectrum of harmonic generation up to 26 eV.

Figure 2.19 shows high-order harmonic spectra observed from the plasmas produced on bulk Zn, Cu, and brass targets. The HHG in a zinc plasma shows strong low-order harmonics up to the 15th order (dotted red curve), while the copper plasma (dashed blue curve) allowed harmonic generation extending towards shorter wavelengths out of the registration range of the used XUV spectrometer. It is interesting to note that the strong Zn III resonances at $\lambda = 67.8$ and 71.4 nm do not enhance the 11th harmonic at $\lambda = 72.7$ nm. This indicates that the comparatively cold plasma is formed with a low concentration of electrons and of multiply charged ions. The brass target contained a mixture of Zn and Cu at a ratio of 35:65, and the plasma produced on this target contained therefore both Zn and Cu atoms and ions. It should be noted, however, that the evaporation of brass with a high concentration of Zn is a complicated process due to the initially preferable evaporation of the Cu, which prevents an efficient evaporation of Zn [127]. Therefore in the brass plasma the concentration of Zn atoms is different from that of the bulk Zn target.

The harmonics from this brass plasma (solid green curve) on the other hand show a yield diminished over the whole spectral range of harmonic generation from the 11th to the 25th order, being lower than those from both Zn and Cu plasmas. While for zinc the decrease amounts to a factor of about five, a decrease of a factor of two is observed for copper. A decrease of the intensity without a sign of constructive interference was observed over the measured HHG spectrum ($\lambda = 35$ – 80 nm, $h\nu = 15.5$ – 35.5 eV) in the mixed plasma. The dispersion of the low-density laser plasma must therefore be weak in this spectral range, maintaining the relative phases of the two emitters.

The origin of this phenomenon is yet clear and further studies are needed for a clarification of the influence of a low cut-off component on the harmonic intensity from another component showing a cut-off at higher photon energies. The goal of the discussed experiments was to study the HHG produced in a macroscopically uniform and isotropic two-component plume. Since HHG is a coherent process, interference can considerably influence the harmonic efficiency. Considering the

Fig. 2.19 Harmonic spectra from Zn (dotted red curve), Cu (dashed blue curve), and brass (solid green curve) plasmas. Reproduced from [117] with permission from Springer Science+Business Media



contributions from two different induced dipole moments the interference is related to the different dipole phases. In that case, the interference mechanism should occur even on a microscopic scale, since the medium is isotropic and uniform. These studies have shown that the relative dipole phase interference is the proper explanation of the observed results.

The delay between the ablation and the driving pulses is crucial for an optimization of HHG. A typical dependence of the harmonic intensity on the delay between these pulses is presented in Fig. 2.20 for the carbon-containing plasma produced on graphite target (black squares) and the silver plasma (blue squares). At short delays of $\Delta t = 10$ ns even low- Z species such as carbon with velocities of typically 1×10^4 m s $^{-1}$ do not reach the optical axis of propagation of the driving beam at about 200 μ m distance from the target surface with sufficient density. An increase of the delay to $\Delta t = 25$ ns led to a strong increase of the harmonic yield in a carbon plasma, because now a high concentration of particles was presented within the beam path of the driving laser. At longer delays a gradual decrease of the yield follows. Corresponding results for plasma from a silver target are shown as blue squares. A strong rise of the high harmonic signal at about 55 ns delay is followed by a plateau in the range between 60 and 80 ns delays, while for larger delays the harmonic intensity started to drop. This demonstrates that there are different optimal delays for harmonics generated in low- Z and high- Z plasmas. Although the velocities of the ablated silver particles are now reduced by about a factor of three, the kinetic energies of active particles from the heavier target (silver, $m = 107.87$ amu) and those from the lighter target (carbon, $m = 12.01$ amu) are about the same.

To directly compare the high-order harmonics generated from plasma media and gas a gas cell (length 0.7 mm, $p_{\text{opt}} = 100$ mbar) and a solid carbon target were

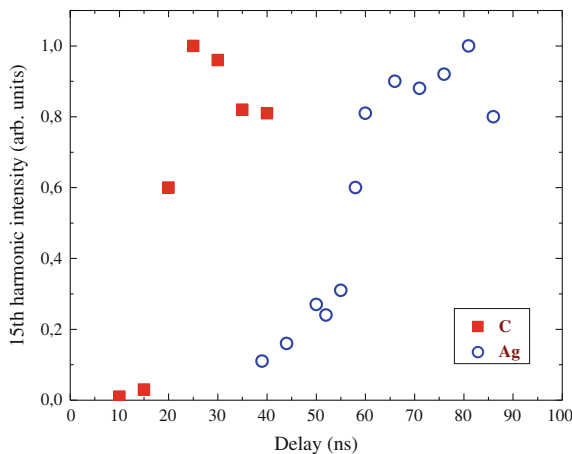


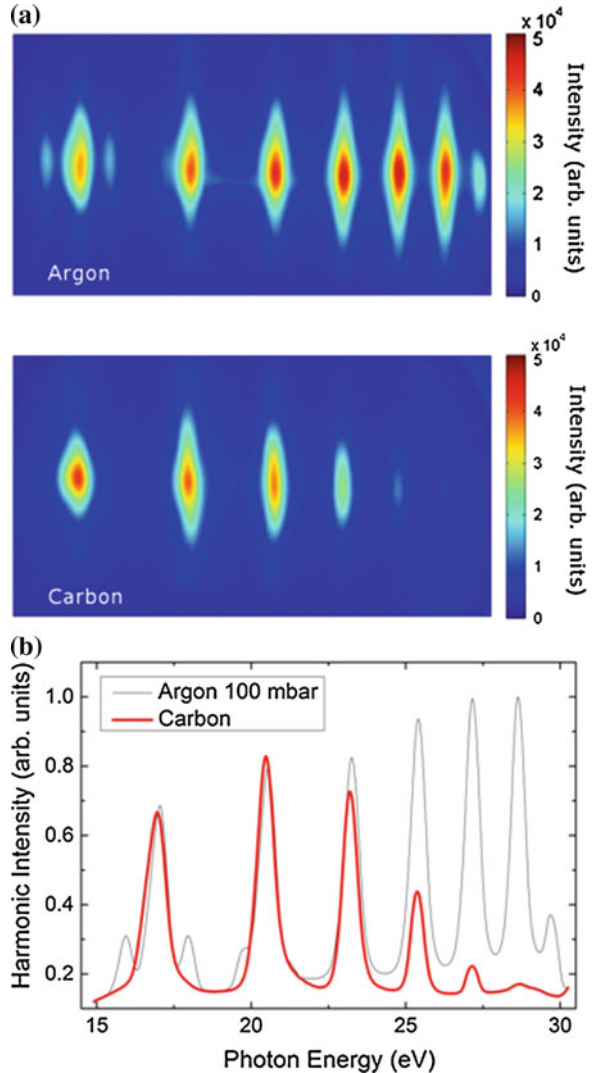
Fig. 2.20 Dependence of the 15th harmonic yield on the delay between the heating and driving pulses in the cases of carbon (*filled squares*) and silver (*empty circles*) plasmas, respectively. The distance between target and driving pulses was maintained at 100 μ m. Adapted from [117] with permission from Springer Science+Business Media

placed in the same vacuum chamber. Previously, a major complication with plasma harmonic experiments compared with gas harmonic experiments was a rapid evaporation and cratering of the solid target surface [25, 34]. This caused the target to deform, thus changing the conditions of plasma formation. The rotating rod system allowed a considerable reduction of these influences on the stability of HHG. The debris from the ablation also coats the window from which the picosecond ablating pulse enters the vacuum chamber, thus reducing the fluence of heating radiation on the target with time. To exclude this effect a protective microscope slide was installed between the target and the entrance window which could be easily replaced from time to time.

The efficiency and characteristics of high-order harmonics from the carbon plasma were compared with those from the argon gas cell, using the 40 fs laser as the main driving pulse. The two upper panels in Fig. 2.21a show the raw images of harmonic spectra optimized with respect to the peak intensity generated in Ar gas and in carbon plasma at equal acquisition times. Under these conditions, the energies of the driving pulse were 0.6 mJ in case of harmonics generated from the carbon plasma plume and 0.9 mJ from gaseous argon, respectively. In both media comparable divergences of the harmonics were observed. In the case of HHG from the carbon plasma an increase of the driving pulse energy led, at the given focusing conditions, to a significant growth of the harmonic divergence. This may indicate that for higher driving pulse energies the energy is converted more preferably by the longer electron trajectory. It further supports the interpretation that these plasma plumes contain nanoparticles, as mentioned above. At driving pulse energies above 0.8 mJ the blue side maxima emerged in the harmonic profile. The decrease of harmonic intensity suggested that the harmonics originated from long and short trajectories do not interfere constructively. It should be noted that due to the larger beam profile it is still possible to generate higher photon fluxes, however, with a higher proportion of the long trajectory contributing to the photon flux. Additionally, when comparing the intensities of Ar and C harmonics it should be kept in mind that the active lengths of the media are estimated to be 0.7 and 0.3 mm for the gas and plasma medium, respectively. Further, the densities are estimated to be about 2.5×10^{18} and $2 \times 10^{17} \text{ cm}^{-3}$, respectively. Integrated intensities of harmonics for both targets are given in Fig. 2.21b.

The relative photon flux of 13th harmonic was determined with a MCP detector and the absolute photon flux with a calibrated photodiode. In both cases a Sn filter was used to suppress the fundamental Ti:sapphire radiation. At a thickness of $d = 300 \text{ nm}$ a pure Sn shows a transmission of $T = 9.9 \%$ [128], and a filter oxidized by a 4 nm thick layer had the transmission $T = 8.1 \%$ [128, 129]. It should be noted that these filters do not withstand the fundamental radiation for a long time without damage, making the usage of a slit of 0.9 mm in front of XUV spectrometer width mandatory. The MCP measurements yielded an intensity ratio of the 11th–15th harmonics generated in C plasma and in Ar gas of 2.5:1.5. For the determination of the conversion efficiency and the photon flux by the calibrated photodiode all three harmonics—the 11th, 13th, and 15th harmonic—which are transmitted by the Sn filter have been measured in the direct beam, because the diffraction efficiency of

Fig. 2.21 **a** Raw images of the 11th to 23rd harmonic spectra from argon gas and carbon plasmas, taken at 0.9 and 0.6 mJ femtosecond pulse energy, respectively. **b** Comparison of the integrated line-outs of harmonic spectra from argon gas (*thin black curve*) and carbon plasma (*thick red curve*). Reproduced from [117] with permission from Springer Science+Business Media



the grating was not known. The relative intensities of the harmonics in this direct beam were taken from the dispersed spectra. The conversion efficiencies of $\eta = 3.2 \times 10^{-7}$ for Ar and $\eta = 5.3 \times 10^{-7}$ for the C plasma in the case of 13th harmonic were defined. This compares well with the relative intensities measured by the MCP. Taking an average fundamental power of 600 mW at 1 kHz repetition rate a photon flux of 9.8×10^{10} photons s^{-1} generated in the C plasma and a flux of 6.0×10^{10} photons s^{-1} generated in the Ar gas were estimated. The measured intensities compare well with the harmonic intensities reported in the literature

Table 2.2 Conversion efficiencies and photon fluxes in the case of HHG in Ar gas and C plasma

Harmonic	Diode sensitivity [A/W]	Argon gas		Carbon plasma	
		Efficiency	Photon flux [s ⁻¹]	Efficiency	Photon flux [s ⁻¹]
11	0.10	2.6×10^{-7}	5.7×10^{10}	2.6×10^{-7}	5.8×10^{10}
13	0.13	3.2×10^{-7}	6.0×10^{10}	5.3×10^{-7}	9.8×10^{10}
15	0.16	3.4×10^{-7}	5.5×10^{10}	4.0×10^{-7}	6.4×10^{10}

Reproduced from [117] with permission from Springer Science + Business Media

[65, 119, 130, 131]. The corresponding results for the 11th, 13th and 15th harmonics are summarized in Table 2.2.

2.5 Concluding Comments

The main goal of the description of HHG in narrow plasmas was to acquaint the reader with most advanced results of this technique achieved so far using the 0.3–0.5 mm long plasma plumes. While presenting the overview of previous results of plasma harmonic studies, we also showed most recent developments in this field.

Particularly in this chapter, we have discussed the measurements of the spatial coherence of the high-order harmonics generated in laser-produced narrow plasma plumes in the cases of resonant and non-resonant harmonics. Reasonably high visibilities in the range of ~ 0.6 – 0.75 were measured for C, Zn, and In targets for harmonics in the range of 15–25 eV. These results have confirmed the assumption that the harmonics from ablation plasmas can be used for applications requiring high spatial coherence such as diffraction imaging. The higher visibility for the plasma harmonics compared with an argon gas target in these experiments was attributed to a reduced production of free electrons during the propagation of femtosecond driving pulse through the preformed plasmas.

We analyzed the application of femtosecond and picosecond laser pulses for plasma formation on the metal targets for non-resonant and resonant high-order harmonic generation using a 1 kHz laser. Efficient HHG was achieved by using a rotating target for plasma formation. These studies revealed that the harmonic yields from the plasmas produced by picosecond and femtosecond pulses of the same fluence were comparable, despite the significantly different intensities of the heating pulses. Further, the resonance enhancement of single harmonics in Sn and In plasmas using picosecond and femtosecond ablating pulses was discussed. The optimization of single harmonics with enhancement factors of $10\times$ and $100\times$ for these harmonics compared to the neighboring ones was achieved. The concentrations of neutrals and ions of Al and Cu at different heating pulse durations were defined using the code ITAP IMD.

The discussed studies also included the demonstration of the generation of high-order harmonics from the Pb plasma using the mode-locked picosecond laser.

The important peculiarity of those studies was the observation and analysis of the enhanced 11th harmonic ($\lambda = 96.7$ nm), which originated from the resonance-induced growth of the nonlinear optical response of lead plasma at the wavelength of the 11th harmonic lying close to the strong ionic transition of lead (Pb II, $\lambda = 96.72$ nm). The conversion efficiency of this harmonic was measured to be 3×10^{-6} . A strong departure from enhanced yield to suppressed state of 11th harmonic in the case of addition of the He in the area of plasma formation clearly indicated the involvement of the propagation effect, which spoiled the favorable conditions for the 11th harmonic generation. The resonance effect of the enhancement of the 11th harmonic in lead was not as strong as in the cases observed in indium and other plasmas, which obviously can be attributed to both the weaker oscillator strength of Pb resonance and better conditions for the observation of the resonance enhancement in the case of the broadband femtosecond radiation of Ti:sapphire lasers. The clear evidence for the availability to monitor the involvement of resonances in HHG through the modulation of phase mismatch was also presented in the case of carbon plasma. The similarity in the behavior of resonance harmonics in the cases of addition of the gas with positive dispersion in the carbon and lead plasmas was an additional proof of the influence of C and Pb ionic transitions on the nonlinear optical response and particular harmonic yields.

We have analyzed the superior harmonic intensity from an aluminum cluster contained plasma compared to atomic and ionic Al plumes. The analysis of HHG in the mixtures of two emitters (Zn and Cu) revealed the destructive interference of the two harmonic sources. Different plasmas were studied at various delays between the ablation and the driving pulse to analyze the role of the atomic mass of different plasma components in the HHG yield. Finally, conversion efficiencies and photon fluxes have been determined for Ar gas and carbon plasma in the case of comparable orders of harmonics. Those results have shown that harmonic generation in a carbon plasma compares favorably with that in an Ar gas.

Concluding this chapter, we would like to stress that the HHG in partially ionized narrow plasmas was actively developed during last few years in different laboratories worldwide. The developments in this area allow us to expect further amendments to this technique of coherent short-wavelength radiation generation. The extended plasma medium is the example of such an amendment of the high-order nonlinear optical processes in the plasma plumes. Chapters 3–7 contain the evidence of this assumption.

References

1. Y. Akiyama, K. Midorikawa, Y. Matsunawa, Y. Nagata, M. Obara, H. Tashiro, K. Toyoda, *Phys. Rev. Lett.* **69**, 2176 (1992)
2. S. Kubodera, Y. Nagata, Y. Akiyama, K. Midorikawa, M. Obara, H. Tashiro, K. Toyoda, *Phys. Rev. A* **48**, 4576 (1993)

3. C.-G. Wahlström, S. Borgström, J. Larsson, S.-G. Pettersson, *Phys. Rev. A* **51**, 585 (1995)
4. W. Theobald, C. Wülker, F.R. Schäfer, B.N. Chichkov, *Opt. Commun.* **120**, 177 (1995)
5. R.A. Ganeev, V.I. Redkorechev, T. Usmanov, *Opt. Commun.* **135**, 251 (1997)
6. K. Krushelnick, W. Tighe, S. Suckewer, *J. Opt. Soc. Am. B* **14**, 1687 (1997)
7. R.A. Ganeev, *J. Opt. Soc. Am. B* **31**, 2221 (2014)
8. R.A. Ganeev, M. Suzuki, P.V. Redkin, M. Baba, H. Kuroda, *Phys. Rev. A* **76**, 023832 (2007)
9. J. Rothhardt, S. Hädrich, S. Demmler, M. Krebs, S. Fritzsche, J. Limpert, A. Tünnermann, *Phys. Rev. Lett.* **112**, 233002 (2014)
10. R. Ganeev, M. Suzuki, M. Baba, H. Kuroda, T. Ozaki, *Opt. Lett.* **30**, 768 (2005)
11. R.A. Ganeev, M. Suzuki, M. Baba, H. Kuroda, *Appl. Phys. B* **81**, 1081 (2005)
12. R.A. Ganeev, M. Baba, M. Suzuki, H. Kuroda, *J. Appl. Phys.* **99**, 103303 (2006)
13. R.A. Ganeev, H. Singhal, P.A. Naik, V. Arora, U. Chakravarty, J.A. Chakera, R.A. Khan, P.V. Redkin, M. Raghuramaiah, P.D. Gupta, *J. Opt. Soc. Am. B* **23**, 2535 (2006)
14. M. Suzuki, M. Baba, R.A. Ganeev, H. Kuroda, T. Ozaki, *Opt. Lett.* **31**, 3306 (2006)
15. R.A. Ganeev, H. Singhal, P.A. Naik, V. Arora, U. Chakravarty, J.A. Chakera, R.A. Khan, I.A. Kulagin, P.V. Redkin, M. Raghuramaiah, P.D. Gupta, *Phys. Rev. A* **74**, 063824 (2006)
16. R.A. Ganeev, P.A. Naik, H. Singhal, J.A. Chakera, P.D. Gupta, *Opt. Lett.* **32**, 65 (2007)
17. R.A. Ganeev, H. Singhal, P.A. Naik, U. Chakravarty, V. Arora, J.A. Chakera, R.A. Khan, M. Raghuramaiah, S.R. Kumbhare, R.D. Kushwaha, P.D. Gupta, *Appl. Phys. B* **87**, 243 (2007)
18. M. Suzuki, M. Baba, H. Kuroda, R.A. Ganeev, L.B. Elouga Bom, T. Ozaki, *Opt. Express* **15**, 4112 (2007)
19. R.A. Ganeev, L.B. Elouga Bom, J.-C. Kieffer, T. Ozaki, *Phys. Rev. A* **76**, 023831 (2007)
20. R.A. Ganeev, M. Baba, M. Suzuki, H. Kuroda, *Phys. Lett. A* **339**, 103 (2005)
21. T. Ozaki, L.B. Elouga Bom, R. Ganeev, J.-C. Kieffer, M. Suzuki, H. Kuroda, *Laser Part. Beams* **25**, 321 (2007)
22. R.A. Ganeev, *Phys. Uspekhi* **52**, 55 (2009)
23. R.A. Ganeev, H. Singhal, P.A. Naik, I.A. Kulagin, P.V. Redkin, J.A. Chakera, M. Tayyab, R.A. Khan, P.D. Gupta, *Phys. Rev. A* **80**, 033845 (2009)
24. R.A. Ganeev, M. Suzuki, T. Ozaki, M. Baba, H. Kuroda, *Opt. Lett.* **31**, 1699 (2006)
25. R.A. Ganeev, *High-Order Harmonic Generation in Laser Plasma Plumes* (Imperial College Press, London, 2012)
26. R.A. Ganeev, *Nonlinear Optical Properties of Materials*, vol. 174 (Springer Series in Optical Sciences, 2013)
27. R. A. Ganeev, *Plasma Harmonics* (Pan Stanford Publishing, 2014)
28. R.A. Ganeev, L.B. Elouga Bom, T. Ozaki, *J. Phys. B: At. Mol. Opt. Phys.* **42**, 055402 (2009)
29. R.A. Ganeev, C. Hutchison, T. Witting, F. Frank, S. Weber, W.A. Okell, E. Fiordilino, D. Cricchio, F. Persico, A. Zaïr, J.W.G. Tisch, J.P. Marangos, *J. Opt. Soc. Am. B* **30**, 7 (2013)
30. R.A. Ganeev, T. Witting, C. Hutchison, F. Frank, M. Tudorovskaya, M. Lein, W.A. Okell, A. Zaïr, J.P. Marangos, J.W.G. Tisch, *Opt. Express* **20**, 25239 (2012)
31. R.A. Ganeev, C. Hutchison, T. Witting, F. Frank, W.A. Okell, A. Zaïr, S. Weber, P.V. Redkin, D.Y. Lei, T. Roschuk, S.A. Maier, I. López-Quintás, M. Martín, M. Castillejo, J.W.G. Tisch, J.P. Marangos, *J. Phys. B: At. Mol. Opt. Phys.* **45**, 165402 (2012)
32. S. Haessler, L.B. Elouga Bom, O. Gobert, J.-F. Hergott, F. Lepetit, M. Perdrix, B. Carré, T. Ozaki, P. Salières, *J. Phys. B: At. Mol. Opt. Phys.* **45**, 074012 (2012)
33. S. Haessler, V. Strelkov, L.B. Elouga Bom, M. Khokhlova, O. Gobert, J.-F. Hergott, F. Lepetit, M. Perdrix, T. Ozaki, P. Salières, *New J. Phys.* **15**, 013051 (2013)
34. Y. Pertot, S. Chen, S.D. Khan, L.B. Elouga Bom, T. Ozaki, Z. Chang, *J. Phys. B: At. Mol. Opt. Phys.* **45**, 074017 (2012)
35. C. Hutchison, R.A. Ganeev, T. Witting, F. Frank, W.A. Okell, J.W.G. Tisch, J.P. Marangos, *Opt. Lett.* **37**, 2064 (2012)
36. G.S. Boltaev, R.A. Ganeev, I.A. Kulagin, N.K. Satlikov, T. Usmanov, *Quantum Electron.* **42**, 899 (2012)

37. R.A. Ganeev, C. Hutchison, A. Zaïr, T. Witting, F. Frank, W.A. Okell, J.W.G. Tisch, J.P. Marangos, *Opt. Express* **20**, 90 (2012)
38. R.A. Ganeev, V.V. Strelkov, C. Hutchison, A. Zaïr, D. Kilbane, M.A. Khokhlova, J.P. Marangos, *Phys. Rev. A* **85**, 023832 (2012)
39. R.A. Ganeev, C. Hutchison, T. Siegel, A. Zaïr, J.P. Marangos, *Phys. Rev. A* **83**, 063837 (2011)
40. L.B. Elouga Bom, S. Haessler, O. Gobert, M. Perdrix, F. Lepetit, J.-F. Hergott, B. Carré, T. Ozaki, P. Salières, *Opt. Express* **19**, 3677 (2011)
41. L.B. Elouga Bom, F. Bouzid, F. Vidal, J.-C. Kieffer, T. Ozaki, *J. Phys. B: At. Mol. Opt. Phys.* **41**, 215401 (2008)
42. H. Singhal, V. Arora, B.S. Rao, P.A. Naik, U. Chakravarty, R.A. Khan, P.D. Gupta, *Phys. Rev. A* **79**, 023807 (2009)
43. Y. Pertot, L.B. Elouga Bom, V.R. Bhardwaj, T. Ozaki, *Appl. Phys. Lett.* **98**, 101104 (2011)
44. L.B. Elouga Bom, Y. Pertot, V.R. Bhardwaj, T. Ozaki, *Opt. Express* **19**, 3077 (2011)
45. M. Kumar, H. Singhal, J.A. Chakera, P.A. Naik, R.A. Khan, P.D. Gupta, *J. Appl. Phys.* **114**, 033112 (2013)
46. H. Singhal, P.A. Naik, M. Kumar, J.A. Chakera, P.D. Gupta, *J. Appl. Phys.* **115**, 033104 (2014)
47. R.A. Bartels, A. Paul, H. Green, H.C. Kapteyn, M.M. Murnane, S. Backus, I.P. Christov, Y. Liu, D. Attwood, C. Jacobsen, *Science* **297**, 376 (2002)
48. R.L. Sandberg, A. Paul, D.A. Raymondson, S. Hadrich, D.M. Gaudiosi, J. Holtsnider, R.I. Tobey, O. Cohen, M.M. Murnane, H.C. Kapteyn, *Phys. Rev. Lett.* **99**, 098103 (2007)
49. D. Gauthier, M. Guizar-Sicairos, X. Ge, W. Boutu, B. Carré, J.R. Fienup, H. Merdji, *Phys. Rev. Lett.* **105**, 093901 (2010)
50. A. Morlens, J. Gautier, G. Rey, P. Zeitoun, J. Caumes, M. Kos-Rosset, H. Merdji, S. Kazamias, K. Cassou, M. Fajardo, *Opt. Lett.* **31**, 3095 (2006)
51. D. Descamps, C. Lynga, J. Norin, A. L'Huillier, C.G. Wahlström, J. Hergott, H. Merdji, P. Salières, M. Bellini, T.W. Hänsch, *Opt. Lett.* **25**, 135 (2000)
52. P. Salières, A. L'Huillier, P. Antoine, M. Lewenstein, *Adv. At., Mol., Opt. Phys.* **41**, 1 (1999)
53. T. Ditmire, E.T. Gumbrell, R.A. Smith, J.W.G. Tisch, D.D. Meyerhofer, M.H.R. Hutchinson, *Phys. Rev. Lett.* **77**, 4756 (1996)
54. T. Ditmire, J.W.G. Tisch, E.T. Gumbrell, R.A. Smith, D.D. Meyerhofer, M.H.R. Hutchinson, *Appl. Phys. B* **65**, 313 (1997)
55. L. Le Déroff, P. Salières, B. Carré, D. Joyeux, D. Phalippou, *Phys. Rev. A* **61**, 043802 (2000)
56. V. Strelkov, *Phys. Rev. Lett.* **104**, 123901 (2010)
57. R.A. Ganeev, Z. Abdelrahman, F. Frank, T. Witting, W.A. Okell, D. Fabris, C. Hutchison, J.P. Marangos, J.W.G. Tisch, *Appl. Phys. Lett.* **104**, 021122 (2014)
58. J.S. Robinson, C.A. Haworth, H. Teng, R.A. Smith, J.P. Marangos, J.W.G. Tisch, *Appl. Phys. B* **85**, 525 (2006)
59. T. Witting, F. Frank, C.A. Arrell, W.A. Okell, J.P. Marangos, J.W.G. Tisch, *Opt. Lett.* **36**, 1680 (2011)
60. F. Frank, C. Arrell, T. Witting, W.A. Okell, J. McKenna, J.S. Robinson, C.A. Haworth, D. Austin, H. Teng, I.A. Walmsley, J.P. Marangos, J.W.G. Tisch, *Rev. Sci. Instrum.* **83**, 071101 (2012)
61. K.A. Dick, *Can. J. Phys.* **46**, 1291 (1968)
62. G. Duffy, P. Dunne, *J. Phys. B: At. Mol. Opt. Phys.* **34**, L173 (2001)
63. M.V. Ammosov, N.B. Delone, V.P. Krainov, *Sov. Phys. JETP* **64**, 1191 (1986)
64. M. Smits, C.A. de Lange, A. Stolow, D.M. Rayner, *Phys. Rev. Lett.* **93**, 213003 (2004)
65. R.A. Ganeev, M. Suzuki, M. Baba, H. Kuroda, *J. Opt. Soc. Am. B* **22**, 1927 (2005)
66. R.A. Ganeev, J. Zheng, M. Wöstmann, H. Witte, P.V. Redkin, H. Zacharias, *Eur. Phys. J. D* **68**, 325 (2014)
67. M. Silies, H. Witte, S. Linden, J. Kutzner, I. Uschmann, E. Förster, H. Zacharias, *Appl. Phys. A* **96**, 59 (2009)

68. R.A. Ganeev, M. Suzuki, M. Baba, H. Kuroda, *Phys. Rev. A* **76**, 023805 (2007)
69. M. Suzuki, M. Baba, H. Kuroda, R.A. Ganeev, T. Ozaki, *Opt. Express* **15**, 1161 (2007)
70. E.S. Toma, P. Antoine, A. de Bohan, H.G. Muller, *J. Phys. B: At. Mol. Opt. Phys.* **32**, 5843 (1999)
71. M.B. Gaarde, K.J. Schafer, *Phys. Rev. A* **64**, 013820 (2001)
72. Z. Zeng, R. Li, Y. Cheng, W. Yu, Z. Xu, *Phys. Scripta* **66**, 321 (2002)
73. R. Bartels, S. Backus, E. Zeek, L. Misoguti, G. Vdovin, I.P. Christov, M.M. Murnane, H.C. Kapteyn, *Nature* **406**, 164 (2000)
74. R.A. Ganeev, J.A. Chakera, P.A. Naik, H. Singhal, R.A. Khan, P.D. Gupta, *J. Opt. Soc. Am. B* **28**, 1055 (2011)
75. J. Stadler, R. Mikulla, H.-R. Trebin, *Int. J. Mod. Phys.* **8**, 1131 (1997)
76. M.A.L. Marques, A. Castro, G.F. Bertsch, A. Rubio, *Comput. Phys. Commun.* **151**, 60 (2003)
77. A. Castro, H. Appel, M. Oliveira, C.A. Rozzi, X. Andrade, F. Lorenzen, M.A.L. Marques, E.K.U. Gross, A. Rubio, *Phys. Stat. Sol. B* **243**, 2465 (2006)
78. G.S. Boltaev, R.A. Ganeev, I.A. Kulagin, T. Usmanov, *J. Opt. Soc. Am. B* **31**, 436 (2014)
79. R.A. Ganeev, *Open Spectrosc. J.* **3**, 1 (2009)
80. D.B. Milošević, *Phys. Rev. A* **81**, 023802 (2010)
81. M.V. Frolov, N.L. Manakov, A.F. Starace, *Phys. Rev. A* **82**, 023424 (2010)
82. M. Tudorovskaya, M. Lein, *Phys. Rev. A* **84**, 013430 (2011)
83. L. Plaja, L. Roso, *J. Mod. Opt.* **40**, 793 (1993)
84. P.A. Oleinikov, V.T. Platonenko, G. Ferrante, *J. Exp. Theor. Phys. Lett.* **60**, 246 (1994)
85. C.F. Faria, R. Kopold, W. Becker, J.M. Rost, *Phys. Rev. A* **65**, 023404 (2002)
86. R. Taïeb, V. Vénier, J. Wassaf, A. Maquet, *Phys. Rev. A* **68**, 033403 (2003)
87. V.I. Anikin, V.D. Gora, K.N. Drabovich, A.N. Dubovik, *Sov. J. Quantum Electron.* **6**, 174 (1976)
88. J.F. Reintjes, *Nonlinear Optical Parametric Processes in Liquids and Gases* (Academic Press, Cambridge, 1984)
89. I.A. Kulagin, T. Usmanov, *Quantum Electron.* **30**, 520 (2000)
90. R.A. Ganeev, G.S. Boltaev, N.K. Satlikov, I.A. Kulagin, T. Usmanov, *J. Opt. Soc. Am. B* **29**, 3286 (2012)
91. A. Kramida, Y. Ralchenko, J. Reader, NIST ASD Team, NIST Atomic Spectra Database (ver. 5.1). National Institute of Standards and Technology, Gaithersburg, MD, USA (2013) <http://physics.nist.gov/asd>
92. G.C. Bjorklund, *IEEE J. Quantum Electron.* **11**, 287 (1975)
93. R. Hilbig, A. Lago, R. Wallenstein, *Opt. Commun.* **49**, 297 (1984)
94. R.A. Ganeev, V.V. Gorbushin, I.A. Kulagin, T. Usmanov, *Appl. Phys. B* **41**, 69 (1986)
95. A. McPherson, G. Ginson, H. Jara, N. Johann, I.A. McIntyre, K. Boyer, C.K. Rhodes, *J. Opt. Soc. Am. B* **4**, 595 (1987)
96. M. Ferray, A. L'Huillier, X.F. Li, L.A. Lompré, G. Mainfray, G. Manus, *J. Phys. B: At. Mol. Opt. Phys.* **21**, L31 (1988)
97. L.A. Lompré, A. L'Huillier, M. Ferray, P. Monot, G. Mainfray, G. Manus, *J. Opt. Soc. Am. B* **7**, 754 (1990)
98. T.D. Donnelly, T. Ditmire, K. Neuman, M.D. Perry, R.W. Falcone, *Phys. Rev. Lett.* **76**, 2472 (1996)
99. J.W.G. Tisch, T. Ditmire, D.J. Fraser, N. Hay, M.B. Mason, E. Springate, J.P. Marangos, M.H.R. Hutchinson, *J. Phys. B: At. Mol. Opt. Phys.* **30**, L709 (1997)
100. C. Vozzi, M. Nisoli, J.-P. Caumes, G. Sansone, S. Stagira, S. De Silvestri, M. Vecchiocattivi, D. Bassi, M. Pascolini, L. Poletto, P. Villoresi, G. Tondello, *Appl. Phys. Lett.* **86**, 111121 (2005)
101. C.-H. Pai, C.C. Kuo, M.-W. Lin, J. Wang, S.-Y. Chen, J.-Y. Lin, *Opt. Lett.* **31**, 984 (2006)
102. R.A. Ganeev, M. Suzuki, M. Baba, M. Ichihara, H. Kuroda, *J. Phys. B: At. Mol. Opt. Phys.* **41**, 045603 (2008)
103. R.A. Ganeev, L.B. Elouga Bom, T. Ozaki, *J. Appl. Phys.* **106**, 023104 (2009)

104. H. Singhal, R.A. Ganeev, P.A. Naik, A.K. Srivastava, A. Singh, R. Chari, R.A. Khan, J.A. Chakera, P.D. Gupta, *J. Phys. B: At. Mol. Opt. Phys.* **43**, 025603 (2010)
105. T. Ozaki, L.B. Elouga Bom, J. Abdul-Haji, R.A. Ganeev, *Laser Part. Beams* **28**, 69 (2010)
106. H. Singhal, R.A. Ganeev, P.A. Naik, J.A. Chakera, U. Chakravarty, H.S. Vora, A.K. Srivastava, C. Mukherjee, C.P. Navathe, S.K. Deb, P.D. Gupta, *Phys. Rev. A* **82**, 043821 (2010)
107. S.X. Hu, Z.Z. Xu, *Appl. Phys. Lett.* **71**, 2605 (1997)
108. V. Véniard, R. Taïeb, A. Maquet, *Phys. Rev. A* **65**, 013202 (2001)
109. J.R. Vázquez de Aldana, L. Roso, *J. Opt. Soc. Am. B* **18**, 325 (2001)
110. M. Kundu, S.V. Popruzhenko, D. Bauer, *Phys. Rev. A* **76**, 033201 (2007)
111. T. Kanai, E.J. Takahashi, Y. Nabekawa, K. Midorikawa, *Phys. Rev. Lett.* **98**, 153904 (2007)
112. J. Seres, V.S. Yakovlev, E. Seres, C. Strelly, P. Wobrauschek, C. Spielmann, F. Krausz, *Nature Phys.* **3**, 878 (2007)
113. E.J. Takahashi, T. Kanai, K.L. Ishikawa, Y. Nabekawa, K. Midorikawa, *Phys. Rev. Lett.* **99**, 053904 (2007)
114. T. Kanai, E.J. Takahashi, Y. Nabekawa, K. Midorikawa, *Phys. Rev. A* **77**, 041402R (2008)
115. R.A. Ganeev, H. Kuroda, *Appl. Phys. B* **103**, 151 (2011)
116. R.A. Ganeev, T. Witting, C. Hutchison, F. Frank, P.V. Redkin, W.A. Okell, D.Y. Lei, T. Roschuk, S.A. Maier, J.P. Marangos, J.W.G. Tisch, *Phys. Rev. A* **85**, 015807 (2012)
117. M. Wöstmann, P.V. Redkin, J. Zheng, H. Witte, R.A. Ganeev, H. Zacharias, *Appl. Phys.* **119**, 352 (2015)
118. N.A. Papadogiannis, C. Kalpouzos, E. Goulielmakis, G. Nersisyan, D. Charalambidis, F. Augé, F. Weihe, P. Balcou, *Appl. Phys B* **73**, 687 (2001)
119. J. Hüve, T. Haarlammert, T. Steinbrück, J. Kutzner, G. Tsilimis, H. Zacharias, *Opt. Commun.* **266**, 261 (2006)
120. R.A. Ganeev, M. Baba, M. Suzuki, H. Kuroda, *J. Mod. Opt.* **53**, 1451 (2006)
121. K.E. Schriver, J.L. Persson, E.C. Honea, R.L. Whetten, *Phys. Rev. Lett.* **64**, 2539 (1990)
122. T. Kanai, E.J. Takahashi, Y. Nabekawa, K. Midorikawa, *New J. Phys.* **10**, 025036 (2008)
123. C. Jin, X.-X. Zhou, S.-F. Zhao, *Chin. Phys. Lett.* **27**, 033301 (2010)
124. A. Willner, F. Tavella, M. Yeung, T. Dzelzainis, C. Kamperidis, M. Bakarezos, D. Admas, M. Schulz, R. Riedel, M.C. Hoffmann, W. Hu, J. Rossbach, M. Drescher, N.A. Papadogiannis, M. Tatarakis, B. Dromey, M. Zepf, *Phys. Rev. Lett.* **107**, 175002 (2011)
125. R.A. Ganeev, M. Suzuki, H. Kuroda, *Phys. Rev. A* **89**, 033821 (2014)
126. R.A. Ganeev, M. Suzuki, H. Kuroda, *J. Exp. Theor. Phys. Lett.* **99**, 368 (2014)
127. C.C. Garcia, H. Lindner, A. von Bohlen, C. Vadla, K. Niemax, *J. Anal. At. Spectrom.* **23**, 470 (2008)
128. B.L. Henke, E.M. Gullikson, J.C. Davis, *At. Data Nucl. Data Tabl.* **54**, 181 (1993)
129. F.W. Salt, J.G.N. Thomas, *Nature* **178**, 434 (1956)
130. G. Tsilimis, C. Benesch, J. Kutzner, H. Zacharias, *J. Opt. Soc. Am. B* **20**, 246 (2003)
131. M. Schnürer, Z. Cheng, M. Hentschel, G. Tempea, P. Kalman, T. Brabec, F. Krausz, *Phys. Rev. Lett.* **83**, 722 (1999)

Chapter 3

HHG in Extended Plasmas

In this chapter, we analyze the nonlinear optical properties of the long (~ 5 mm) plasma plumes used for the high-order harmonic generation of laser radiation. We present these studies along the different ranges of XUV using the single color and two-color pumps of the extended plasmas produced on various metal surfaces, which allowed the efficient odd and even harmonics generation. We also demonstrate the methods of modulation of the spatial characteristics of laser plasma. Finally, we show the methods of characterization of the plasma harmonic produced at these conditions.

3.1 Advanced Properties of Extended Plasmas for Efficient High-Order Harmonic Generation

The harmonic intensity increases as the square of medium length in the case of weak reabsorption and at the optimum phase matching conditions [1]. However, once the medium length exceeds the coherence length (L_{coh}), the harmonic intensity start to show the oscillations due to phase mismatch [2]. To analyze this process in the laser-produced plasmas, one has to carefully define the best conditions of plasma HHG in the extended medium, while taking into account the peculiar properties of different materials used for laser ablation.

The advantages of the HHG in laser-produced plasmas were realized when low-excited, low-ionized plasma was applied for the harmonic generation [3]. The application of such plasmas immediately followed with the observation of strong harmonics, which became comparable with those reported in gas HHG studies. Moreover, as it was shown in Chap. 2, a substantial increase in the highest order of generated harmonics, emergence of a plateau in the energy distribution of harmonics, high efficiencies obtained with several plasma formations, resonance-induced enhancement of individual harmonics, efficient harmonic generation from the plasma plumes containing clusters of different materials, and other features have demonstrated the attractiveness of plasma HHG.

Previously, plasma harmonic yield has been increased by proper optimization of the fluency of heating pulse [4], delay between the heating pulse and the driving femtosecond pulse [5], focal position of the laser pulse in the plasma plume [6], pulse duration of the heating radiation [7], chirp of the driving radiation [8], use of the clustered targets [9], plasma characteristics [10], etc. The majority of those plasma harmonic studies were carried out using the short length plasma plumes (≤ 0.5 mm). The sizes of plasma plumes were defined by the focusing conditions of the spherical lenses used for ablation of the targets. In the meantime, one could expect that application of longer plasmas would further enhance the conversion efficiency due to the quadratic dependence of the nonlinear optical response of the medium on the length of laser-matter interaction. To create an extended area of ablation on the target surface, one has to carefully choose the conditions of plasma formation. The absorption of extended plasma can prevent the enhancement of harmonic yield. The presence of free electrons and excited ions in the extended plasma plumes can cause the growth of some impeding processes, such as phase mismatch and Kerr effect, during propagation of the laser pulse through the medium. To achieve higher HHG conversion efficiency, the length of the medium might be increased provided the phase mismatch between the laser field and the harmonic radiation maintains low [11–14]. Below we describe a series of experiments showing the advanced properties of extended plasma as the efficient media for harmonic generation [15].

The uncompressed radiation of Ti:sapphire laser (central wavelength 802 nm, pulse duration 370 ps, pulse energy up to $E_{hp} = 4$ mJ, 10 Hz pulse repetition rate) was used for extended plasma formation. These heating pulses were focused using a 200 mm focal length cylindrical lens inside the vacuum chamber containing an ablating target to create the extended plasma plume (Fig. 3.1). The intensity of heating pulse on the target surface was varied up to 5×10^9 W cm $^{-2}$. The plasma sizes were 5×0.08 mm 2 . The driving compressed pulse from the same laser with the energy up to $E_{dp} = 4$ mJ and 64 fs pulse duration was used, after 45 ns delay, for

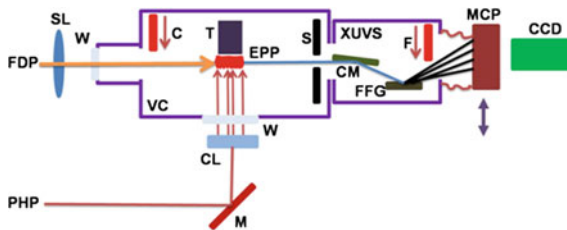


Fig. 3.1 Experimental scheme for harmonic generation in extended plasma plumes. *FDP* femtosecond driving pulse; *PHP* picosecond heating pulse; *SL* spherical lens; *CL* cylindrical lens; *VC* vacuum chamber; *W* windows of vacuum chamber; *C* nonlinear crystal (BBO); *T* target; *EPP* extended plasma plume; *S* slit; *XUVS* extreme ultraviolet spectrometer; *CM* cylindrical mirror; *FFG* flat field grating; *F* metallic filter; *MCP* movable micro-channel plate registrar; *CCD* charge coupled device camera. Reproduced with permission from [15]. Copyright 2014. AIP Publishing LLC

odd harmonics generation in the long plasma plumes. The driving pulse was focused by using the 400 mm focal length spherical lens onto the prepared plasma from the orthogonal direction, at a distance of $\sim 100 \mu\text{m}$ above the target surface. The intensity of driving pulse at the focus area was varied up to $8 \times 10^{14} \text{ W cm}^{-2}$. The confocal parameter of the focused radiation was 12 mm.

The harmonic emission was analyzed by the XUV spectrometer containing a gold-coated cylindrical mirror and a 1200 grooves/mm flat field grating (FFG) with variable line spacing. The spectrum was recorded on a MCP detector with the phosphor screen, which was imaged onto a CCD camera. The movement of MCP along the focusing plane of FFG allowed the variation of the range of XUV observations.

Various materials (Ag, Mn, Zn, In, Cr, C, Mo) were studied as the ablating targets. The sizes of these targets where the ablation occurred were 5 mm. A three-coordinate manipulator allowed to move the target and to control a zone of interaction of the driving radiation and the plasma relative to the target surface.

At the conditions of weak absorption, the unsaturated harmonic yield (I_H) should follow the quadratic dependence on the length (d) of nonlinear medium ($I_H \propto d^l$, where $l = 2$ [16]). The important issue is the influence of the ionic resonances possessing high oscillator strength on the $I_H(d)$ dependence, which will be discussed below in the case of indium plasma.

These dependences were analyzed for different harmonics in a few plasma plumes. Figure 3.2 presents these results in the case of zinc plasma at the heating pulse intensity of $2 \times 10^9 \text{ W cm}^{-2}$ and fluence of 0.8 J cm^{-2} . The length of the plasma plume was varied in the range of 0.3–5 mm with the step of 0.3 mm by

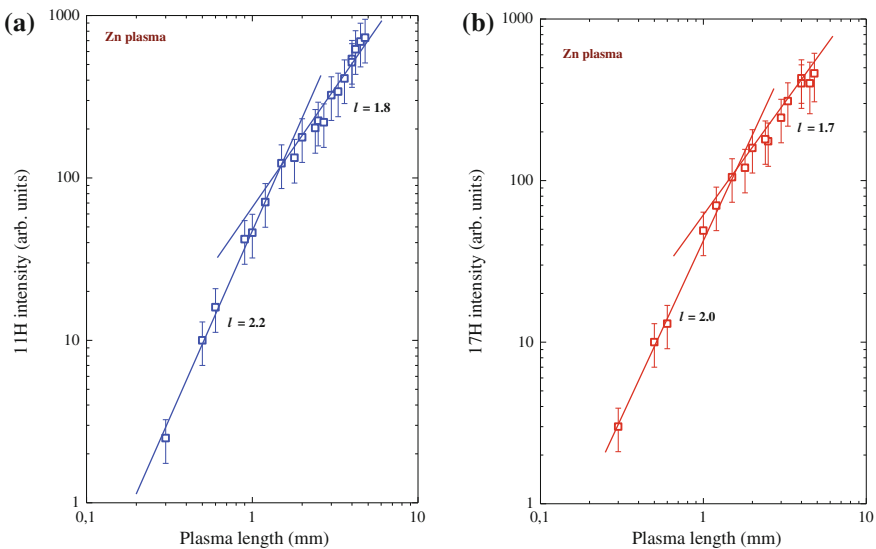


Fig. 3.2 Dependences of the **a** 11th and **b** 17th harmonic intensities on the length of zinc plasma. Reproduced with permission from [15]. Copyright 2014. AIP Publishing LLC

inserting a slit of variable width in the path of the heating beam after the cylindrical focusing lens.

In the case of 11th harmonic (Fig. 3.2a), this dependence had a slope $l \approx 2.2$ up to the $d = 1.5$ mm, with further decrease of the slope ($l \approx 1.8$). One can see a significant and almost unsaturated increase of 11th harmonic yield with the growth of plasma length along the whole range of variations of this parameter.

These studies showed that the free electrons, absorption of plasma, phase mismatch, Kerr effect, etc. did not play a significant role in the variation of this dependence at the optimal excitation of the target when the low-density weakly ionized plasma was produced. Analogous behavior was observed for different harmonics (see the $I_H(d)$ dependence for the 17th harmonic, Fig. 3.2b). A few other plasmas (C, Cr, Mo, Ag, Mn) have also proven the advanced properties of extended media for achieving the efficient HHG. Among them, carbon plasma seems an attractive example of the efficient use of long plasma plumes for the enhancement of harmonics along the whole spectrum.

Almost all those plasmas have shown the $I_H(d)$ dependences similar to the zinc plasma (see, for example, the dependence in the case of the 29th harmonic generating in the chromium plasma, Fig. 3.3a). It was confirmed that in most cases, when the targets were ablated at the fluences of a few hundred millijoules per square centimeter, the extended plasma produced along the path of femtosecond driving radiation showed insignificant saturation properties, with the $I_H(d)$ slope of 2 or close to this value.

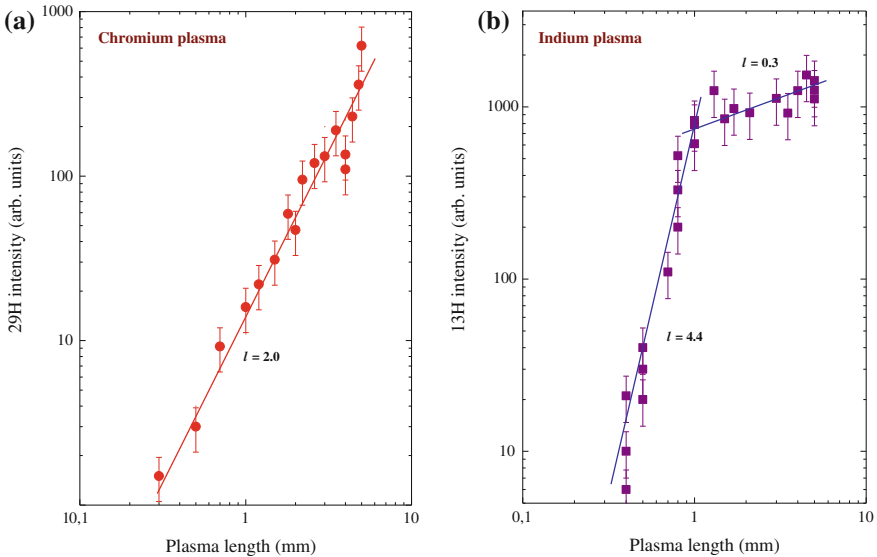


Fig. 3.3 Dependences of **a** the 29th harmonic generating in chromium, and **b** the 13th harmonic generating in indium on the lengths of plasma plumes. Reproduced with permission from [15]. Copyright 2014. AIP Publishing LLC

Another pattern was observed in the case of resonantly enhanced harmonics, particularly in the case of ablated indium target. This plasma has long been considered as an example of efficient generation of the resonantly enhanced 13th harmonic of Ti:sapphire lasers, which was almost two orders of magnitude stronger than the neighbor harmonics [17, 18] (see also Chap. 2). The $I_H(d)$ dependence was analyzed for both the nonresonant and resonant harmonics generating in the indium plasma. Whilst the nonresonant harmonic yields for the 11th and 19th orders showed the similar nearly quadratic dependences with the growth of plasma length, the 13th harmonic had a specific peculiarity. The slope of $I_{13H}(d)$ dependence from the very beginning (i.e., for the shortest plasma lengths) was notably larger than 2 (Fig. 3.3b; l was defined to be close to 4) with the abrupt change of the slope at the plasma length exceeding 1.3 mm ($l \approx 0.3$). The yield of 13th harmonic at $d > 1.5$ mm became unstable. Note that such behavior was not observed in the case of the 29th harmonic generating from the chromium plasma (Fig. 3.3a). This harmonic has also shown some resonance-related properties, both in discussed and earlier [19] experiments with chromium plasma. The observed influence of the length of nonlinear medium on the yield of resonantly enhanced harmonic in the case of indium plasma was considerably stronger compared with the case of Cr plasma due to a significant difference in the enhancement factors of resonant harmonics (13th and 29th orders, respectively) with regard to the neighboring harmonics.

The resonances, which enhance the yield of specific harmonics in the In and Cr plasmas are related with the excitation of ionic transitions. Enhanced 13th harmonic from In-contained plasma has been explained as effect of resonance with one of the strong In II transitions [17]. Particularly, an exceptionally strong transition was observed at 19.92 eV (62.1 nm) corresponding to the $4d^{10}5s^21S_0 \rightarrow 4d^95s^25p$ (2D) 1P_1 transition of In II. The oscillator strength of this transition has been calculated to be 1.11, which is more than 12 times larger than the gfs of other transitions of In II. This transition can be driven into resonance with the 13th harmonic (61.7 nm, 20.17 eV) of 802 nm radiation.

Previous studies of photoabsorption and photoionization spectra of Cr plasma in the range of 41–42 eV have demonstrated the presence of strong transitions. In particular, the region of the “giant” $3p$ – $3d$ resonances of Cr II spectra has the strong transitions, which could both enhance and diminish the optical and nonlinear optical response of the plume. Note the role of the $3d^5(^6S)$ state in determining the special position of Cr among the $3d$ elements. The calculations of gf values in the photon energy range of 40–60 eV showed a group of the transitions in the 44.5–44.8 eV region possessing strong oscillator strengths (with gf varying between 1 and 2.2), which considerably exceeded those of other transitions in the range of 40–60 nm. These transitions were assumed to be responsible for the observed enhancement of the 29th harmonic.

Thus the ionization state, which may play a decisive role in the enhancement of the nonlinear optical response of plasma medium, is dominantly related with the singly charged particles of above species (In, Cr). The densities of plasma plumes at these conditions were defined by the conditions of excitation using the heating pulse and have been calculated using the code ITAP IMD. The typical

concentrations of plasma plumes at maximal yields of harmonics were in the range of 1×10^{17} – $4 \times 10^{17} \text{ cm}^{-3}$ depending on the target material.

These studies showed that the nearly quadratic rule of $I_H(d)$ dependence is maintained along the whole plasma length only in the case of weakly excited targets. The growth of target excitation increases the plasma concentration, which in turn should increase the harmonics yield. In this connection, a fluence of the heating pulse on the target surface becomes an important parameter for optimization of high-order harmonic emission. The dependences of harmonic efficiency on the energy of heating pulse on the surfaces of few targets were measured while maintaining the same geometry of extended ablation beam on the targets (Fig. 3.4). The common feature of those measurements was an observation of a maximum of the $I_{33H}(E_{hp})$ and $I_{47H}(E_{hp})$ dependences obtained from the Ag and Mn extended plasmas, respectively ($E_{hp} \approx 3 \text{ mJ}$ for both cases), with the following gradual decrease of harmonic yield during irradiation of the targets using stronger heating pulses. The reason of these observations is related with the over-excitation of target, which led to appearance of the abundance of free electrons in the extended plasma plume. The long plasma plumes obtained at optimal conditions of ablation allowed generation of the harmonics extended towards the shorter-wavelength edge of XUV in various ionized media. Particularly, the harmonics above the 100th order were observed in the case of long Mn plasma.

The similarity in the $I_H(d)$ dependences in the cases of most plasmas demonstrates that these samples have no specific features (neither strong absorption and phase mismatch, nor resonance-induced enhancement of the nonlinear optical response of the medium) in the XUV range. Meanwhile, the carbon plasma has demonstrated some peculiarities of the $I_H(d)$ dependence, which were assumed to be related with the structural properties of this medium, particularly with the presence of the small-sized nanoparticles. Those observations have demonstrated

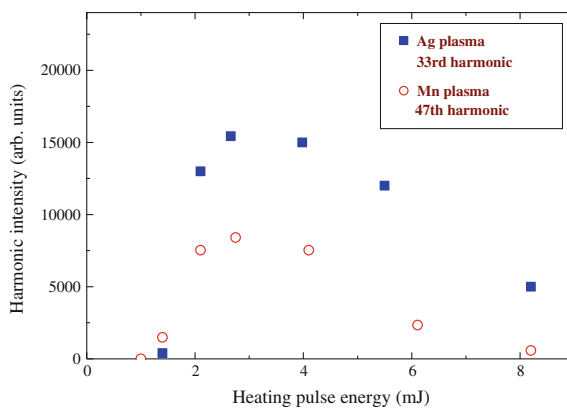


Fig. 3.4 33rd and 47th harmonic yields from the Ag (*filled squares*) and Mn (*open circles*) plasmas as the functions of heating pulse energy. The intensity of driving pulse was maintained at $4 \times 10^{14} \text{ W cm}^{-2}$. Reproduced with permission from [15]. Copyright 2014. AIP Publishing LLC

that the plasma harmonic generation using the extended media can be considered as a tool for the nonlinear optical spectroscopic analysis of the materials and for the comparison of the role of the macro- and micro-processes governing HHG.

These studies have demonstrated the attractive properties of extended plasmas as the media for HHG. There might be a question about why the harmonics are phase matched over such a relatively long length. At high fluences of heating ablation pulse, the growth of electron density (N_e) may cancel all advantages of extended nonlinear optical medium. A growth of plasma concentration using the increase of the fluence of heating pulse may decrease the harmonic yield because the phase mismatch caused a destructive interference of the harmonic photons generated in the first half and the second half of the source. The variation of N_e allows the adjustment of the coherence length for the efficient generation of harmonics in different spectral ranges. The adjustment of N_e could be easily accomplished during the plasma harmonic generation, compared with the gas harmonic generation, through the proper variation of the fluence of ablating beam on the target surface to achieve a required concentration of the free electrons in the plasma plumes.

The application of conditions when electron concentration contains at moderate level allows the maintenance of the phase matching of interacting waves in the longer plasmas. The dependence of the harmonic yield on the heating pulse energy is presented to confirm the above assumptions. Indeed, those studies have shown how and why the heating pulse energy matters. The over-heating of target leads to the appearance of large amount of free electrons, which cancel the phase matching conditions. This assumption also explains why the increase of harmonic yield changes slope for the longest lengths. The application of stronger excitation leads to decrease of the coherence length with the following change of the harmonic yield from the quadratic to lesser slope for longer lengths. As for the observation of the resonantly enhanced harmonic in indium, which exhibited a completely different $I_{13H}(d)$ dependence, the explanation is related with the influence of the resonance on the dispersion of the indium plasma in the region of 13th harmonic.

Thus, the demonstration of harmonic enhancement in the extended line plasmas and the observation of the saturation of this process at over-excitation of the targets shown in discussed research can be considered as the first steps for the further studies to overcome the latter obstacle by using the quasi-phase-matching (see Chap. 4).

3.2 Enhanced Harmonic Generation Using Different Second-Harmonic Sources for the Two-Color Pump of Extended Laser-Produced Plasmas

One could expect that the application of a two-color pump may lead, at appropriate conditions of extended plasma formation, to further growth of the coherent XUV yield of these sources. The use of two-color pump schemes for HHG is a well

known approach for broadening of the spectrum of generated short-wavelength radiation. The two-color pump using fundamental and second harmonic fields has become a practical method of harmonic enhancement in the gas media [20–27]. As suggested in [25], a strong harmonic generation in the case of a two-color field is possible due to (i) formation of a quasi-linear field, (ii) selection of a short quantum path component, which has a denser electron wave packet, and (iii) higher ionization rate compared with the single-color pump. The orthogonally polarized second field also participates in the modification of the trajectory of the accelerated electron from being two-dimensional to being three-dimensional, which leads to removal of the medium symmetry. With suitable control of the relative phase between the fundamental and second harmonic waves, the latter field enhances the short path contribution while diminishing other electron paths, resulting in a clean high-harmonic spectrum. This approach has been applied for plasma harmonic generation as well. In [28], the first demonstration of an increase in the harmonic conversion efficiency from the narrow (~ 0.3 -mm-long) plasma plumes irradiated by an intense two-color femtosecond laser pulse, wherein the fundamental radiation and its weak second-harmonic (at the energy ratio of 50:1) were linearly polarized orthogonal to each other, was reported. At the same time, no proper analysis of this process at different rates of overlapping of the two pumps in the plasma medium was carried out. Note that application of extended plasma at these conditions of excitation may offer some attractive peculiarities related with better matching of the two pump waves in the nonlinear optical medium.

Below we discuss the results of HHG using the single-color and two-color pumps of the long (5 mm) plasmas produced on various metal surfaces using different sources of second-harmonic pump [29]. Barium borate (BBO) crystals of different thickness were applied to manipulate the overlapping of two pumps in the extended plasma area. Different relations between the delays and intensities of these pumps allowed the definition of the optimal length of BBO for the efficient generation of even and odd harmonics using the targets possessing various ablation characteristics. We analyze enhanced even harmonics, which become stronger than the odd ones, while using a relatively weak second field.

The experimental scheme was similar to one described in Sect. 3.1. To analyze even and odd harmonic generation in the extended plasmas, the two-color pump scheme was used. Part of the driving pulse was converted to the second harmonic in the nonlinear crystal (BBO, type I) placed inside the vacuum chamber on the path of the focused driving beam at a distance of 150 mm from the plasma plume, as shown in Fig. 3.1. The crystals of 0.02-, 0.3-, 0.5-, 0.7-, and 1-mm thicknesses were used to analyze the conditions of optimal overlapping of the two pulses in the plasma medium. The corresponding second harmonic conversion efficiencies in those crystals were 0.6, 5, 9, 11, and 13 %. The driving and second-harmonic beams were focused inside the plasma plume. The polarizations of these two pumps were orthogonal to each other.

The installation of the nonlinear crystal inside the vacuum chamber in the path of focused radiation allows excluding the spatial walk-off effect and the influence of the dispersion of window and focusing lens. The spatial overlapping between the

two beams became sufficient for the interaction of two waves in the extended plasma plume. At the same time, the group velocity dispersion in BBO led to a temporal separation of two pulses. Due to this effect in the type-I BBO crystal, the 802 nm pulse (ω) was delayed ($\Delta_{\text{cryst}} = d \left[(n_{\omega}^o)_{\text{group}}/c - (n_{2\omega}^e)_{\text{group}}/c \right] \approx 57$ fs for the 0.3-mm-long BBO) with respect to the 401 nm pulse (2ω) due to $n_{\omega}^o > n_{2\omega}^e$ in this negative uniaxial crystal. Here d is the crystal length, $c/(n_{\omega}^o)_{\text{group}}$ and $c/(n_{2\omega}^e)_{\text{group}}$ are the group velocities of the ω and 2ω waves in the BBO crystal, c is the light velocity, and n_{ω}^o and $n_{2\omega}^e$ are the refractive indices of the ω and 2ω waves. The duration of second harmonic pulse is given by $t_{2\omega} \approx [(\Delta_{\text{cryst}})^2 + 0.5(t_{\omega})^2]^{1/2}$ [30]. Hence, the 401 nm beam has longer pulse duration, corresponding to the induced delay and a certain percentage (~ 50 %) of the fundamental pulse duration. The latter is because the energy of the fundamental radiation is in general not high enough in the pulse wings to effectively generate the second-order harmonic. $t_{2\omega}$ at the output of the 0.3-mm-long BBO crystal can be estimated to be about 72 fs. One can assume from these calculations that the 802 and 401 nm pulses were only partially overlapped while entering the linear plasma. This partial overlap has decreased the ratio between the overlapped second harmonic and driving radiation and diminished the influence of the 401 nm wave on the output spectrum of generating harmonics.

Nevertheless, as will be shown below, even at these unfavorable conditions the efficiencies of even and odd harmonics were comparable in the cases of the 0.3- and 0.5-mm-long crystals. Note that application of longer crystals (type-I BBO, $d = 0.7$ and 1 mm) led to a considerable change of the role of the second-harmonic wave. While conversion efficiency toward the second-harmonic wave in these cases was higher than in the case of shorter BBO crystals, the delay between pump pulses allowed only insignificant temporal overlap in the plasma. The second-harmonic wave in that case behaved as a separate driving source, which created the odd harmonics of this radiation. The example of plasma harmonic spectrum in the case of 0.7-mm-long BBO is shown in the bottom panel of Fig. 3.5a. One can clearly see the enhanced 14th, 18th, and 22nd harmonics of 802 nm radiation generated in the zinc plasma, which corresponded to the 7th, 9th, and 11th harmonics of the 401 nm pump. The absence of 16th and 20th harmonics clearly points out the lack of overlapping of the two pumps. The upper panel of Fig. 3.5a shows the featureless spectrum of the broadband odd harmonics in the case of a single-color pump.

The temporal delays between the fundamental and second harmonic waves, as well as the pulse durations of 401 nm radiation in the cases of different BBO crystals, are summarized in Table 3.1. Here we also show the conversion efficiencies in those crystals and the relative intensities of the overlapped parts of 2ω and ω pulses in the plasma area. The dispersion properties of plasma plumes were not taken into account due to the low concentration of the medium ($\sim 3 \times 10^{17} \text{ cm}^{-3}$). One can see from this table that the ratios between two (2ω and ω) overlapped pumps in the cases of 0.02-, 0.7-, and 1-mm-long crystals are notably smaller compared with the cases of 0.3- and 0.5-mm-long BBO. These calculations

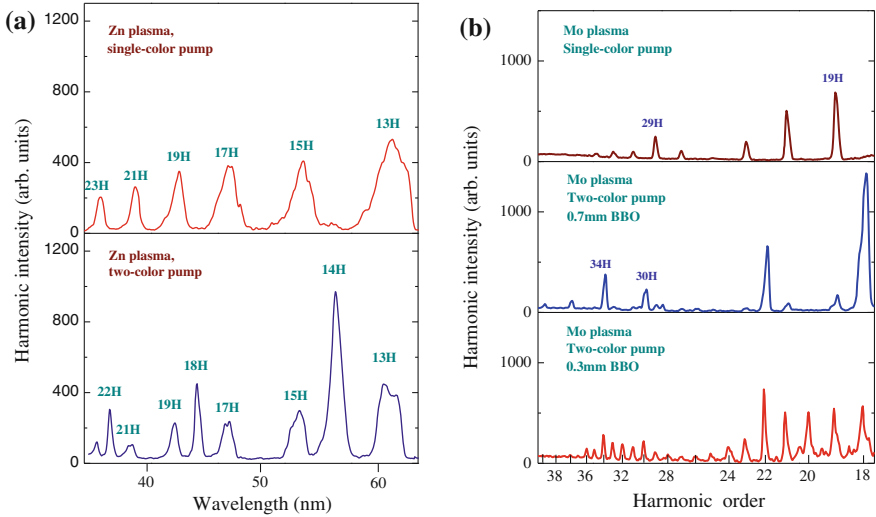


Fig. 3.5 **a** Harmonic spectra from single-color (*upper panel*) and two-color (*bottom panel*) pumps of extended zinc plasmas. In the latter case a 0.7-mm-long BBO crystal was used for second harmonic generation. **b** Harmonics spectra from extended molybdenum plasma using the single-color pump (*upper panel*) and two-color pump (two other panels). The middle and bottom panels were obtained in the cases of using the 0.7- and 0.3-mm-long BBO crystals, respectively. Reproduced from [29] with permission from Optical Society of America

Table 3.1 Second harmonic pulse durations, delays between ω and 2ω pulses, conversion efficiencies, and two pumps ratios in the plasmas for different BBO crystals used for second harmonic generation

Crystal thickness (mm)	Conversion efficiency of 2ω	2ω pulse duration (fs)	Delay between pulses (fs)	Ratio between 2ω and ω pulses overlapped in plasma
0.02	0.004	65	1	0.004
0.3	0.05	72	57	0.03
0.5	0.09	105	95	0.04
0.7	0.11	140	133	0.01
1	0.13	195	190	0.007

Reproduced from [29] with permission from Optical Society of America

show that in the case of second-harmonic generation in the 0.02-, 0.7-, and 1-mm-long crystals one cannot expect the effective interaction of two waves in the plasma area.

Another example of separately generated harmonics is shown in Fig. 3.5b. The two upper panels show the harmonic spectra generated from the molybdenum plasma in the cases of single- and two-color pumps. In the latter case, the use of 0.7-mm-long BBO crystal led to generation of the strong odd harmonics of 401 nm radiation. The presence of the ionic transitions possessing strong oscillator strengths

may be responsible for the enhanced 29th harmonic in the case of the 802 nm pump as well as the enhanced 30th and 34th harmonics in the case of the 802 + 401 nm pump. One can assume the orthogonal polarizations of the strong harmonics originated from the 401 nm pump and the weaker harmonics originated from the 802 nm pump. For comparison, here also presented the harmonic spectrum obtained in the case of application of the 0.3-mm-long BBO crystal (bottom panel). This spectrum shows equal odd and even harmonics along the whole range of observation. In that case the polarizations of all harmonics were defined by the polarization of the main (802 nm) pump. The similarity of the polarizations of odd and even harmonics at these conditions was proven in separate experiments when we found the same polarizations of the 3rd and 4th harmonics.

Below we discuss the HHG spectra from manganese plasma obtained at similar conditions (i.e., using the 0.7-mm-long BBO). The upper panel of Fig. 3.6a shows part of the extended plateau-like spectrum using the single-color pump. This spectrum consists of two parts: the right one (“first plateau”) containing the 17th to 31st harmonics, and the left one (“second plateau”) starting from the enhanced 33rd harmonic, which has already been reported during early studies of the HHG in this plasma [31]. The two-color pump using 0.7-mm-long BBO caused both the enhancement of some odd harmonics and the appearance of the strong even harmonics corresponding to the odd harmonics of 401 nm radiation (see the spectrum of Mn harmonics presented in the bottom panel of Fig. 3.6a), similarly to the cases

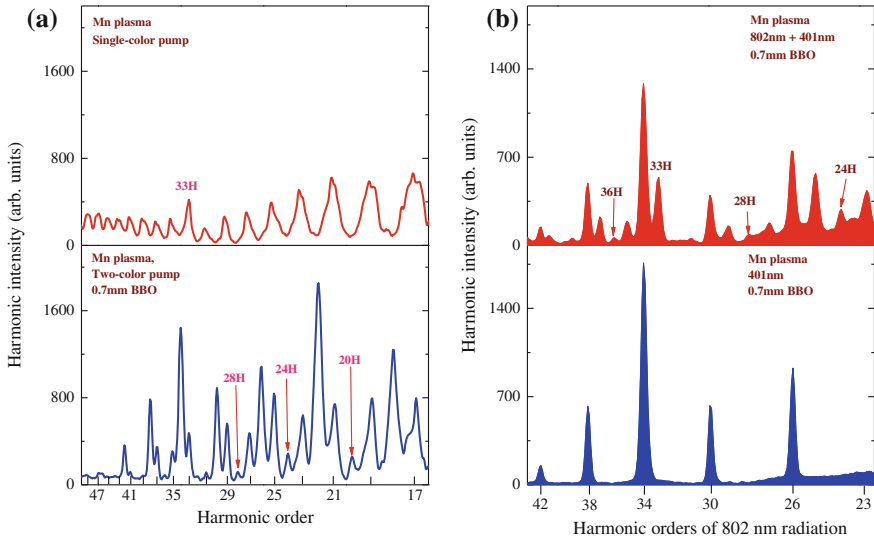


Fig. 3.6 **a** Harmonic spectra from single-color (*upper panel*) and two-color (*bottom panel*) pumps of Mn plasmas in the case of using a 0.7-mm-long BBO crystal. **b** Higher-order harmonics spectra from Mn plasma using the two-color (802 + 401 nm) pump (*upper panel*) and single-color pump when only 401 nm pulses were used for the HHG (*bottom panel*). Adapted from [29] with permission from Optical Society of America

shown in Fig. 3.5a (bottom panel) and Fig. 3.5b (middle panel). The harmonic cutoff was decreased compared with the single-color pump (Fig. 3.6b, upper panel), probably due to a decrease of fundamental (802 nm) radiation intensity and the self-phase modulation occurring in the crystal. In the meantime, one can distinguish some weak even harmonics (20th, 24th, 28th, etc.), which do not originate from the 401 nm pump alone but are the result of interaction of two waves.

To prove this assumption, the higher-order harmonics generated from the two-color scheme (Fig. 3.6b, upper panel) were compared with the single-color scheme when the 802 nm radiation was suppressed by inserting the UV filter placed after the 0.7-mm-long crystal (Fig. 3.6b, bottom panel). The latter spectrum shows only odd harmonics of the 401 nm pump, while the former spectrum contains both strong and weak even harmonics of 802 nm radiation alongside the odd harmonics. This means that the tails of the two pumps still slightly overlap and influence each other in the extended plasma plume. Correspondingly, the polarizations of strong odd and even harmonics are orthogonal to each other since they originated from different sources possessing orthogonal polarizations, while the polarization of weak even harmonics follows the polarization of strong odd harmonics.

In all the above cases when the 0.7-mm-long BBO was applied for second-wave generation, the harmonics generated from this source were stronger compared with the odd ones originated from the 802 nm wave. It is known that the shorter wavelength source can generate less extended but rather stronger harmonics compared with longer wavelength radiation of similar intensity. At the same time, note that the intensities of the two pumps in the plasma plumes were significantly different while the rule of prevailing harmonics from the shorter wavelength source remained the same. This observation underlines the influence of the extended medium on the dynamics of HHG from different sources.

The important issue of two-color pump HHG in laser plasma is the observation of additional resonantly enhanced harmonics in the vicinity of some strong ionic transitions, such as the 34th harmonic generated in the molybdenum plasma (Fig. 3.6b, middle panel), which could not be distinguished in the case of a single-color pump. This enhancement is also clearly seen in Fig. 3.6 in the case of Mn plasma where the 17th harmonic of the 401 nm pump (corresponding to the 34th harmonic of 802 nm radiation, $E_p = 52.4$ eV) was significantly enhanced even compared with the 33rd harmonic ($E_p = 50.9$ eV), which has shown excellent resonance-induced properties during the experiments using few-cycle pulses [32]. One can assume better conditions of enhancement for the 34th harmonic compared with the 33rd one in the vicinity of the giant $3p \rightarrow 3d$ resonances of Mn [33] around the 51–52 eV range, where the metastable states are located.

The observation of some new resonantly enhanced harmonics using the two-color pump has been reported for the first time in [34], where the enhancement of the 22rd harmonic generated in the Ag plasma has been attributed to its closeness with the strong ionic resonance of silver. The reviewed studies have revealed some additional resonantly enhanced even harmonics in the extended plasmas. Note that the use of narrow plasma plumes (of the sizes of ≤ 0.5 mm) did not allow the observation of the peculiarities shown in Figs. 3.5b (middle panel) and 3.6b (upper

panel). Thus the two-color pump of extended media could be used for the high-order nonlinear optical spectroscopy of various plasmas.

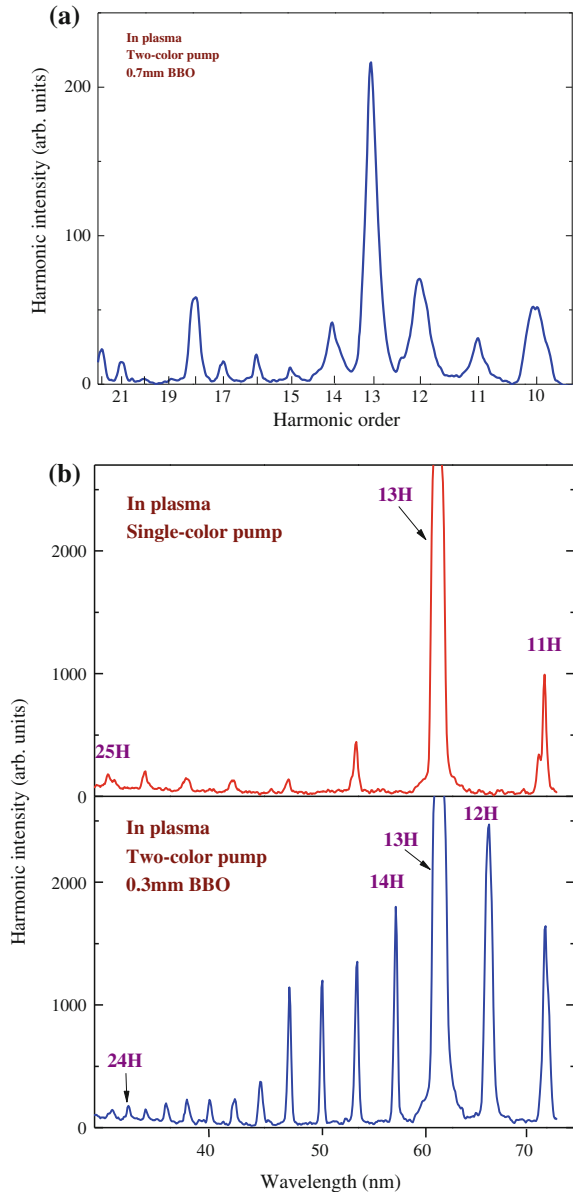
The role of resonance enhancement of a single harmonic in the extended plasma during two-color pump using a 0.7-mm crystal was clearly shown in the case of indium plasma. This medium is characterized by the appearance of an extremely strong 13th harmonic of Ti:sapphire laser radiation, which has been reported by various researchers using narrow plasma plumes [17, 18, 35, 36]. In present studies of extended plasmas, the strong 13th harmonic was also observed during single-color HHG experiments (see also Sect. 3.1), while using the 0.7-mm-long BBO, the odd 5th, 7th, and 9th harmonics of the 401 nm pump have demonstrated similar enhancement shown in other (Mn, Zn, and Mo) plasmas. In the meantime, the enhanced 12th harmonic was observed during those studies (Fig. 3.7a). The intensity of this radiation was stronger compared with the abovementioned harmonics. The generation of the 12th harmonic is forbidden in the case of temporally separated 802 and 401 nm pumps. However, the closeness of the wavelength of the 12th harmonic (67 nm) to the extremely strong ionic transition of In II led to an enhancement of this harmonic even using the weakly overlapped leading and trailing parts of the two pulses. The origin of such enhancement could be attributed to both the single ion response and propagation effect. Notice the absence of 12th harmonic emission in the case of using a single-color 401 nm pump of indium plasma, which confirms the origin of this radiation in the former experiments as a result of interaction of two waves in the extended plasma area.

The application of a longer (1-mm) crystal led to both the larger separation of pulses in the plasma plume and the self-phase modulation of driving 802 nm radiation causing a considerable spectral broadening of the propagating radiation and generating harmonics. Contrary to that, the equal odd and even harmonics generated in the indium plasma (excluding the 13th order) became the common feature of this process once the 0.3-mm-long BBO was applied for second-harmonic generation (Fig. 3.7b). The better overlapping of the two pumps in the plasma allowed both generation of equal odd and even harmonics and enhancement of a whole generating spectrum.

Figure 3.8a shows the raw images of lower-order harmonic spectra produced from the extended silver plasma in the cases of irradiation by single-color (802 nm) or two-color (802 and 401 nm) pumps using the 0.5-mm-long BBO crystal at the conditions of the weak excitation of the target (i.e., at a fluence of 0.2 J cm^{-2}). These spectra were obtained at identical conditions of experiment, just by moving the BBO crystal in and out of the path of the 802 nm pump. The saturated image of two-color induced harmonics is presented for better visibility for the reader to distinguish a difference in the harmonic emission in these two cases of pump. While the image of harmonics from the single-color pump is barely seen, the image of harmonics from the two-color pump is extremely strong at similar conditions of plasma formation and collection time. Note that the line-outs of all above spectra were taken from the unsaturated data.

The enhancement factor of odd (19th, 21th, and 23rd) harmonics compared with the single-color case exceeded $50\times$ (Fig. 3.8b). The even harmonics were stronger

Fig. 3.7 **a** Harmonic spectrum using the two-color pump of indium plasma in the case of using a 0.7-mm-long BBO crystal. **b** Harmonic spectra from In plasma at the cases of single-color pump (*upper panel*) and two-color pump using a 0.3-mm-long BBO crystal (*bottom panel*). Reproduced from [29] with permission from Optical Society of America



compared with the odd ones at the longer-wavelength range, while in the shorter wavelength range their intensities became almost equal. The advanced properties of the two-color pump of extended silver plasma were also emphasized while compared with the odd and even harmonic generation in the narrow (0.5-mm-long) plasma plume. In the latter case, the even harmonics did not extend over the whole

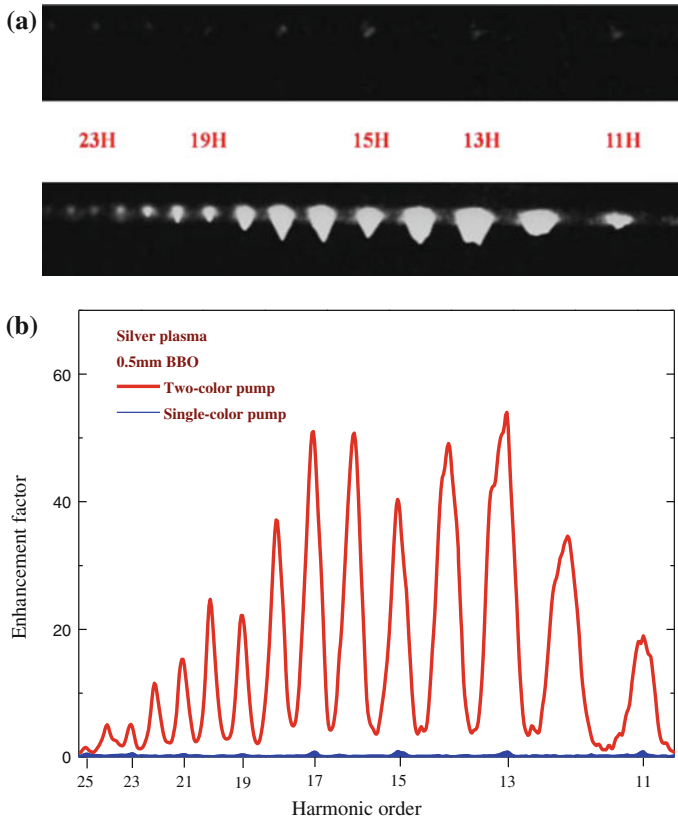


Fig. 3.8 **a** Raw images of harmonic spectra obtained at identical conditions of plasma formation using the single-color (*upper panel*) and two-color (*bottom panel*) pumps of extended silver plasma. **b** Enhancement factors of the harmonics generating during two-color pump compared with the case of single-color pump. Reproduced from [29] with permission from Optical Society of America

spectrum of generation of the odd harmonics. Moreover, the intensity of the former harmonics was a few times smaller compared with the odd harmonics, contrary to the HHG in the extended plasmas.

The enhancement of two-color pump induced harmonic yield was also obtained in the V and Zn plasmas, though the enhancement factors for the odd harmonics ($5\times$ and $7\times$, respectively) were not as high as in the case of silver plasma. Meanwhile, the extended graphite plasma showed a specific peculiarity in the cases of single- and two-color pumps. The low-order harmonics in the case of single-color pump of this plasma were considerably stronger compared with other metal ablations at optimal conditions of target excitation. The application of additional field led to the growth of harmonic intensity, though the enhancement factor in the former medium was smaller than in the cases of Ag, V, and Zn plasmas.

In the case of the two-color pump, the advantages of using a second wave for the growth of tunnel ionization rate, compared with the single fundamental 802 nm field, play less role in the graphite plasma due to possible involvement of the ablation-induced carbon nanoparticles in the HHG. It is unclear whether the ionization rate of nanoparticles increases in the presence of an additional weak field or whether the expected enhancement overpasses the amendments related with the involvement of nanoparticles, rather than monomers, in the harmonic generation in graphite plasma.

The difference in application of 0.3- and 0.5-mm-long BBO was mostly related with the enhancement factor of generating odd and even harmonics. In the latter case, the enhancement was larger compared with the shorter crystal due to a higher ratio between the overlapped second and fundamental waves. In the case of silver plasma, the complete spectra of even harmonics were obtained by using only the 0.3- and 0.5-mm-long BBO crystals, since in those cases the separation between the central parts of pumps still allowed a sufficient overlap between the temporal wings of those pulses (see Table 3.1, right column). Note that once the thin (0.3- and 0.5-mm-long) crystals were placed outside the vacuum chamber on the path of the focused driving radiation, the propagation of the 802 and 401 nm radiation through the 5-mm-thick MgF_2 input window of the vacuum chamber led to a considerable separation of the two pumps since the second-harmonic pulse became ~ 320 fs delayed with respect to the fundamental wave. This delay caused the generation of only odd harmonics from the 401 nm source, together with the odd harmonics from the 802 nm radiation, analogous to the case of using the thicker second-harmonic converters.

The peculiarities of a two-color pump, compared with a single-color pump, are related to the interaction of the second field with fundamental radiation in the presence of atoms, ions, and electrons in the plasma plume. The difference of the phases of the two waves governs both the efficiency of the nonlinear optical process, such as HHG, and the symmetry properties of the medium. The harmonics are generated mainly from the short trajectories of accelerated electrons. The electrons ionized in this time period are also the main contributors to phase-matched harmonic generation. In accordance with [21], the tunneling ionization rate for the two-color field is much larger than that for the fundamental field; that is, the electron wave packet at the time of ionization is significantly denser. Consequently, an orthogonally polarized two-color field can generate stronger harmonics than the single fundamental field, once the overlap of two pulses becomes sufficient for the efficient interaction in the extended medium. The observations of this process in Ag, V, Zn, and other plasmas show the significant advantages of the two-color pump induced HHG in the extended plasma formations at relatively small ratios (0.03–0.04) of the two overlapping waves.

The application of two-color pump has successfully been demonstrated in the case of narrow gas jets, which led to both the generation of odd and even harmonics and the growth of conversion efficiency. The enhancement factor in the case of a 1:10 ratio of the second and fundamental fields was varied in the range of 3–8, while the theoretical calculations predicted a 100-fold enhancement [20, 37], which

was confirmed only in the case of application of the higher ratio of two fields (1:5, [21]). The two-color pump at a lower ratio of second and fundamental waves has also been applied in the case of low-sized plasma HHG [38], and approximately the same amendments as for the gas harmonics were demonstrated. The discussed enhancement factors of the two-color pump HHG (0.5-mm-long BBO, 1:25 ratio between the 2ω and ω waves) in the extended plasma considerably exceed those reported earlier for the weak second waves and are close to those reported at a 1:5 ratio of the two pumps of gaseous medium [21]. One can attribute these enhancements to the application of long plasmas allowing better overlapping of the pump pulses, proper use of the second-harmonic converters of the optimal thickness, and better phase relations between the interacting waves.

In the case of longer delay between the 802 and 401 nm waves inside the plasma jets, caused by the group velocity dispersion in relatively thick (0.7- and 1-mm) BBO crystals, the temporal difference between pulse envelopes caused the enhancement of the odd harmonics generated from two separated and non-interacting sources at the long-wavelength range. The enhancement factor was varied in the range of 7–15. The application of thinner crystals (0.3 and 0.5 mm) led to a decrease of the delay between the two pumps. The shape of the generating spectrum was considerably modified compared with the case of insufficient overlapping of the two pumps inside the plasma. The range of enhanced harmonics was extended toward the shorter wavelength region, in spite of the relatively small ratio of the 401 and 802 nm pump energies of the overlapping pulses in the extended plasma (0.03 and 0.04 in the cases of 0.3- and 0.5-mm-long crystals, respectively; see Table 3.1).

The chirp induced by crystals does not play a significant role while using relatively long multi-cycle pulses (64 fs), which were not broadband enough to observe the variation of the central wavelength and pulse broadening after propagation of the crystals. To analyze the influence of chirp effect the distance between the gratings in the compressor stage was varied, which did not lead to any significant changes of the harmonic spectra but just a decrease of the entire harmonic yield with the increase of pulse duration.

3.3 Modification of Modulated Plasma Plumes

As it was already mentioned, the quasi-phase-matching is an important method for resolving the phase mismatch problem during HHG in the XUV. The QPM is based on the variation of the phases of interacting waves in such a way that the destructive processes become less significant compared with the constructive ones. One of the methods of the variation of the phases used in gas HHG studies explores the division of extended medium on a few jets where the constructive accumulation of XUV photons was maintained along the whole length of single gas jet, with the following optimal dephasing before entering the next jet [39–41].

First demonstrations of the QPM in the modulated plasmas [42–44] have revealed both the enhancement of the groups of harmonics generating in the

multi-jet silver, vanadium, chromium, and manganese plasmas in different spectral ranges and the definition of N_c in the plasma plumes using the relation between the jet sizes, electron concentration, and maximally enhanced harmonic order.

In this section, we discuss the results of the studies, which have shown the variation of the periodicity and sizes of plasma plumes by different means [45]. This approach allowed a fine tuning of the quasi-phase-matched conditions along the XUV. We discuss the modification of plasma shape allowing the formation of periodic plasma plumes with the sizes of single plume ranging between 0.1 and 1 mm. This method proved to be useful for the fine tuning of the quasi-phase-matched high-order harmonics generated in these modulated structures. The details of QPM will be discussed in Chap. 4.

Various methods could be applied to change the sizes and number of multi-jet plasmas. Among them are (i) the interference of two heating beams on the target surface with the variable angle between the interacting beams, (ii) the tilting of the multi-slit shield (MSS) placed in front of ablating target, which allows a decrease of the distance between the heating zones, as well as their sizes, and (iii) installation of MSS inside the telescope placed on the path of heating radiation. The most applicable methods are (ii) and (iii) since they allow fine tuning of the sizes of plumes by tilting or moving the MSS.

To analyze these two methods, the plasma formation was modeled by studying the spatial distribution of the HeNe laser radiation propagated through the MSS. Figure 3.9a shows the experimental setup allowing the analysis of intensity distribution of the 0.63 μm radiation propagated through the MSS. The MSS is shown in the inset in Fig. 3.9b. This MSS consisted of the slits separated at the distance of 0.3 mm from each other. The width of each slit was 0.3 mm. The laser radiation was propagated through the magnified telescope ($6\times$, L_1 , L_2) and then focused using the 250 mm focal length cylindrical lens (L_3). The CCD camera was placed at the focal plane of this lens.

The line shape of focused radiation is shown in the upper panel of Fig. 3.10a. Then the MSS was placed inside the telescope at different positions (1–5) shown in Fig. 3.9a. The shapes of laser beam at positions 1, 3, and 5 of MSS are shown in the three bottom panels of Fig. 3.10a. The installation of MSS at the position 1 (Fig. 3.9a) allowed the formation of two 3-mm-long beams, with weak interference-induced beam between them (position 1, Fig. 3.10a). The movement of MSS along the axis of telescope led to a decrease of the sizes of separated beams (positions 3 and 5, Fig. 3.10a).

Similar images, as in Fig. 3.10a (position 5), were observed in the case of installation of the MSS on the position 6 (Fig. 3.10b, upper panel). Two other panels of Fig. 3.10b show the modification of laser beam shapes by tilting the MSS. One can see a decrease in the sizes of beams once the MSS was tilted at 50° with regard to the focal plane of cylindrical lens.

Those above model experiments showed that the spatially modulated laser beams on the focal plane of cylindrical lens could be gradually tuned by changing the position of MSS. One can assume that the application of intense pulses at these

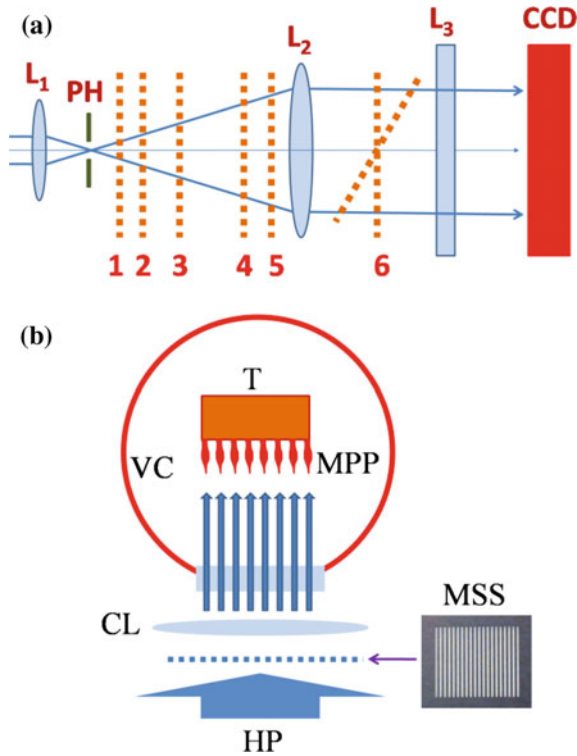


Fig. 3.9 **a** Experimental setup for the modeling of the spatial distribution of HeNe laser radiation in the focal plane of cylindrical lens (L_3) measured by CCD camera at different positions (1–6) of multi-slit shield. L_1 and L_2 are the lenses of magnifying telescope and PH is the pinhole of telescope allowing the spatial filtering of laser radiation. **b** Multi-plume plasma formation on the target surfaces. HP heating pulse; CL cylindrical lens; MSS multi-slit shield; T target; MPP multi-plume plasma; VC vacuum chamber. Reproduced with permission from [45]. Copyright 2014. AIP Publishing LLC

conditions will allow the formation of modulated plasma plumes during ablation of the target placed on the focal plane of cylindrical lens.

A single pulse from Nd:YAG laser (wavelength 1064 nm, pulse duration 38 ps, pulse energy up to 6 mJ) was used for plasma formation on the target surface (Fig. 3.9b). 5-mm-long manganese and silver plates were used as the targets. The laser radiation was focused using the 250 mm focal length cylindrical lens inside the vacuum chamber that contained the target to create the line plasma plume with the dimensions 5 mm \times 70 μ m. The intensity of heating pulse on the target surface was $\sim 4 \times 10^{10}$ W cm $^{-2}$. The images of plasma formations were captured by a CCD camera. Upper panel of Fig. 3.11a shows the image of 5-mm-long Mn plasma.

The installation of MSS at different positions inside and outside the telescope led to formation of the variable multi-jet structures. The sizes and distances between plumes were varied similarly to above-described model experiments using HeNe

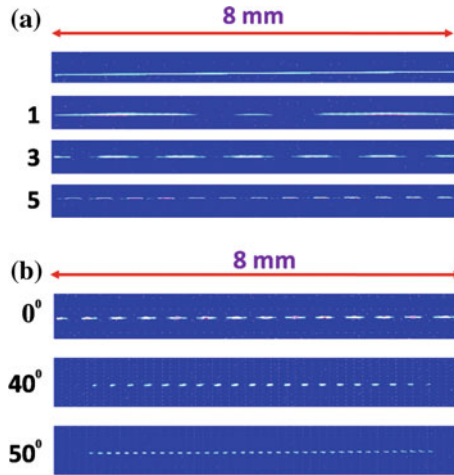


Fig. 3.10 **a** Raw images of spatial distribution of the 633 nm radiation in the focal plane of 250-mm focal length cylindrical lens without (*upper panel*) and with (panels 1, 3, and 5) installation of MSS on the positions 1, 3, and 5 of Fig. 3.9a. **b** Raw images obtained during installation of MSS on the position 6 (Fig. 3.9a) at different angles between the focal plane and MSS (*upper panel*: 0°, *middle panel*: 40°, *bottom panel*: 50°). Reproduced with permission from [45]. Copyright 2014. AIP Publishing LLC

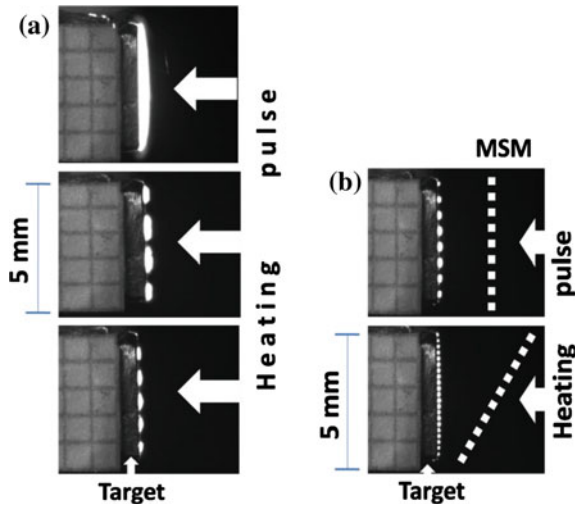


Fig. 3.11 **a** Images of manganese plasma obtained using the ablation by Nd:YAG laser without insertion of the MSS on the path of heating pulse (*upper panel*), with MSS placed on the position 3 of Fig. 3.9a (*middle panel*), and with MSS placed on the position 4 of Fig. 3.9a (*bottom panel*). **b** Images of manganese plasma obtained by insertion of MSS on the position 6 of Fig. 3.9a orthogonally to the direction of heating beam (*upper panel*) and with the MSS tilted at the 50° (*bottom panel*). Reproduced with permission from [45]. Copyright 2014. AIP Publishing LLC

laser. Middle and bottom panels of Fig. 3.11a show the multi-jet structures formed on the manganese target by installation of the MSS at the positions 3 and 4 of Fig. 3.9a. In that case, the four- and five-jet structures were formed, with the sizes of individual jet of 0.6 mm or shorter.

The installation of MSS at the position 6 (Fig. 3.9a) led to formation of eight jets along the whole surface of ablated target (Fig. 3.11b, upper panel). The gradual tilting of MSS at these conditions up to the angle of 50° allowed the growth of the number of plasma jets up to 21 (Fig. 3.11b, bottom panel). This method showed the formation of the bunch of ~ 0.1 -mm long plasma jets, which could be useful for the extension of the maximally enhanced groups of harmonics towards the highest orders of the radiation of Ti:sapphire laser. Similar modification of plasma plumes was obtained in the case of silver target.

The target materials (Mn and Ag) were chosen due to the attractive properties of the plasmas formed on their surfaces. Previously, these plasmas were used for generation of the highest harmonic orders [31, 46]. However, the gradual decrease of harmonic conversion efficiency did not allow the generation of strong coherent emission in the range of 8–30 nm due to the growing influence of the phase mismatch between the interacting waves in the short-wavelength region. The described technique of plasma modulation allows the use of QPM concept for the enhancement of different groups of harmonics by tuning the geometry of plasma plumes. The proposed technique can also find further developments using different targets, which allows the analysis of electron density in the plasmas formed during ablation of various materials.

The harmonic generation experiments using multi-jet plasmas will be discussed in Chap. 4. Below, we analyze the preparation of the targets for the HHG in the multi-jet plasmas of different sizes produced using above-described method by applying the laser commonly used for harmonic generation. The variation of plasma jet sizes was accomplished by moving the MSS inside the telescope. The uncompressed radiation of Ti:sapphire laser was used as a heating pulse (central wavelength 802 nm, pulse duration 370 ps, pulse energy 4 mJ, 10 Hz pulse repetition rate) to ablate the target for plasma formation. The heating pulse was focused using the 200 mm focal length cylindrical lens inside the vacuum chamber containing an ablating target to create the extended plasma plume above the target surface. The intensity of heating pulses on a plain target surface was maintained at $\sim 3 \times 10^9$ W cm $^{-2}$. Silver was used as the ablating target. The length of the target was 5 mm.

The arrangement for perforated plasma formation and harmonic generation is shown in Fig. 3.12a. The compressed driving pulse from the same laser with the energy of 4 mJ and 64 fs pulse duration was used, after 43 ns delay from the beginning of plasma ablation, for harmonic generation in the plasma plume. The details of experimental setup for harmonic generation in the plasmas are presented in [42]. The MSS was installed inside the telescope placed on the path of heating pulse, or in front of the cylindrical focusing lens. Figure 3.12b shows a few shapes of plasmas formed on the silver target. Those include the extended 5-mm-long plasma and multi-jet plasmas produced by the heating pulse after propagation

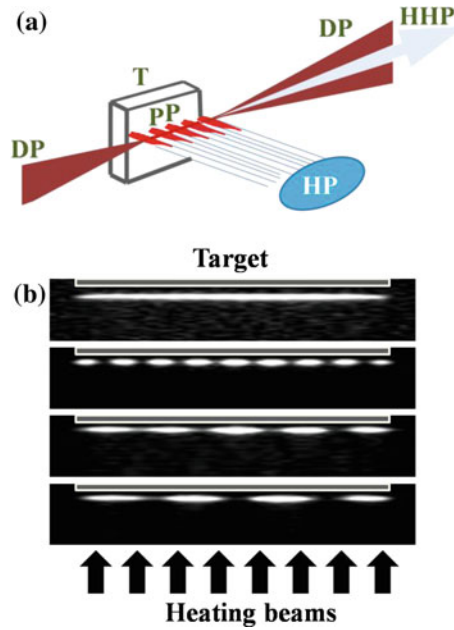


Fig. 3.12 **a** Experimental scheme of harmonic generation in multi-jet plasmas at the conditions of variation of jet sizes by placing the MSS at different positions inside the telescope. *DP* driving pulse; *HHP* high-order harmonic pulse; *HP* heating pulse; *T* target; *PP* plasma plumes. **b** Images of plasma formations on the silver target at the conditions of ablation using Ti:sapphire laser without the MSS (*upper panel*) and at different positions of MSS (other panels). Reproduced with permission from [45]. Copyright 2014. AIP Publishing LLC

through the MSS placed at different positions. The plasma jets were moved out of target at a relatively small divergence ($<15^\circ$). This angle was measured by analyzing the sizes of the debris deposited on the glass plate installed at the distance of 10 cm from the target. This angle can also be estimated from the image of the luminescence of the plasma jets. Thus, the sizes of plasma jets at the distance of $200\ \mu\text{m}$ from target were almost similar to the areas of ablation.

The sizes of jets were tuned between 0.3 and 0.8 mm. Their sizes were defined by measurement of the ablated areas on the target surface, rather than by measurement of the images of plasma emission. In the latter case, the image of plasma emission did not accurately correspond to the actual sizes of jets. At the same time, the ablated areas were corresponded to the sizes of homogeneously distributed modulated heating beam. The jet sizes were also calculated from the geometrical characteristics of the radiation propagated through the MSS.

The energy of heating pulse was decreased after propagation through the MSS. However, the fluence of heating pulse on the target surface remained same, since the sizes of ablated area were decreased as well. It means that the electron and plasma densities in these two cases (extended homogeneous plasma and multi-jet plasma) were almost similar to each other.

3.4 Characterization of the High-Order Harmonics of 64 fs Pulses Generated in Extended Plasma Plumes

The amendments of HHG in extended ablations are related with the application of laser produced plasmas for the analysis of various properties of ablated materials through the studies of their high-order nonlinear optical characteristics. Laser ablation induced HHG may offer various advantages of the material studies due to an abundance of the solid-state samples available for plasma formation compared with a few gases. The advantage of a new approach in application of the HHG was confirmed during the studies of the properties of ablated DNA components [47]. Alongside the attractive way for the application of this fast developing branch of nonlinear optics, one can expect the growth of harmonic yield from various plasma formations, particularly extended and perforated plasma jets.

The important issue for application of generated XUV radiation is the characterization of various parameters of harmonics. First attempts in the analysis of the temporal characteristics of plasma harmonic pulses were reported in [48, 49]. It was shown that the temporal structure of harmonic pulses follows the one of the driving pulse, or becoming even shorter. Other important parameters of generated XUV radiation include the spatial coherence, divergence, and spatial shape of harmonic beams. The knowledge of these parameters allows better application of XUV radiation in surface science, chemistry, plasma physics, microlithography, etc. Particularly, the high coherence of harmonic radiation is required for seeding of the harmonics in a free electron laser, short-wavelength interferometry, holography, and coherent diffraction imaging.

The nontraditional approaches in the plasma harmonic studies may also offer some unexpected advantages. Particularly, the use of long (nanosecond) or short (femtosecond) heating pulses may drastically change the dynamics of formation and spreading of the laser plasma compared to the case of commonly used picosecond ablating pulses. First attempts to analyze this issue in the case of narrow (0.3-mm-long) plasma plumes were reported in [7], while the dynamics of extended plasmas using pulses of different duration has yet been studied.

In this section, we analyze the conditions of HHG during the plasma formation using nanosecond, picosecond, and femtosecond pulses and discuss the spatial coherence, divergence, and shape of the harmonics produced in the extended plasmas [50]. Harmonics with the photon energies of up to ~ 150 eV were achieved while studying the optimally prepared ablation plumes as the nonlinear media. The use of femtosecond pulses for narrow plasma formation was analyzed in Sect. 2.3.1.

The experimental arrangements were similar to those described in Sect. 3.1. Various metal and non-metal samples were studied as the 5-mm-long ablating targets. The application of different targets enabled the observation of the peculiarities of harmonic generation along a broad spectral range using the XUV spectrometer (3–90 nm). The traditional schemes for plasma harmonic generation,

as well as other methods of the HHG in partially ionized plasmas, were used in the reviewed studies.

Plasma formation during HHG in gases has long been considered as a restricting factor, which diminishes the optimal conditions for the HHG in the XUV. Various methods were used to decrease the influence of free electrons on the phase matching conditions and XUV radiation divergence. The (i) prolonged gas media, (ii) waveguides with variable diameter, (iii) optimization of coherence length, (iv) adaptive control of the phase relations between the driving and harmonic waves, (v) quasi-phase-matching, etc. were applied to decrease the influence of free electrons and to enhance the harmonic conversion efficiency in the XUV region. Since during HHG experiments the driving radiation intensity exceeded the barrier suppression intensity of used gases, the presence of ions and free electrons was considered as an inevitable factor limiting the harmonic efficiency. In the meantime, in the case of harmonic generation from the laser ablation of solid targets, the ions were considered as the main emitters of harmonics [51].

Early studies of the HHG from laser plumes, which were carried out at the conditions of highly-charged plasmas, have shown the low harmonic cut-offs and the absence of the plateau-like distribution of harmonics in the short-wavelength range [52–54]. Contrary to that, the application of low-excited, singly charged plasma allowed the considerable improvement of the conditions of harmonic generation from the ablated species. The important parameter here is the duration of the heating pulse ablating target surface. Since almost all of previous HHG studies from the narrow plasma plumes were carried out by using the heating radiation of a few hundred picosecond pulse duration, the conclusion was drawn about the optimal intensity of the heating pulse radiation at the target surface (3×10^9 – $8 \times 10^9 \text{ W cm}^{-2}$, depending on the absorptive properties of targets). It is important to compare HHG from the extended plasmas produced by the pulses of different duration to clarify which parameter (energy fluence or intensity) of these pulses plays a crucial role in the formation of optimal plasma. This term refers to the conditions allowing the maximum yield of harmonics in the XUV. Below we discuss the results of HHG studies from the 5-mm-long plasma plumes produced by the nanosecond, picosecond, and femtosecond pulses.

Sources of different heating pulses were the uncompressed radiation from chirped pulse amplification Ti:sapphire laser (370 ps), the same radiation compressed in a double grating compressor (80 fs), and the Q-switched Nd:YAG laser radiation (40 ns). These pulses were maintained at the energies of 1.5 mJ for the 80 fs pulses, 3 mJ for the 370 ps pulses, and 12 mJ for the 40 ns pulses and were focused by a cylindrical lens to create a plasma plume. The maximal energy fluences on the target surfaces were 0.75, 1.5, and 4.5 J cm^{-2} correspondingly, with the sizes of ablating area of $5 \times 0.04 \text{ mm}^2$. The intensities of those pulses on the target surfaces were 9×10^{12} , 3×10^9 , and $2 \times 10^8 \text{ W cm}^{-2}$. One can see that, while the energy fluences in these three cases were of the same order of magnitude, the intensities of heating pulses were varied by more than four orders of magnitude. The delays between heating (370 ps or 80 fs) and driving (64 fs) pulses were ~ 40 –50 ns, while this parameter was varied in the range of 10–1000 ns in the case of

nanosecond heating pulses to maximize the harmonic yield. The experiments were carried out at loose focusing conditions ($b > L_p$). Here b is the confocal parameter of the focused radiation, and L_p is the plasma length ($b = 12$ mm, $L_p = 5$ mm). The spectra of generated harmonics were analyzed by an XUV spectrometer.

These studies showed that the 370 ps pulses were most suitable for formation of the plasmas producing strongest harmonics. The harmonic emission from the nanosecond and femtosecond pulses induced ablations were obtained as well, though the harmonic yields in these cases were smaller compared to the picosecond pulse induced plasmas. Below we analyze a few examples of the plasma harmonic spectra observed in these three cases.

The ablation produced by 40 ns pulses allowed generation of the harmonics up to the 93rd order (145 eV) in the case of Mn target, as well as of strong low-order harmonic emission in the case of zinc plasma, while the use of indium plasma led to extremely strong 13th harmonic emission (Fig. 3.13a), similarly to early studies of the latter medium using the picosecond pulse induced ablation. Variation of the delay between heating and driving pulses from 40 to 350 ns led to a gradual decrease of harmonic emission from those plasmas due to late propagation of the driving pulse above the target surface. At longer delays, the most part of plasma plume was already moved out of the surface.

In the case of 80 fs ablation pulses, the plasma plumes were insufficiently fitted to the requirements of strong harmonic generation in the long medium. Though the harmonic emission was observed from the silver, chrome, and gold extended

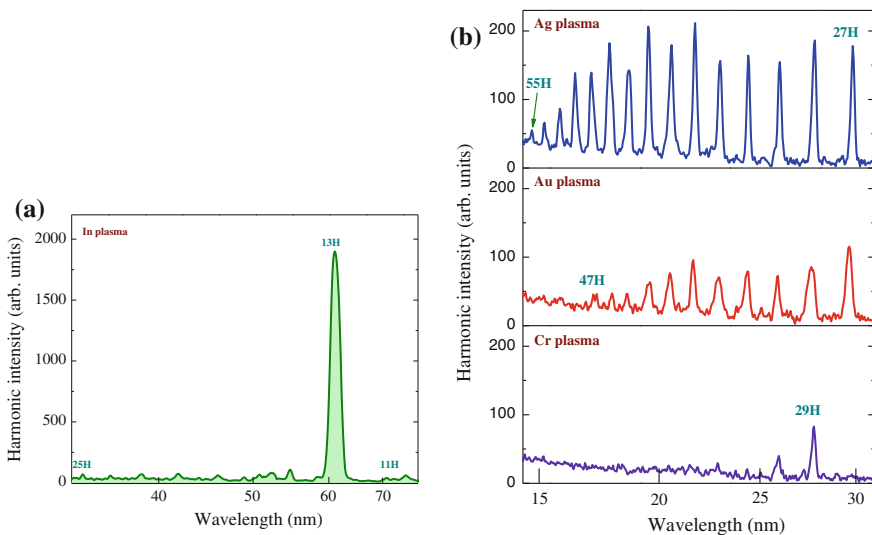


Fig. 3.13 **a** Harmonic spectrum from the indium plasma produced by 40 ns heating pulses. **b** Harmonic spectra from the plasmas produced by 80 fs heating pulses in the cases of Ag (*upper panel*), Au (*middle panel*), and Cr (*bottom panel*) plasmas. Reproduced from [50] with kind permission of The European Physical Journal (EPJ)

plasmas (Fig. 3.13b), the whole pattern of the formation of ablation cloud at these conditions has demonstrated strong incoherent emission together with the lower harmonic yields compared with the longer pulse induced ablation.

Plasma formation using 370 ps radiation has shown that the pulse duration in the subnanosecond range (<1 ns) is most suitable for harmonic generation from target ablation compared with the pulses in nanosecond and femtosecond ranges. At optimal conditions of the ablation by these pulses, most of targets produced the plasma plumes, which did not show strong incoherent emission while allow the efficient harmonic generation. The stable harmonic emission was lasted for a longer time compared with the cases of plasma formation using femtosecond and nanosecond pulses. The high-order harmonics in the case of silver ablation using 370 ps pulses have demonstrated highest yield among all studied samples.

These studies showed that pulse duration of heating radiation influences the harmonic generation efficiency from the extended plasmas. In both three cases of plasma formation using the heating pulses of different duration the energy fluence has proven to be the main factor for the medium formation suitable for efficient harmonic emission, while the laser intensity on the target surface has played less important role. Note that the discussed studies were carried out using the extended plasma formations, one order of magnitude longer than those used in previous similar studies of plasma harmonics [7]. The application of extended plasmas can lead to both the increase and decrease of harmonic yield due to the quadratic growth of harmonic intensity in longer media and the growing influence of the phase mismatch and absorption. Each of these processes behaves by their own manner when using different pulses for plasma formation. Since the most important task of these studies was the definition of the conditions for highest yield of harmonic emission from different plasma formations, the use of the long plasmas produced by picosecond radiation has proven to be most efficient approach for achieving this goal.

These studies showed that both the nanosecond and femtosecond pulses could be used for extended plasma formation and harmonic generation. However, the application of subnanosecond pulses for ablation has demonstrated the best opportunity for plasma harmonic generation (i.e. strongest harmonic yield, stability, extended harmonic cut-off, etc.). Moreover, from one hand, the 370 ps pulses did not cause strong plasma emission, while maintaining high conversion efficiency of harmonics. From another hand, it may cause the formation of nanoparticles in the plasma cloud, which also lead to the growth harmonic yield, particularly in the case of graphite ablation. Similar observations were reported in previous studies [55, 56]. At the same time in the case of narrow plasmas [57], ablation using femtosecond and picosecond pulses showed approximately same harmonic yields (see Sect. 2.3). Probably, larger concentrations of electrons appeared during ablation by femtosecond pulses caused stronger detrimental effects in the case of longer plasma plumes.

Spatial characteristics of plasma harmonics are of special interest due to potential applications of this coherent radiation in plasma physics, nonlinear optics, surface physics, biomedicine, etc. Additionally to the characterization of the coherence

properties of harmonic emission, the analysis of the shape of harmonic beam and its divergence allows defining the possibility of the tight focusing of this XUV radiation, which is the main requirement for modification and analysis of various species. It is reasonable to compare the spatial shape of harmonics with that of the driving beam. The difference in the divergences of those two beams provides the information about the usefulness of converted short-wavelength radiation for the focusing on a tiny spot to create high photon fluence on the surface under study.

The spatial characteristics of the high-order harmonics generating in the extended Ag plasma produced by 370 ps pulses were analyzed in the following set of experiments. A few harmonics were selected in the plateau range using the metal filters and then the shape of those harmonics was analyzed using the multi-channel plate detector. To select these harmonics, the 650-nm-thick aluminum and 150-nm-thick titanium filters were installed in front of the MCP. The short-wavelength transmission edge of Al filter is ~ 17.4 nm, while the long-wavelength transmission edge of Ti filter is ~ 22 nm. Simultaneous application of those two filters allowed separation of the harmonics generating in the spectral range of 18–21 nm. The harmonic spectra from silver plasma with and without those filters are shown in Fig. 3.14a. Harmonics, which correspond to this range, are the 37th, 39th, 41st, 43rd, and 45th orders. Those five harmonics are clearly seen in the upper panel of Fig. 3.14a. The 37th harmonic ($\lambda = 21.7$ nm) was suppressed due to closeness to the absorption edge of Ti filter. Another group of spectral lines in the

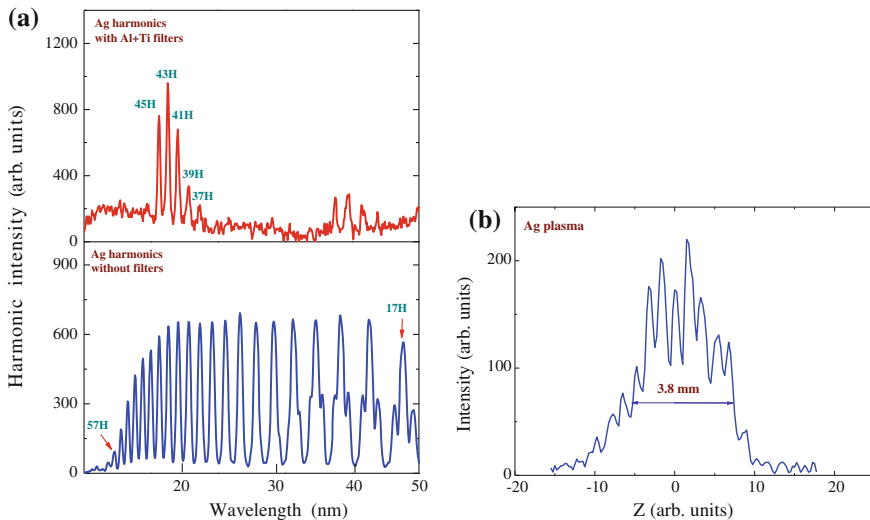


Fig. 3.14 **a** Harmonic spectra from silver plasma obtained using Ti and Al filters (*upper panel*) and without filters (*bottom panel*). The spectra were collected during 100 shots and 10 shots correspondingly. The spectral lines in the 35–43 nm range (*upper panel*) correspond to the second-order diffraction of the 37th to 45th harmonics. **b** Spatial distribution of the group of harmonics (from 37th to 45th orders). The spatial modulation was caused by the mesh structure of metallic filters. Reproduced from [50] with kind permission of The European Physical Journal (EPJ)

40 nm region belongs to the second-order diffraction of above harmonics, which also can be seen in the bottom panel. Due to weak transmission of the Ti filter in the region of transmission cut-off, 100 laser shots were used to collect this spectrum (upper panel), while the filter-free spectrum (bottom panel) was collected during 10 shots.

These few harmonics were directly sent to the MCP by removing the cylindrical mirror (Fig. 3.1) from the path of driving beam and harmonics. The whole shape of harmonic beams was restricted in the horizontal axis due to propagation through the slit of XUV spectrometer. The spatial distribution of the beam along the vertical axis is shown in Fig. 3.14b. The size of this beam was 3.8 mm. Taking into account the focusing geometry of the driving beam (diameter 15 mm, 400-mm focal length lens, 710 mm distance from the plasma area to the MCP, 802 nm beam size on the MCP plane 27 mm), the divergence of harmonic beam was decreased with a factor of 7 compared with the divergence of driving beam. This decrease of divergence is attributed to the preferential involvement of the short trajectory of accelerated electron in higher-order harmonic generation. Indeed, no harmonic emission was appeared from a whole spectrum out of the axis of driving radiation once a flat mirror was used instead of a cylindrical one in the XUV spectrometer. Notice that the involvement of the long trajectory of accelerated electron should cause the increase of the divergence of harmonics.

These studies showed that the harmonics in the range of 17–20 nm possess small divergence, which allows their further focusing into the tiny spot for different applications. One can expect the 40-fold decrease of harmonic divergence for the forties orders with regard to the driving beam divergence. The observation of higher divergence of XUV harmonics could be related with the heterogeneous conversion of different parts of the driving beam waist [58].

Studies of the spatial coherence of high-order harmonic radiation allow identifying mechanisms that can degrade the coherence. Gas HHG showed the degradation of coherence with the growth of laser intensity due to significant instant ionization of the neutral medium and appearance of large amount of the free electrons, which cause the rapidly varying phase along the harmonic beam [59–61]. The latter process decreases the spatial coherence of harmonics if the rate of formation of free electrons varies at different points across the focused beam leading to decorrelation of the time-dependent fields due to density or laser-intensity variations across the laser focus.

In this connection, the difference between gas HHG and plasma HHG can be analyzed through the comparison of the reported values of the coherence of gas harmonics and the measurements of the same for plasma harmonics. The initial consistencies of these two media are differing from each other. The former medium contains neutral particles, while the latter medium represents the preformed plasma containing neutrals, ions, and clusters with a density distribution determined by the ablation dynamics and subsequent evolution of the plasma. This evolution depends on the target composition and ablation pulse parameters in a complex way. The measurements of the spatial coherence (i.e. complex coherence factor) of the high-order harmonics generating in narrow (0.5-mm long) laser-produced plasma plumes at resonant and nonresonant conditions of harmonic generation were

reported in [62, 63] (see also Chap. 2). The high visibilities of the interference fringes in the Young double slit scheme in the range 0.6–0.75 were measured in the case of HHG in the C, Zn, and In plasmas [63]. In those studies the higher visibility for the plasma harmonics compared with the argon gas target was attributed to a reduced production of free electrons during propagation of the femtosecond driving pulse through the preformed plasma. We remind that the application of extended plasmas leads to considerable growth of harmonic yield compared with the narrow plasmas. The point of interest here is whether the coherence properties of those enhanced harmonics are worsening after propagation through the extended plasmas.

The studies of 5-mm-long plasmas showed that the plasma harmonics possess reasonably good coherence properties similarly to the case of narrow plasmas and can be used in the applications requiring high spatial coherence. Below we analyze the measurements of spatial coherence of the odd and even harmonics generated in different plasmas produced by 370 ns pulses. The harmonic shapes along the vertical axis were analyzed using a XUV spectrometer containing a flat mirror, a flat field grating, and a MCP viewed by a CCD camera. The use of flat mirror enables the analysis of the divergence and coherence of harmonic emission. The spatial coherence of harmonics was measured using the double-slit interference scheme. A pair of slits was mounted on a translation stage and placed 15 cm from the plasma area and 55 cm from the MCP (Fig. 3.1), just in front of the enhance slit of the XUV spectrometer. The slits were made in a stainless steel foil and had 30 μm spacing, 10 μm width and were 10 mm long. Double slits were moved in and out the harmonic beam to produce a pure harmonic spectrum or an interference pattern of fringes from which the coherence of the radiation was determined. Each interference pattern measured in those experiments was integrated over 200 laser shots. A series of measurements were made for different plasmas in the photon energy range of 14–30 eV.

For each pattern, the fringe visibility was determined through the relation $V = (I_{\text{max}} - I_{\text{min}})/(I_{\text{max}} + I_{\text{min}})$, where I_{max} and I_{min} are the maximum and minimum intensities of the interference pattern. The diameter of harmonic beam at the double slit was 0.8 mm, which is significantly larger than the slit separation. This led to the same harmonic intensity at two slits. With equal intensity at both slits the fringe visibility at the centre of the fringe pattern is equal to the modulus of the complex coherence factor.

The visibilities of fringes near the centre of the fringe patterns obtained during harmonic generation in the Zn plasma were measured to be 0.62 (for the 10th harmonic), and 0.55 (for the 11th harmonic). Other used plasmas also demonstrated the high coherence properties of generated low-order harmonics. Figure 3.15a, b show the line-outs of the interference patterns of the 9th and 11th harmonics generated in the manganese and chromium plasmas. The visibilities of these interference fringes were 0.54 and 0.73, respectively. The interference images of lower-order harmonics showed clean fringes arising from the interference of the two beams propagated through the double slit. The plasma lines appearing during laser ablation of targets did not show the interference fringes, which confirms the low coherence of plasma radiation.

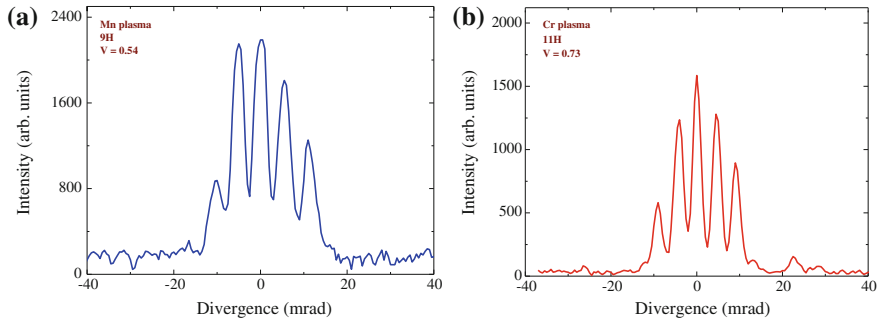


Fig. 3.15 Line-outs of the interference patterns of the 9th and 11th harmonics generated in the **a** manganese and **b** chromium plasmas. Reproduced from [50] with kind permission of The European Physical Journal (EPJ)

3.5 Concluding Comments

We analyzed the advanced properties of extended plasma plumes for the efficient harmonic generation compared with the short-length plasmas used in previous studies. We showed the dependences of the harmonic yield on the length of non-linear medium and found some peculiarities in the cases of indium and carbon plasmas, which were related with the resonance and morphology properties of these media. The demonstration of plasma HHG has been shown along the whole XUV range, particularly including the resonantly enhanced conditions for harmonics generation. The possibility of using such plasmas for quasi-phase-matching experiments was discussed.

We presented studies of HHG using the single-color and two-color pumps of extended (5-mm-long) plasmas produced on the surfaces of various materials using different sources of second-harmonic pump. The BBO crystals of different thickness were applied to manipulate the overlapping of the two pumps in the extended plasma area. Different delays and ratios between the intensities of these pumps in the plasmas allowed the definition of the optimal length of BBO for the efficient generation of even and odd harmonics using targets possessing various ablation characteristics. The $50\times$ enhancement of lower order odd harmonics was achieved in the case of the two-color pump compared with the single-color pump of silver plasma, which is a considerable amendment compared with the case of the narrow (0.4-mm-long) plasma plumes used in previous studies. Some other extended plasmas also showed the advanced properties and enhancement of the two-color pump induced HHG. The two-color pump allowed revealing some resonantly enhanced even harmonics in the extended Mo, In, and Mn plasmas.

Further, we discussed the technique allowing a fine tuning of the distance between the laser-produced plasma jets on the surfaces of ablating materials (Mn and Ag), as well as the variation of the sizes of these jets. The multi-jet plasmas with the sizes of single jet ranging between 0.1 and 1 mm were produced.

This method has proposed to be useful for the tuning and extension of the QPM-enhanced harmonics of Ti:sapphire laser radiation.

Among the advantages of the demonstrated approach is the formation of QPM conditions in different spectral ranges by manipulation of the position of multi-slit shield. The discussed studies showed the tunable variation of the sizes of plasma jets for efficient generation of the groups of enhanced harmonics, which can lead to the demonstration of the coherent superposition of the interacting waves in different spectral ranges.

The application of the heating pulses of different duration covering the range of a few tens of femtoseconds and a few tens of nanoseconds revealed the advanced nonlinear optical features of the extended plasmas produced by picosecond pulses. We have shown that the optimal extended plasma formation, which is crucial for achieving the efficient harmonic generation, mostly depends on the energy fluence rather than the intensity of heating pulse on the target surface. Various samples of harmonic emission spectra were analyzed to support the conclusion about the attractiveness of the subnanosecond pulses for extended plasma formation and HHG.

Finally, we analyzed the spatial and coherence characteristics of the harmonics generated in the extended plasmas produced by 370 ps pulses. It was demonstrated that the divergence of plasma harmonics was seven times smaller than the divergence of the driving femtosecond pulses used for HHG. The visibilities of the lower-order harmonics were in the range of 0.54–0.73 depending on the harmonic order and plasma species. Those studies confirmed that the harmonics from extended plasma ablation can be used for the applications requiring high spatial coherence and low divergence.

References

1. P. Balcou, R. Haroutunian, S. Sebban, G. Grillon, A. Rousse, G. Mullot, J.-P. Chambaret, G. Rey, A. Antonetti, D. Hulin, L. Roos, D. Descamps, M.B. Gaarde, A. L'Huillier, E. Constant, E. Mevel, D. von der Linde, A. Orisch, A. Tarasevitch, U. Teubner, D. Klöpffel, W. Theobald, *Appl. Phys. B* **74**, 509 (2002)
2. H.R. Lange, A. Chiron, J.F. Ripoche, A. Mysyrowicz, P. Breger, P. Agostini, *Phys. Rev. Lett.* **81**, 1611 (1998)
3. R.A. Ganeev, *High-Order Harmonic Generation in Laser Plasma Plumes* (Imperial College Press, 2012)
4. R.A. Ganeev, H. Singhal, P.A. Naik, U. Chakravarty, V. Arora, J.A. Chakera, R.A. Khan, M. Raghuramaiah, S.R. Kumbhare, R.P. Kushwaha, P.D. Gupta, *Appl. Phys. B* **87**, 243 (2007)
5. M. Oujja, R. de Nalda, M. López-Arias, R. Torres, J.P. Marangos, M. Castillejo, *Phys. Rev. A* **81**, 043841 (2010)
6. H. Singhal, R.A. Ganeev, P.A. Naik, V. Arora, U. Chakravarty, P.D. Gupta, *J. Appl. Phys.* **103**, 013107 (2008)
7. R.A. Ganeev, M. Suzuki, M. Baba, H. Kuroda, *Phys. Rev. A* **76**, 023805 (2007)
8. R.A. Ganeev, M. Suzuki, P.V. Redkin, M. Baba, H. Kuroda, *Phys. Rev. A* **76**, 023832 (2007)
9. R.A. Ganeev, M. Suzuki, M. Baba, M. Ichihara, H. Kuroda, *J. Phys. B: At. Mol. Opt. Phys.* **41**, 045603 (2008)

10. L.B. Elouga Bom, F. Bouzid, F. Vidal, J.-C. Kieffer, T. Ozaki, *J. Phys. B: At. Mol. Opt. Phys.* **41**, 215401 (2008)
11. H. Singhal, V. Arora, B.S. Rao, P.A. Naik, U. Chakravarty, R.A. Khan, P.D. Gupta, *Phys. Rev. A* **79**, 023807 (2009)
12. V. Tosa, E. Takahashi, Y. Nabekawa, K. Midorikawa, *Phys. Rev. A* **67**, 063817 (2003)
13. A. Rundquist, C.G. Durfee, Z. Chang, C. Herne, S. Backus, M.M. Murnane, H.C. Kapteyn, *Science* **280**, 1412 (1998)
14. R.A. Bartels, A. Paul, H. Green, H.C. Kapteyn, M.M. Murnane, S. Backus, I.P. Christov, Y. Liu, D. Attwood, C. Jacobsen, *Science* **297**, 376 (2002)
15. R.A. Ganeev, M. Suzuki, H. Kuroda, *Phys. Plasmas* **21**, 053503 (2014)
16. J.F. Reintjes, *Nonlinear Optical Parametric Processes in Liquids and Gases* (Academic Press, New York, 1984)
17. R.A. Ganeev, M. Suzuki, T. Ozaki, M. Baba, H. Kuroda, *Opt. Lett.* **31**, 1699 (2006)
18. R.A. Ganeev, H. Singhal, P.A. Naik, V. Arora, U. Chakravarty, J.A. Chakera, R.A. Khan, I.A. Kulagin, P.V. Redkin, M. Raghuramaiah, P.D. Gupta, *Phys. Rev. A* **74**, 063824 (2006)
19. R.A. Ganeev, M. Suzuki, M. Baba, H. Kuroda, *Appl. Phys. Lett.* **86**, 131116 (2005)
20. E. Cormier, M. Lewenstein, *Eur. Phys. J. D* **12**, 227 (2000)
21. I.J. Kim, C.M. Kim, H.T. Kim, G.H. Lee, Y.S. Lee, J.Y. Park, D.J. Cho, C.H. Nam, *Phys. Rev. Lett.* **94**, 243901 (2005)
22. J. Mauritsson, P. Johnsson, E. Gustafsson, A. L'Huillier, K.J. Schafer, M.B. Gaarde, *Phys. Rev. Lett.* **97**, 013001 (2006)
23. T. Pfeifer, L. Gallmann, M.J. Abel, D.M. Neumark, S.R. Leone, *Opt. Lett.* **31**, 975 (2006)
24. Y. Yu, X. Song, Y. Fu, R. Li, Y. Cheng, Z. Xu, *Opt. Express* **16**, 686 (2008)
25. I.J. Kim, G.H. Lee, S.B. Park, Y.S. Lee, T.K. Kim, C.H. Nam, T. Mocek, K. Jakubczak, *Appl. Phys. Lett.* **92**, 021125 (2008)
26. X.-S. Liu, N.-N. Li, *J. Phys. B: At. Mol. Opt. Phys.* **41**, 015602 (2008)
27. D. Charalambidis, P. Tzallas, E.P. Benis, E. Skantzakis, G. Maravelias, L.A.A. Nikolopoulos, A.P. Conde, G.D. Tsakiris, *New J. Phys.* **10**, 025018 (2008)
28. R.A. Ganeev, H. Singhal, P.A. Naik, I.A. Kulagin, P.V. Redkin, J.A. Chakera, M. Tayyab, R.A. Khan, P.D. Gupta, *Phys. Rev. A* **80**, 033845 (2009)
29. R.A. Ganeev, M. Suzuki, H. Kuroda, *J. Opt. Soc. Am. B* **31**, 911 (2014)
30. G. Lambert, J. Gautier, C.P. Hauri, P. Zeitoun, C. Valentin, T. Marchenko, F. Tissandier, J.P. Goddet, M. Ribiere, G. Rey, M. Fajardo, S. Sebban, *New J. Phys.* **11**, 083033 (2009)
31. R.A. Ganeev, L.B. Elouga Bom, J.-C. Kieffer, T. Ozaki, *Phys. Rev. A* **76**, 023831 (2007)
32. R.A. Ganeev, T. Witting, C. Hutchison, F. Frank, M. Tudorovskaya, M. Lein, W.A. Okell, A. Zaïr, J.P. Marangos, J.W.G. Tisch, *Opt. Express* **20**, 25239 (2012)
33. H. Kjeldsen, F. Folkmann, B. Kristensen, J.B. West, J.E. Hansen, *J. Phys. B: At. Mol. Opt. Phys.* **37**, 1321 (2004)
34. R.A. Ganeev, C. Hutchison, A. Zaïr, T. Witting, F. Frank, W.A. Okell, J.W.G. Tisch, J.P. Marangos, *Opt. Express* **20**, 90 (2012)
35. R.A. Ganeev, L.B. Elouga Bom, J.-C. Kieffer, T. Ozaki, *Phys. Rev. A* **75**, 063806 (2007)
36. R.A. Ganeev, T. Witting, C. Hutchison, V.V. Strelkov, F. Frank, M. Castillejo, I. Lopez-Quintas, Z. Abdelrahman, J.W.G. Tisch, J.P. Marangos, *Phys. Rev. A* **88**, 033838 (2013)
37. D.A. Telnov, J. Wang, S.-I. Chu, *Phys. Rev. A* **52**, 3988 (1995)
38. R.A. Ganeev, V.V. Strelkov, C. Hutchison, A. Zaïr, D. Kilbane, M.A. Khokhlova, J.P. Marangos, *Phys. Rev. A* **85**, 023832 (2012)
39. J. Seres, V.S. Yakovlev, E. Seres, C.H. Strelt, P. Wobrauschek, C.H. Spielmann, F. Krausz, *Nat. Phys.* **3**, 878 (2007)
40. A. Pirri, C. Corsi, M. Bellini, *Phys. Rev. A* **78**, 011801 (2008)
41. V. Tosa, V.S. Yakovlev, F. Krausz, *New J. Phys.* **10**, 025016 (2008)
42. R.A. Ganeev, M. Suzuki, H. Kuroda, *Phys. Rev. A* **89**, 033821 (2014)
43. R.A. Ganeev, M. Suzuki, H. Kuroda, *JETP Lett.* **99**, 368 (2014)
44. R.A. Ganeev, M. Suzuki, H. Kuroda, *J. Phys. B: At. Mol. Opt. Phys.* **47**, 105401 (2014)

45. R.A. Ganeev, M. Suzuki, H. Kuroda, *Phys. Plasmas* **22**, 012302 (2015)
46. L.B. Elouga Bom, J.-C. Kieffer, R.A. Ganeev, M. Suzuki, H. Kuroda, T. Ozaki, *Phys. Rev. A* **75**, 033804 (2007)
47. C. Hutchison, R.A. Ganeev, M. Castillejo, I. Lopez-Quintas, A. Zair, S.J. Weber, F. McGrath, Z. Abdelrahman, M. Oppermann, M. Martín, D.Y. Lei, S.A. Maier, J.W.G. Tisch, J.P. Marangos, *Phys. Chem. Chem. Phys.* **15**, 12308 (2013)
48. L.B. Elouga Bom, S. Haessler, O. Gobert, M. Perdrix, F. Lepetit, J.-F. Hergott, B. Carré, T. Ozaki, P. Salières, *Opt. Express* **19**, 3677 (2011)
49. S. Haessler, L.B. Elouga Bom, O. Gobert, J.-F. Hergott, F. Lepetit, M. Perdrix, B. Carré, T. Ozaki, P. Salières, *J. Phys. B: At. Mol. Opt. Phys.* **45**, 074012 (2012)
50. R.A. Ganeev, M. Suzuki, H. Kuroda, *Eur. Phys. J. D* **68**, 332 (2014)
51. R.A. Ganeev, *J. Phys. B: At. Mol. Opt. Phys.* **40**, R213 (2007)
52. Y. Akiyama, K. Midorikawa, Y. Matsunawa, Y. Nagata, M. Obara, H. Tashiro, K. Toyoda, *Phys. Rev. Lett.* **69**, 2176 (1992)
53. R.A. Ganeev, V.I. Redkorechev, T. Usmanov, *Opt. Commun.* **135**, 251 (1997)
54. K. Krushelnick, W. Tighe, S. Suckewer, *J. Opt. Soc. Am. B* **14**, 1687 (1997)
55. Y. Pertot, S. Chen, S.D. Khan, L.B. Elouga Bom, T. Ozaki, Z. Chang, *J. Phys. B: At. Mol. Opt. Phys.* **45**, 074017 (2012)
56. R.A. Ganeev, T. Witting, C. Hutchison, F. Frank, P.V. Redkin, W.A. Okell, D.Y. Lei, T. Roschuk, S.A. Maier, J.P. Marangos, J.W.G. Tisch, *Phys. Rev. A* **85**, 015807 (2012)
57. R.A. Ganeev, J. Zheng, M. Wöstmann, H. Witte, P.V. Redkin, H. Zacharias, *Eur. Phys. J. D* **68**, 325 (2014)
58. O. Kornilov, R. Willcox, O. Gessner, *Rev. Sci. Instrum.* **81**, 063109 (2010)
59. T. Ditmire, E.T. Gumbrell, R.A. Smith, J.W.G. Tisch, D.D. Meyerhofer, M.H.R. Hutchinson, *Phys. Rev. Lett.* **77**, 4756 (1996)
60. T. Ditmire, J.W.G. Tisch, E.T. Gumbrell, R.A. Smith, D.D. Meyerhofer, M.H.R. Hutchinson, *Appl. Phys. B* **65**, 313 (1997)
61. L. Le Déroff, P. Salières, B. Carré, D. Joyeux, D. Phalippou, *Phys. Rev. A* **61**, 043802 (2000)
62. M. Kumar, H. Singhal, J.A. Chakera, P.A. Naik, R.A. Khan, P.D. Gupta, *J. Appl. Phys.* **114**, 033112 (2013)
63. R.A. Ganeev, Z. Abdelrahman, F. Frank, T. Witting, W.A. Okell, D. Fabris, C. Hutchison, J.P. Marangos, J.W.G. Tisch, *Appl. Phys. Lett.* **104**, 021122 (2014)

Chapter 4

Quasi-Phase-Matching of Harmonics in Laser-Produced Plasmas

In this chapter, we analyze the formation of quasi-phase-matching conditions in modulated plasmas. Particularly, we analyze (a) perforated target ablation for the formation of the modulated plasma for quasi-phase-matched harmonic generation, (b) quasi-phase-matching of harmonics using the variable multi-jet plasmas, and (c) QPM-induced enhancement of HHG during two-color pump of multi-jet plasmas. We also discuss the peculiarities of QPM harmonics using different targets and pump schemes and the influence of plasma jet sizes and pulse energies on the characteristics of QPM harmonics.

The HHG of laser radiation in the extended gaseous media has long been considered as an inefficient process due to exceeding of the medium length over the coherence length (L_{coh}) of HHG. Across a distance equal to the L_{coh} a phase mismatch of π grows and causes destructive interference between the driving and harmonic waves. This process is one of the major limitations of the HHG conversion efficiency, especially in the case of abundant presence of the free electrons in the medium. Quasi-phase-matching either “reversing” or cancelling the nonlinear process in the medium region where the polarization and the harmonic field are initially out of phase. In “perturbative” nonlinear optics, QPM is routinely used to correct the phase mismatch, e.g., by reversing periodically the orientation of the nonlinear crystal at intervals L_{coh} . For gas harmonics in the XUV region, QPM aims at cancelling the out-of-phase emission. As it has been shown in multiple gas jet schemes, once the waves depart from the medium, their phase flips [1–4]. The process of frequency conversion can then be efficiently continued in another bunch of medium.

The assumption on the enhancement of harmonic yield using extended media is correct for the moderate excitations of target surfaces, while, at high fluences of heating ablation pulse, the abundance of the free electrons appearing in plasma may cancel the advantages of this extended nonlinear optical medium. A growth of plasma concentration using the increase of the fluence of heating pulse may decrease the harmonic yield because the phase mismatch causes a destructive interference of the harmonic photons generated in the first half and the second half of the extended source. The onset of destructive interference can be shifted to higher plasma densities, and hence enhanced harmonic yields, by subdividing the overall interaction length of plasma d into M sections of thickness d/M and moving

them apart such that diffraction induced changes in the laser phase and amplitude between two adjacent sections can shift the phase of the atomic dipole oscillations by π (at the input of the next section with respect to the exit of the previous one) for the q th harmonic. This approach embodies the basic concept of QPM.

As in the case of gases, separation of the extended plasma plume into a few small sized plasma jets may restore the proper phase relationship between the driving and harmonic waves and give way for further enhancement of the yield in different XUV spectral ranges. To create QPM conditions, one has to maintain a modulation of the coupling between the driving and harmonic waves, which is periodic along the generation path. At these conditions, the enhancement of harmonics will occur only when the interference between propagating signal and newly generated signal becomes constructive.

The attractiveness in the application of the QPM for the amendment of plasma HHG is related with the adjustment of the electron concentration in the periodically modulated plasma plume by the “optimal excitation” of the ablating target. The variation of N_e allows the manipulation of the coherence length of harmonics in different spectral ranges. The adjustment of N_e could be easily accomplished during harmonic generation in the plasma medium through the proper variation of the fluence of ablating beam on the target surface to achieve a required concentration of the free electrons in the plasma jets.

Among the approaches for plasma harmonic QPM one can consider the following techniques: (a) use of the microlithographic targets, analogously to those suggested in [5], (b) interference of the two heating beams on the target surface with variable distance between the maximums of interference pattern, (c) use of the perforated targets allowing a separation in time for the plasma jets to reach the axis of propagation of the driving beam, (d) use of the multiple strips with different distance between them as the masks installed in front of the ablating targets, which allow achieving the adjustable separation between the multiple plasma jets. Until recent time, all these approaches for plasma harmonic QPM have yet been analyzed experimentally, whilst their application would allow the optimization of the active areas of plasmas to match with the coherence lengths of different groups of harmonics. In this chapter, we will discuss the findings reported using the (c) and (d) approaches.

The optimization of multi-jet formation for HHG requires the manipulation of the relative phases of driving and harmonic waves. One of the ways, which can change a dephasing between these waves, is an application of additional driving field. The use of two-color pump schemes is a well known approach for the broadening of the spectrum of generated XUV radiation and the enhancement of the harmonic yield [6–8]. This peculiarity has been demonstrated long time ago [9] and currently it is a well elaborated technique.

The two-color pump using fundamental and second harmonic fields has become a practical way of harmonic enhancement in the gas media. This approach has also been applied for plasma harmonic generation as well. One can assume the importance of the correlation between the phases of two pumps and harmonics at the conditions of QPM in the multi-jet plasmas.

There is another reason for the analysis of the plasma QPM using two driving pulses. In the case of plasma plumes, the two-color pump scheme offers the opportunity in observation of the resonance induced enhancement at the additional wavelengths coinciding with the even harmonics, as has been demonstrated using the narrow plasma plumes [10]. This effect could be either emphasized or diminished in the extended plasmas. The propagation effects can start to play a decisive role in the variation of the resonance induced enhancement of harmonics in the plasmas [11]. The joint influence of the processes at the microscale range related with the mechanisms described in the four-step model of HHG [12–14] and the macroscopic processes related with the phase matching of the interacting waves in the perforated plasma can create the conditions for the generation of an intense emission and the suppression of harmonics induced by additional ionization and absorption in the long heterogeneous medium.

Thus the QPM can be considered as an attractive approach to resolve the phase mismatch problem for the efficient HHG of laser radiation in the XUV. Until recent time, there were no reports on the studies of the QPM for enhancement of the high-order harmonics in the plasma media produced using the laser ablation, though the plasma harmonic approach has been intensively studied during last ten years [15]. This chapter is aimed to acquaint the reader with the recent breakthrough in the field of plasma HHG at the conditions of QPM.

4.1 Perforated Target Ablation for the Formation of the Modulated Plasma for Quasi-Phase-Matched Harmonic Generation

The uncompressed radiation of Ti:sapphire laser was used as a heating pulse (central wavelength $\lambda = 802$ nm, pulse duration 370 ps, pulse energy $E_{hp} = 4$ mJ) to ablate the targets for extended plasma or multi-jet plasma formation depending on the structure of target. The heating pulse was focused using the 200 mm focal length cylindrical lens inside the vacuum chamber containing an ablating target to create the plasma plume (Fig. 4.1). The sizes of ablated area were defined by the length of plain targets (5 mm). The focusing of heating pulse on the ablating surface in the case of plain targets led to formation of the line plasma. The intensity of heating pulses on a plain target surface was varied in the range of $1 \times 10^9 - 3 \times 10^9$ W cm⁻².

The compressed driving pulse from the same laser with the energy of $E_{dp} = 5$ mJ and 64 fs pulse duration was used, after 45 ns delay from the beginning of plasma ablation, for harmonic generation in the plasma plumes. The driving pulse was focused using the 400 mm focal length spherical lens onto the extended plasma from the orthogonal direction, at a distance of ~ 100 μ m above the target surface. The maximum intensity of 802 nm driving pulse from this laser at the focus area was 7×10^{14} W cm⁻². The harmonic emission was analyzed by an XUV spectrometer.

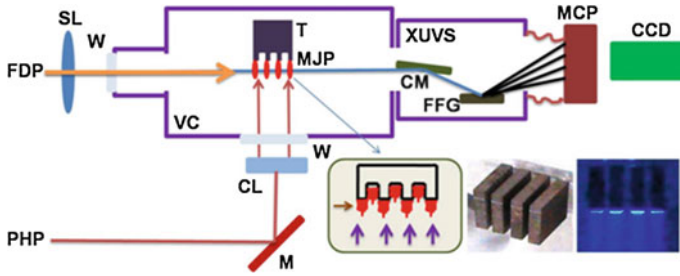


Fig. 4.1 Experimental scheme for harmonic generation in multiple plasma jets. *FDP* femtosecond driving pulse; *PHP* picosecond heating pulse; *SL* spherical lens; *CL* cylindrical lens; *VC* vacuum chamber; *W* windows of vacuum chamber; *T* target; *MJP* multi-jet plasma; *XUVS* extreme ultraviolet spectrometer; *CM* cylindrical mirror; *FFG* flat field grating; *MCP* micro-channel plate registrar; *CCD* charge coupled device camera. *Left inset* shows the principle of plasma formation at different distances from the axis of propagation of the driving pulse. *Central inset* shows the image of perforated Mn target. *Right inset* shows the image of the plasma jets formed on the perforated Mn target. Reproduced from [16] with permission from Springer Science + Business Media

Ag, V, and Mn were used as the ablating targets. The application of these targets enabled the observation of harmonic generation along a broad spectral range and allowed the study of the variation of phase matching conditions for some groups of harmonics. The separated plates of 0.5 mm long Ag, 0.5 mm long V, and 1 mm long Mn were used to create multiple plasma jets. The principle of perforated plasma formation is shown in the left inset of Fig. 4.1, while the image of perforated Mn target and the plasma formation on this target are shown in the central and right insets. The plain 5 mm long Ag, V, and Mn plates were also used for ablation and comparative studies of the HHG from extended homogeneous and perforated plasmas. Below we discuss the observed harmonic spectra at the conditions of different plasma plumes [16].

Figure 4.2a shows the plateau like harmonic spectra obtained from the 5 mm long silver plasma at different energies of the heating pulse. The intensities of harmonics did not change much with the growth of the energy of the heating pulse, while the concentration of plasma (N_p) was increased from $1 \times 10^{17} \text{ cm}^{-3}$ (at 1.1 mJ heating pulse) to $2.5 \times 10^{17} \text{ cm}^{-3}$ (at 3 mJ heating pulse).

A separation of this extended plasma onto four 0.5 mm long plasma jets at the conditions of perforated Ag target excitation has dramatically changed the shape of generated harmonic spectra. The envelopes of harmonic spectra in the case of perforated plasmas were changed from the featureless shape (Fig. 4.2a) to the significantly modulated pattern (Fig. 4.2b). A clear evidence of constructive and destructive interference in different parts of studied spectral range is presented on the panel showing the excitation using the 1.7 mJ heating pulses.

The influence of plasma effect or, by other words, ionization on the dynamics of HHG could be easily checked by analyzing the dependence of harmonic yield I_H on the length d of extended plasma. These $I_H(d)$ dependences were analyzed for different harmonics in a few plasma plumes produced by relatively weak heating

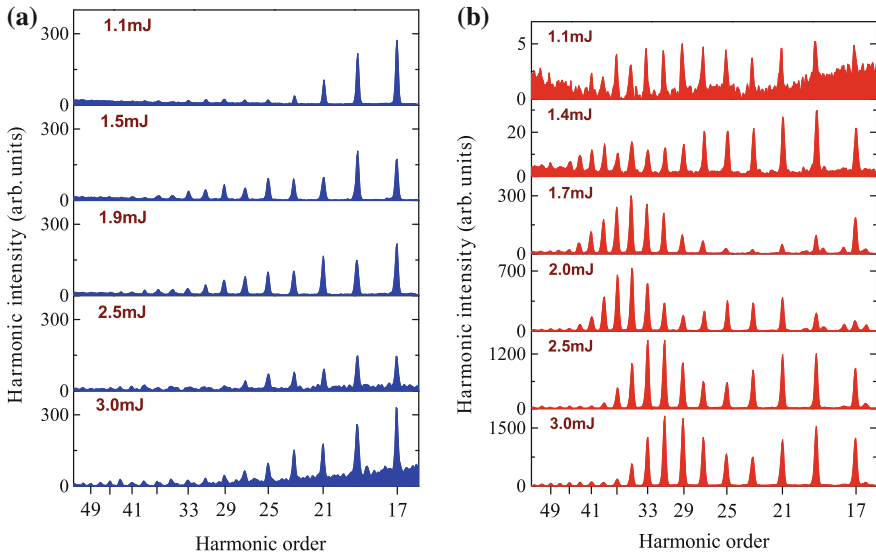


Fig. 4.2 Comparative harmonic spectra from **a** the extended 5-mm-long plasma produced on the plain silver target and **b** four 0.5-mm-long jets formed on the perforated silver target at different energies of heating pulse. Reproduced from [16] with permission from Springer Science + Business Media

pulses. It was found that they had the slopes in the range of 1.8–2.2, i.e., close to the quadratic dependence.

These studies showed that the free electrons appearing during both laser ablation and propagation of driving pulse did not play a decisive role in the variation of this dependence at the optimal excitation of the target. The comparative measurements of the harmonic yields for extended and perforated plasmas at similar heating fluence showed a 20-fold enhancement of the QPM enhanced harmonics. The shortage of the length (compared with extended 5 mm line plasma) should lead to a 6.25-fold decrease of harmonic yield $((5/2)^2)$ in the case of four 0.5 mm long plasmas. Instead, the $20\times$ growth of QPM harmonic yield was achieved. If one assumes the method of enhancement factor calculations introduced in [2], then one has to multiply this enhancement factor by 6.25. With these assumptions, the achieved enhancement is comparable or higher with regard to those reported for gas QPM ($36\times$ [17], $90\times$ [2], $300\times$ [18]).

The measurements of the absolute values of HHG conversion efficiency were carried out using the technique described in [19]. For the 2 mJ heating pulse exciting target at a 10 Hz pulse repetition rate, the conversion efficiency for the 35th harmonic generated from four-jet Ag plasma was measured to be 10^{-5} . This efficiency corresponded to the flux of the 35th harmonic of 5×10^9 photons per pulse. This flux is significantly larger than the reported flux per pulse of the enhanced 41st

harmonic in the case of the gas QPM scheme using counter-propagating beams (10^7 photons per pulse [18]).

Here, we address the observed optimization of QPM for shorter wavelengths at less excitation of target during formation of multi-jet plasma (Fig. 4.2b; compare the spectral maxima of QPM harmonics for the 1.7 and 3 mJ heating pulses). To create the QPM conditions, one has to modulate the coupling between the driving and harmonic waves, which is periodic along the generation path. For a given distance between the 0.5 mm long jets (~ 0.5 mm), the QPM for the q th harmonic could be realized at a fixed product qN_e (since $L_{\text{coh}} \sim (qN_e)^{-1}$ [20]). A decrease of N_e (at less excitation of target) should lead to optimization of the QPM for higher q to keep the product qN_e unchanged at the fixed spatial characteristics of plasma jets. This assumption has found the confirmation in these experiments (Fig. 4.2b).

There are four factors that contribute to phase mismatch: atomic/ionic dispersion, Gouy phase shift, intensity dependent dynamical phase shift in nonlinear dipole moments, and plasma (actually electron) dispersion. The first one refers to the variation in the refractive index of the atomic/ionic components of plasma, which show a considerably less influence than the dispersion induced by the presence of free electrons (fourth factor) in the plasma. Gouy phase shift could also be excluded from consideration when the confocal parameter of focused driving radiation exceeds plasma length, which was the case of those experiments (correspondingly 12 and 5 mm). The intensity of used femtosecond radiation in the plasma area was $\sim 5 \times 10^{14}$ W cm $^{-2}$. At these conditions the phase mismatch induced by second factor can be estimated to be 8 cm $^{-1}$. Finally, the phase mismatch due to plasma electrons was considerably larger (~ 50 cm $^{-1}$ for the thirties harmonics) compared with other factors.

There is some another interesting feature in Fig. 4.2b, which requires further consideration. While increasing the electron density, a second enhancement peak around the 19th harmonic was observed. Probably, this could be due to a higher-order QPM process. Such a possibility has been analyzed previously in [21].

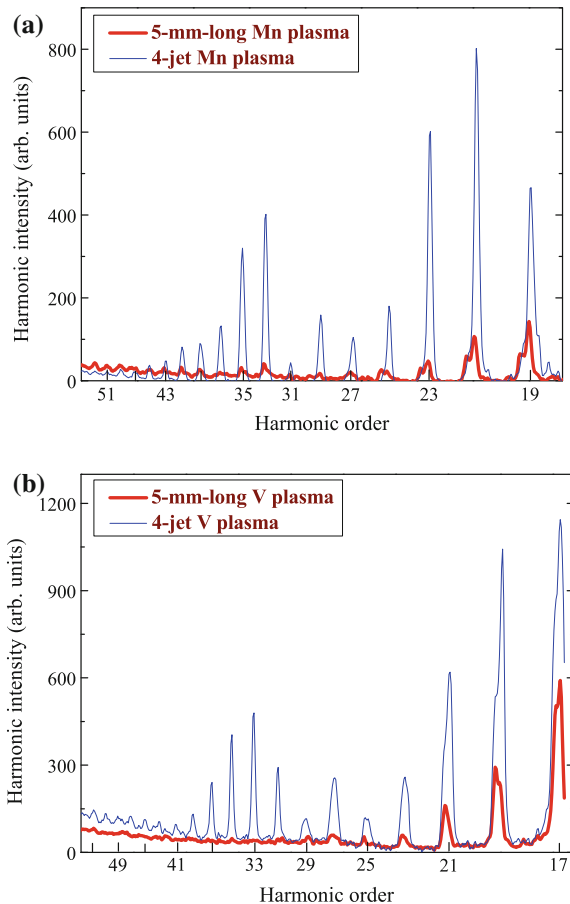
It was shown during previous QPM studies in gases using counterpropagating pulses [22] that QPM is highly selective as the number of contributing zones increases. The plain silver target was irradiated by the modulated heating beam using the multi-slit shield to create the multiple plasma jets. The multi-slit shield was installed after the focusing cylindrical lens in such a manner, that it allowed the division of the extended continuous 5 mm long plasma onto the set of a few plasma jets. These studies showed that the QPM occurred for the same harmonics (approximately centered at 35–37th orders) for the 2-, 3-, 4-, and 5-jet plasma structures. Simultaneously, the broadening for the QPM envelope with the growth of the contributing zones was observed, which points out a decrease of selectivity. Note that QPM of plasma harmonics did not depend much on the distance between the zones. This was probably due to the prevailing influence of the modulation of density of particles (both electrons and atoms/ions) over the distance between these modulations.

The signature of QPM is the growth of harmonic yield $\sim n^2$, where n is the number of coherent zones contributing to the HHG. The intensity of harmonics was

studied as a function of the number of plasma jets. The number of heating zones on the target surface was shielded step-by-step. The anticipated featureless shape of harmonic spectra from the single 0.5 mm long plasma jet was similar to those observed in the case of 5 mm long plasma. With the addition of each next jet, the spectral envelope was drastically changed, with the 37th harmonic intensity in the case of five-jet configuration becoming 22 times stronger compared with the case of single jet plasma. The expected growth factor of 25 in the case of five-jet medium was almost matched with the experimentally measured enhancement factor.

The HHG in perforated V and Mn plasmas also revealed similar properties. In the discussed experiments with 5 mm long manganese plasma, the enhanced 33rd harmonic was followed with a gradual decrease of higher-order harmonics (Fig. 4.3a, thick curve), analogously to earlier reported studies [23]. In the meantime, the use of perforated manganese plasma led to the enhancement in the range of so called second plateau (i.e., above the 33rd order) and in the longer wavelength range (Fig. 4.3a, thin curve). The QPM induced enhancement of harmonics in the

Fig. 4.3 **a** Comparative harmonic spectra from extended line plasma produced on the plain manganese target (*thick curve*) and four 1-mm-long jets of Mn plasma (*thin curve*). **b** Comparative harmonic spectra from extended line plasma produced on the plain vanadium target (*thick curve*) and four 0.5-mm-long jets of V plasma (*thin curve*). Reproduced from [16] with permission from Springer Science + Business Media



range of 21st order was related with the use of broader plasma plumes compared with the case of silver plasma (1 and 0.5 mm, respectively). The shift of QPM towards the lower-order harmonics corroborates with the $q_{\text{opt}} \sim (L_{\text{jet}}N_e)^{-1}$ relation for the fixed size of single jet (L_{jet}). Once L_{jet} is increased, the optimal harmonic orders (q_{opt}) at fixed N_e , for which the QPM is fulfilled, become smaller and move towards the longer wavelength range.

The 5 mm long vanadium plasma showed very weak harmonics above the 29th order (Fig. 4.3b, thick curve), with barely seen higher orders. As in the case of Ag and Mn, this pattern was drastically changed by using four 0.5-mm-long jets (Fig. 4.3b, thin curve). Along with some enhancement of lower-order harmonics, a notable appearance of the group of harmonics centered in the range of 33rd order showed a clear evidence of the amendment of this nonlinear optical process due to the constructive interference of harmonics in this spectral region. The 30 \times enhancement of these harmonics was measured compared with the case of non-perforated 5-mm-long vanadium plasma.

Such plasmas as Ag, Mn, and B allow generation of up to the sixties harmonics and above (up to the hundredth in the case of manganese). The limits of plasma QPM HHG technique are defined by the properties of plasma plumes. Probably, maximal photon energies at which plasma QPM could be realized at present stage of the developments of plasma HHG in laser produced plumes would not exceed 130–150 eV.

4.2 Quasi-Phase-Matching of Harmonics Using the Variable Multi-jet Plasmas

The experimental setup of used laser system was similar to the above described experiments. The sizes of ablated area of the targets were defined by the length of these targets. Ag and Mn were studied as the ablating targets. The length of the targets was 5 mm. The application of these targets enables the observation of harmonic generation along a broad spectral range [23–26]. The arrangement for perforated plasma formation and harmonic generation is shown in Fig. 4.4. The multi-slit shields (MSS) were used to create the multi-jet plasmas. The example of such shield is shown in the inset in Fig. 4.4. The slit sizes of this shield were 0.3 mm, and the distance between the slits was 0.3 mm. Other multi-slit shields had the 0.9 and 0.45 mm slits and the distances between these slits were 0.9 and 0.45 mm, respectively. These MSS were installed between the focusing cylindrical lens and the ablating target in such a manner, that they allowed the division of the 5 mm long plasma onto the set of a few plasma jets of different sizes. Figure 4.5 shows the images of plasmas in the cases of (1) the absence of MSS and (2,3) the application of different shields leading to the formation of multi-jet plasmas. The sizes of these individual jets produced on the 5 mm long plain targets using the 0.9 and 0.3 mm MSS were ~ 0.9 (2) and ~ 0.4 mm (3). The sizes of plasma jets were defined by the measurements of the ablated areas of the targets.

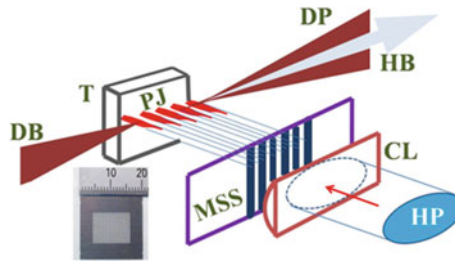
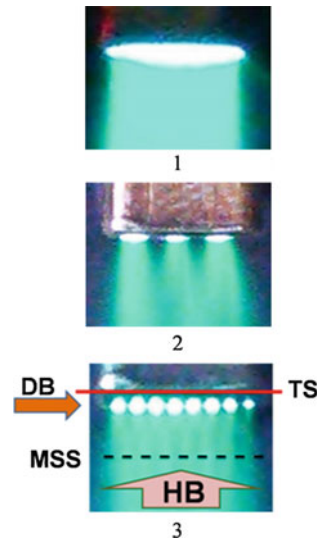


Fig. 4.4 Experimental arrangement for multi-jet plasma formation using the multi-slit shields. *DB* driving beam; *HB* harmonic beam; *HP* heating pulse; *CL* cylindrical lens; *MSS* multi-slit shield; *T* target; *PJ* plasma jets. *Inset* image of multi-slit shield with the slit sizes of 0.3 mm. Reproduced from [27] with permission from World Scientific Publishing

Fig. 4.5 Images of plasma. 1 extended plasma obtained without inserting the multi-slit shield; 2 0.9-mm-long plasma jets; 3 0.4-mm-long plasma jets. *TS* target surface; *HB* heating beam; *DB* driving beam; *MSS* multi-slit shield. Reproduced from [27] with permission from World Scientific Publishing



Below we discuss the enhanced harmonic spectra for the specific orders obtained using the MSS and separated plasma plumes [27]. The harmonics were generated from the ablated silver and manganese atoms and singly-charged ions, which was confirmed from the observed harmonic cut-offs corroborating with the three-step model of HHG. The spectroscopy studies of plasmas also showed the neutral and singly charged ionic lines.

The Ag and Mn plasma concentrations calculated using the code ITAP IMD (at the 1.2 J cm^{-2} fluence of heating radiation on the surfaces of Ag and Mn targets at the distance of $100 \text{ }\mu\text{m}$ above the surfaces and the delay between heating and driving pulses of 43 ns) were 2.7×10^{17} and $1.8 \times 10^{17} \text{ cm}^{-3}$, respectively. One can estimate the length of nonlinear medium at which the coherence properties of the macro-processes become significant for the specific harmonics generating at these conditions. The coherence length for the q th harmonic at a wavelength of

$\lambda \sim 800$ nm is $L_{\text{coh}} \sim 1.4 \times 10^{18}/qN_e$, where L_{coh} is the length measured in millimeters and N_e is the free electron density measured per cubic centimeter [20, 28]. For the thirties harmonics, the L_{coh} at the conditions of plasma formation using the laser fluence of >1.5 J cm $^{-2}$ becomes less than 0.7 mm, which led to a destructive interference of those harmonics along the propagation through the long (5 mm) plasma. The lower-order harmonics were also decreased due to a decrease of constructive interference; however, the phase mismatch at these conditions was not as strong as in the case of higher-order harmonics, which allowed the observation of the harmonics alongside the incoherent emission of plasma.

The harmonic spectra from the 5 mm long plasma in the case of the absence of incoherent plasma emission (i.e., at a fluence of ~ 0.9 J cm $^{-2}$) showed a featureless plateau-like shape, with a gradual decrease of harmonic intensity at the shorter wavelength range (see the thick curves in Fig. 4.6). The harmonic cut-off was in the

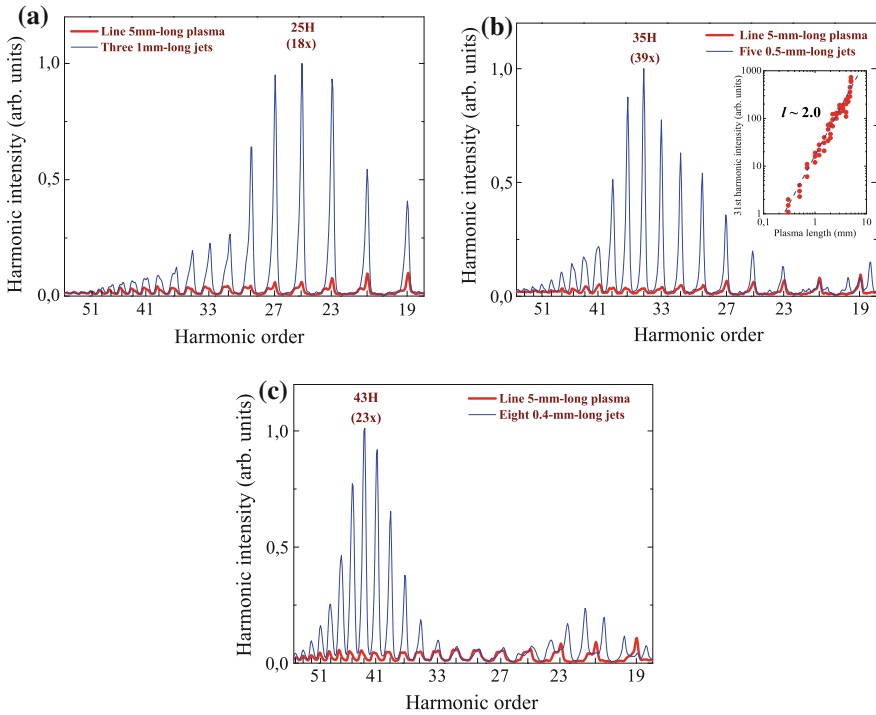


Fig. 4.6 Normalized harmonic spectra in the cases of multi-jet plasmas (*thin curves*) and line 5-mm-long plasmas (*thick curves*) produced on the surface of silver target. Sizes of jets were **a** 0.9 mm, **b** 0.5 mm, and **c** 0.4 mm. The heating pulse fluence of 0.9 J cm $^{-2}$ was used during all these studies. The *enhanced lines* in the lower-order side of spectrum **c** correspond to the second-order diffraction of the QPM-enhanced harmonics. The numbers on the plots show the maximally enhanced harmonic orders and the enhancement factors. *Inset* in Fig. 4.6b: Dependence of the 31st harmonic yield on the length of line plasma plume measured at the 0.4 J cm $^{-2}$ fluence of heating pulse on the target surface. Reproduced from [27] with permission from World Scientific Publishing

region of fifties orders. The harmonic conversion efficiency in the plateau range at these conditions was estimated to be 4×10^{-6} using the method of harmonic yield measurements described in [19].

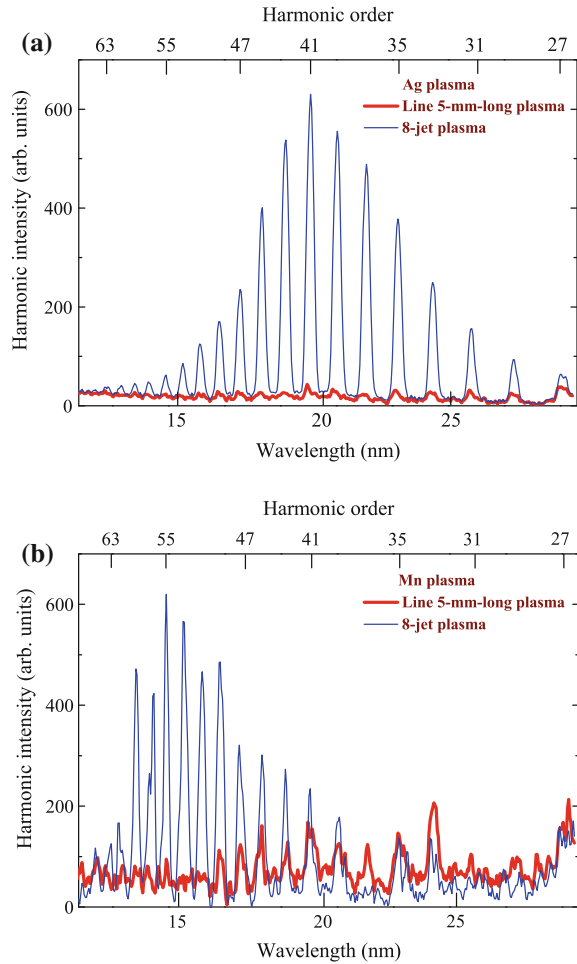
This pattern of featureless harmonic spectrum was drastically changed once we introduced the MSS on the path of heating radiation. Thin curves in Fig. 4.6 comprise three spectra of the plasma harmonics obtained using the multi-slit shields allowing the formation of the 0.4-, 0.5-, and 0.9-mm long plasma jets. No any other changes were introduced in these experiments, but just the insertion of the MSS in and out of the path of the heating radiation (i.e., at similar conditions of silver target ablation using the heating pulse fluence of 0.9 J cm^{-2}).

In each of these cases a characteristic growth of the group of harmonics in different spectral ranges was observed. The maximum enhancements were observed for the 25th, 35th, and 43rd harmonics in the cases of the sizes of individual plasma jets of 0.9, 0.5, and 0.4 mm, respectively. The enhancement factors of those harmonics compared with the case of using the homogeneous 5-mm-long plasma were $18\times$, $39\times$, and $23\times$, respectively. One can see a considerable enhancement and separation of the groups of harmonics, which clearly confirm the involvement of the QPM effect. The energy and photon flux of the enhanced 35th harmonic generated in the five-jet silver plasma was calculated to be $2 \times 10^{-7} \text{ J}$ and 3×10^{10} photons per pulse. In the case of eight plasma jets (Fig. 4.6c, thin curve), the harmonics outside the 33rd–51st orders were suppressed (see the absence of 21st–25th harmonics in this curve; the spectral peaks in this region are attributed to the second-order diffraction of the strong short wavelength harmonics from the flat-field grating of XUV spectrometer).

Below we discuss the comparative studies of the QPM of plasma harmonics in two different materials at the conditions when eight 0.4-mm-long jets were produced on the surfaces of Ag and Mn plain targets. Figure 4.7 shows the spectra of enhanced groups of harmonics in the regions of $\sim 20 \text{ nm}$ (Ag plasma; 41st harmonic, Fig. 4.7a, thin curve) and $\sim 15 \text{ nm}$ (Mn plasma; 55th harmonic, Fig. 4.7b, thin curve). Here, we also show the harmonic spectra from the extended 5 mm long plasmas produced on the same targets. The enhancement factor for the 41st harmonic produced from the Ag plasma jets and the 55th harmonic produced from the Mn plasma jets were $\sim 25\times$ and $15\times$ respectively. Latter material showed the resonantly enhanced 33rd harmonic in the case of line plasma (Fig. 4.7b, thick curve), which has already been observed in previous studies of Mn plasma harmonics [23]. The discussed studies have shown that the enhancement induced by the optimal phase relations between the harmonic and driving waves was prevailed over the resonance induced enhancement of 33rd harmonic. This is a clear evidence of the stronger influence of the macro-processes over the micro-processes during plasma HHG.

Among the advantages of the demonstrated approach for the formation of QPM conditions using MSS are the simplicity in regulation of the electron concentration in the multiple plasma jets, high enhancement factors, and availability of the express analysis of N_e . Two former advantages were demonstrated during previous description. As for the latter advantage, the definition of the maximally enhanced

Fig. 4.7 QPM-enhanced harmonic spectra generated in the **a** Ag and **b** Mn eight-jet plasmas. The length of each jet was 0.4 mm. The *thin curves* show the harmonic spectra obtained from the eight-jet plasmas. *Thick curves* show the harmonic spectra obtained from extended line plasmas. The spectra were measured at similar conditions of plasma formation by moving the multi-slit shield in and out the path of the heating pulse. Reproduced from [27] with permission from World Scientific Publishing



harmonics at the fixed sizes of separated plasma jets allows the calculation of N_e from the above-mentioned relation (see also Chap. 6). Particularly, the electron concentration in the case of various multiple jets produced at similar excitation of the silver target could be defined through the above relation for the N_e as 6.2×10^{16} , 8×10^{16} , and $8.1 \times 10^{16} \text{ cm}^{-3}$ assuming the experimentally measured parameters of L_{coh} and q_{coh} in the cases of used multi-slit shields. Here q_{coh} is the harmonic order in the QPM region showing the highest intensity and L_{coh} corresponds to the sizes of individual plasma jets at which the corresponding QPM enhancement of the group of harmonics was observed. A reasonable coincidence of these measurements of N_e with each other, as well as with the calculations based on the code ITAP IMD ($N_e = 7.2 \times 10^{16} \text{ cm}^{-3}$) was obtained. At the same time, the comparative studies of the HHG from the multi-jet structures produced on the Ag and Mn targets at similar conditions of surface ablation have shown the difference in the q_{coh} of these species

(correspondingly 41st and 55th harmonics), which was explained by different concentrations of electrons in those plasma jets.

Thus the potential of the proposed plasma harmonic QPM approach is related with the express analysis of the plasma characteristics, alongside with the amendments of harmonic yield in different spectral regions. These studies showed the realization of the advanced properties of perforated plasma, as the source of harmonics, through the demonstration of the coherent superposition of the interacting waves. The claim regarding the control of the coherent superposition of harmonics from successive sources is supported by the data shown in Fig. 4.6. The experimental results presented in Figs. 4.6 and 4.7 clearly indicate that, by varying the sizes of jets and target material, one can manipulate the phase matching in different spectral regions. In that case, different ranges of harmonic spectra show the destructive or constructive interference.

Similar results were reported in [29]. A significant enhancement of the thirties and forties harmonics in the perforated Ag plasma was due to involvement of the multiple plasma jets in the harmonic generation. The enhancement factor of 13 in the case of five 0.5 mm long plasma jets compared with the 6 mm long line plasma was achieved for the 33rd harmonic. The enhancement factors for different harmonics along the 18–38 nm spectral range are shown in Fig. 4.8. The comparative studies of the harmonic spectra generated from the five-jet structure at different fluences of heating 370 ps pulses on the target surface were accomplished by changing the energy of heating radiation using the calibrated filters. A tuning of the maximum of spectral envelope towards the higher-order harmonics with a decrease of the fluence of heating radiation was observed.

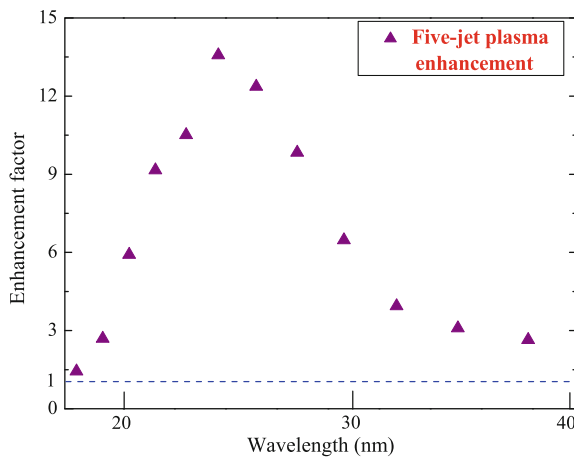


Fig. 4.8 Harmonic enhancement factors for the five-jet medium along the 18–38 nm spectral range. Reproduced from [29] with permission from American Physical Society © 2014

4.3 QPM-Induced Enhancement of HHG During Two-Color Pump of Multi-jet Plasmas

As in the case of gas medium, separation of the extended plasma plume into a few small-sized plasma jets may restore the proper phase relationship between the driving and harmonic waves and give way for further enhancement of the yield in different spectral ranges. To create QPM conditions, one has to maintain a modulation of the coupling between the driving and harmonic waves, which is periodic along the generation path. At these conditions, the enhancement of harmonics will occur, as it has already been mentioned in previous sections of this chapter, only when the interference between propagating harmonic and newly generated harmonic becomes constructive.

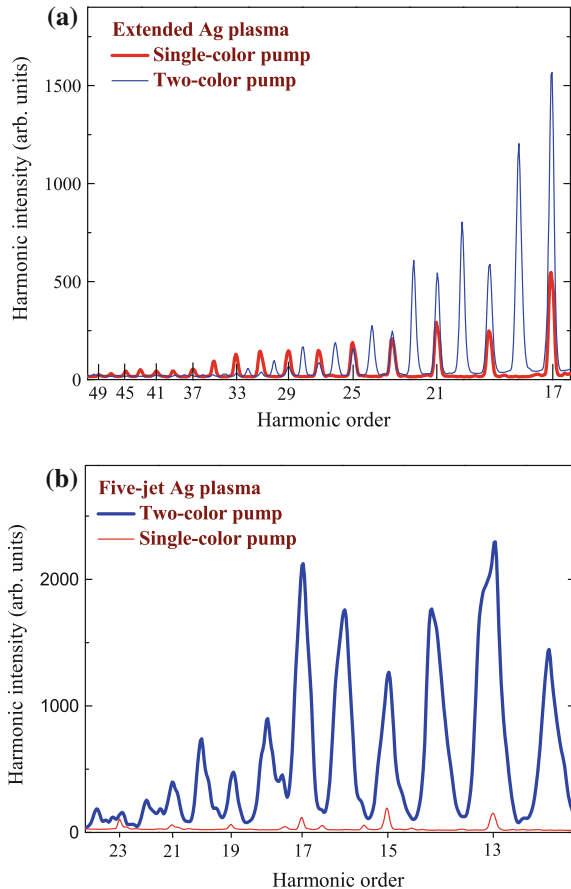
Below we discuss the two-color pump induced HHG studies using the multi-jet plasmas [30]. The experimental setup was described in Sect. 4.2. To analyze the odd and even harmonic generation in long extended plasma and multi-jet plasma the two-color pump scheme was used. The nonlinear optical crystal (BBO, type I, crystal length 0.3 mm, second-harmonic conversion efficiency 5 %) was inserted in the vacuum chamber using the translation stage in the path of the focused driving radiation at a distance of 150 mm from the plasma plume. The translation stage allowed the movement of crystal in and out of the path of driving radiation. The driving and second harmonic beams were then focused inside the plasma plume. The polarizations of these two pumps were orthogonal to each other. To vary the overlap of two-color waves in the plasma the BBO crystals of different thicknesses (0.3 and 0.5 mm) were used.

Ag and Cr were studied as the ablating targets. A three coordinate manipulator was used to change the targets and to control a zone of interaction of the two-color driving radiation with the plasma relative to the target surface. To create multi-jet plasma a thin glass plate with the 0.5 mm long aluminum strips separated from each other at a distance of 0.5 mm was used. This multi-slit mask was installed between the focusing cylindrical lens and target, which allowed the division of the extended continuous 6 mm long plasma onto six 0.5 mm long plasma jets with the distance between them ~ 0.5 mm. The jets were expanded from the target surface at the angle of divergence of $\sim 20^\circ$ towards the axis of propagation of the driving two-color beams. The number of plasma jets was varied by shielding the open parts of multi-slit mask (from single jet to six jets).

Here we describe the single- and two-color pump induced HHG experiments in the perforated plasmas. Figure 4.9a shows the harmonic spectra produced from the extended (6 mm long) silver plasma in the case of irradiation by single-color (802 nm) or two-color (802 and 401 nm) pumps by using the 0.5 mm long BBO crystal (second harmonic conversion efficiency of 9 %) at the conditions of the weak ablation of target by heating pulse (i.e., at a fluence of 0.2 J cm^{-2}). One can distinguish the equality of odd and even harmonic intensities along the almost whole range of generation. The advanced properties of extended plasmas were also emphasized while comparing with the odd and even harmonics generated in the

0.5 mm long plasma plume (see also Chap. 3). In the latter case, the even harmonics did not extend over the whole spectrum of generation of the odd harmonics. Moreover, their intensity was a few times weaker compared with odd harmonics, contrary to the case of the HHG produced in the extended plasma. However, once the fluence of heating radiation on the target surface was increased from 0.2 to 0.6 J cm^{-2} , a decrease of conversion efficiency of both the odd and even harmonics was observed. The plasma emission became stronger while the emission of harmonics was diminished. The destructive processes, such as the phase mismatch due to the growth of the electron density in the plasma, stopped the efficient HHG in the extended over-excited silver plasma, similarly to the cases described in Chap. 2. At these conditions, the modification of extended plasma being divided on a few separated jets restored the strong emission of harmonics in the low-order harmonic range (Fig. 4.9b). Note a considerably stronger harmonic yield in the case of two-color pump compared with the single-color pump at these conditions of strong ablation and multi-jet formation (compare Fig. 4.9a and b).

Fig. 4.9 **a** Single—(802 nm, *thin curve*) and two—(802 nm + 401 nm, *thick curve*) color induced harmonic spectra from the extended line plasma at a weak excitation of silver target. **b** Spectra of the low-order harmonics generated in the multi-jet plasma at strong excitation of silver target in the case of single-color (*thin line*) and two-color (*thick line*) pumps. The 0.5-mm-thick BBO crystal was used in both cases. Reproduced from [30] with permission from IOP Publishing. All rights reserved



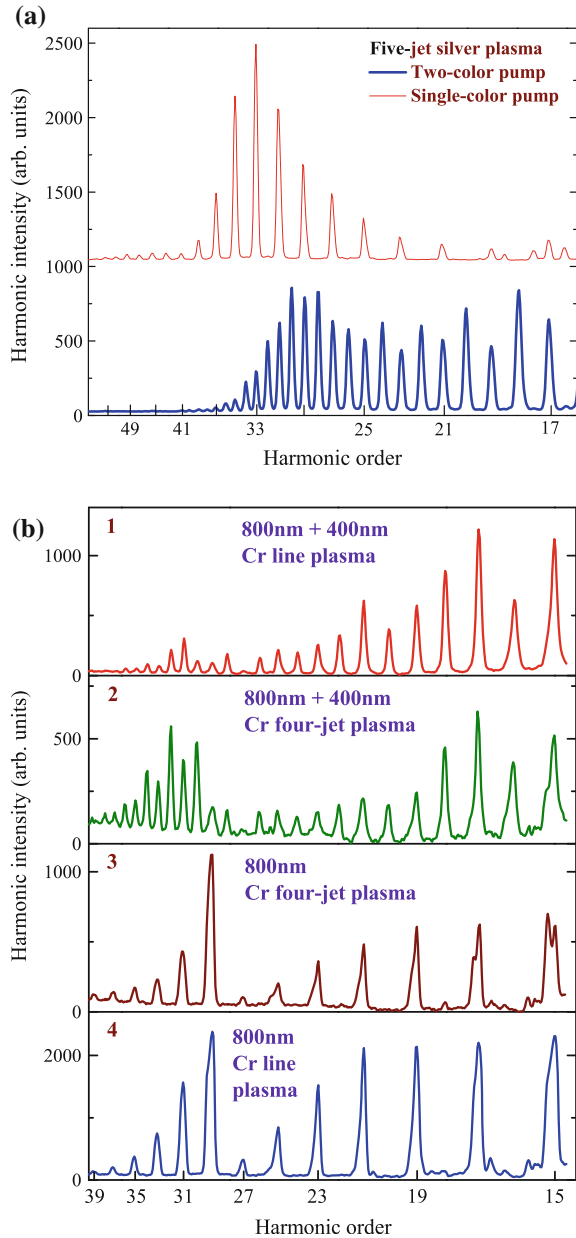
The application of two-color pump at latter conditions led to the modification of the selectivity of harmonics and the decrease of the q_{coh} . Figure 4.10 shows the comparative harmonic spectra from the five-jet Ag plasma in the cases of single-color (Fig. 4.10a, upper panel) and two-color (Fig. 4.10a, bottom panel) pumps. A clear selectivity of a group of harmonics centered around the 33rd order in the case of single-color pump (upper panel) was more pronounced compared with the less selective pattern of a group of odd and even harmonics at a longer wavelength spectral range (bottom panel). These experiments were carried out using the thinner (0.3 mm) BBO crystal.

The calculated silver plasma density was $4 \times 10^{17} \text{ cm}^{-3}$. The electron density in the multiple jets produced on the silver target at similar excitation could be defined from the relation $N_e \approx 1.4 \times 10^{18}/(L_{\text{coh}} \times q_{\text{coh}})$ as $8 \times 10^{16} \text{ cm}^{-3}$ assuming the experimentally measured parameters of L_{coh} and q_{coh} in the case of used multi-slit shield. Here q_{coh} corresponds to the harmonic order in the QPM region showing the highest intensity (33rd harmonic, Fig. 4.10a) and L_{coh} corresponds to the sizes of individual plasma jets (0.5 mm) at which this enhancement was observed. A reasonable coincidence of these measurements of N_e with the calculations of electron concentration based on the code ITAP IMD ($N_e = 7 \times 10^{16} \text{ cm}^{-3}$) was obtained.

The same experiments using chromium multi-jet plasma showed better selectivity of a group of harmonics in the case of two-color pump (compare two middle panels of Fig. 4.10b). The use of extended plasma without the second field led to the strong 29th harmonic generation related with the resonance induced enhancement (bottom panel) [31] while the application of two-color pump at these conditions led to a decrease of resonance enhanced harmonic (upper panel). Notice the insignificant difference in the harmonic spectral shapes for extended (5 mm long) plasma and four 0.4-mm-long jets in the case of single-color pump (two bottom spectra), while in the case of the two-color pump of multi-jet plasma a clear enhancement of a group of odd and even harmonics (between the 30th and 38th orders) was observed (second panel from the top).

Below, we discuss the results of the studies of the two-color pump induced harmonics from the multi-jet plasmas using the variable amount of jets. Figure 4.11a shows the low-order harmonic spectra generated from the chromium plasma. A steady and homogeneous growth of all harmonics generated out of the range of QPM enhancement was observed with the increase of the number of plasma jets. One can expect a growth of harmonic intensity (I_H) to be proportional to n^2 , where n is a number of the jets participating in the harmonic generation. These studies have confirmed this quadratic dependence. No harmonic enhancement related with the QPM was observed in this spectral region (i.e., for the 11th to 19th harmonics, $\sim 40\text{--}80 \text{ nm}$). These studies were carried out using the single-color pump. Another pattern of $I_H(n)$ dependence was observed in the case of higher-order harmonics and two-color pump (Fig. 4.11b) of silver target. The shapes of single- and two-jet induced harmonic spectra (two upper panels) resemble the one obtained from the extended line plasma (bottom panel). However, with the growth of the number of plasma jets, the intensity of a group of harmonics in the

Fig. 4.10 a Harmonic spectra from the silver five-jet plasma in the case of single-color (*upper curve*) and two-color (*bottom curve*) pumps. The curves were separated for better visibility. **b** The same dependences in the case of chromium line plasma (*upper and bottom panels*) and four-jet plasma (*two middle panels*) using the single-color (*two bottom panels*) and two-color (*two upper panels*) pumps. The 0.3-mm-long BBO crystal was used in both cases. Reproduced from [30] with permission from IOP Publishing. All rights reserved



range of the 26th–28th orders became stronger compared with the lower orders. One can compare the harmonic spectra from the extended 6 mm long plasma and five-jet plasma, when the characteristic shape of plateau like harmonics was changed on the enhanced odd and even harmonics in the cut-off region.

The QPM for this two-color scheme was not as pronounced as in the case of single-color scheme (Fig. 4.10a, upper panel). Nevertheless, the enhancement factor for the 28th harmonic in the five-jet configuration compared with the same harmonic generating in the extended plasma was ~ 25 while recalculating the emission yields at the equivalent lengths of two media. The best obtained conversion efficiencies of the plateau like harmonics (i.e., around the thirties orders) in the case of gaseous media were reported in the range of 10^{-5} – 10^{-6} . The estimates and comparison with [19] show that, in the discussed experiments, the absolute value of the conversion efficiency of the QPM enhanced 33rd harmonic was 3×10^{-5} .

The installation of the nonlinear crystal in the vacuum chamber on the path of focused radiation allows excluding the walk-off effect and the dispersion of the window and focusing lens, though the second harmonic conversion efficiency becomes less compared with the case of plane wave propagation. The spatial overlapping between the beams in the former case became sufficient for interaction of the two waves in the extended plasma plume. At the same time, the group velocity dispersion in BBO leads to some separation of two pulses.

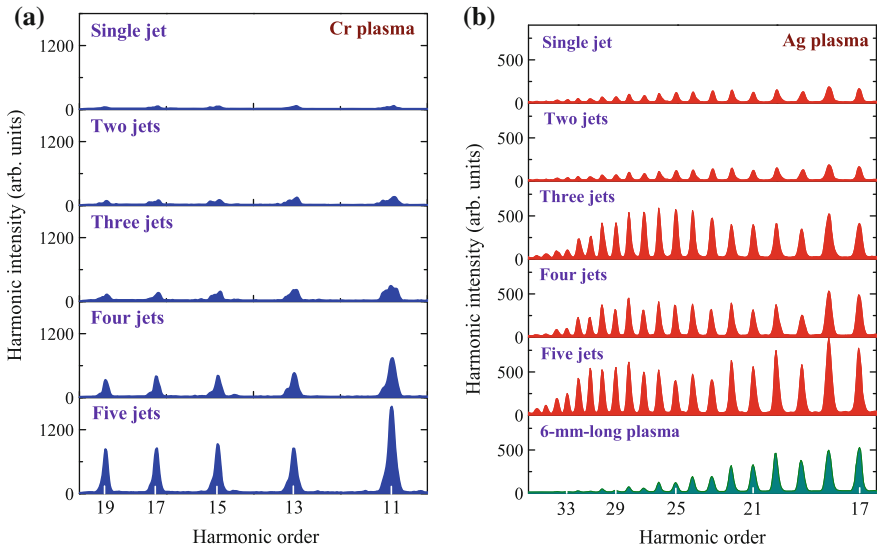


Fig. 4.11 **a** Low-order harmonic spectra from the chromium ablation at different number of the plasma jets used for the single-color HHG. **b** High-order harmonic spectra generated in the perforated silver plasma using the two-color pump and different number of jets (*five upper panels*) and 6-mm-long extended plasma plume (*bottom panel*). Reproduced from [30] with permission from IOP Publishing. All rights reserved

4.4 Peculiarities of QPM Harmonics Using Different Targets and Pump Schemes

The below-described studies [32] used the perforated targets, which were irradiated by a cylindrically focused heating pulse. Aluminum was used as the ablating target. The shape of target is shown in the left inset in Fig. 4.12. The depth of perforation of the aluminum surface was 2 mm. The plasma was formed on the upper and bottom parts of target surface, as shown in the image of plasma jets presented in the right inset of Fig. 4.12. The driving pulse propagates through the plasma jets formed on the upper part of target surface. Other plasma jets did not participate in the harmonic generation, since they reach the axis of propagation of the driving beam after a few hundred nanoseconds from the beginning of ablation, when the femtosecond pulse has already propagated near the target surface. This separation of the upper and bottom parts of the plasma jets allowed the formation of a non-linear optical medium, which matches the requirements of QPM. The HHG spectrum from the multi-jet aluminum plasma at different regimes of excitation of the perforated surface is shown in Fig. 4.12a. Here we also show the harmonic spectrum obtained from the line-shaped 5 mm-long plasma. One can clearly see the enhancement of the groups of harmonics, which were tuned depending on the fluence of the heating pulse. The optimization of QPM was observed for shorter

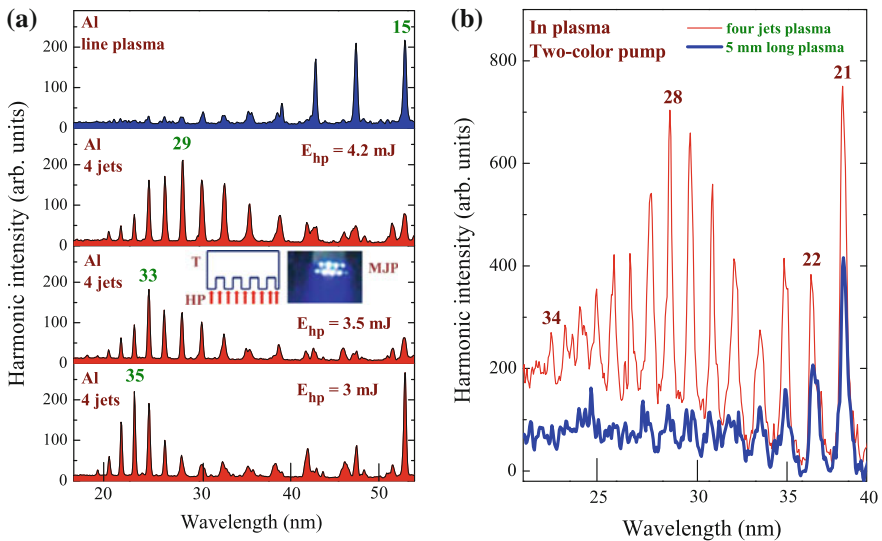


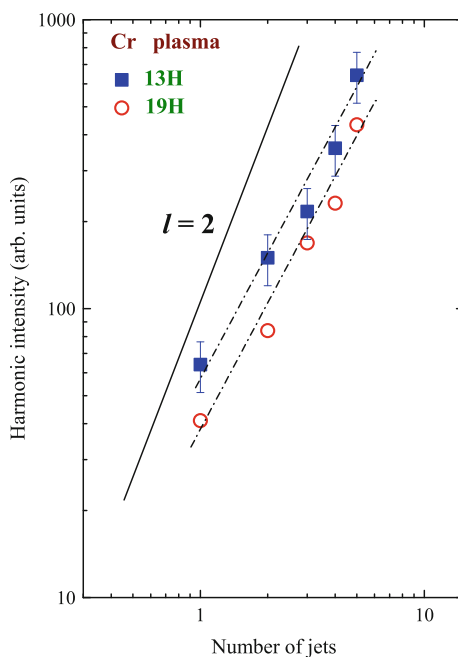
Fig. 4.12 **a** Harmonic spectra from aluminum plasma in the cases of (from *top to down*) linear 5-mm-long plasma plume and four-jet plasma plumes produced on the perforated surface by 4.2-, 3.5- and 3-mJ heating pulses. **b** Variation of spectral envelope of the harmonic distribution obtained during two-color pump of 5-mm-long and four-jet indium plasmas produced using the multi-slit shield at similar conditions of the heating pulse fluence. © Astro Ltd. Reproduced from [32] with permission from IOP Publishing. All rights reserved

wavelengths at less excitation of the target during the formation of multi-jet plasma (Fig. 4.12a; compare the spectral maxima of QPM harmonics for the 3, 3.5, and 4.2 mJ heating pulses).

Figure 4.12b shows the modulation of the harmonic spectrum in the case of a four-jet indium plasma produced using the multi-slit shield compared with the linear plasma plume in the case of a two-color pump. The BBO crystal was placed inside the vacuum chamber contained targets to convert part of the focused driving radiation into the second harmonic (401 nm, 5 % conversion efficiency). The harmonic cut-off in the case of a two-color pump of the extended plasma did not exceed the 24th order. The application of a multi-slit shield allowed the formation of four 0.5 mm-long jets, which led to extension of the harmonic cut-off (up to the 34th order) and significant enhancement of a group of harmonics around the 28th order.

As it was discussed in previous sections, the signature of QPM is the growth of harmonic yield $\sim n^2$, where n is the number of coherent zones contributing to the signal. While this rule was maintained for the QPM-enhanced harmonics at the moderately excited plasmas, the $I_h \propto n^2$ dependence was not fulfilled for the lower order harmonics. Figure 4.13 shows the declination of this dependence from the quadratic rule and less steep slope of the log-log curve. Here also shown the quadratic slope (solid line) to compare with the measurements of the 13th and 19th harmonics generated in the multi-jet chromium plasmas. Those harmonic orders did not belong to the group of QPM-enhanced harmonics.

Fig. 4.13 13th (filled squares) and 19th (empty circles) harmonic yields as the functions of the number of chromium plasma jets participating in harmonic generation. The slopes of these dependences were less than 2 (compare the dash-dotted lines with the solid line corresponding to the anticipated slope of $l = 2$). © Astro Ltd. Reproduced from [32] with permission from IOP Publishing. All rights reserved



The important parameter of the QPM studies in the plasma plumes is the concentration of plasma and free electrons. The molecular dynamics based laser ablation simulation was carried out for the Al target using optimal experimental parameters of laser radiation by means of the code ITAP IMD [33]. Although it is possible to predict material properties from ab initio simulations to high accuracy, the method has some drawbacks. The long computational time required for these calculations makes them unpractical for typical treatments of laser ablation. The system sizes, which can be simulated on modern computers, are still in the order of a few hundreds of atoms, which is far too small. In the case of molecular dynamics simulations, the system is simplified by not treating the ions and electrons separately. The modeled atoms are assumed not to have inner degrees of freedom, and they interact with each other as classical particles. For the solution of the many-body problem, the classical Hamiltonian equations of motion were integrated. By solving the standard Hamiltonian equations it is possible to characterize a system, which does not change particles (N), volume (V), or energy (E). In statistical mechanics, such system is called a microcanonical ensemble (NVE ensemble). It should be noted that during laser ablation, the total energy of the system is changed, but during one integration step of the equations of motion, the energy is unchanged, therefore the NVE ensemble is sufficient for simulation of laser ablation. Further details of the method could be found in [34]. The use of short heating pulses (370 ps) allowed a direct simulation of the ablation process at a fluence of $\sim 1 \text{ J cm}^{-2}$. After leaving the surface of the sample all particles were considered as non-interacting with the field and were removed from further simulation time steps. For all particles, which left the surface after a given simulation time step, one can choose those with the kinetic energies sufficient to be in the interaction volume ($\sim 100 \text{ }\mu\text{m}$ above the surface) exactly after the supposed delay.

In order to calculate the concentrations of plasma and electrons the single atom ionization probabilities were simulated by time-dependent density functional theory using the Octopus package [35]. The ionization probability was computed as the occupation of all but the 10 lowest states. For 370 ps ablation pulses a series of calculations over 50 fs with constant intensities was performed. This approach allowed the definition of ionization probability over the envelope of the ablating pulse, which was approximated by a least-squares fit to yield a continuous time-dependent function of the ionization probability. Then, at every time step of the molecular dynamics simulation, the number of particles with velocities sufficient to reach the interaction region after a given delay was multiplied by this ionization probability. This yields the concentration of ionized particles in the interaction region with the driving pulse. The calculated concentrations of plasma and electrons during ablation of aluminum are presented in Table 4.1. These data correspond to different delays between pulses at a fixed distance from the target surface.

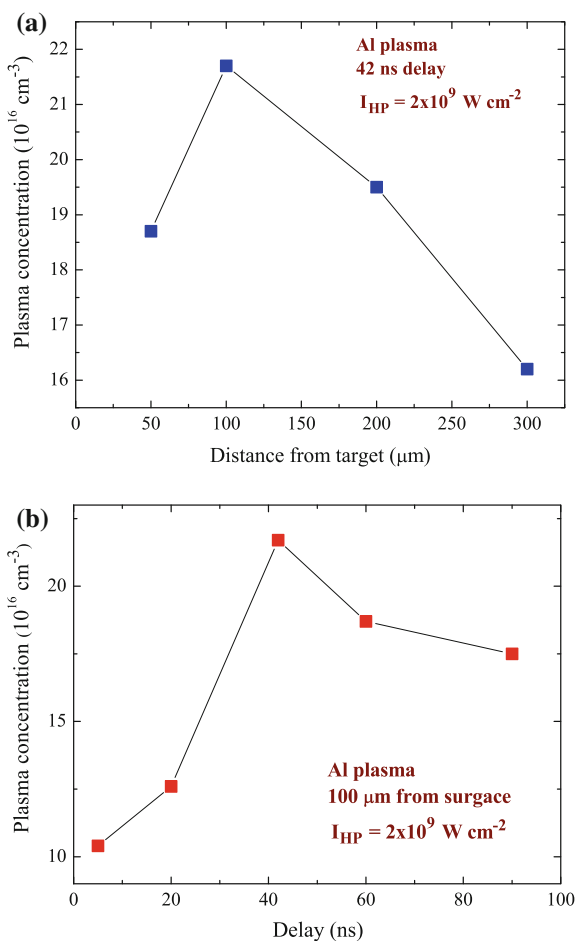
The dependences of aluminum plasma concentration on the delay between heating and driving pulses and on the distance between the target surface and axis of propagation of the driving beam at 42 ns delay are shown in Fig. 4.14. One can define the optimal delays and distances, which corresponded to the maximal

Table 4.1 Calculations of plasma and electron densities in the interaction volume (in 10^{17} cm^{-3}) for 3 mJ, 370 ps ablation pulses at a fluence of 0.6 J cm^{-2} on the Al target and at different delays between ablating and driving pulses

Delay (ns)	Al target	
	Plasma	Electrons
5	1.67	0.11
30	2.79	0.15
40	2.61	0.13
75	1.45	0.10

© Astro Ltd. Reproduced from [32] with permission from IOP Publishing. All rights reserved

Fig. 4.14 Calculated dependences of aluminum plasma concentration at **a** variable distance from the target surface at a 42 ns delay between the heating and driving pulses and **b** variable delay at a fixed distance (100 μm) from the target surface. © Astro Ltd. Reproduced from [32] with permission from IOP Publishing. All rights reserved



harmonic yields. The ionization state of most plasma plumes at a fluence of heating pulse of 0.6 J cm^{-2} was in the range of 5 % (i.e., the electron concentration was about $2 \times 10^{16} \text{ cm}^{-3}$). At these concentrations of free electrons, the coherence lengths of enhanced harmonics in the region of mid-thirties orders were close to the sizes plasma jets. The calculations of coherence lengths using the estimations of free electron concentration are discussed below.

For harmonics in the XUV, dispersion in the partially ionized plasma is mostly attributed to the free electrons generated by the heating and driving radiation. These pulses produce free carriers during ablation of targets and propagation of femtosecond pulses through the partially ionized plasma. The phase mismatch Δk for the q th harmonic depends on the medium dispersion and on the Gouy phase shift ($\Delta k = \Delta k_{\text{disp}} + \Delta k_{\text{geom}}$). Here $\Delta k_{\text{disp}} = k_q - qk_1$, with $k_1 = n_1\omega_1/c$ (n_1 is the refractive index of the medium at the wavelength of driving pulse, ω_1 is the frequency of the driving radiation and c the speed of light in vacuum) and $k_q = n_q\omega_q/c$ (n_q is the refractive index of the q th harmonic and ω_q is the frequency of the q th harmonic) and $\Delta k_{\text{geom}} = (1 - q) \tan^{-1}(z/b)$, where z denotes the direction of propagation and b is the confocal parameter, which is given by $b = 2\pi r^2 n_1 / \lambda$ (where r is the radius of the beam at focus). The values of Δk_{geom} as a function of pressure were found to be three orders of magnitude smaller than Δk_{disp} at the conditions when the confocal parameter exceeds the sizes of nonlinear optical medium [36]. In the discussed study, b was larger than the plasma length; thus Δk_{geom} can be neglected in the calculations and one can simply admit $\Delta k \approx \Delta k_{\text{disp}}$.

The plasma dispersion-induced phase mismatch is equal to $\Delta k_{\text{disp}} = qN_e e^2 \lambda / 4\pi m_e \epsilon_0 c^2$ [37, 38], where e is the charge of the electron, m_e is the mass of the electron, and ϵ_0 is the vacuum permittivity. For Al plasma with 0.2 ionization state at a plasma concentration of $5 \times 10^{17} \text{ cm}^{-3}$ produced at the fluence of heating pulse of $\sim 1 \text{ J cm}^{-2}$, the enhanced 35th harmonic of 802 nm radiation had a $\Delta k_{\text{disp}} \approx 79 \text{ cm}^{-1}$. The calculated coherence length of this harmonic at the used conditions was $L_{\text{coh}} = 4\pi^2 m_e \epsilon_0 c^2 / q N_e e^2 \lambda \approx 0.4 \text{ mm}$, which is close to the length of the jets (0.5 mm) formed on the perforated aluminum surface.

The enhancement factor of QPM harmonics can be simply compared with the theoretical expectation for a single source of plasma at the same density and with a length equivalent to the sum of the individual sources in the array. This parameter could also be applied to the conditions of a growing number of plasma jets, when the quadratic growth of HHG for the harmonic orders, for which the QPM is fulfilled, is maintained.

The ionization-related dispersion at relatively loosely focused configuration ($b = 12 \text{ mm}$, $L_p = 5 \text{ mm}$) is the only factor taken into account in the calculations for the estimation of the coherence length. This is especially underlined in the case of partially ionized plasma compared with the neutral gas jets where the ionization occurs during barrier suppression ionization of harmonic emitters.

Simultaneous or selective quasi-phase-matching of the short and long paths makes it possible to control their relative weight. The studies of the divergence of QPM-enhanced harmonics from the Al plasma have confirmed this assumption.

These harmonics possessed considerably smaller divergence compared with those of lower orders, thus increasing the brightness of short-wavelength radiation (see the following section).

4.5 Influence of Plasma Jet Sizes and Pulse Energies on the Characteristics of QPM Harmonics

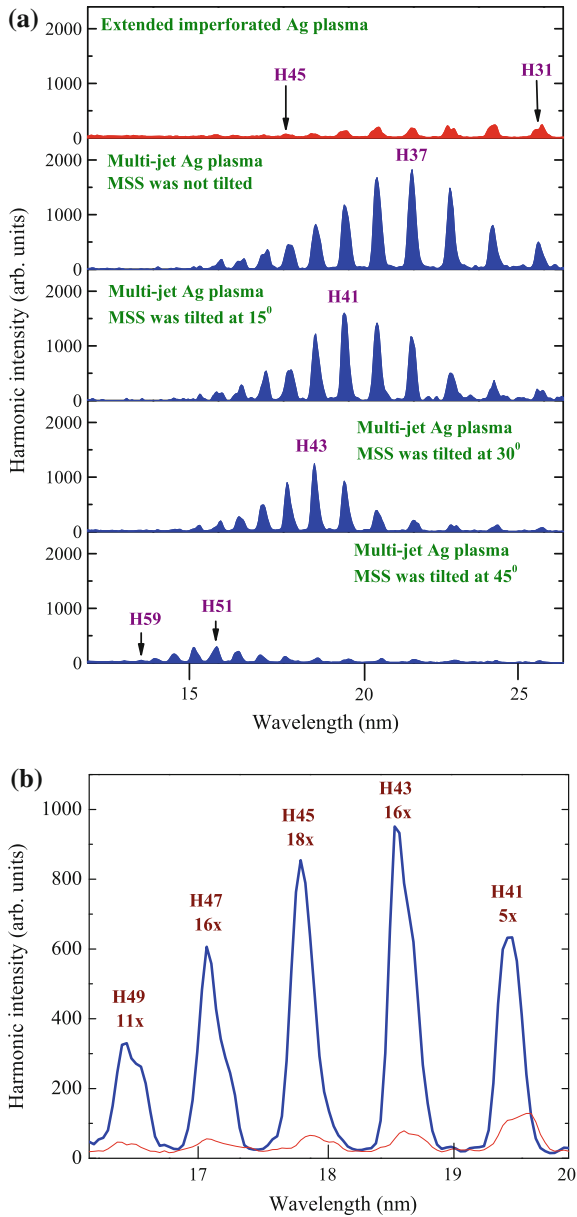
The harmonic spectra from the 5-mm-long silver plasma at a fluence of heating radiation of $\sim 0.9 \text{ J cm}^{-2}$ showed a featureless plateau-like shape, with a gradual decrease of harmonic intensity at the shorter-wavelength range (Fig. 4.15a, upper panel) [39]. The harmonic cut-off was in the region of 50s orders. Other panels of Fig. 4.15a show four spectra of the harmonics obtained using the insertion of the multi-slit shield on the path of heating beam. The MSS was tilted at different angles (0° , 15° , 30° , and 45°) with regard to the heating beam. The tilting of MSS led to a decrease of the sizes of single jet and to the growth of the number of jets. A characteristic QPM-induced growth of the groups of harmonics in different spectral ranges was observed in all these cases. The maximum enhancements were achieved for the 37th, 41st, 43rd, and 51st harmonics respectively. The maximally enhanced harmonic orders approximately corresponded to the rule when the product $L_{\text{coh}} \times q_{\text{qpm}}$ (where L_{coh} corresponded to the sizes of single jet) was maintained constant at a fixed electron density (since $L_{\text{coh}} \times q_{\text{qpm}} \approx 1.4 \times 10^{18}/N_e$).

A significant enhancement of the groups of harmonics compared to the extended imperforated plasma was due to involvement of the multi-jet plasmas in the harmonic generation allowing the achievement of QPM. The enhancement factors of 16 and 18 in the case of nine plasma jets compared with the 5-mm-long line plasma was achieved for the 43rd and 45th harmonics respectively. The enhancement factors along the 16–20 nm spectral range for this multi-jet medium are shown in Fig. 4.15b.

Similar variations of harmonic spectra were observed in the case of perforated manganese plasma. In the discussed experiments with 5-mm-long manganese plasma, the enhanced 33rd harmonic was followed with a gradual decrease in higher-order harmonics and significant decrease of the 31st order (Fig. 4.16, upper panel), analogously to earlier reported studies [23]. The use of perforated manganese plasma led to the enhancement of some groups of harmonics in the region of so called second plateau. The shift of QPM towards the higher-order harmonics in the case of shorter sizes of jets was corroborated with the $q_{\text{qpm}} \sim (L_{\text{jet}}N_e)^{-1}$ relation at the fixed electron density, similarly to the experiments with silver plasma. q_{qpm} was tuned from H43 to H55 while tilting the MSS from 0° to 45° (Fig. 4.16, three bottom panels).

The interesting observation in the case of non-tilted MSS is the appearance of the second group of enhanced harmonics centered at H73 (Fig. 4.16, second panel from the top). The intensities of the harmonics surrounding H73 were significantly smaller compared with those centered near the H43. However, they were clearly

Fig. 4.15 a Harmonic spectra generated in different multi-jet silver plasmas produced by tilting the MSS. *Upper panel* shows the harmonic spectrum generated in the 5-mm-long Ag plasma. **b** Enhancement factors of the QPM-enhanced harmonics. *Thick and thin curves* correspond to the harmonic spectra obtained in the multi-jet and imperforated silver plasmas correspondingly at similar fluences of heating radiation. Reproduced from [39] with permission from American Physical Society. Copyright 2015



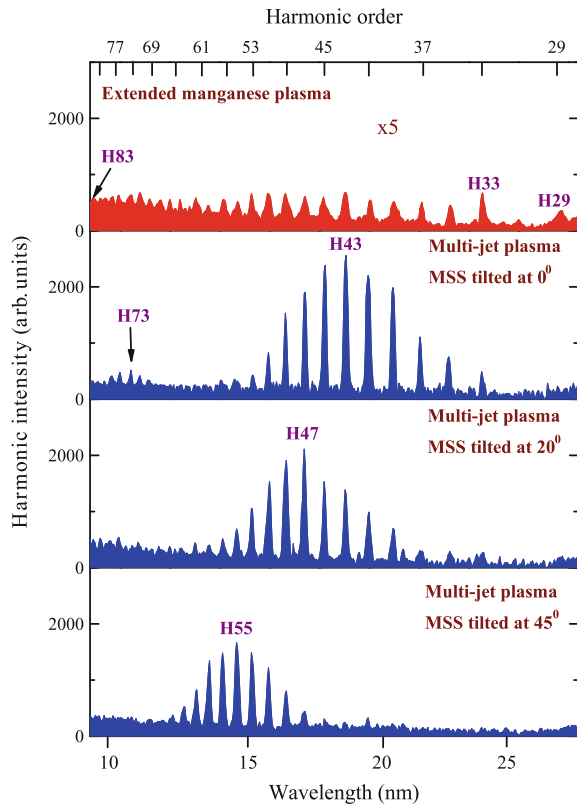
stronger than the lower-order harmonics (H57–H67). The maximally enhanced harmonic in this range (H73) did not correspond to the doubly shortened wavelength of the H43, so one cannot expect the involvement of the second-order QPM processes. The tilting of MSS led to disappearance of this group of harmonics since

they expected to be shifted towards the shorter-wavelength region where the conditions of HHG in the Mn plasma were less favorable.

To analyze the role of driving pulse intensity on the variations of QPM conditions different energies of these pulses were used. The aim of those studies was to define whether the increase of the cross-section of tunneling ionization caused by the growth of driving pulse intensity leads to the variation of the QPM conditions due to the growing number of free electrons. More discussion on that matter will be presented below. Here we show the observation, which points out the insignificance of the additionally appeared tunneled electrons in the variations of QPM conditions.

Figure 4.17 shows two harmonic spectra obtained in the eight-jet Ag plasma using the 1.85 and 5 mJ driving pulses. The q_{qpm} in these two cases were approximately same (H37 and H39). The difference between these two spectra is mostly related with the broadening of the envelope of enhanced harmonics in the latter case, which points out the decrease of selectivity of a small group of harmonics due to less favorable conditions of QPM for different parts of the driving beam. Another observation is related with the difference in the divergences of the harmonics generated in the multi-jet and imperforated plasmas. In the case of 1.85 mJ pulses, the sizes of these harmonics were approximately equal to each other

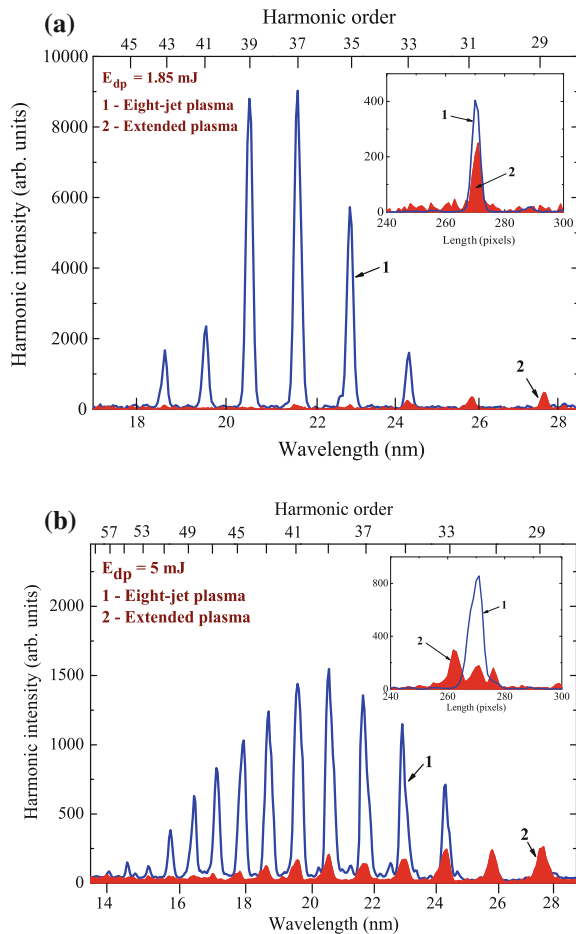
Fig. 4.16 Harmonic spectra from different multi-jet manganese plasmas produced by tilting the MSS. *Upper panel* shows the harmonic spectrum obtained in imperforated 5-mm-long Mn plasma, which was multiplied (5 \times) for better comparison with the *bottom panels*. Note the equality of the Y-axes. Reproduced from [39] with permission from American Physical Society. Copyright 2015



(see the inset in Fig. 4.17a showing the spatial distributions of 37th harmonic in the far field). The growth of driving pulse energy from 1.85 to 5 mJ led to a significant spectral modulation of the harmonics generated in the extended plasma, while the sizes of the QPM-enhanced harmonics generated in the multi-jet plasma formation showed some insignificant broadening compared with previous case (inset in Fig. 4.17b).

Thus the growth of the tunneling ionization cross-section leading to the appearance of additional free electrons in the multi-jet medium did not spoil the conditions of QPM. Figure 4.18 (empty circles) shows the almost similar q_{qpm} along a broad range of variations of the driving pulse energy. A considerably different behavior of QPM was observed once we changed the heating pulse energy, which led to variation of the plasma and electron densities (Fig. 4.18, filled squares).

Fig. 4.17 Variation of the spectral and spatial shapes of the harmonics generated in the extended and multi-jet silver plasmas using the **a** 1.85 mJ and **b** 5 mJ driving pulses. *Insets* in **(a)** and **(b)** show the far field images of the 37th harmonic in the cases of (1) multi-jet and (2) extended imperforated plasmas. One can see the equal divergences of the 37th harmonic generated in the extended and perforated plasmas in the case of 1.85 mJ driving pulse, while in the case of 5 mJ pulse, the harmonic beam from extended plasma became more divergent and strongly modulated compared with the one generated from the eight-jet plasma. Reproduced from [39] with permission from American Physical Society. Copyright 2015



The comparative studies of the harmonic spectra generated from the eight-jet silver plasma at different fluences of heating 370 ps pulses on the target surface were accomplished by changing the energy of heating radiation using the calibrated filters. The energy of heating pulse was varied to analyze the influence of this parameter on the dynamics and shape of the envelope of harmonic distribution using the same multi-jet plasma. The group of harmonics gradually tuned towards the lower orders (i.e., longer-wavelength region) with the growth of the heating pulse energy. A decrease of N_e at weaker excitation of the target should lead to the optimization of the QPM for higher q_{qpm} to keep the product $q_{\text{qpm}} \times N_e$ unchanged at the fixed spatial characteristics of plasma jets, which was demonstrated in Fig. 4.18. Thus the additional electrons appearing during stronger ablation of targets significantly influence the QPM conditions.

The spectral analysis of the shape of QPM harmonic beam and its divergence showed the possibility of the tight focusing of this radiation on various materials, which is the main requirement for the XUV-induced modification and analysis of those species. It is reasonable to directly compare the spatial shapes of the QPM and non-QPM harmonics with that of the driving beam. The difference in the divergences of the former beams proves the usefulness of the developed QPM concept for the focusing of those harmonics in a tiny spot to create a high fluence on the surface under study.

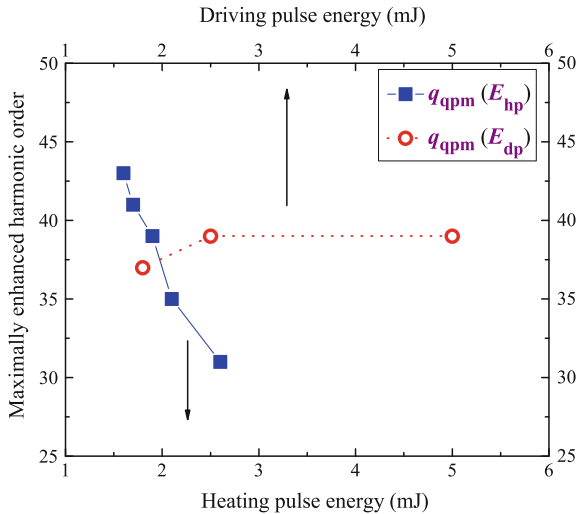


Fig. 4.18 Variations of maximally enhanced harmonic order at different energies of heating (*filled squares*) and driving (*empty circles*) pulses. One can see that the three-fold growth of driving pulse energy (from 1.85 to 5 mJ) did not significantly change the q_{qpm} . In the meantime, the q_{qpm} was strongly dependent on the variation of the heating pulse energy. *Solid and dotted lines* are inserted for better viewing of the influence of heating and driving pulse energies on the QPM conditions. Reproduced from [39] with permission from American Physical Society. Copyright 2015

Below we present the analysis of the spatial characteristics of the high-order harmonics generated in the extended and multi-jet Mn and Ag plasmas produced by the 370 ps pulses. In the case of imperforated manganese plasma, a few harmonics were selected in the second plateau range using the metal filters and then defined the shape of those harmonics using the MCP. To select a few harmonics, the 650-nm-thick aluminum and 150-nm-thick titanium filters were installed in front of the MCP (see also Chap. 3). The short-wavelength transmission edge of Al filter is ~ 17.4 nm, while the long-wavelength transmission edge of Ti filter is ~ 22 nm. Simultaneous application of those two filters allowed separation of the harmonics generated in the spectral range of ~ 18 to 20 nm.

These few harmonics ranging between the 39th and 45th orders were directly viewed by the MCP by removing the cylindrical mirror from the path of driving beam and harmonics (Fig. 4.19a). The spatial shape of those harmonics is shown in the left inset of Fig. 4.19a. The right inset in this figure shows the background emission observed in the case of using the circularly polarized driving radiation when the quarter-wave plate was inserted in the path of driving beam. In that case, no harmonics are expected to generate, which was confirmed by both the direct measurements of emission spectra and the spatial measurements of emitted radiation. The spatial distribution of the H39–H45 beams along the vertical axis (Z) is shown in Fig. 4.19a. The divergence of the harmonic beam generated in the imperforated Mn plasma was decreased with a factor of ~ 5 compared with the divergence of the fundamental radiation. This decrease of divergence was attributed to the preferential involvement of the short trajectory of accelerated electron in the harmonic generation.

Similar arrangements were used for the analysis of the spatial characteristics of the QPM-enhanced harmonics generated in the multi-jet silver plasma. A few orders (Fig. 4.19b, thick curve) from the group of QPM-enhanced harmonics (Fig. 5.20b, thin curve) were selected using the single (Ti) filter, which allowed the definition of the shapes of selected H41–H47 beams using the MCP. The spatial distribution of those harmonics is shown in the Fig. 4.19c (thick curve). Here also shown the spatial distribution of the same harmonics generated from the extended imperforated silver plasma (thin curve) and the spatial distribution of 802 nm radiation on the plane of MCP (dotted curve). The homogeneous 9.2 nm emission of the lanthanum plasma is also presented for comparison. These studies of the spatial shapes of harmonics at different conditions of generation showed that the QPM-enhanced harmonics in the 17–19 nm range possess smallest divergence. This divergence was 11 times lower than the one of the driving radiation, thus showing the excellent properties of this coherent XUV radiation for the tight focusing.

To further prove the role of QPM in the observed peculiarities of harmonic spectra the intensity (I_H) of harmonics was investigated as a function of the number of plasma jets. This experiment was aimed to confirm the involvement of the coherent accumulation of harmonic yield along the whole length of divided non-linear optical medium and to find the limitations of this approach. The heating zones on the target surface were shielded step-by-step to create different number of plasma jets (from single-jet to eight-jet formations). Figure 4.20a shows the results

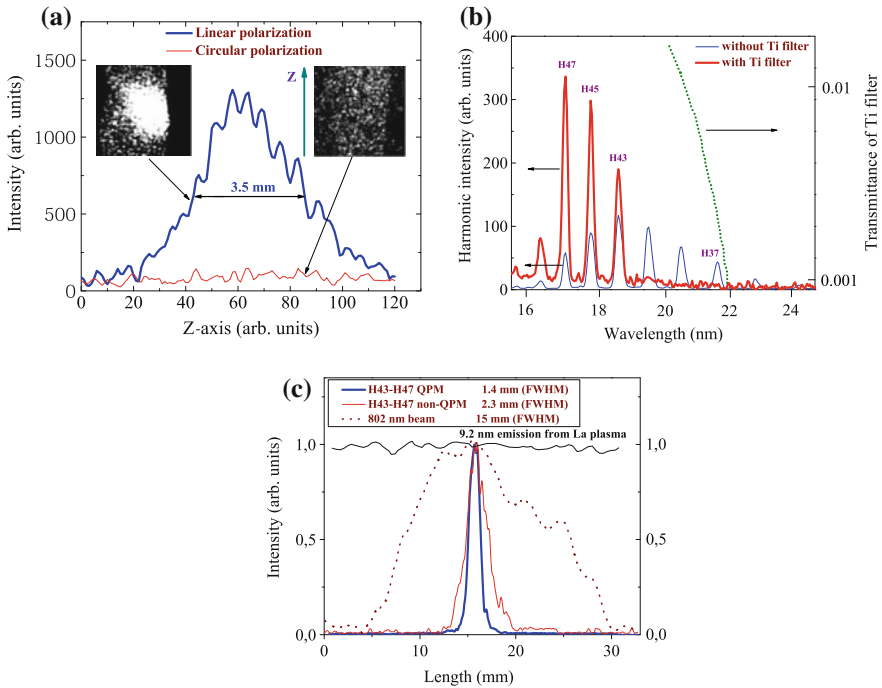


Fig. 4.19 **a** Spatial distributions of the 39th–45th harmonics in the case of linearly polarized driving beam (*thick curve*) and of the plasma emission in the case of circularly polarized driving beam (*thin curve*). *Left inset* raw image of the harmonic beam obtained in the case of linearly polarized driving pulse. *Right inset* raw image of XUV emission in the case of circularly polarized driving pulse. **b** Harmonic spectrum generated in the multi-jet silver plasma in the range of 16–24 nm (*thin curve*) and part of the same spectrum after propagation through the Ti thin film filter (*thick curve*). *Dotted curve* shows the transmittance of Ti filter. **c** Shapes of H43–H47 in the cases of harmonic generation in the multi-jet plasma (*thick curve*) and in the extended imperforated plasma (*thin curve*). *Dotted curve* shows the shape of driving beam on the MCP plane. Here also shown the homogeneous distribution of the 9.2 nm emission obtained from the lanthanum plasma

of these measurements carried out using similar fluence of the heating pulse on the target surface. Note the equal Y axes of those spectra, which allow to directly compare the variations of the spectral shape of harmonic distribution using different contributing zones and to demonstrate the growth of QPM-enhanced harmonics during the addition of plasma jets.

The anticipated featureless shape of harmonic spectrum from the single 0.3-mm-long plasma jet was similar to that observed in the case of 5-mm-long plasma (compare the upper and bottom panels of Fig. 4.20a). With the addition of each next jet, starting from the three-jet structure, the spectral envelope has been drastically changed, with the 43rd harmonic intensity in the case of three-jet configuration becoming almost 8 times higher compared with the case of single-jet

plasma. As it was mentioned earlier, one can anticipate the n^2 growth of harmonic yield for the n -jet configuration compared with the single jet once the phase mismatch becomes suppressed, which gives the expected growth factor of 9 in the case of three-jet medium. While this rule was, to some extent, maintained for the QPM-enhanced harmonics, the $I_H \propto n^2$ dependence was not fulfilled, as expected, for the lower-order harmonics (see also Sect. 4.1).

Note that the maximum enhancement factor in the QPM region may deviate from the $I_H \propto n^2$ dependence at the conditions when absorption processes are turned on, or in the case of unequal properties of the jets, which can arise from the heterogeneous excitation of the extended target. Another reason of the deviation from the quadratic rule could be the influence of the driving pulse on the variation of phase relations in the case of a larger amount of contributing zones. These assumptions were proved by further addition of jets. The fourth jet still allowed the observation of significant enhancement, while other jets (from jet No. 5 to jet No. 8) did not contribute properly and did not allow the anticipated 64-fold enhancement of the harmonic yield for the phase-matched orders compared with the case of single jet. Moreover, one can see that the q_{qpm} was slightly tuned towards the longer wavelength range (from H43 to H39) in the case of larger amount of jets. Some

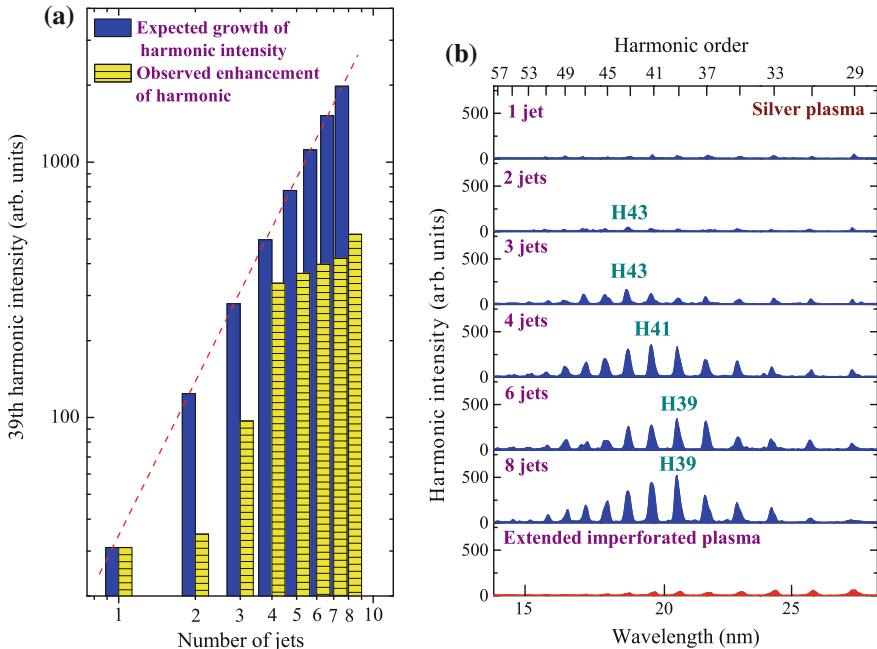


Fig. 4.20 **a** Harmonic spectra generated in the multi-jet silver plasma using different number of jets. *Bottom panel* shows the harmonic emission generated in the extended imperforated plasma. **b** Observed and anticipated enhancements of the 39th harmonic with the growth of the number of plasma jets. *Dashed line* corresponds to the slope 2

broadening of the envelope of QPM-enhanced harmonics was observed with the growth of the number of contributing zones, which also points out a decrease of selectivity induced by above-mentioned reasons. Figure 4.20b summarizes the observed and expected enhancements of the 39th harmonic with the growth of the number of contributing plasma jets. The experimentally obtained enhancement of this QPM harmonic falls short compared to the expected slope of two for this dependence.

4.6 Concluding Comments

We have discussed the new approach in plasma HHG allowing the enhancement of a group of harmonics through the involvement of the macroprocesses. The method of QPM of the high-order harmonics generating in the multiple plasma jets produced on the surfaces of perforated silver, vanadium, and manganese targets was demonstrated for the first time. The $20\times$ and $30\times$ enhancement factors of QPM harmonics in the cases of silver and vanadium plasmas were achieved. This technique allowed the manipulation of the phases of interacting waves in the laser-produced plasmas and the enhancement of a group of harmonics in different spectral ranges.

We have also presented the analysis of the harmonic generation in the long (~ 5 mm) plasma plumes divided onto a set of small jets using the modulation of the heating beam on the target surface. We have shown both the QPM induced enhancement of some groups of harmonics along the plateau range and the tuning of maximally enhanced harmonic order at different regimes of multi-jet plasma formation. The tuning of QPM enhanced harmonics was accomplished by changing the sizes of multiple plasma jets. The enhancement factors for the QPM enhanced harmonics up to $40\times$ were achieved in some multi-jet plasmas. We have shown the potential of the proposed plasma harmonic QPM approach for the express analysis of the plasma characteristics.

Further, we have analyzed the QPM induced variations of harmonic spectra in the case of the two-color pump of perforated plasma formations. This effect was observed in the Ag and Cr plasmas. In the latter case the joint influence of QPM and resonance enhancement allowed observation of harmonic selection caused by the former process rather than the resonance-induced microprocess. The enhancement factor for the 33rd harmonic generated using single-color pump in the multi-jet configuration, compared with the line silver plasma of the equivalent length, was ~ 13 . In the case of two-color pump, the enhancement factor of 28th harmonic was ~ 25 in the five-jet configuration compared with the same harmonic generating in the extended silver plasma. We have analyzed two cases of second harmonic sources using thinner (0.3 mm) and thicker (0.5 mm) BBO crystals; however, the difference between them was not explicitly seen as compared with longer BBO crystals. The application of thinner crystal was advantageous from the point of view of lesser delay between the pump pulses in the plasma area thus allowing the

achievement of the favorable conditions for the formation of the group of enhanced harmonics.

Finally, we have discussed the influence of driving and heating pulse energies on the enhancement of QPM harmonics, analyzed the spatial characteristics of a few harmonics in the region below 20 nm produced in the extended perforated and multi-jet plasmas, showed the fine tuning of those enhanced harmonics by tilting the multi-slit mask placed in front of the Ag and Mn targets, analyzed the enhancement factors of harmonics in different spectral ranges, demonstrated the small divergence of QPM-enhanced harmonics compared with larger divergence and modulated shape of the “ordinary” harmonics generated in the extended plasmas, etc.

Overall, the use of single-color pump has shown more explicitly formed group of enhanced harmonics compared with the case of two-color pump. This result can be explained by more sophisticated conditions of HHG in the presence of second wave, insufficient phase matching, and difference in the characteristics of fundamental and second harmonic radiation.

References

1. J. Seres, V.S. Yakovlev, E. Seres, C.H. Strel, P. Wobrauschek, C.H. Spielmann, F. Krausz, *Nature Phys.* **3**, 878 (2007)
2. A. Pirri, C. Corsi, M. Bellini, *Phys. Rev. A* **78**, 011801 (2008)
3. V. Tosa, V.S. Yakovlev, F. Krausz, *New J. Phys.* **10**, 025016 (2008)
4. T. Fok, Ł. Węgrzyński, M. Kozłova, J. Nejd, P.W. Wachulak, R. Jarocki, A. Bartnik, H. Fiedorowicz, *Photonics Lett. Poland* **6**, 14 (2014)
5. A.H. Sheinfux, Z. Henis, M. Levin, A. Zigler, *Appl. Phys. Lett.* **98**, 141110 (2011)
6. I.J. Kim, C.M. Kim, H.T. Kim, G.H. Lee, Y.S. Lee, J.Y. Park, D.J. Cho, C.H. Nam, *Phys. Rev. Lett.* **94**, 243901 (2005)
7. T. Pfeifer, L. Gallmann, M.J. Abel, D.M. Neumark, S.R. Leone, *Opt. Lett.* **31**, 975 (2006)
8. I.J. Kim, G.H. Lee, S.B. Park, Y.S. Lee, T.K. Kim, C.H. Nam, T. Mocek, K. Jakubczak, *Appl. Phys. Lett.* **92**, 021125 (2008)
9. E. Cormier, M. Lewenstein, *Eur. Phys. J. D* **12**, 227 (2000)
10. R.A. Ganeev, C. Hutchison, A. Zaïr, T. Witting, F. Frank, W.A. Okell, J.W.G. Tisch, J.P. Marangos, *Opt. Exp.* **20**, 90 (2012)
11. R.A. Ganeev, T. Witting, C. Hutchison, V.V. Strelkov, F. Frank, M. Castillejo, I. Lopez-Quintas, Z. Abdelrahman, J.W.G. Tisch, J.P. Marangos, *Phys. Rev. A* **88**, 033838 (2013)
12. K.J. Schafer, B. Yang, L.F. DiMauro, K.C. Kulander, *Phys. Rev. Lett.* **70**, 1599 (1993)
13. P.B. Corkum, *Phys. Rev. Lett.* **71**, 1994 (1993)
14. M. Lewenstein, P. Balcou, M.Y. Ivanov, A. L’Huillier, P. Corkum, *Phys. Rev. A* **49**, 2117 (1994)
15. R.A. Ganeev, *High-Order Harmonic Generation in Laser Plasma Plumes* (Imperial College Press, London, 2012)
16. R.A. Ganeev, M. Suzuki, H. Kuroda, *JETP Lett.* **99**, 368 (2014)
17. T. Augustine, B. Carré, P. Salières, *Phys. Rev. A* **76**, 011802 (2007)
18. X. Zhang, A.L. Lytle, T. Popmintchev, X. Zhou, H.C. Kaptayn, M.M. Murnane, O. Cohen, *Nature Phys.* **3**, 270 (2007)

19. R.A. Ganeev, M. Baba, M. Suzuki, H. Kuroda, *Phys. Lett. A* **339**, 103 (2005)
20. A.V. Andreev, R.A. Ganeev, H. Kuroda, S.Y. Stremoukhov, O.A. Shoutova, *Eur. Phys. J. D* **67**, 22 (2013)
21. K. O'Keeffe, T. Robinson, S.M. Hooker, *Opt. Exp.* **20**, 6236 (2012)
22. A.L. Lytle, X. Zhang, R.L. Sandberg, O. Cohen, H.C. Kapteyn, M.M. Murnane, *Opt. Exp.* **16**, 6544 (2008)
23. R.A. Ganeev, L.B. Elouga Bom, J.-C. Kieffer, T. Ozaki, *Phys. Rev. A* **76**, 023831 (2007)
24. L. B. Elouga Bom, J.-C. Kieffer, R.A. Ganeev, M. Suzuki, H. Kuroda, T. Ozaki, *Phys. Rev. A* **75**, 033804 (2007)
25. R.A. Ganeev, H. Singhal, P.A. Naik, U. Chakravarty, V. Arora, J.A. Chakera, R.A. Khan, M. Raghuramaiah, S.R. Kumbhare, R.P. Kushwaha, P.D. Gupta, *Appl. Phys. B* **87**, 243 (2007)
26. T. Ozaki, L.B. Elouga Bom, R. Ganeev, J.-C. Kieffer, M. Suzuki, H. Kuroda, *Laser Part. Beams* **25**, 321 (2007)
27. R.A. Ganeev, M. Suzuki, P.V. Redkin, H. Kuroda, *J. Nonlin. Opt. Phys. Mater.* **23**, 1450013 (2014)
28. C. Kan, N.H. Burnett, C. Capjack, R. Rankin, *Phys. Rev. Lett.* **79**, 2971 (1997)
29. R.A. Ganeev, M. Suzuki, H. Kuroda, *Phys. Rev. A* **89**, 033821 (2014)
30. R.A. Ganeev, M. Suzuki, H. Kuroda, *J. Phys. B: At. Mol. Opt. Phys.* **47**, 105401 (2014)
31. R.A. Ganeev, M. Suzuki, M. Baba, H. Kuroda, *Appl. Phys. Lett.* **86**, 131116 (2005)
32. R.A. Ganeev, M. Suzuki, S. Yoneya, H. Kuroda, *Laser Phys.* **24**, 115405 (2014)
33. J. Stadler, R. Mikulla, H.-R. Trebin, *Int. J. Mod. Phys.* **8**, 1131 (1997)
34. R.A. Ganeev, C. Hutchison, T. Witting, F. Frank, W.A. Okell, A. Zaïr, S. Weber, P.V. Redkin, D.Y. Lei, T. Roschuk, S.A. Maier, I. López-Quintás, M. Martín, M. Castillejo, J.W.G. Tisch, J.P. Marangos, *J. Phys. B: At. Mol. Opt. Phys.* **45**, 165402 (2012)
35. A. Castro, H. Appel, M. Oliveira, C.A. Rozzi, X. Andrade, F. Lorenzen, M.A.L. Marques, E.K.U. Gross, A. Rubio, *Phys. Stat. Sol. (b)* **243**, 2465 (2006)
36. N. Kortsalioudakis, M. Tatarakis, N. Vakakis, S.D. Moustazis, M. Franco, B. Prade, A. Mysyrowicz, N.A. Papadogiannis, A. Couairon, S. Tzortzakis, *Appl. Phys. B* **80**, 211 (2005)
37. A. Paul, R.A. Bartels, R. Tobey, H. Green, S. Weiman, I.P. Christov, M.M. Murnane, H.C. Kapteyn, S. Backus, *Nature* **421**, 51 (2003)
38. L. Zheng, X. Chen, S. Tang, R. Li, *Opt. Exp.* **15**, 17985 (2007)
39. R.A. Ganeev, V. Tosa, K. Kovács, M. Suzuki, S. Yoneya, H. Kuroda, *Phys. Rev. A* **91**, 043823 (2015)

Chapter 5

Peculiarities of the HHG in the Extended Plasmas Produced on the Surfaces of Different Materials

The metals were among mostly used targets for laser ablation and HHG, while only in a few cases the crystals and semiconductor compounds being studied using this approach. In the meantime, the non-metal species could be the attractive media being ablated for harmonic generation. In this chapter, we discuss recent HHG studies in the extended plasma plumes produced on the surfaces of various non-metal materials (elemental semiconductors, oxygen- and fluorine-contained crystals, and carbon-contained clusters). We acquaint the reader with the attractive properties of those plasmas. We analyze the optimization of HHG in the extended plasma plumes using different approaches.

The application of various materials for high-order harmonic generation in the extreme ultraviolet region during propagation of the femtosecond pulses through the laser plasmas produced on the surfaces of those species may reveal the attractive features related with the specific properties of the elemental components of materials. This approach in the studies of the nonlinear optical properties of metal-based plasmas has been developed in the 1990s [1–6] and currently is applied for the analysis of the characteristics of various solids [7]. The metals were among mostly used targets for laser ablation and HHG [8–11], while only in a few cases the crystals (such as LiF [6]) and semiconductor compounds (such as GaAs and InSb [12, 13]) were studied using this approach.

In the meantime, the non-metal species could be the attractive media being ablated for harmonic generation. Particularly, laser ablation induced HHG spectroscopy of semiconductors can reveal the resonance-induced enhancement of some harmonic orders in the XUV as well as the cluster-induced growth of harmonic yield. The latter assumption has been demonstrated in [14] where third and fifth harmonic generation of an IR (1064 nm) pulsed laser has been studied in ablation plasmas of the wide bandgap compounds CdS and ZnS. The study of the temporal behavior of the harmonic emission has revealed the presence of distinct compositional populations in these complex plasmas. Species ranging from atoms to nanometer-sized particles have been identified as emitters, and their nonlinear optical properties were studied separately due to strongly differing temporal behavior. It was found that, at short distances from the target, atomic species are mostly responsible for harmonic generation at early times from the beginning of ablation (<500 ns), while clusters mostly contribute at longer times (>1 μ s).

Harmonic generation thus emerges as a powerful and universal technique for ablation plasma diagnosis and as a tool to determine the nonlinear optical susceptibility of ejected semiconductor clusters or nanoparticles.

Such plasmas may contain ions with the transitions near the wavelengths of those harmonics. Thus, the resonance-induced growth of single harmonic could be realized in the plasma particles produced during laser ablation of semiconductors. Other methods of harmonic enhancement from the plasmas include the application of extended media and two-color pump. Most of previous HHG studies were carried out using the narrow plasmas ($L \leq 0.5$ mm). In the meantime, recent studies have revealed the usefulness of the application of the longer plasma media for efficient harmonic generation [15]. One has to maintain the extended plasma formation at the conditions when the length of nonlinear optical medium does not exceed the coherence length of harmonics. To resolve the phase mismatch problem one can use the quasi-phase-matching of harmonics by division of extended medium onto the group of separated plasma jets.

Crystals restrict high-order harmonic generation of ultrafast laser pulses due to the strong absorption beyond the bandgap edge. Even using a long-wavelength laser radiation, only limited harmonic orders are expected to be generated without the strong absorption inside the solids. In the strong-field limit, harmonic generation in bulk crystals is fundamentally different from that in the atomic case owing to the high density and periodic structure. The first observation of HHG in a bulk crystalline solid using a long-wavelength few-cycle laser was reported in [16]. The harmonics spectra were extended beyond the band edge of the ZnO crystal, showed a clear nonperturbative character, and exhibited a cutoff that scales linearly with the electric field of the driving laser. It was shown that the efficiency is limited by phase velocity mismatch for emission below the bandgap and by absorption above the bandgap of solids. Thus the limitation based on the absorption of short-wavelength light above the bandgap edge of solids becomes a main restricting factor in the HHG studies in crystals. To overcome this problem, one has to considerably reduce the concentration of the medium, particularly using a laser ablation technique. The only study of the ablation of dielectric crystal (LiF) and HHG in plasma has been reported almost 20 years ago [6] with the maximal 19th harmonic generated using a 248 nm laser.

Various approaches have been proposed to increase the conversion efficiency (η) of the HHG of laser radiation in the extreme ultraviolet. One of approaches is the application of the QPM conditions using the gas multi-jets or modulated waveguides and counter propagating beams. Another strategy to improve η is the consideration of the microscopic processes related with the response of single atoms or ions. The involvement of the resonance processes in the enhancement of the nonlinear optical response of the gaseous medium has been analyzed in [17–22]. However, the limited number of gaseous media did not allow the practical application of this effect for the HHG in the XUV. Alternatively, it was found that the laser plasmas could be considered as the suitable media, where the resonances can enhance the nonlinear optical response for a single harmonic [23].

The additional method that has also been explored to increase the η of HHG is the use of clusters as the nonlinear media. The harmonic enhancement using the gaseous clusters was reported in [24–26]. The increase of η was attributed to the growth of the concentration of emitters and the specific properties of clusters. The cross-section of recombination of the accelerated electron with the parent particle in the case of clusters is higher compared with the atoms [27]. In the meantime, the uncertainty in the exact mechanism of the HHG from clusters has previously been underlined in a few studies [27–29]. Among additional mechanisms, the ionization and recombination to the same ion, to the neighboring ions, and to the whole nanoparticle have been proposed. The experiments with gas clusters have revealed some difficulties in disentangling the harmonics produced by different species (monomers and clusters of different sizes). One has to note that the comparative studies of HHG in the plasmas consisted of clusters and monomers showed that, at equal experimental conditions, the latter emitters provide considerably weaker harmonic yield, thus pointing out the advanced properties of the clustered emitters of harmonics in the nanoparticle-contained plasmas [23]. Recently, it became possible to generate the laser plasma containing a large amount of nanoparticles. The enhancement of harmonics in the metal nanoparticle plasmas has been achieved in various laboratories [30–33].

In the meantime, the plasmas formed on the surfaces of non-metal bulk targets (such as graphite and carbon-contained materials) have demonstrated the relatively high η for the lower-order harmonics compared with the harmonics generated in the gases. The stronger harmonics from the graphite plasma compared with the argon gas were reported in [34, 35]. It was assumed that the laser ablation induced nanoparticle formation led to the enhancement of harmonic radiation from the graphite plasma. In this connection, the laser ablation of carbon-contained clusters has been intensively examined to define the optimal conditions of HHG in the cases of fullerenes [36, 37]. These studies point out the opportunity in formation of the clustered plasma in the case of ablation of the non-metal targets.

In this chapter, we discuss recent HHG studies in the extended plasma plumes produced on the surfaces of various non-metal materials (elemental semiconductors, oxygen- and fluorine-contained crystals, and carbon-contained clusters). We acquaint the reader with the attractive properties of those plasmas. We analyze the optimization of HHG in the extended plasma plumes using different approaches.

5.1 Harmonic Generation in the Plasmas Produced on the 5-mm-Long Crystal Surfaces

The experimental arrangements were similar for these three sets of the high-order nonlinear optical studies of crystal-, semiconductor-, and carbon cluster-base extended plasma plumes. In this section, we discuss the HHG in the plasmas produced on the crystals. The scheme was almost identical to the one described in Chap. 3. The uncompressed radiation of a Ti:sapphire laser (central wavelength

802 nm, pulse duration 370 ps, pulse energy up to $E_{hp} = 6$ mJ, 10 Hz pulse repetition rate) was used for the extended plasma formation on the 5-mm-long targets. The plasma sizes were 5 mm \times 0.08 mm. The driving compressed pulse (the energy up to $E_{dp} = 3$ mJ and 64 fs pulse duration) was used, after 35 ns delay from the beginning of ablation, for harmonic generation in the long plasma plume. The plasma and harmonic emissions were analyzed using the XUV spectrometer (see Sect. 3.1 describing the details of registration of the short-wavelength radiation). The use of the unpolished surfaces of crystals allowed the decrease of the threshold of optical damage and the increase of the absorption of the heating pulses, thus allowing the formation of plasma above the target surfaces using moderate fluences of the heating pulses (≤ 1 J cm $^{-2}$). The sizes of crystals where the ablation occurred were 5 mm.

Two groups of crystals were analyzed based on the common elements presented in the group, F-containing crystals (NaF, CaF $_2$, LiF, and MgF $_2$) and O-containing crystals (KTiOPO $_4$, BaB $_2$ O $_4$, KH $_2$ PO $_4$, and LiB $_3$ O $_5$). Below, we discuss the results of plasma and harmonic studies from the ablations of these two groups of targets [38].

The laser ablation of those crystals was studied in a number of works [39–50]. Particularly, ablation of CaF $_2$, BaF $_2$, LiF, and MgF $_2$ subjected to single-shot irradiation with 248 nm/14 ns laser pulses has been investigated in [46]. The appearance of damage followed with the formation of the plasma containing fluorine ions during the next shots on the same place. In [50], the ion emission characteristics were investigated using CaF $_2$ crystals. The emission of F $^-$ ions was confirmed by using a mass spectrometer. The analysis of laser ablation of CaF $_2$ [39, 41, 47] has shown that the plasma constitutes Ca, F, and CaF atoms, ions, and molecules.

Note that those and other ablation studies were not aimed in the formation of the so called “optimal plasma” suitable for HHG, in which the components of the medium may differ from the plasma produced during strong ablation of the targets. The analysis of the plasma emission spectra of NaF, CaF $_2$, MgF $_2$, and LiF have demonstrated a similarity in the spectra emitted from the optimal plasma. One has to take into account that the plasma formation at these conditions was similar to those used for the most efficient HHG in the crystal plasmas. It means that the conditions of plasma formation in this case were other than those analyzed in previous studies of laser ablation of the crystal species. In the latter cases, the formation of a large amount of free electrons, which is the main factor leading to some impeding processes restricting HHG, was not taken into account.

Figure 5.1 shows the plasma spectra in the XUV range obtained at the “optimal ablation” of these four crystals. This term refers to the conditions of ablation corresponding to the most efficient harmonic generation from those plasma plumes. These spectra were obtained during ablation of the crystals by the 370 ps radiation, without the propagation of the femtosecond pulses through the plasma plume. Each of these spectra was produced using two fluences of the heating pulse (0.3 and 0.7 J cm $^{-2}$), both leading to formation of the plasma suitable for the harmonic generation during propagation of the 64 fs pulses. One can see the similarity of

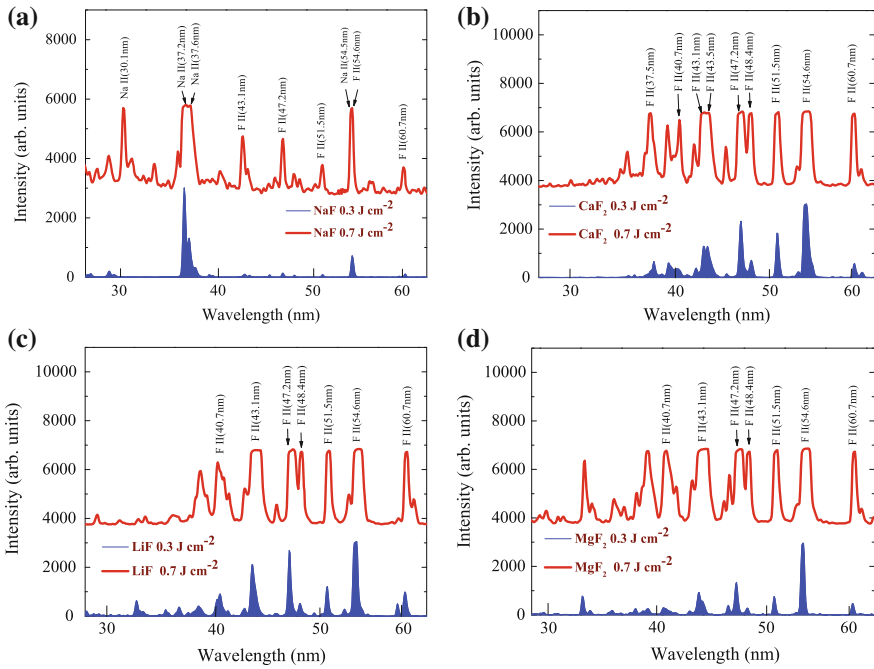


Fig. 5.1 Plasma emission spectra of the ablated F-containing crystals (**a** NaF; **b** CaF₂; **c** LiF; **d** MgF₂) at 0.3 (filled blue curves) and 0.7 J cm⁻² (thick red curves) fluences of heating pulses. The latter curves are shifted vertically for better visibility. Reproduced from [38] with permission from Optical Society of America

most spectral lines, which were assigned to the transitions of F II. Some other strong lines from these plasmas were attributed to the Na and Li singly charged ions.

The common feature of all plasma spectra from these ablated crystals was the presence of strong emission lines at 40.7, 43.1, 43.5, 47.2, 48.4, 51.5, 54.6, and 60.7 nm, which are the transitions of singly charged fluorine [51]. The similarity in the plasma spectra from the ablation of NaF, CaF₂, MgF₂, and LiF crystals points out the involvement of similar species in the formation of harmonic spectra. The presence of plasma emission was observed alongside the harmonic generation during propagation of ultrashort laser pulses through these plasmas (Fig. 5.2a). The harmonic cut-offs from these plasmas were approximately similar to each other (59th, 55th, 57th, and 55th harmonics in the cases of NaF, CaF₂, MgF₂, and LiF plasmas, respectively). These observations allow suggesting the involvement of the same component of those plasmas in the generation of higher-order harmonics. Moreover, the appearance of strong ionic lines of F also points out on the role of singly charged fluorine ions as the emitters of harmonics in the short-wavelength range.

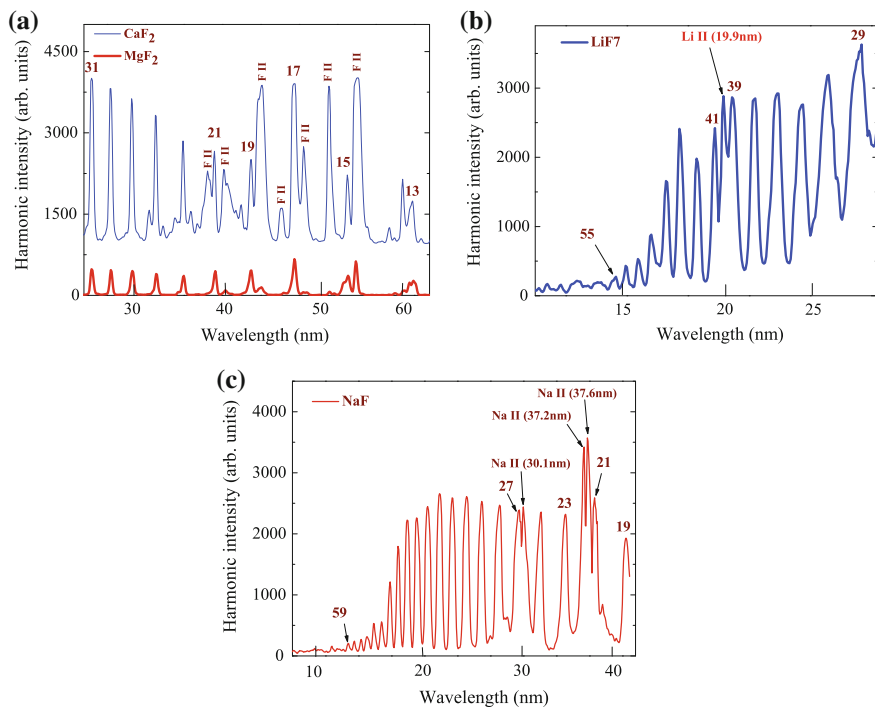


Fig. 5.2 a Low- and b, c high-order harmonic spectra obtained during propagation of the femtosecond pulses through the plasmas produced on the surfaces of F-containing crystals. The curve of plasma spectrum from CaF₂ ablation is vertically shifted for better visibility. Reproduced from [38] with permission from Optical Society of America

The HHG was optimized by different means, particularly using different delays between pulses, target excitation, plasma density, and so forth. The common feature of the observed spectra was the generation of harmonics in the range of 50s orders (Fig. 5.2b, c). Most efficient HHG was observed in the case of the ablation of CaF₂ crystal. A few emission lines of fluorine were also presented in these spectra alongside the harmonic emission. The harmonic cut-offs were well suited with the estimates based on the three-step model of HHG [52–54], barrier suppression intensity for singly ionized fluorine, and second ionization potential of fluorine (32.5 eV).

One should not rule out the involvement of the NaF, CaF₂, MgF₂, and LiF molecules in the process of harmonic generation. However, the first ionization potentials of these neutral molecules point out that they can be involved only in the lower-order harmonic generation. The ionization potentials of NaF, LiF, CaF₂, and MgF₂ are 9.8, 10.0, 8.7, and 7.8 eV, respectively. The corresponding cut-offs from these molecules do not exceed the 30 s harmonics. So the assumption of the involvement of the above molecules could be true for the lower-order harmonics, while in the case of generation of higher-order harmonics the role of singly charged ions of fluorine could be decisive.

All O-containing samples (KTiOPO_4 , BaB_2O_4 , KH_2PO_4 , and LiB_3O_5) are dubbed as the nonlinear crystals (correspondingly, KTP, BBO, KDP, and LBO). Investigation of the plasma parameters can give information about the plasma components of the above crystals. In the discussed studies, the goal was to analyze the high-order nonlinear optical properties of the ablated particles of these nonlinear optical crystals. Similarly to F-containing species, the ablation of O-containing crystals was analyzed using different fluences of heating pulses. Thin curves in Fig. 5.3 show the incoherent emission spectra from four crystals during ablation of their surfaces at the 0.9 J cm^{-2} fluence of a 370 ps pulse. The coincidence of most spectral lines observed during ablation of these crystals points out the involvement of the same emitter in these cases. These plasma emission lines were mostly attributed to the singly ionized oxygen. One can assume that, similarly to F-containing crystals, the presence of O II in the plasmas can cause similar harmonic spectra.

In the meantime, the harmonic spectra from the ablation of the O-containing crystals at the optimal fluence (0.6 J cm^{-2}) have demonstrated a difference in the highest generated harmonic orders. The harmonic cut-offs were varied between the

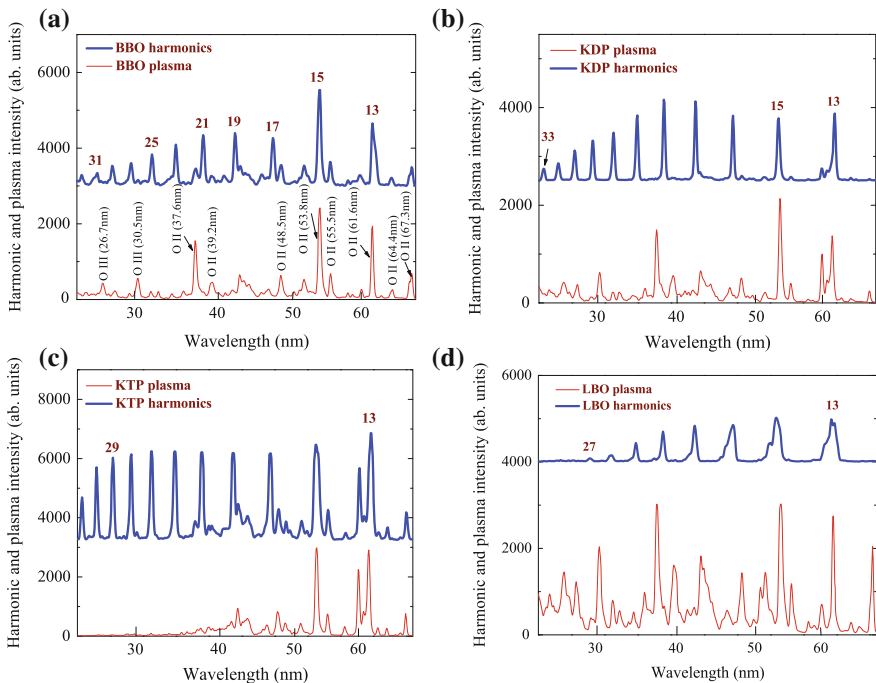


Fig. 5.3 Plasma emission spectra of the ablated O-containing crystals at 0.9 J cm^{-2} fluence (*thin curves*). Harmonic spectra obtained during propagation of the femtosecond pulses through the plasmas produced on the surfaces of O-containing crystals at a fluence of 0.6 J cm^{-2} (*thick curves*). The thick curves are vertically shifted for better visibility. Reproduced from [38] with permission from Optical Society of America

27th (in the case of LBO) and 39th (in the case of KTP) orders (Fig. 5.3, thick curves). The analysis of harmonic cut-offs from the singly ionized oxygen using the three-step model formula showed the harmonic generation up to the 41st order at the conditions when the restricting processes in the plasmas play an insignificant role. The intensity of harmonics was weaker compared with the case of F-containing crystals. In some cases, the strong ionic transitions coincided with the harmonics (see the coincidence of the 13th harmonic, $\lambda = 61.69$ nm, and $2s^2p^4(^3P) 3s^2P_{3/2} - 2s^2p^3D_{5/2}$ transition of the O II, $\lambda = 61.63$ nm, as well as of the 15th harmonic, $\lambda = 53.47$ nm, and $2s^2p^4(^3P) 3s^2P_{1/2} - 2s^2p^3D_{3/2}$ transition of the O II, $\lambda = 53.78$ nm [51]). This coincidence did not change the 13th and 15th harmonic yields, thus pointing out the insignificant influence of those transitions on the nonlinear optical micro- and macro-processes in the plasma medium.

The analysis of the observed plasma and harmonic emission from the ablation of crystals also included the studies of various factors influencing the HHG in those plasma media. Among the most important factors of this process are the length of plasma, delay between heating and driving pulses, heating pulse energy and fluence, and distance between the crystal and propagating femtosecond pulse.

These studies were carried out using the extended plasma plumes ($L = 5$ mm), contrary to most previous studies of plasma harmonics in which the narrow plasmas ($L \leq 0.5$ mm) were used as the nonlinear media. One can estimate the beginning of the restricting factors by analyzing the harmonic intensity dependence $I_H(L)$, which should follow the quadratic rule until the phase mismatch and absorption start to play a significant role. The studies of crystal ablation showed a weak increase and further decrease of the conversion efficiency of plasma harmonics in the case of the growth of plasma length, probably due to absorption and/or phase mismatch. Note that in most cases of the ablation of metal targets the application of extended plasma allowed a significant enhancement of harmonic yield compared with the short-length plasma [15] (see also Chap. 3).

The delay between heating and driving pulses (Δt) is crucial for optimization of the harmonic generation in the plasma plumes. At the initial stages of plasma formation and spreading out of the crystal surface, the concentration of particles (atoms, molecules, and singly charged ions) is insufficient, since the particles possessing $\sim 8 \times 10^3$ m s⁻¹ velocities cannot reach the optical axis of propagation of the driving beam (150 μ m above the target surface) during a few nanoseconds. The increase of delay allowed the appearance of plasma particles along the path of the driving pulse, which led to the growth of harmonic yield from crystal plasma. Further growth of delay led to the saturation of harmonic generation at 30 ns and the gradual decrease of $I_H(\Delta t)$ dependence at longer delays ($\Delta t > 70$ ns).

The growth of heating pulse energy on the crystal surface increased the plasma concentration, which in turn led to the growth of harmonic yield. In this connection, a fluence of the heating pulse on the crystal surface becomes an important parameter for optimization of the high-order harmonic emission. The dependences of the harmonic intensity on the energy of heating pulses on the surface of crystals were analyzed, while maintaining the same geometry of the extended ablation beam on the targets. The common feature of these measurements was an observation of

the maximum of the $I_H(E_{\text{hp}})$ dependence (at $E_{\text{hp}} \approx 4$ mJ) with the following saturation and a decrease of harmonic yield during ablation of the crystals using stronger heating pulses. The reason for these observations is related with the abundance of free electrons in the extended plasma plume. As it was already mentioned, a large amount of free electrons leads to the phase mismatch between driving and harmonic waves.

The influence of the distance between the crystals and the optical axis of propagation of the driving radiation was studied at a fixed delay between pulses (35 ns). This distance (d) was varied by a manipulator, which controlled the position of the crystals with regard to the waist of the driving femtosecond radiation. An abrupt decrease of harmonic yield was observed during the growth of d corresponding to the $I_H \propto 1/d^{1.5}$ dependence.

The analysis of above dependences allowed maximizing the harmonic yield from the crystal-ablated plasmas. The conversion efficiency of the 15th harmonic generating from the ablation of an F-containing crystal (CaF_2) was estimated to be 3×10^{-6} . The corresponding flux of 15th harmonic radiation was 2×10^9 photons per pulse.

5.2 Application of the Laser Plasmas Produced on the Extended Surfaces of Elemental Semiconductors

Below, we discuss the harmonic generation in other non-metal based plasma medium, elemental semiconductor ablation [55]. The experimental setup was similar to the one described in previous section. Here we describe the ablation of 5-mm-long tellurium, selenium, silicon, arsenic, antimony, and germanium targets. The analysis of $I_H(\Delta t)$, $I_H(E_{\text{hp}})$, $I_H(L)$, and $I_H(d)$ dependences allowed maximizing the harmonic yield from the plasmas produced on the surfaces of semiconductors. Different methods were applied for enhancement of the coherent XUV radiation generated in the semiconductor plasmas. Particularly, the presence of strong ionic lines was studied in the vicinity of some harmonics, alongside with the enhancement of those harmonics, contrary to the case of crystal ablation. Some of these results will be discussed below. During discussion of these results we present the studies of the resonance-induced growth of single harmonics at the optimal conditions of experiments. The term “optimal conditions”, as in above-described studies, refers to the experimentally defined maximal output of harmonics based on the analysis of above dependences. In the case of most semiconductor targets, the following parameters were used for achieving the maximal harmonic yield, the efficient resonance enhancement, and two-color pump induced odd and even harmonic generation in the extended plasmas: 35 ns delay between the heating and driving pulses, propagation of the driving pulse 100 μm above the target surface, 0.8 J cm^{-2} fluence of the heating pulse, $8 \times 10^{14} \text{ W cm}^{-2}$ intensity of the focused driving radiation, and 0.3-mm-long BBO crystal for the two-color pump.

Figure 5.4 shows the harmonic spectra obtained from the plasmas produced on the germanium, tellurium, and antimony targets. The Ge, Te, and Sb plasmas showed the enhanced 21st, 27th, and 21st harmonics, respectively, with the enhancement factors of $2\times$ – $3.5\times$ compared with the neighboring lower-order harmonics. Though the data about the ionic transitions involved in the enhancement of these harmonics are scarce, some conclusions could be drawn from the studies reported in [56–60].

The enhancement factor for the 21st harmonic generated in the 5-mm-long antimony plasma ($2\times$) was smaller compared with the case of narrower plasma plume. Previous studies of the 3-mm-long Sb plasma showed the $10\times$ growth of the 21st harmonic of 795 nm radiation compared with the 19th and 23rd orders [61]. The difference in the enhancement factors could be related with the use of different wavelengths of driving radiation (802 and 795 nm), which led to better conditions of enhancement in the latter case.

The strong Sb II transitions ($4d^{10}5s^25p^3P_2 - 4d^95s^25p^3(2D)^3D_3$ and $4d^{10}5s^25p^1D_2 - 4d^95s^25p^3(2D)^3F_3$) at the wavelengths of 37.82 and 37.55 nm could be responsible for the observed enhancement. The XUV spectra of antimony plasma

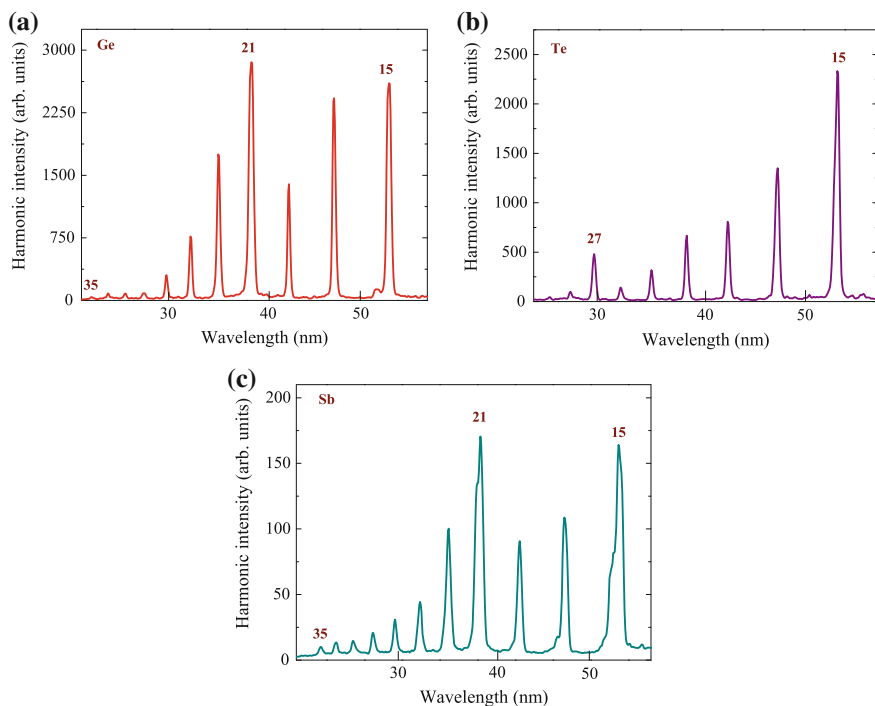


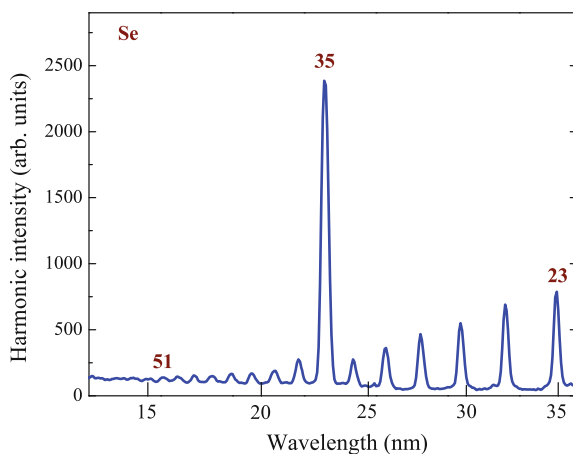
Fig. 5.4 Harmonic spectra obtained from the **a** Ge, **b** Te, and **c** Sb plasmas. These plasmas were produced using the 4 mJ, 370 ps pulses. The intensity of driving pulses was $8 \times 10^{14} \text{ W cm}^{-2}$. Reproduced with permission from [55]. Copyright 2014. AIP Publishing LLC

have been analyzed in [56]. The oscillator strengths of $4d^{10}5s^25p^3P_2 - 4d^95s^25p^3(^2D)^3D_3$ and $4d^{10}5s^25p^1D_2 - 4d^95s^25p^3(^2D)^3F_3$ transitions have been calculated to be 1.36 and 1.63, respectively, which were a few times larger than those of the neighboring transitions. The wavelength of 21st harmonic in discussed experiments (38.19 nm) was farther from above resonance transitions compared with the case of the 21st harmonic of 795 nm radiation (37.85 nm). This difference may lead to lesser influence of the resonance transitions on the nonlinear optical response of Sb plasma in the case of 802 nm pulses. The measurements of the 21st harmonic yield at different wavelengths of driving radiation, which were reported in [61], confirm the above assumption.

Discrete structures of plasma emission due to $4d \rightarrow 5p$ transitions of Te I–Te IV ions have previously been observed in the 37–45 eV range using the dual laser plasma technique [59]. The appearance of some ionic transitions in the region of ~ 42 eV, which correspond to the enhanced 27th harmonic generating in the tellurium plasma, has been shown in the theoretical calculations presented in [57], while their experimental data were reported only for the photon energies above 50 eV. It is not clear whether those transitions enhance the nonlinear optical response of tellurium plasma during propagation of the 802 nm pulses. The observations of enhanced 27th and neighboring even harmonics using both single-color and two-color pumps point out the influence of the group of transitions, rather than the single one, on the harmonic yield in the 29–32 nm spectral range.

Figure 5.5 shows the harmonic spectrum obtained from the selenium plasma. The enhancement factor of the single (35th) harmonic generated in the selenium plasma was considerably larger compared with the resonance enhancement in the Ge, Sb, and Te plasmas. It was twelve times stronger compared with the neighboring harmonics. This resonance-enhanced single harmonic has a shortest wavelength reported so far ($\lambda_{35H} = 22.91$ nm). The HHG experiments with circularly polarized femtosecond pulses did not reveal the strong emission in this spectral region.

Fig. 5.5 Harmonic spectrum obtained from the Se plasma. This plasma was produced using the 4 mJ, 370 ps pulses. The intensity of driving pulses was 8×10^{14} W cm $^{-2}$. Reproduced with permission from [55]. Copyright 2014. AIP Publishing LLC



The doubly ionized selenium atom has the ground configuration $4s^24p^2$ and the excited configurations $4s^4p^3$, $4s^24pnd$ ($n > 4$), and $4s^24pns$ ($n > 5$). The studies of doubly charged Se were reported in [62] with the shortest wavelength of 40 nm. The photoionization cross-section measurements for the Se II were reported in [60]. The photon energy studied in those experiments was ranged between 18.0 and 31.0 eV. However, they also reported the strong third-order line corresponded to the 54.62 eV energy without the deliberation of the origin of this transition. Note that this transition is close to the enhanced 35th harmonic ($h\nu = 54.11$ eV).

The studies of high-order nonlinear processes through exploitation of intermediate resonances show that the proximity of the wavelengths of specific harmonic orders and the strong emission lines of ions does not necessarily led to the growth of the yield of single harmonics. The response of the medium during propagation of intense pulse includes the resonance-induced enhancement of specific nonlinear optical processes, the absorption of emitted radiation, and the involvement of collective macro-processes, such as the phase-matching between the interacting waves [63]. The mechanism for improvement of the phase-matching conditions for the single harmonic in the described case can be interpreted as follows. The refractive index of plasma in the vicinity of some resonant transitions can be decreased due to anomalous dispersion thus allowing the coincidence of the refractive indices of plasma at the wavelengths of the driving and harmonic waves. To analyze this process in depth, one has to define (i) the bandwidths of those resonances, (ii) the relative role of the nonlinear enhancement of harmonic emission and the absorption properties of plasma in the vicinity of resonances, and (iii) the influence of plasma length on the enhancement of single harmonic.

The important goal of those studies of semiconductor plasma was the enhancement of harmonic yield by different means. Various approaches have previously been examined in the case of plasma harmonics to increase the conversion efficiency of coherent XUV radiation. Methods of harmonic enhancement from the plasmas, apart from resonance induced approach, include the application of two-color pump and quasi-phase-matching.

The application of additional field for the HHG in isotropic medium can considerably modify the generating spectrum. This assumption has been confirmed earlier during numerous two-color pump HHG experiments using gases and plasmas as the small-sized ($L = 0.3\text{--}0.5$ mm) nonlinear media (for example, [64, 65]). Those studies have revealed both the enhancement of harmonic yield and the generation of strong even harmonics, alongside the odd ones. The physical mechanism responsible for the observed enhancement of odd and even harmonics in the case of two-color pump at low ratios between the energies of second harmonic and fundamental pulses was attributed to the growth of ionization rate due to the influence of a weak shorter wavelength pump and the involvement of larger amount of accelerated electrons in harmonic generation. Below, we discuss the two-color pump of the extended (5-mm-long) plasmas produced on the semiconductor targets at the 95:5 ratio between the intensities of fundamental and second-harmonic waves [55].

Part of the driving pulse was converted in the nonlinear crystal (BBO, type I, crystal length 0.3 mm, 401 nm conversion efficiency 5 %) placed inside the vacuum chamber on the path of the focused driving beam. The BBO crystals of different thicknesses were also used for the analysis of HHG at different ratios of two pumps. Figure 5.6 shows the harmonic spectrum obtained from the extended Te plasma in the case of the two-color pump. One can distinguish the prevalence of even harmonics over the odd ones along the almost whole range of generation. The significant difference in the intensities of two pumps does not play important role in the case of extended plasma. The advanced properties of extended plasma were emphasized while comparing with the odd and even harmonics generated in the 0.5-mm-long tellurium plasma. In the latter case, the cut-off of even harmonics was significantly lower compared with the one of odd harmonics. Moreover, the intensity of even harmonics was three to four times smaller compared with the odd ones, contrary to the case of extended plasma.

The experiments at different delays between the pump pulses were conducted by using the BBO crystals of different length. The 0.02, 0.3, 0.5, 0.7, and 1.0 mm crystals were used for second harmonic generation. The group velocity dispersion in the BBO crystal leads to a temporal separation of two pulses. The 802 and 401 nm pulses only partially overlapped while entering the semiconductor plasma. This partial overlap decreased the ratio between the overlapped second harmonic and driving pulses and diminished the influence of the 401 nm wave on the output spectrum of generating harmonics.

The second harmonic conversion efficiencies and the temporal overlaps of the driving and second harmonic waves, as well as the pulse durations of 401 nm radiation in the cases of different BBO crystals are summarized below. In the case

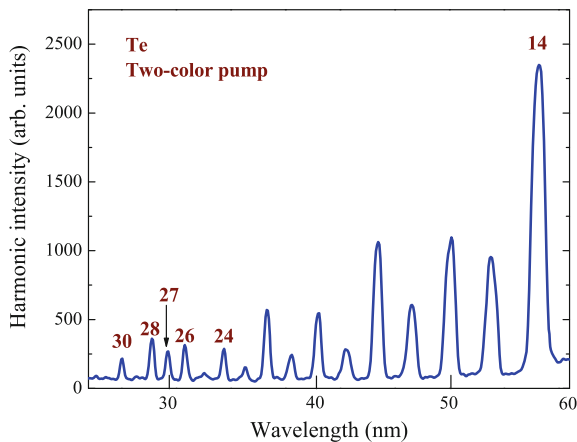


Fig. 5.6 Two-color pump induced odd and even harmonic spectra obtained from the Te plasma. This plasma was produced using the 4 mJ, 370 ps pulses. The intensity of driving pulses was $8 \times 10^{14} \text{ W cm}^{-2}$. The ratio of 401 and 802 nm pulse energies was 5:95. The polarizations of two pump waves were orthogonal to each other. Reproduced with permission from [55]. Copyright 2014. AIP Publishing LLC

of above mentioned lengths of crystals allowing the 0.4, 5, 9, 11, and 13 % second harmonic conversion efficiencies, the ratios of overlapped pulses inside the plasma were 0.004, 0.03, 0.04, 0.01, and 0.007, respectively. One can see the prevalence of using the 0.3- and 0.5-mm-long BBO, since other crystals did not allow the observation of efficient odd and even harmonics generation due to insignificant overlap inside the semiconductor plasma plume. Moreover, the duration of second harmonic pulse increased in the case of longer crystals (65, 72, 105, 140, and 195 fs correspondingly; compare with the 64 fs driving pulse). The decrease of the intensity of second harmonic also diminishes the role of this radiation in the variation of HHG spectra.

The important peculiarity of the two-color pump HHG in the semiconductor plasma is the observation of additional resonantly enhanced harmonics near some strong ionic transitions, analogously to the case of single-color pump. This process is clearly seen in Fig. 5.6 where the 13th and 14th harmonics of 401 nm pump (corresponding to the 26th and 28th harmonics of 802 nm radiation) were comparable or stronger than the 12th harmonic of this radiation. One can assume the influence of the same group of ionic transitions, which led to the enhancement of the 27th harmonic of 802 nm radiation in the case of single color pump (Fig. 5.4b), on the efficiency of 26th and 28th harmonics in the case of tellurium plasma.

Below we discuss the harmonic cut-offs achieved in those plasmas. In the case of As plasma, the observed higher-order harmonics were assumed to be originated predominantly from the singly charged ions. This assumption was drawn from the three-step model of HHG, taking into account the ionization potential of singly charged arsenic ions and barrier suppression intensity of those particles. The highest possible photon energy of harmonic spectrum is defined by the formula $E_c \approx I_p + 3.17U_p$ [53], where I_p is the ionization potential of the particle emitting harmonics and U_p is the ponderomotive energy of accelerated electron ($U_p = e^2 E^2 / 4 m \omega^2 = 9.33 \times 10^{-14} I_L \lambda^2$, where e and m are the electron charge and mass, and E , ω , I_L , and λ are the field's amplitude, frequency, intensity, and wavelength, respectively).

To achieve highest possible cut-off energy, one has to increase the ponderomotive energy or to choose the emitter possessing higher ionization potential. The ponderomotive energy of electrons at a fixed wavelength strongly depends on the laser intensity. However, if the nonlinear medium is ionized before the peak of laser pulse, the cut-off energy is defined by the saturation intensity ($I_{BSI} < I_L$), which is related with the barrier-suppression ionization. To calculate the cut-off energy at the used conditions of experiments, one has to estimate the I_{BSI} of low-charged semiconductor ions by using the expression for the barrier suppression ionization $I_{BSI} = c(I_p)^4 / 128\pi e^6 (Z_i)^2 = 4 \times 10^9 \times (I_p)^4 / (Z_i)^2$, where c is the light velocity and Z_i is the degree of ionization. The I_{BSI} of the singly charged ions, with the ionization potentials of 16.3, 15.9, 18.6, 21.2, 15.3, and 16.5 eV for the Si, Ge, As, Se, Te, and Sb singly charged ions, were calculated to be 7×10^{13} , 6×10^{13} , 1.2×10^{14} , 2×10^{14} , 6×10^{13} , and 7×10^{13} W cm⁻², respectively. One can see that I_{BSI} of all samples were lower than the laser intensity used in those studies (5×10^{14} – 1×10^{15} W cm⁻²).

The harmonic cut-offs were calculated to be corresponded to the 19th, 17th, 27th, 37th, 17th, and 19th orders, assuming the involvement of singly charged ions in the HHG. These results do not match with the experimentally observed cutoffs (27th, 35th, 35th, 51st, 31st, and 35th harmonics for the Si, Ge, As, Se, Te, and Sb plasmas, respectively). This discrepancy could be explained by the assumption of the partial involvement of the doubly charged ions as the emitters of higher-order harmonics.

5.3 Application of Carbon Cluster-Contained Extended Plasmas for the High-Order Harmonic Generation of Ultrashort Pulses

Multi-walled carbon nanotube (CNT), carbon nanofiber (CNF), diamond nanoparticle (DN), and C_{60} powders, as well as 5-mm-long bulk graphite, were studied as the extended ablating targets for HHG [66, 67]. The powders of above materials were glued on the 5-mm-long glass plates and installed in the vacuum chamber for ablation. The sizes of DN were in the range of 3–8 nm. The diameter of CNTs was ~ 15 nm with the lengths of nanotubes varied in a range of 500 nm–20 μm . The CNFs were presented with a variety of fibers with the diameters of 30–200 nm and the lengths varied between hundreds of nanometers and tens of micrometers. The fullerene powder was presented in the shape of the agglomerates of C_{60} .

The raw image of the low-order harmonic spectrum obtained from the CNT plasma is shown in the upper panel of Fig. 5.7. The broadened harmonics between the 11th and 17th orders were presented alongside the plasma emission from carbon monomer ions. One can see a difference in the divergences of plasma and harmonic emissions. The raw image of the spectrum generated in the silver plasma (Fig. 5.7,

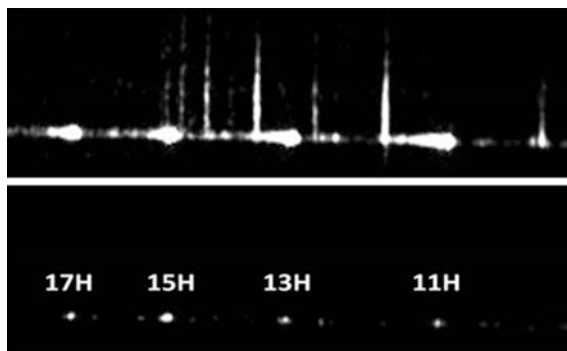


Fig. 5.7 Raw images of the low-order harmonics obtained from the CNT (*upper panel*) and Ag (*bottom panel*) plasmas. Reproduced with permission from [66]. Copyright 2014. AIP Publishing LLC

bottom panel) is also presented here, which shows the narrow spectral distribution of harmonics, without the appearance of plasma emission (other spectral components in this image correspond to the second-order diffraction of higher-order harmonics). The harmonic spectra obtained from plasmas (Fig. 5.8) were measured at the optimal conditions of ablation. The optimization was carried out by varying the fluence of heating pulse on the target surface. The low-order harmonic spectrum from the silver plasma is presented for comparison with other spectra. This medium allows the generation of strongest high-order harmonics among other metal plasmas

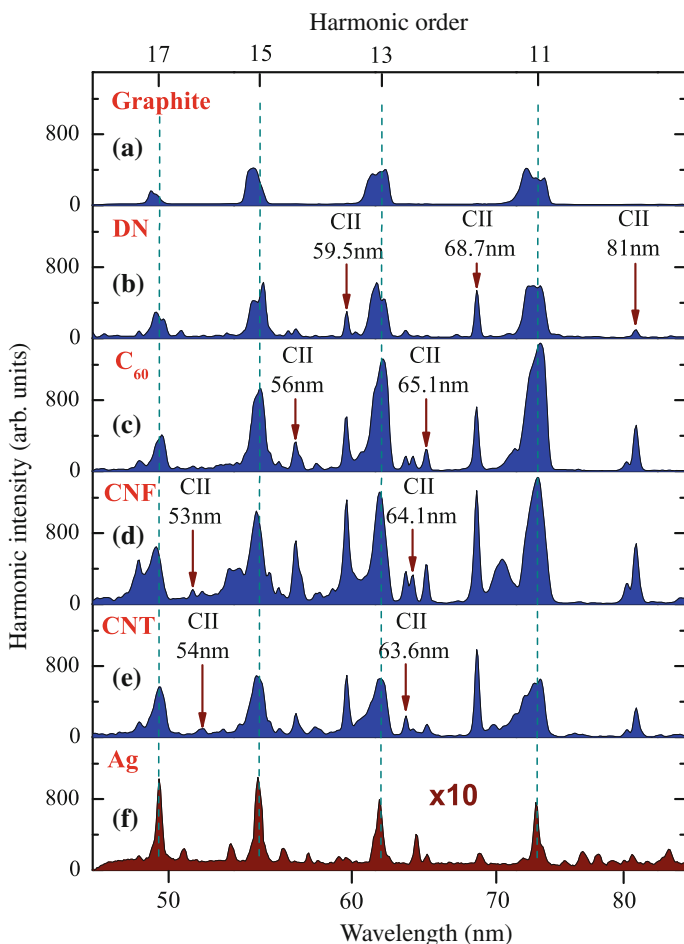


Fig. 5.8 Harmonics obtained from the graphite, diamond nanoparticle, fullerene, carbon nanofiber, carbon nanotube, and silver plasmas. Each image represents the collection of 10 laser shots. The plot (f) of Ag harmonics was ten times multiplied for better visibility. *Dashed lines* show the corresponding harmonic orders. *Arrows* show the C II spectral lines of carbon-contained plasmas. Reproduced with permission from [66]. Copyright 2014. AIP Publishing LLC

[68]. These spectra were obtained at similar conditions of registration to allow the comparison of harmonic generation from all used plasmas at the maximum yields of lower-order harmonics.

The graphite plasma harmonics have previously shown the highest conversion efficiency (η) among other bulk targets ablated for the HHG in the 35–80 nm spectral range. One can see that all cluster-contained plasmas (Fig. 5.8b–e) demonstrate stronger yields of harmonics compared with the harmonics generated from the ablation of bulk graphite, while the latter plasma provided stronger harmonics with regard to the silver plasma (compare Fig. 5.8a, f); silver harmonic spectrum is multiplied ten times for better visibility). The appearance of ionic emission, alongside the harmonics in the case of almost all ablations of clusters, did not significantly affect the harmonic yield. Those plasma lines were assigned mostly to the singly charged carbon (see similar C II emission lines appeared in most spectra from the cluster-contained plasmas, Fig. 5.8).

The absence of the plasma emission associated with the higher-charged ions can be explained by the moderate ablation of targets. The driving pulse also did not cause the appearance of strong ionic emission from the higher-charged carbon ions. Note that the appearance of plasma emission in the case of ablation of the bulk targets (graphite and silver) was followed with a decrease of harmonic yield due to the growing influence of the free electrons appearing during ionization of the medium. This effect was less influential in the case of cluster-contained targets, which can be attributed to the prevalence of the advanced properties of nanoparticle-contained plasma over the phase mismatch.

Other important peculiarities of those spectra are the significant broadening of harmonic bandwidths and the blue shift of the shorter-wavelength parts of harmonics. These features have been analyzed previously in a few studies of carbon-induced harmonics. The origin of the broader width of harmonics and the extended short-wavelength lobes has been studied in [69] and was attributed to the influence of the self-phase modulation of the driving femtosecond pulse during propagation through the plasma plume. The presence of nanoparticles in the plasma plume may also contribute to the broadening of the harmonic bandwidth.

The temperature of graphite plasma at the intensity of heating pulse $I_{\text{hp}} = 3 \times 10^9 \text{ W cm}^{-2}$ was estimated to be 14 eV, and the particle density in the plasma area was calculated to be $2 \times 10^{17} \text{ cm}^{-3}$. The ionization potentials of C atoms and singly charged ions are 11.25 and 24.38 eV, respectively. Such plasma mainly consisted of the excited neutral atoms (C I) and singly ionized particles (C II), which was confirmed during spectral measurements of plasma emission.

The comparative studies of the 0.5-mm- and 5-mm-long plasmas of similar ablated clusters showed the $3\times$ to $8\times$ growth of harmonic yield in the latter case. These enhancement factors of harmonic emission are significantly smaller compared with the expected quadratic growth of η with the increase of plasma length ($100\times$), probably due to the growing phase mismatch between the interacting waves at the conditions when the coherence length of harmonics becomes shorter than the length of extended medium. The estimations show that absorption did not play an important role in the 5-mm-long plasmas at the optimal conditions of ablation

(i.e., at the plasma concentrations of $\sim 2 \times 10^{17} \text{ cm}^{-3}$). In the meantime, the coherence length of the q th harmonic calculated from the relation $L_{\text{coh}} = 1.4 \times 10^{18}/qN_e$ [70] for the 11th–19th harmonics was in the range of 3–4 mm at the electron concentration of carbon plasma of $N_e = 3 \times 10^{16} \text{ cm}^{-3}$. The latter value, as well as plasma concentration, was defined using the code ITAP IMD [71]. From these estimations, one can conclude about the restrictions of using the longer (5 mm) cluster-contained plasma. In that case, the destructive interference between the driving and harmonic waves leads to the decrease of the η of HHG.

The studies of plasma emission from the over-excited bulk graphite showed the similarity of this emission with those observed from the cluster-contained plasmas (Fig. 5.9a, b). The availability of harmonic generation during ablation of the pure

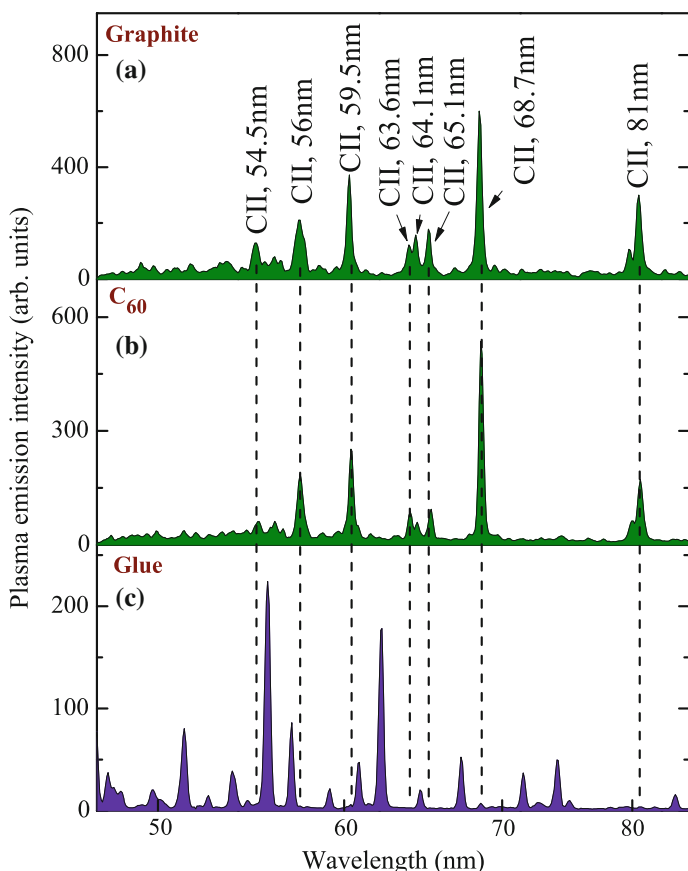
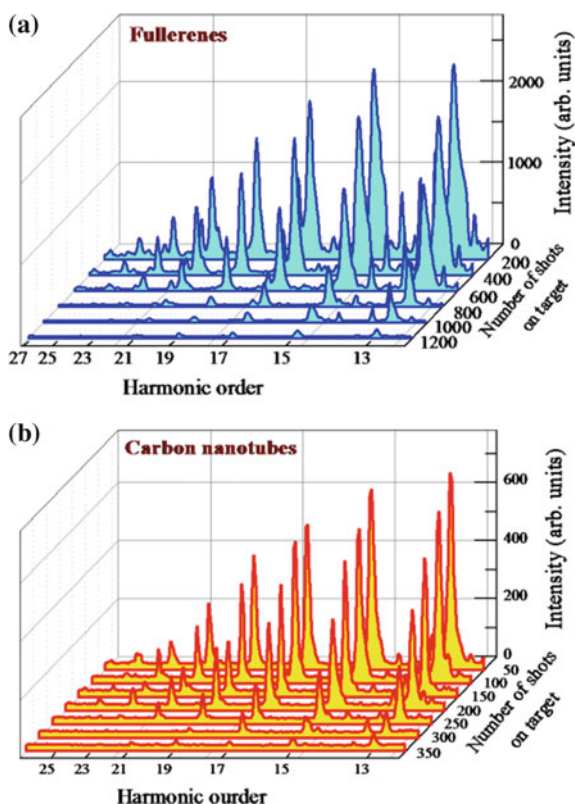


Fig. 5.9 Plasma spectra during over-excitation of targets in the cases of **a** bulk graphite, **b** powdered fullerene, and **c** glue. Note a similarity of the carbon spectral lines obtained from the ablation of graphite and C_{60} , while the plasma spectrum of glue did not coincide with the carbon lines, as indicated by the *dashed lines*. Reproduced with permission from [66]. Copyright 2014. AIP Publishing LLC

glue was also analyzed. No harmonics were observed in that case. The over-excitation of glue led to plasma formation and emission (Fig. 5.9c), which could be distinguished from the emission generated in the carbon-contained plasmas.

The studies of the decay of the harmonic yield from the cluster-contained plasmas were performed at 10 Hz pulse repetition rate, without the movement of targets from shot to shot. This led to deterioration of the optimal plasma formation after a few hundred shots on the same spot of cluster-contained target, while in the case of bulk samples (silver, graphite) ablation the stable harmonic generation was maintained for a considerably longer time. This effect has been observed in previous studies of powdered target ablation [30–33, 72, 73] and was attributed to the modification of target surface (i.e., evaporation of powder, melting of heated area, modification of surface properties, etc.). The variations of harmonic spectra from the cluster-contained targets with the number of laser shots on the same spot of target are shown in Fig. 5.10 in the cases of fullerene and carbon nanotube plasmas. The estimates show that, in accordance with the three-step model [52–54], the involvement of singly charged fullerene clusters ($I_p = 15.6$ eV [74]) should lead to harmonic generation above the forties orders. One can conclude about the prevailing role of the neutral fullerenes ($I_p = 7.6$ eV) in the harmonic generation.

Fig. 5.10 Dependences of the harmonic decay on the number of laser shots on the same position of target. **a** Fullerene harmonic spectrum. **b** Carbon nanotube harmonic spectrum. Reproduced with permission from [66]. Copyright 2014. AIP Publishing LLC



The theoretical studies of HHG in clusters have a long history [28, 29, 75–78]. Meanwhile, there are only a few experimental studies of HHG using the gas clusters [24–27]. In this connection, the use of the ablation technique allowing the formation of cluster-contained plasma by the evaporation of nanoparticles seems the advanced development of cluster studies. Moreover, the carbon-based clusters demonstrate the attractive nonlinear optical properties, which will be discussed below.

From a practical point of view, the CNT and CNF targets lack a number of the serious drawbacks of other molecular structures. The chemical bonding between carbon atoms in nanotubes is rather strong, which means that their deformation and dissociation in intense fields take place on longer time scales than that of aromatic molecules. The lack of hydrogen atoms in nanotubes contributes to the same stability effect. The HHG spectra of CNT have been theoretically studied in [79–84]. It was suggested that there are many reasons for using the nanotubes to generate high-order harmonics. The advanced properties of CNT were revealed during the first experimental studies of their high-order nonlinear optical properties [85], which have demonstrated high conversion efficiency of harmonics exceeding those obtained using other ablated species.

Similarly, various attractive peculiarities have been identified during the theoretical studies of the HHG from the fullerenes [86–89]. It has been shown that in large structures, such as C_{60} , the following additional degrees of freedom are introduced: electronic degrees of freedom, including collective effects such as the formation of plasmons, vibrational degrees of freedom, and fragmentation. A giant resonance at 20 eV in C_{60} has been predicted theoretically in [90] and confirmed later in an experiment [91]. When compared with metal clusters, where collective resonances occur at a few eV, a 20 eV giant resonance of 12 eV bandwidth is quite remarkable. The importance of this giant broadband resonance for simultaneous enhancement of a few neighboring harmonics within the bandwidth of this resonance was confirmed during first experimental studies of the HHG in fullerenes [36].

Regarding the large spherical nanoparticles, forced nucleation of laser-induced vapor has been widely used to generate small metal [92, 93] and semiconductor [94] particles. It was reported that small particles can be formed in the ablation plume induced by ultrashort laser pulses [95–97], and the ultrafast laser ablation has been suggested as a simplest method for small nanoparticles generation. An important advantage of ultrafast laser ablation is the accuracy in material removal due to the ultrashort pulse duration [98–101]. Note that those conditions of nanoparticle formation are unsuitable for the efficient HHG in plasma since they provide large amount of free electrons, which lead to the growing phase mismatch between the driving and harmonic waves. The only way here is a “mild” ablation of the nanoparticles already existing on the target surface to keep the cluster-contained plasma free from the abundance of electrons.

The exact mechanism of the HHG from clusters is still debated. Various extensions of the three-step model have been proposed in [28, 29, 78, 102]. The generally considered dominant channel is ionization and recombination to the same atom (atom-to-itself). Since clusters can be considered as the dense media, there is

also a possibility of recombination to the neighboring ions [28, 29]. This atom-to-neighbor emission can produce incoherent radiation due to a lack of phase locking between the two atomic wave functions [78]. Another contribution to harmonic emission may come from a wave function partially delocalized over the whole cluster, from which electrons tunnel out of and to which they recombine coherently (cluster-to-itself). From an experimental point of view, a particular difficulty consists in disentangling the harmonics produced by different species (monomers and clusters of different sizes) and possibly different mechanisms. In [27], an experimental study of HHG from xenon clusters, which was aimed at disentangling the harmonic signal from clusters and monomers, was reported. They attributed the harmonic emission to the tunneling of delocalized electrons from a cluster and recollision coherently to the whole cluster. Although laser-irradiated clusters have allowed the efficient emission of low-order harmonics, no significant yield of high-order harmonics was achieved in their experiments even for very high laser intensities.

Similar features were observed during above-discussed studies of carbon clusters. These studies have shown that the divergence and spectral width of the harmonics produced in the nanoparticle plumes were considerably larger than those from the atom-contained plasmas. The larger divergence of the harmonics generated from clusters arises from a stronger influence of the long trajectories of accelerated and recombined electrons on the yield of the harmonic radiation. This explanation can be related with the growth of recombination cross section when larger particles have a higher probability to recombine with the returning electron moving on the long trajectory. The cluster-contained plasma concentration was small enough ($\sim 10^{17} \text{ cm}^{-3}$) to exclude the role of the optical scattering in this low-dense medium. The influence of the Kerr nonlinearities responsible for the refraction could also be excluded due to the same reasons (i.e., small amount of particles). The comparison of the 0.5-mm- and 5-mm-long cluster-contained plasmas did not show a significant difference in the divergences of harmonics. In the meantime, the appearance of spectral lobes of harmonics was pronounced in the case of longer plasma.

5.4 Morphology of Laser-Produced Carbon Nanoparticle Plasmas and High-Order Harmonic Generation of Ultrashort Pulses in Extended Clustered Media

The availability of different metal nanoparticles in the market allows formation of the plasmas containing various clusters. This follows with the enhancement of the harmonics generating in the metal cluster plasmas. The importance of the involvement of such clusters for the HHG was pointed out earlier; however no suggestions were presented on the optimal shape and structure of those species. With regard to this, clustered carbon species provide a variety of morphological shapes (such as spherical nanoparticles and fullerenes, as well as extended

nanofibers and nanotubes), contrary to the less variable shapes of spherical metal nanoparticles.

Here, we analyze plasma morphology at conditions of the laser ablation of nanoparticles suitable for the efficient HHG in carbon cluster-containing plasmas. Time-of-flight mass spectrometry and harmonic generation studies of laser plasma suggested that the origin of the observed growth of η from such clustered plasmas was probably related to the involvement of lower-sized nanoparticles, rather than higher-sized ones, as the emitters of efficient harmonics. We discuss the efficient HHG of Ti:sapphire laser pulses in the range of 15–33 eV using optimally prepared 5-mm-long carbon-based cluster plasma plumes. Among the peculiarities of this process are the two-color pump of carbon clusters and the use of clustered multi-jet plasma formations [67].

CNT powder, CNF powder, diamond nanoparticle powder, C₆₀ powder, and 5-mm-long bulk graphite and silver were studied as the ablating targets. The morphology of powders was analyzed using the transmission electron microscopy of original clusters and plasma debris. The content of the plasmas was analyzed using time-of-flight mass spectrometry (TOFMS). Figure 5.11 shows the TEM images of the as-supplied clusters of CNT, CNF, C₆₀, and DN. Spatial characterization of the used clusters is presented in Sect. 5.3.

Ablation debris collected on the substrates placed near to the ablation area at the optimal and non-optimal conditions of clustered plasma formation were also analyzed. These terms refer to the strong and weak harmonic yields from those plasmas. The analysis of post-ablation conditions of the deposited debris can provide useful information about the plasma components, despite the difference between the composition of the plasma at the early stage of formation and the deposited material, which can be modified due to the aggregation on the substrate [103]. To compare the dependence of the properties of the deposits under different ablating conditions, the clusters were ablated using the 370 ps pulses of the Ti:sapphire laser at a repetition rate of 10 Hz and variable fluence. Figure 5.12 shows the TEM images of the material ejected upon ablation of CNT, CNF, C₆₀ and DN. One can see that the characteristic sizes of the deposited material were close to those of the initial cluster targets. In these studies, the moderate laser ablation intensities (up to $3 \times 10^9 \text{ W cm}^{-2}$) corresponding in each case to the conditions of efficient HHG were used. Over-excitation of the nanoparticle-containing targets, by using higher intensities and fluences, did not yield similar nanostructured deposits, but rather groups of chaotically formed aggregates. Note that at high ablation fluences, the HHG yield was significantly decreased or completely disappeared after a few hundred shots.

The deposits generated upon laser ablation of the bulk graphite at conditions that ensured the efficient harmonic generation in the plasma plume were also analyzed. Under these conditions of using the moderate fluences of heating pulses the collected deposits showed evidence of $\sim 10\text{--}20$ nm nanoparticles. Production of carbon nanoparticles by laser ablation of graphite at high fluences of heating ultrashort pulses is a well-studied phenomenon. However, the use of high ablation fluences results in the appearance of a large number of free electrons, which is a detrimental

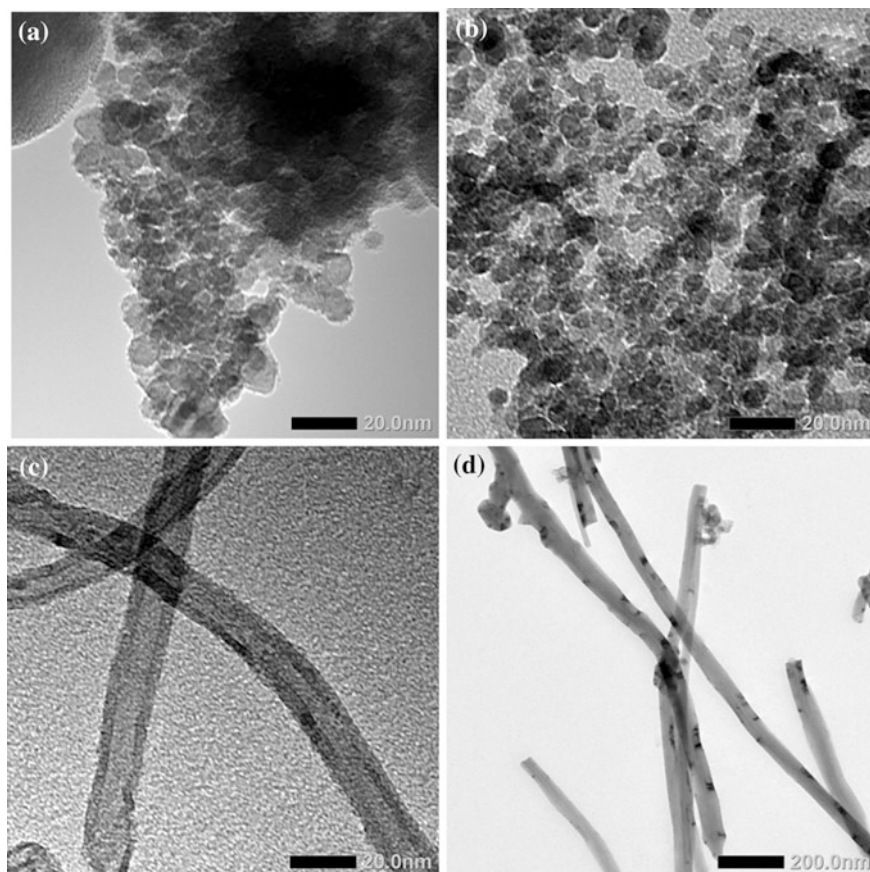


Fig. 5.11 TEM images of clustered targets: **a** fullerene agglomerates, **b** diamond nanoparticles, **c** carbon nanotubes, **d** carbon nanofibers. *Black markers* correspond to **a–c** 20 nm and **d** 200 nm. Reproduced from [67] with permission from IOP Publishing. All rights reserved

factor for the HHG due to the growing contribution of the free electrons to the phase mismatch between the driving and harmonic waves. This explains why, under the ablation conditions leading to nanoparticle formation in the plasmas of some bulk metal targets, the HHG signals were extremely weak. In that case, the presence of nanoparticles in the extended plasma does not compensate for the deteriorated phase relations between the interacting waves caused by over-ionization and production of a large number of electrons. Meanwhile, the cluster formation during ablation of graphite occurs at rather low laser fluences, which allowed the maintenance of a moderate level of electron concentration.

Figures 5.13, 5.14 and 5.15 show the mass-resolved spectra of the clustered plasmas using the TOFMS. These studies reveal that most of the studied laser plumes contained C_5 – C_{25} clusters. To ascertain the presence of neutral species in

Fig. 5.12 TEM images of deposited debris: **a** carbon nanotubes, **b** fullerene agglomerates, **c** diamond nanoparticles. *Black markers* correspond to **a** 100 nm, **b** 20 nm, and **c** 50 nm. Reproduced from [67] with permission from IOP Publishing. All rights reserved

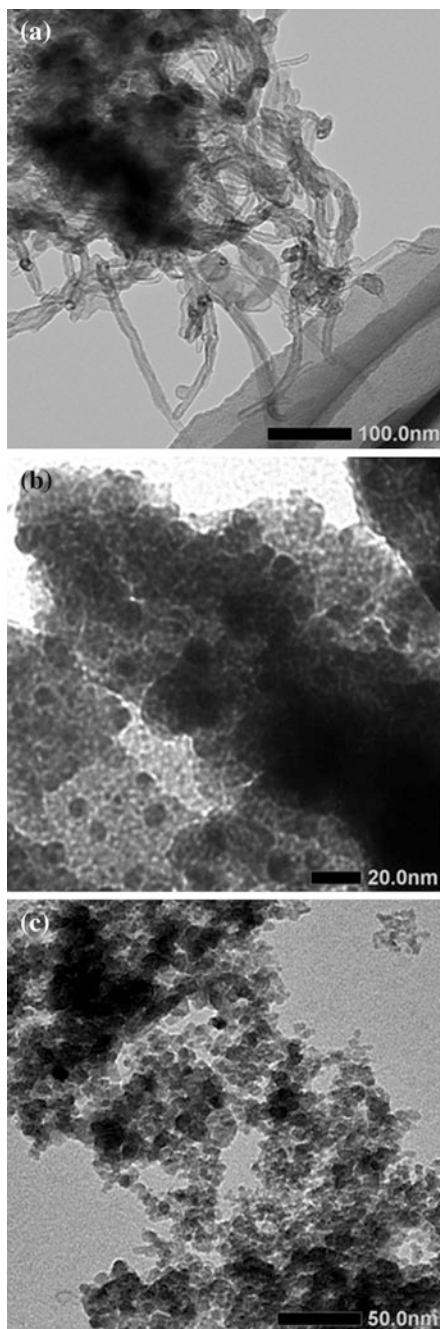
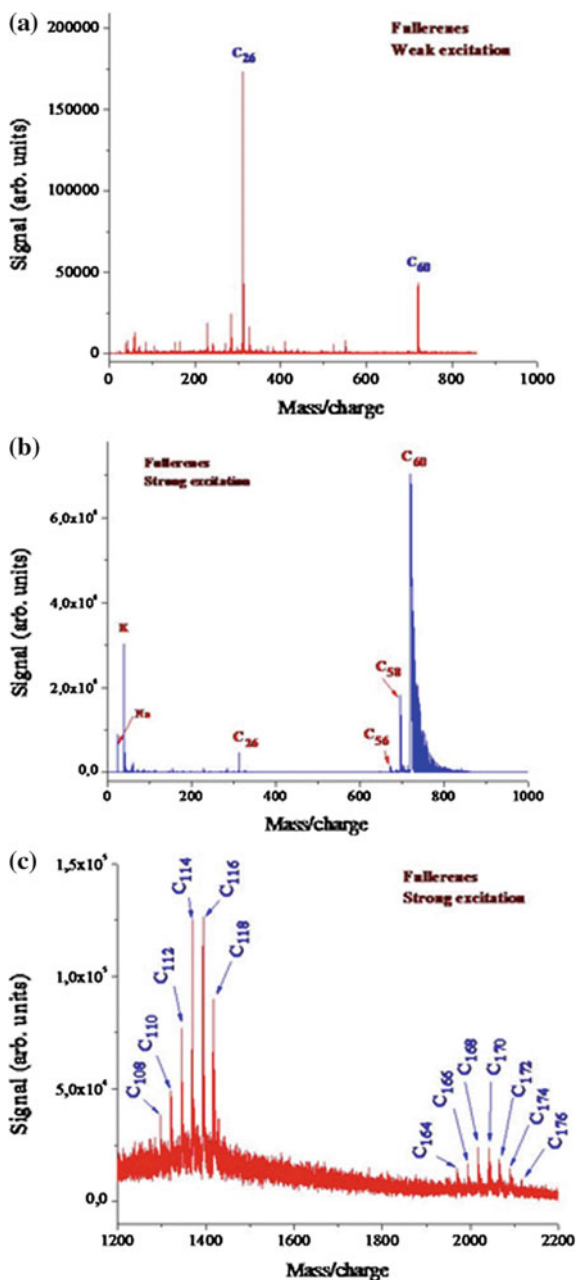
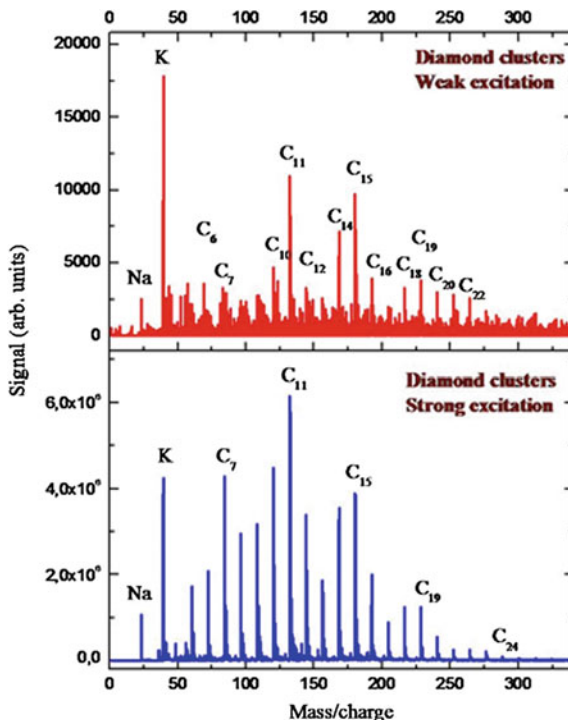


Fig. 5.13 Time-of-flight mass spectra of ablated fullerene powder at **a** weak and **b, c** strong excitation of targets. *Bottom plot c* shows the spectra of higher mass fullerenes. Reproduced from [67] with permission from IOP Publishing. All rights reserved



the ablated plasma, an additional source of ionization should be used. Notice that previous studies (see for example [104]) have shown the presence of neutral carbon clusters at similar conditions of ablation.

Fig. 5.14 Mass spectra of the low-sized diamond nanoparticles at weak (*upper panel*) and strong excitation of targets. Reproduced from [67] with permission from IOP Publishing. All rights reserved

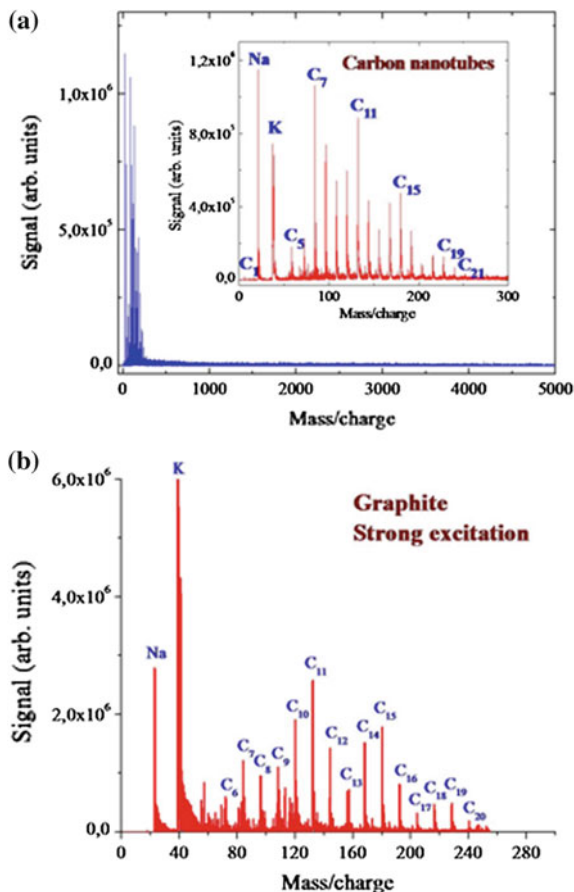


Ablation of C_{60} at a weak fluence revealed the appearance of fullerene ions, while a strong signal from C_{26} clusters pointed out the preferable disintegration of the C_{60} molecule rather than its ionization (Fig. 5.13a). The growth of heating pulse fluence on the target surface has considerably modified this mass spectrum (Fig. 5.13b). While C_{26} still remained in this spectrum, a very strong signal from C_{60} ion dominated over the whole spectrum, together with the appearance of some lighter clusters (C_{56} , and C_{58}). Moreover, two additional groups of clusters appeared in the high-mass/charge range with the masses ranged between C_{108} and C_{118} and between C_{164} and C_{176} (Fig. 5.13c). The sodium and potassium lines were originated from the substrate containing ablating species.

The mass spectra of ablated DNs in the cases of weak and strong excitation are shown in Fig. 5.14. In both cases the appearance of a group of light clusters was observed. At each of these conditions the stronger signals came from the clusters obeying the rule of magic numbers $4n + 3$. The clusters with numbers of carbon atoms of 7, 11, 15, and 19 dominated these spectra. No other ionic clusters were observed in these studies while searching up to a few tens of thousands of the mass/charge units.

CNTs and CNFs showed similar spectra as the DNs, though these targets were completely different from each other by the initial morphology. As in the previous case, no ions higher than low-sized carbon clusters were observed in the CNT mass

Fig. 5.15 Mass spectra of **a** carbon nanotube ablation and **b** graphite ablation. Reproduced from [67] with permission from IOP Publishing. All rights reserved



spectra while searching up to 10,000 mass/charge units (Fig. 5.15a). Those small sized particles almost completely repeated the structure of the ionic components of DN plasma (compare the bottom panel of Fig. 5.14 and the inset of Fig. 5.15a).

The ablation of the graphite target also showed the appearance of the same group of clusters (Fig. 5.15b). These studies revealed a similarity in the properties of almost all studied plasmas from the point of view of the presence of lower-mass carbon clusters. The ease of formation of these nanoparticles from the clustered media may lead to their stronger influence on the HHG. This assumption was confirmed during subsequent studies, which revealed the stronger yields of harmonics from the CNT, CNF, DN and C₆₀ plasma plumes compared with the graphite ablation.

The time-of-flight mass spectra of most ablated carbon clusters (at conditions of maximum harmonic yield) resembled those obtained by many researchers [105–111]. As mentioned, the $(4n + 3)$ clusters had a greater presence compared with the neighboring ones. These clusters (C₇, C₁₁, C₁₅, C₁₉) could probably be

considered as the most effective emitters of harmonics among all the clusters. This assumption can be generally attributed to a lower ionization potential of these clusters rather than to their exceptional structural stability.

At optimal plasma conditions, when the highest harmonic conversion efficiency from the carbon cluster ablation was obtained, the TEM images revealed the presence of nanoparticles in the deposited debris with sizes similar to the initial material (in particular, $\sim 5\text{--}10$ nm diamond nanoparticles and $\sim 20 \times 2000$ nm² nanotubes). It is possible that, in the case of the carbon base plasmas produced at these conditions, the harmonics could originate from different nanoparticles, particularly with the sizes below the limit of detection using TEM. The mass spectrometry of the plasmas has confirmed the presence of small nanoparticles in the cases of ablation of the diamond nanoparticles, nanotubes and bulk graphite. The presence of those particles coincided with the maximum conversion efficiency of the 11th–23rd harmonics.

Almost all harmonic spectra from clustered plasmas have contained the plasma emission at maximal harmonic yields, contrary to the case of graphite ablation when the appearance of ionic emission was followed with a deterioration of the optimal plasma conditions for HHG. In the case of cluster ablation, the plasma lines in the longer-wavelength range of the spectrum (45–90 nm) were assigned mostly to the C II. The absence of plasma emission from higher charged ions in this spectral range was related with the moderate conditions of excitation of the targets by the heating pulses. The driving pulses propagating through the plasma did not cause the appearance of strong ionic lines from the higher-charged carbon ions. The appearance of ionic emission, along with harmonics in the case of almost all cluster ablations, did not affect the harmonic yield much. Plasma emission during over-excitation of bulk graphite showed the similarity of this emission with those observed from the clustered plasmas. The availability of harmonic generation during ablation of pure glue, without the inclusion of clusters was also analyzed. No harmonics were observed in that case. The over-excitation of glue led to plasma formation and emission, which was clearly distinguished from the emission generated in the carbon-contained plasmas.

The shorter wavelength spectra of ablated clustered plasmas did not show the efficient emission of harmonics above the 25th order, which points out the prevailing involvement of the neutrals, rather than ionized clusters, in the coherent emission generation due to smaller harmonic cut-off from the neutrals. To amend this, both the over-excitation of targets and the increase of driving pulse intensity were used; however, neither of those methods allowed the extension of harmonic cut-off. Instead, the growing plasma emission in the range of 10–43 nm in the cases of DN, CNT, and CNF (Fig. 5.16a, three upper panels) was observed.

Those emissions were assigned to the C III and C IV ions. The only clustered species, which allowed harmonic generation at these conditions, was the fullerene plasma (Fig. 5.16a, second panel from the bottom). This peculiarity could be attributed to the better survival of fullerene molecules in the strong laser fields. Contrary to the emissions from clustered media, the ‘clean’ harmonic spectrum up to the 65th order, without any plasma emission, was observed from the silver

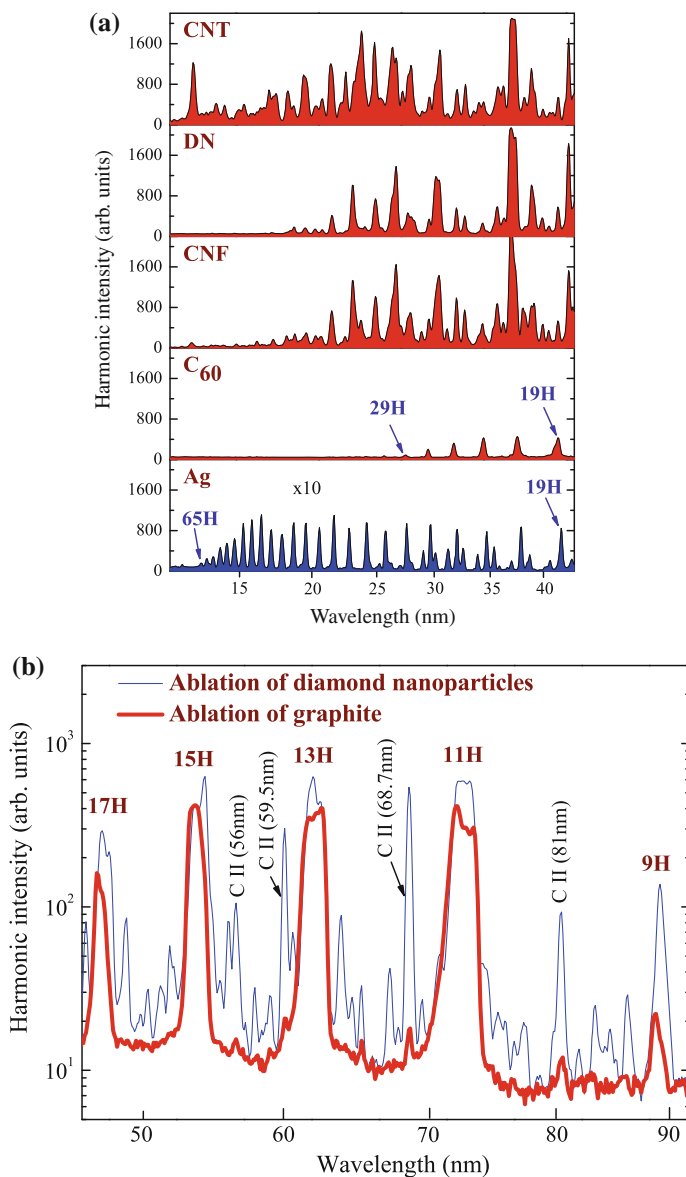


Fig. 5.16 **a** Plasma emission and harmonic spectra from carbon clusters and silver ablations in the short-wavelength range. Silver harmonic spectrum was multiplied with the factor of 10 for better visibility. Lines other than harmonics in silver spectrum represent second-order diffractions of higher order harmonics. **b** Comparative lower-order harmonic spectra from the bulk graphite (*thick curve*) and diamond nanoparticles (*thin curve*) ablations. Reproduced from [67] with permission from IOP Publishing. All rights reserved

ablation thus demonstrating the advanced features of this material for the generation of higher-order harmonics (Fig. 5.16a, bottom panel; the harmonic spectrum was magnified ten times for better visibility). Note that the efficiency of harmonics from silver plasma in the plateau range was smaller than those of the 19th–27th harmonics generating in the fullerene plasma.

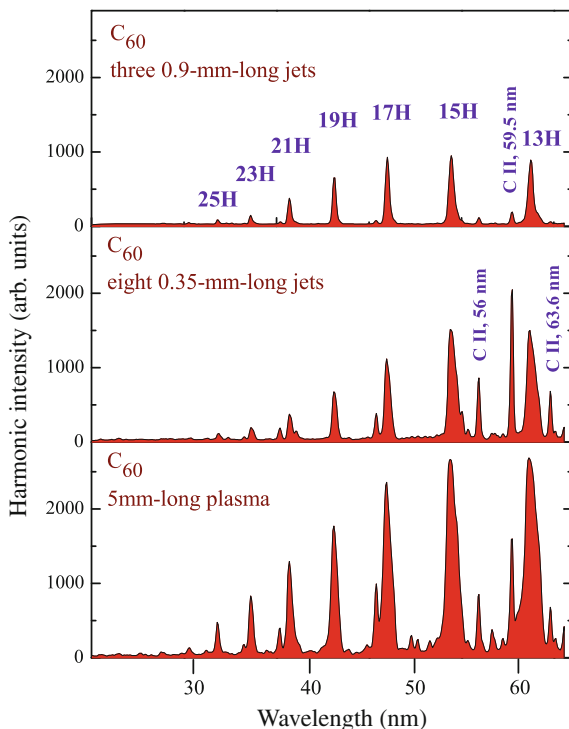
The spectra presented in Fig. 5.16a were collected during ten laser shots. The comparative harmonic spectra from the bulk graphite (thick curve) and diamond nanoparticle (thin curve) ablations are shown in Fig. 5.16b. These studies showed better conversion efficiency in the latter medium, though the instability of harmonics and the plasma emission diminish the advantages of this clustered plasma as a robust medium for HHG.

The presence of free electrons and excited ions in the extended plasma plumes can cause the growth of the phase mismatch between the driving and harmonic waves along the propagation of the femtosecond laser pulse through the extended medium. One way to overcome this obstacle is the division of a whole extended plasma onto a group of small jets to create quasi-phase-matching for plasma harmonics. The multi-slit shields were used to produce multiple clustered plasma jets of different sizes, similarly to the studies described in Chap. 4. The slit sizes of the first MSS were 0.3 mm, and the distance between slits was 0.3 mm. The slit sizes of the second shield were 0.9 mm, and the distance between slits was 0.7 mm. These MSSs were installed between the focusing cylindrical lens and extended plasma plume in such a way as to allow the division of the extended continuous 5 mm long plasma onto the set of a few plasma jets. The sizes of eight jets produced on the 5 mm long plain targets using the 0.3 mm MSS were ~ 0.35 mm, with the distance between them ~ 0.25 mm. The second MSS allowed the formation of three 0.9 mm long jets separated from each other at a distance of ~ 0.7 mm. These plasma jets were compared with the extended 5 mm long plasma.

The harmonic spectra in these three cases are presented in Fig. 5.17. Those studies did not reveal the QPM-induced enhancement of specific harmonics due to the low harmonic cut-off from the C_{60} plasma. The range of enhanced harmonics could be defined from the relation $q_{\text{coh}} = 1.4 \times 10^{18}/(L_{\text{coh}} \times N_e)$ [70], where L_{coh} and N_e are measured correspondingly in millimeters (which was defined by the size of a single jet) and reciprocal cubic centimeters. In the case of the optimal ablation of bulk graphite, the calculations based on the code ITAP IMD show $N_e \sim 2 \times 10^{16} \text{ cm}^{-3}$. The ablation of clustered targets at these conditions leads to a lower concentration of free electrons. Correspondingly, the q_{coh} for C_{60} plasma would be larger than 31, which is far from the harmonics observed in those experiments. The intensities of the harmonics generated from multi-jet plasmas were weaker as compared to the extended plasmas. Contrary to that, in the case of silver plasma, a considerable enhancement of a few harmonics around the 35th order was observed, while using the multi-jet scheme [112], which is clear evidence of the QPM concept being realized in the perforated plasma.

The use of two-color pump schemes for the HHG is another well-known approach for the harmonic enhancement and the modification of the spectrum of generated radiation (see Chap. 3). The two-color pump, using fundamental and

Fig. 5.17 Fullerene harmonic spectra obtained from different plasma formations. *Upper panel* three 0.9-mm-long jets separated from each other at a distance of 0.7 mm. *Middle panel* eight 0.35-mm-long jets separated from each other at a distance of 0.25 mm. *Bottom panel* extended 5-mm-long plasma generated without the insertion of MSS. Reproduced from [67] with permission from IOP Publishing. All rights reserved



second harmonic fields, has become a practical way of harmonic enhancement in the plasma media. The CNT and CNF harmonic spectra using single- and two-color pump schemes are shown in Fig. 5.18. In both cases, no changes or further optimizations of HHG were carried out in the cases of single- and two-color pumps. The BBO crystal was moved in and out of the path of the driving beam to generate odd and even harmonics. One can see some enhancement of harmonic yields using the two-color pump of CNT and CNF plasmas. The appearance of even harmonics points out the sufficient overlapping of the 802 and 401 nm pulses in the plasma area. The eight-jet plasma configuration was used in both these cases. Similar spectra were obtained for the 5 mm long extended plasmas.

The important issue of cluster HHG studies is the comparison between the known experimental results for the harmonic generation from gas atoms, gas clusters, surface, ablated bulk targets and nanoparticle targets. Though the scales of these studies performed using various lasers differ from each other, such a comparison can give the qualitative estimates between the cut-offs and harmonic efficiencies.

The maximum η of harmonics in the plateau-like range from gaseous atomic media are about 10^{-6} , while the cut-offs are the largest among the sources of HHG (up to a few thousand harmonics, or few keV photon energy). Clustered gaseous media show a significant decrease of cut-offs (around 100 eV); however, the

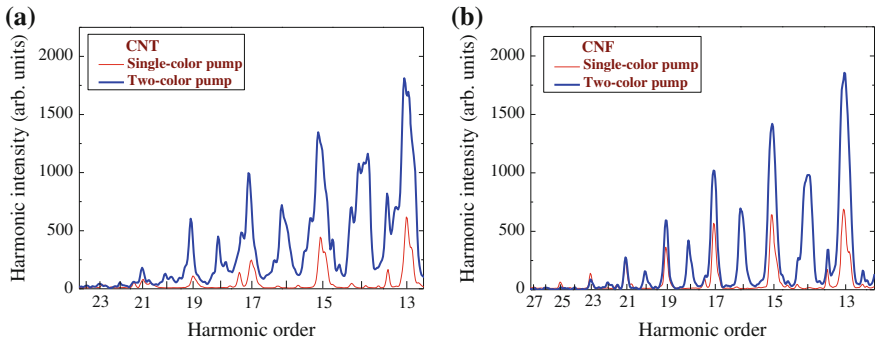


Fig. 5.18 Harmonic spectra obtained using single-color (*thin lines*) and two-color (*thick lines*) pumps of the eight-jet plasma formations of **a** CNT and **b** CNF. Reproduced from [67] with permission from IOP Publishing. All rights reserved

reported yields are a few times higher compared with the atomic gaseous media. HHG during specular reflection from the surfaces show the extended cutoffs (up to 1 keV photon energy), while suffering a fast decrease of harmonic yield in the 100 eV range and higher. The ablated targets allow generation up to the 90 s harmonics in the ionic plasmas, with the η (up to 10^{-5}) comparable or higher than in the case of gaseous harmonics. Harmonic generation from ablated metal clusters shows stronger harmonic yield compared with ablated atoms and ions, although it suffers with the instability of converted radiation. Finally, lower-order harmonics generating from the carbon clusters may be considered as the strongest among the harmonics produced by different means.

5.5 Graphene-Contained Extended Plasma: A Medium for the Coherent Extreme Ultraviolet Light Generation

The unique optical and nonlinear optical properties of graphene have been in the center of various recent theoretical and experimental studies [113–118]. Particularly, a new scheme based on bilayer graphene as a nonlinear optical material was proposed in [117] with an extremely large second-order optical susceptibility ($\chi^{(2)} \sim 10^5 \text{ pm V}^{-1}$). Recent experiments have shown that the nonlinear generation of laser harmonics could be detected even through single layer graphene [114]. The theory of the nonlinear electromagnetic response of graphene has been developed in [115, 116, 118]. It has been demonstrated in [118] that it is possible to realize significant nonlinear optical interactions at a few photon level in graphene nanostructures. The high-order harmonic generation from a graphene sheet exposed to intense femtosecond laser pulses has been theoretically studied in [119] based on the three-step model of HHG. It was predicted that graphene may generate more

intense harmonic signals than gas-phase atoms or molecules and serve as a useful tool for selective harmonic generation when exposed to an intense driving laser field, though the experimental evidence of HHG in this medium has not been reported.

In the meantime, the laser ablation based HHG experiments have been advanced towards the molecules of increasing complexity such as fullerenes [36] and carbon nanotubes [85]. Previous estimates of similar plasma structures produced on the surfaces of powdered nanomaterials during laser ablation have shown that the concentration of particles becomes close to $\sim 10^{17} \text{ cm}^{-3}$ [36], which should be enough to induce the nonlinear optical processes.

The purpose and advantage of generating harmonics of ultrashort pulses in laser ablation based materials are related with the higher conversion efficiency. In the meantime, the method of “mild” ablation of graphene, when the structure of material remains intact in the plasma plume, could be the ideal approach for the analysis of the high-order nonlinear optical properties of this medium. Below, we analyze the HHG of femtosecond pulses in the laser ablation plume containing graphene nanoparticles [120]. Graphene nanoparticle powder was studied as the ablating target using the experimental setup described in Sect. 3.1. To compare the yield of harmonics from cluster-containing and monomer-containing plasmas the carbon nanotube powder, diamond nanoparticle powder, and 5-mm-long bulk graphite and bulk silver were used as the targets as well. The powders of above materials were glued on the 5-mm-long glass plates and were installed in the vacuum chamber for ablation.

In the case of graphene nanoparticles, the ablation plasma plume may contain various species of carbon, i.e., neutrals and ions, small molecules, small and large clusters, aggregates, etc., which can contribute to harmonic generation in various extents. It is important to determine their presence in the region where the driving laser beam interacts with the expanding plasma. The morphological TEM studies confirmed the presence of relatively large multi-plate wrapped graphene species deposited on the nearby substrates at the conditions of the optimal ablation using the 370 ps pulses. Thus, the possible components in the laser heated graphene plume, at 45 ns after laser ablation, when the driving laser pulse interacts with plume, could be the large sheets of fullerenes. The monolayer, bilayer, trilayer, etc. nanosized chunks were observed during TEM measurements depending on the conditions of ablation.

Powdered targets are difficult to keep intact for a long time during their continuous ablation. Previous method to hold the stable harmonic emission from plasma was based on the rotation of target (cylindrical rod) and the ablation of its surface using the narrow heating beam [121]. In the discussed case, this method was unacceptable since the plain graphene containing target was used to create the extended graphene plasma. Since the harmonic yield at a given spot on the target became weaker after hundreds of laser shots, this effect was taken into account during the optimization of laser ablation for HHG.

The comparative studies of 0.5-mm-long and 5-mm-long graphene plasmas showed the $\sim 7\times$ growth of harmonic yield in the case of extended medium. During

these experiments, the 0.5- and 5-mm-long targets were ablated at the same fluence of heating radiation. The analysis of the dependence of the highest-order harmonic yield on the plasma length showed that the quadratic rule was maintained up to the $L = 3.5$ mm, with further saturation and gradual decrease in the harmonic yield. This observation gives a rough estimate of the coherence length for the highest-order harmonics observed in those experiments.

Figure 5.19a shows the low-order harmonic spectra from the graphene, graphite, and silver 5-mm-long plasmas at the conditions of optimal ablation. One can see the prevalence of both graphene and graphite plasma harmonics over the Ag plasma harmonics. The graphite and silver plasmas were used due to known harmonic conversion efficiencies in these media, which allowed the estimation of the photon yield from the graphene plasma.

The harmonic spectra from the graphene plasma in most cases contained the plasma emission at maximum harmonic yield. The plasma lines in the longer-wavelength range of spectrum (50–90 nm) were assigned to the singly ionized carbon. The absence of plasma emission from higher charged ions in this spectral range was attributed to the moderate ablation of graphene. The driving pulse also did not cause the appearance of strong spectral lines from the higher-charged carbon ions. Figure 5.19b shows the harmonic distribution in the cutoff region in the cases of using the graphene and graphite plasmas. The harmonics up to the 33rd order were generated in the graphene plasma. The over-excitation of graphene target or the growth of driving pulse intensity (from

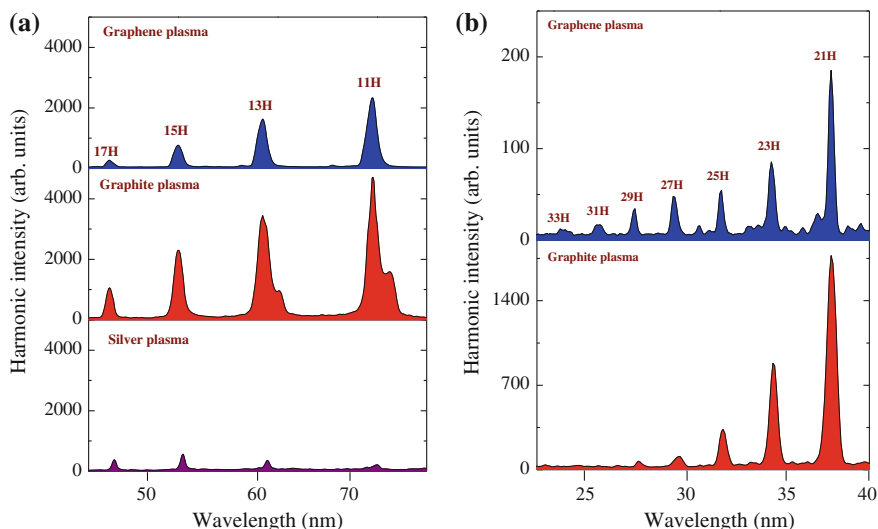
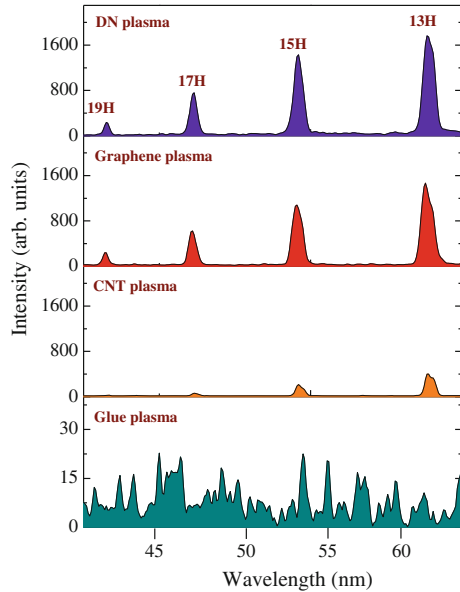


Fig. 5.19 **a** Lower-order harmonic spectra from the graphene (*upper panel*), graphite (*middle panel*), and silver (*bottom panel*) plasmas. **b** Harmonic spectra near the cut-off region from the graphene (*upper panel*) and graphite (*bottom panel*) plasmas. Reproduced from [120] with permission from Springer Science + Business Media

Fig. 5.20 Low-order harmonic spectra from the DN (upper panel), graphene (second panel), and CNT (third panel) plasmas. Bottom panel shows the plasma spectrum from the ablation of pure glue. Reproduced from [120] with permission from Springer Science + Business Media



3×10^{14} to $6 \times 10^{14} \text{ W cm}^{-2}$) did not increase the harmonic cut-off but rather led to the growth of plasma emission and deterioration of the HHG.

The comparative harmonic spectra from three different clustered plasmas (CNT, DN, and graphene) are shown in the three upper panels of Fig. 5.20. Here also shown the plasma emission observed in the case of the excitation of pure glue, without the insertion of clustered powders of above species. The ratio between the harmonic yields from graphene and bulk carbon ablation was $\sim 1:3$. Taking into account the reported conversion efficiency from the bulk graphite ablation (10^{-4} [122]), the conversion efficiency from the graphene plasma was estimated to be 3×10^{-5} for the 11th–17th harmonics. The corresponding photon yield of these harmonics was 2×10^{10} per pulse.

5.6 Concluding Comments

The studies discussed in this chapter have demonstrated the usefulness of the plasma harmonic approach for the analysis of the nonlinear optical and spectroscopic properties of the extended laser-produced plasmas formed on the non-metal surfaces.

We have analyzed the peculiarities of the HHG in the extended non-metal plasmas (crystals and semiconductors). Summarizing the current vision of the generation process in the crystal ablations, one can consider the following scenario. Initially, the ablation of the unpolished surfaces of crystals causes the heating, melting, evaporation, ionization, and disintegration of the molecules comprising

crystals. Thus the plasma under consideration is close to the gas-like medium rather than to the crystalline state. During propagation of ultrafast pulses through the mixed medium containing neutral molecules, singly ionized molecules and atoms, ionized components of disintegrated molecules, electrons, and probably clusters, the most suitable species start to emit harmonics. In the case of a group of F-containing crystals the fluorine ions became responsible for the most efficient harmonic generation compared with other components of plasmas. The latter components may also contribute, to some extent, to the growth of lower-order harmonic yield. However, this contribution seems insignificant in the shorter-wavelength region. These assumptions of the generation process and sources of harmonics were supported by both spectroscopic and nonlinear optical studies. Though the O-containing crystals have shown some other peculiarities, the harmonic generation can also be described by the same mechanism.

We have discussed the generation of the high-order harmonics of ultrafast laser radiation in the plasma plumes produced on the surfaces of fluorine—(NaF, CaF₂, LiF, and MgF₂) and oxygen—(BBO, KDP, KTP, and LBO) containing crystals. The analysis of observed plasma and harmonic emission from the ablation of crystals was supported with the studies of various factors influencing the HHG in these media. Among them the length of plasma, delay between heating and driving pulses, heating pulse energy, and distance between the crystal and propagating femtosecond pulse are the most important factors, which allowed maximizing the harmonic yield.

We have analyzed the studies of the high-order harmonics of ultrashort pulses generated in the plasma plumes produced by ablation of various elemental semiconductors (Te, Se, Si, As, Sb, and Ge). These plasma media were distinguished by the harmonic cut-offs ranging between the 27th and 51st orders. Application of two-color pump allowed generation of both odd and even harmonics, with the intensities of latter harmonics stronger than those of former ones. Strong resonance-induced 35th harmonic, with the enhancement factor of 12× compared with the neighboring harmonic orders, was observed in the case of the selenium plasma. The resonance-induced enhancement of single harmonics was also observed in the Ge, Sb, Te, and As plasmas. The application of used targets for the laser ablation and high-order harmonic generation during propagation of femtosecond pulses through the laser-produced plasmas has revealed the attractive nonlinear optical peculiarities related with the specific properties of elemental semiconductors.

We discussed the studies of the high-order harmonic generation of ultrafast laser pulses in the extended carbon cluster-contained plasmas (fullerenes, nanofibers, diamond nanoparticles, and nanotubes). These studies have shown the usefulness in the application of the carbon cluster media for the HHG. The comparison with the harmonic generation from the ablated bulk graphite showed that the probable sources of efficient harmonics in the range of 15–33 eV ($\lambda = 80\text{--}40$ nm) are the low-sized nanoparticles produced during ablation of large clusters and agglomerates of carbon-contained materials. The reason for stronger harmonic yield from cluster ablation compared with the ablation of bulk material in the case of carbon-based

species is the easiness in low-sized nanoparticles formation. The latter species can lead to the growth of lower-order harmonic yield due to enhanced probability of recombination of the accelerated electron with the whole cluster, while keeping the weak absorptive properties of the extended medium.

Previously, it was revealed that, in the case of the Al nanoparticles of different sizes, the enhancement of the harmonic signal from large nanoparticles (≥ 100 nm), with respect to that of the bulk target, was found to be negligible. Ablation of the targets constituted by larger nanoparticles most probably leads to the entrainment of larger clusters in the plume, which causes a reduction of the local field effect and contributes to a larger absorption probability of the generated short-wavelength radiation. This effect is probably exaggerated in the case of extended plasmas. The optimal sizes of the nanoparticles participating in harmonic generation is still an unresolved issue that should be investigated further due to the necessity of defining the relative role of different competitive mechanisms of the HHG in clustered plasmas. The presence of large neutral clusters and agglomerates in the extended CNF, CNT, C_{60} and DN plasmas did not enhance the harmonics. The absence of large clusters in the graphite plasmas and the similar efficiency of lower-order harmonics in the case of the ablation of bulk graphite and clustered carbon species allows concluding on the prevailing role of small carbon clusters over the large ones in the growth of η from those plasmas.

Finally, we analyzed the high-order harmonic generation of femtosecond pulses in the extended plume containing graphene nanoparticles. The harmonics up to the 33rd order were observed. The presence of graphene nanoparticles in the laser plasma was confirmed during the analysis of ablation debris. The comparative studies of harmonic generation from the ablation of graphene, carbon nanotubes, and diamond nanoparticles showed the advanced properties of the latter medium.

References

1. Y. Akiyama, K. Midorikawa, Y. Matsunawa, Y. Nagata, M. Obara, H. Tashiro, K. Toyoda, *Phys. Rev. Lett.* **69**, 2176 (1992)
2. S. Kubodera, Y. Nagata, Y. Akiyama, K. Midorikawa, M. Obara, H. Tashiro, K. Toyoda, *Phys. Rev. A* **48**, 4576 (1993)
3. C.-G. Wahlström, S. Borgström, J. Larsson, S.-G. Pettersson, *Phys. Rev. A* **51**, 585 (1995)
4. W. Theobald, C. Wülker, F.R. Schäfer, B.N. Chichkov, *Opt. Commun.* **120**, 177 (1995)
5. R.A. Ganeev, V.I. Redkorechev, T. Usmanov, *Opt. Commun.* **135**, 251 (1997)
6. K. Krushelnick, W. Tighe, S.J. Suckewer, *J. Opt. Soc. Am. B* **14**, 1687 (1997)
7. R.A. Ganeev, *High-Order Harmonic Generation in Laser Plasma Plumes* (Imperial College Press, 2012)
8. R.A. Ganeev, H. Singhal, P.A. Naik, U. Chakravarty, V. Arora, J.A. Chakera, R.A. Khan, M. Raghuramaiah, S.R. Kumbhare, R.P. Kushwaha, P.D. Gupta, *Appl. Phys. B* **87**, 243 (2007)
9. R.A. Ganeev, L.B.E. Bom, J.-C. Kieffer, T. Ozaki, *Phys. Rev. A* **76**, 023831 (2007)
10. T. Ozaki, L.B.E. Bom, R. Ganeev, J.-C. Kieffer, M. Suzuki, H. Kuroda, *Laser Part. Beams* **25**, 321 (2007)
11. R.A. Ganeev, *J. Opt. Soc. Am. B* **31**, 2221 (2014)

12. R.A. Ganeev, H. Singhal, P.A. Naik, V. Arora, U. Chakravarty, J.A. Chakera, R.A. Khan, P. V. Redkin, M. Raghuramaiah, P.D. Gupta, *J. Opt. Soc. Am. B* **23**, 2535 (2006)
13. R.A. Ganeev, P.A. Naik, H. Singhal, J.A. Chakera, P.D. Gupta, *Opt. Lett.* **32**, 65 (2007)
14. R. de Nalda, M. Lopez-Arias, M. Sanz, M. Oujja, M. Castillejo, *Phys. Chem. Chem. Phys.* **13**, 10755 (2011)
15. R.A. Ganeev, M. Suzuki, H. Kuroda, *Phys. Plasmas* **21**, 053503 (2014)
16. S. Ghimire, A.D. DiChiara, E. Sistrunk, P. Agostini, L.F. DiMauro, D.A. Reis, *Nat. Phys.* **7**, 138 (2011)
17. L. Plaja, L. Roso, *J. Mod. Opt.* **40**, 793 (1993)
18. E.S. Toma, P. Antoine, A. de Bohan, H.G. Muller, *J. Phys. B: At. Mol. Opt. Phys.* **32**, 5843 (1999)
19. M.B. Gaarde, K.J. Schafer, *Phys. Rev. A* **64**, 013820 (2001)
20. Z. Zeng, R. Li, Y. Cheng, W. Yu, Z. Xu, *Phys. Scr.* **66**, 321 (2002)
21. C.F. Faria, R. Kopylov, W. Becker, J.M. Rost, *Phys. Rev. A* **65**, 023404 (2002)
22. R. Taïeb, V. Vénier, J. Wassaf, A. Maquet, *Phys. Rev. A* **68**, 033403 (2003)
23. R.A. Ganeev, *J. Mod. Opt.* **59**, 409 (2012)
24. T.D. Donnelly, T. Ditmire, K. Neuman, M.D. Pery, R.W. Falcone, *Phys. Rev. Lett.* **76**, 2472 (1996)
25. J.W.G. Tisch, T. Ditmire, D.J. Fraser, N. Hay, M.B. Mason, E. Springate, J.P. Marangos, M. H.R. Hutchinson, *J. Phys. B: At. Mol. Opt. Phys.* **30**, L709 (1997)
26. C. Vozzi, M. Nisoli, J.-P. Caumes, G. Sansone, S. Stagira, S.D. Silvestri, M. Vecchiocattivi, D. Bassi, M. Pascolini, L. Poletto, P. Villorresi, G. Tondello, *Appl. Phys. Lett.* **86**, 111121 (2005)
27. H. Ruf, C. Handschin, R. Cireasa, N. Thiré, A. Ferré, S. Petit, D. Descamps, E. Mével, E. Constant, V. Blanchet, B. Fabre, Y. Mairesse, *Phys. Rev. Lett.* **110**, 083902 (2013)
28. P. Moreno, L. Plaja, L. Roso, *Europhys. Lett.* **28**, 629 (1994)
29. V. Vénier, R. Taïeb, A. Maquet, *Phys. Rev. A* **65**, 013202 (2001)
30. R.A. Ganeev, M. Suzuki, M. Baba, M. Ichihara, H. Kuroda, *J. Appl. Phys.* **103**, 063102 (2008)
31. R.A. Ganeev, L.B.E. Bom, T. Ozaki, *J. Phys. B: At. Mol. Opt. Phys.* **42**, 055402 (2009)
32. H. Singhal, R.A. Ganeev, P.A. Naik, A.K. Srivastava, A. Singh, R. Chari, R.A. Khan, J.A. Chakera, P.D. Gupta, *J. Phys. B: At. Mol. Opt. Phys.* **43**, 025603 (2010)
33. R.A. Ganeev, C. Hutchison, M. Castillejo, I. Lopez-Quintas, F. McGrath, D.Y. Lei, J. P. Marangos, *Phys. Rev. A* **88**, 033803 (2013)
34. Y. Pertot, S. Chen, S.D. Khan, L.B.E. Bom, T. Ozaki, Z. Chang, *J. Phys. B: At. Mol. Opt. Phys.* **45**, 074017 (2012)
35. R.A. Ganeev, T. Witting, C. Hutchison, F. Frank, P.V. Redkin, W.A. Okell, D.Y. Lei, T. Roschuk, S.A. Maier, J.P. Marangos, J.W.G. Tisch, *Phys. Rev. A* **85**, 015807 (2012)
36. R.A. Ganeev, L.B.E. Bom, J. Abdul-Hadi, M.C.H. Wong, J.P. Brichta, V.R. Bhardwaj, T. Ozaki, *Phys. Rev. Lett.* **102**, 013903 (2009)
37. R.A. Ganeev, P.A. Naik, H. Singhal, J.A. Chakera, M. Kumar, U. Chakravarty, P.D. Gupta, *Opt. Commun.* **285**, 2934 (2012)
38. R.A. Ganeev, M. Suzuki, S. Yoneya, H. Kuroda, *J. Opt. Soc. Am. B* **31**, 3105 (2014)
39. M. Oujja, R. de Nalda, M. López-Arias, R. Torres, J.P. Marangos, M. Castillejo, *Phys. Rev. A* **81**, 043841 (2010)
40. R.C. Estler, E.C. Apfel, N.S. Nogar, *J. Opt. Soc. Am. B* **4**, 281 (1987)
41. R. Mitzner, A. Rosenfeld, R. König, *Appl. Surf. Sci.* **69**, 180 (1993)
42. W.M. Lau, I. Bello, M. Sayer, L. Zou, *Appl. Phys. Lett.* **64**, 300 (1994)
43. S. Gogoll, E. Stenzel, H. Johansen, M. Reichling, E. Matthias, *Nucl. Instrum. Methods Phys. Res. Sect. B* **116**, 279 (1996)
44. K. Hanamoto, M. Sasaki, T. Miyashita, Y. Kido, Y. Nakayama, M. Fujiwara, R. Kaigawa, *Nucl. Instrum. Methods Phys. Res. Sect. B* **129**, 228 (1997)
45. C.M.S. Rauthan, G.S. Virdi, B.C. Pathak, A. Karhigeyan, *J. Appl. Phys.* **83**, 3668 (1998)

46. M. Reichling, J. Sils, H. Johansen, E. Matthias, *Appl. Phys. A* **69**, S743 (1999)
47. B.S. Zhao, M. Castillejo, D.S. Chung, B. Friedrich, D. Herschbach, *Rev. Sci. Instrum.* **75**, 146 (2004)
48. F.J. Gordillo-Vázquez, A. Perea, A.P. McKiernan, C.N. Afonso, *Appl. Phys. Lett.* **86**, 181501 (2005)
49. S.J. Henley, G.M. Fuge, M.N.R. Ashfold, *J. Appl. Phys.* **97**, 023304 (2005)
50. T. Sakai, A. Kaimai, T. Otake, K. Yashiro, T. Kawada, J. Mizusaki, M. Nishioka, *Solid State Ionics* **177**, 1601 (2006)
51. A. Kramida, Y. Ralchenko, J. Reader, and NIST ASD Team, NIST Atomic Spectra Database (ver. 5.1) (National Institute of Standards and Technology, 2013). Available at <http://physics.nist.gov/asd>
52. J.L. Krause, K.J. Schafer, K.C. Kulander, *Phys. Rev. Lett.* **68**, 3535 (1992)
53. P.B. Corkum, *Phys. Rev. Lett.* **71**, 1994 (1993)
54. M. Lewenstein, P. Balcou, M.Y. Ivanov, A. L'Huillier, P.B. Corkum, *Phys. Rev. A* **49**, 2117 (1994)
55. R.A. Ganeev, M. Suzuki, S. Yoneya, H. Kuroda, *J. Appl. Phys.* **117**, 023114 (2015)
56. R. D'Arcy, J.T. Costello, C. McGuinness, G. O'Sullivan, *J. Phys. B: At. Mol. Opt. Phys.* **32**, 4859 (1999)
57. L. Gaynor, N. Murphy, D. Kilbane, A. Cummings, G.O. Sullivan, J.T. Costello, P. van Kampen, E.T. Kennedy, *J. Phys. B: At. Mol. Opt. Phys.* **38**, 2895 (2005)
58. K.R. Rao, S.G.K. Murti, *Proc. R. Soc. A* **145**, 681 (1934)
59. N. Murphy, J.T. Costello, E.T. Kennedy, C. McGuinness, J.P. Mosnier, B. Weinmann, G. O'Sullivan, *J. Phys. B: At. Mol. Opt. Phys.* **32**, 3905 (1999)
60. D.A. Esteves, R.C. Bilodeau, N.C. Sterling, R.A. Phaneuf, A.L.D. Kilcoyne, E.C. Red, A. Aguilar, *Phys. Rev. A* **84**, 013406 (2011)
61. M. Suzuki, M. Baba, H. Kuroda, R.A. Ganeev, T. Ozaki, *Opt. Express* **15**, 1161 (2007)
62. A. Tauheed, A. Hala, *Phys. Scr.* **85**, 025304 (2012)
63. R.A. Ganeev, *Plasma Harmonics* (Pan Stanford Publishing, 2014)
64. J. Kim, G.H. Lee, S.B. Park, Y.S. Lee, T.K. Kim, C.H. Nam, T. Mocek, K. Jakubczak, *Appl. Phys. Lett.* **92**, 021125 (2008)
65. R.A. Ganeev, C. Hutchison, A. Zair, T. Witting, F. Frank, W.A. Okell, J.W.G. Tisch, J. P. Marangos, *Opt. Express* **20**, 90 (2012)
66. R.A. Ganeev, M. Baba, M. Suzuki, H. Kuroda, *J. Appl. Phys.* **115**, 183101 (2014)
67. R.A. Ganeev, M. Baba, M. Suzuki, H. Kuroda, *J. Phys. B: At. Mol. Opt. Phys.* **47**, 135401 (2014)
68. R.A. Ganeev, M. Baba, M. Suzuki, H. Kuroda, *Phys. Lett. A* **339**, 103 (2005)
69. R.A. Ganeev, H. Singhal, P.A. Naik, I.A. Kulagin, P.V. Redkin, J.A. Chakera, M. Tayyab, R. A. Khan, P.D. Gupta, *Phys. Rev. A* **80**, 033845 (2009)
70. C. Kan, N.H. Burnett, C. Capjack, R. Rankin, *Phys. Rev. Lett.* **79**, 2971 (1997)
71. J. Stadler, R. Mikulla, H.-R. Trebin, *Int. J. Mod. Phys.* **8**, 1131 (1997)
72. R.A. Ganeev, M. Suzuki, M. Baba, M. Ichihara, H. Kuroda, *J. Opt. Soc. Am. B* **25**, 325 (2008)
73. R.A. Ganeev, M. Suzuki, M. Baba, M. Ichihara, H. Kuroda, *J. Phys. B: At. Mol. Opt. Phys.* **41**, 045603 (2008)
74. G. Javahery, H. Wincel, S. Petrie, D.K. Bohme, *Chem. Phys. Lett.* **204**, 467 (1993)
75. J.R.V. de Aldana, L. Roso, *J. Opt. Soc. Am. B* **18**, 325 (2001)
76. K. Nobusada, K. Yabana, *Phys. Rev. A* **70**, 043411 (2004)
77. S.V. Popruzhenko, M. Kundu, D.F. Zaretsky, D. Bauer, *Phys. Rev. A* **77**, 063201 (2008)
78. D.F. Zaretsky, P. Korneev, W. Becker, *J. Phys. B: At. Mol. Opt. Phys.* **43**, 105402 (2010)
79. G.Y. Slepuyan, S.A. Maksimenko, V.P. Kalosha, J. Hermann, E.E.B. Campbell, I.V. Hertel, *Phys. Rev. A* **60**, R777 (1999)
80. O.E. Alon, V. Averbukh, N. Moiseyev, *Phys. Rev. Lett.* **85**, 5218 (2000)

81. G.Y. Slepuyan, S.A. Maksimenko, V.P. Kalosha, A.V. Gusakov, J. Herrman, *Phys. Rev. A* **63**, 053808 (2001)
82. H. Hsu, L.E. Reichl, *Phys. Rev. B* **74**, 115406 (2006)
83. J. Sun, Z. Guo, W.Z. Liang, *Phys. Rev. B* **75**, 195438 (2007)
84. A. Bahari, N. Daneshfar, H. Khosravi, *Carbon* **47**, 457 (2009)
85. R.A. Ganeev, P.A. Naik, H. Singhal, J.A. Chakera, M. Kumar, M.P. Joshi, A.K. Srivastava, P.D. Gupta, *Phys. Rev. A* **83**, 013820 (2011)
86. G.P. Zhang, *Phys. Rev. Lett.* **95**, 047401 (2005)
87. M.F. Ciappina, A. Becker, A. Jaroń-Becker, *Phys. Rev. A* **76**, 063406 (2007)
88. M.F. Ciappina, A. Becker, A. Jaroń-Becker, *Phys. Rev. A* **78**, 063405 (2008)
89. R.A. Ganeev, C. Hutchison, T. Witting, F. Frank, S. Weber, W.A. Okell, E. Fiordilino, D. Cricchio, F. Persico, A. Zaïr, J.W.G. Tisch, J.P. Marangos, *J. Opt. Soc. Am. B* **30**, 7 (2013)
90. G.F. Bertsch, A. Bulgac, D. Tomanek, Y. Wang, *Phys. Rev. Lett.* **67**, 2690 (1991)
91. A.V. Hertel, H. Steger, J. de Vries, B. Weisser, C. Menzel, B. Kamke, W. Kamke, *Phys. Rev. Lett.* **68**, 784 (1992)
92. T.G. Dietz, M.A. Duncan, D.E. Powers, R.E. Smalley, *J. Chem. Phys.* **74**, 6511 (1981)
93. T. Seto, Y. Kawakami, N. Suzuki, M. Hirasawa, N. Aya, *Nano Lett.* **1**, 315 (2001)
94. M. Hirasawa, T. Orii, T. Seto, *Appl. Phys. Lett.* **88**, 093119 (2006)
95. A.V. Bulgakov, I. Ozerov, W. Marine, *Thin Solid Films* **453–454**, 557 (2004)
96. S. Eliezer, N. Eliaz, E. Grossman, D. Fisher, I. Gouzman, Z. Henis, S. Pecker, Y. Horovitz, M. Fraenkel, S. Maman, Y. Lereah, *Phys. Rev. B* **69**, 144119 (2004)
97. S. Amoruso, G. Ausanio, R. Bruzzese, M. Vitiello, X. Wang, *Phys. Rev. B* **71**, 033406 (2005)
98. D. Du, X. Liu, G. Korn, J. Squier, G. Mourou, *Appl. Phys. Lett.* **64**, 3071 (1994)
99. B.N. Chichkov, C. Momma, S. Nolte, F. von Alvensleben, A. Tünnermann, *Appl. Phys. A* **63**, 109 (1996)
100. S. Nolte, C. Momma, H. Jacobs, A. Tünnermann, B.N. Chichkov, B. Wellegehausen, H. Welling, *J. Opt. Soc. Am. B* **14**, 2716 (1997)
101. E.G. Gamaly, A.V. Rode, B. Luther-Davies, *J. Appl. Phys.* **85**, 4213 (1999)
102. S.X. Hu, Z.Z. Xu, *Phys. Rev. A* **56**, 3916 (1997)
103. M. Sanz, M.E. López-Arias, E. Rebollar, R. de Nalda, M. Castillejo, *J. Nanopart. Res.* **13**, 6621 (2011)
104. E.A. Rohlfing, *J. Chem. Phys.* **89**, 6103 (1988)
105. W.R. Creasy, J.T. Brenna, *Chem. Phys.* **126**, 453 (1988)
106. S.C. O'Brien, J.R. Heath, R.F. Curl, R.E. Smalley, *J. Chem. Phys.* **88**, 220 (1988)
107. S.B.H. Bach, J.R. Eyler, *J. Chem. Phys.* **92**, 358 (1990)
108. Y.-K. Choi, H.-S. Im, K.-W. Jung, *Int. J. Mass Spectrom.* **189**, 115 (1999)
109. A. Kaplan, M. Lenner, C. Huchon, R.E. Palmer, *Appl. Phys. A* **92**, 999 (2008)
110. J. Houška, N.R. Panyal, E.M. Peña-Méndez, J. Havel, *Rapid Commun. Mass Spectrom.* **23**, 1125 (2009)
111. R.A. Ganeev, C. Hutchison, T. Witting, F. Frank, W.A. Okell, A. Zaïr, S. Weber, P.V. Redkin, D.Y. Lei, T. Roschuk, S.A. Maier, I. López-Quintás, M. Martín, M. Castillejo, J.W. G. Tisch, J.P. Marangos, *J. Phys. B: At. Mol. Opt. Phys.* **45**, 165402 (2012)
112. R.A. Ganeev, M. Suzuki, H. Kuroda, *Phys. Rev. A* **89**, 033821 (2014)
113. K. Geim, K.S. Novoselov, *Nat. Mater.* **6**, 183 (2007)
114. E. Hendry, P.J. Hale, J. Moger, A.K. Savchenko, *Phys. Rev. Lett.* **105**, 097401 (2010)
115. K.L. Ishikawa, *Phys. Rev. B* **82**, 201402 (2010)
116. S.A. Mikhailov, *Phys. Rev. B* **84**, 045432 (2011)
117. S. Wu, L. Mao, A.M. Jones, W. Yao, C. Zhang, X. Xu, *Nano Lett.* **12**, 2032 (2012)
118. M. Gullans, D.E. Chang, F.H.L. Koppens, F.J. García de Abajo, M.D. Lukin, *Phys. Rev. Lett.* **111**, 247401 (2013)

119. S.A. Sørngård, S.I. Simonsen, J.P. Hansen, *Phys. Rev. A* **87**, 053803 (2013)
120. R.A. Ganeev, M. Suzuki, M. Baba, S. Yoneya, H. Kuroda, *J. Exp. Theor. Phys. Lett.* **100**, 434 (2014)
121. C. Hutchison, R.A. Ganeev, T. Witting, F. Frank, W.A. Okell, J.W.G. Tisch, J.P. Marangos, *Opt. Lett.* **37**, 2064 (2012)
122. L.B. Elouga Bom, Y. Pertot, V.R. Bhardwaj, T. Ozaki, *Opt. Express* **19**, 3077 (2011)

Chapter 6

New Opportunities of Extended Plasma Induced Harmonic Generation

In this chapter, we present the studies of low-order harmonic generation of picosecond laser radiation in the perforated plasma plumes. The periodic plasma structures were produced on the perforated aluminum targets, the copper strips, and the bunch of pencil leads. Further, we discuss the enhancement of single harmonic in the In_2O_3 and Sn cluster-contained plasmas, which allowed both the efficient generation of lower-order harmonics of ultrashort pulses and the resonance enhancement of single harmonics. The comparison of the harmonic spectra obtained using the plasmas produced on bulk and clustered materials showed that similar enhancement of single harmonics occurs in the case of the strong excitation of nanoparticle-contained targets, while weaker excitation causes generation of featureless lower-order harmonic spectra. Finally, we analyze the method of the measurements of electron density in the low-dense, low-ionized laser-produced plasmas using the nonlinear optical process of high-order harmonic generation of ultrashort pulses at the conditions of the quasi-phase-matching of driving and harmonic waves.

The extended plasmas can offer various opportunities during interaction with short pulses. Here we present the studies of low- (third and fourth) order harmonic generation of picosecond laser radiation in the perforated plasma plumes. The periodic plasma structures were produced on the perforated aluminum targets, the copper strips, and the bunch of pencil leads. We analyze the influence of the distance between plasma jets and the low-order harmonic intensity using single-color and two-color pumps of the extended periodic plasmas produced on various surfaces. While the shortening of the length of extended homogeneous plasmas led to a considerable decrease of plasma harmonic intensity, the application of perforated plasmas led to the enhancement of the lower-order harmonics at the smallest used sizes of plasma jets. The $8\times$ enhancement of third harmonic yield was observed from the set of 0.15-mm-long plasma jets compared with the plain aluminum plasma.

We discuss the enhancement of single harmonic in the nanoparticle-contained plasmas. The results of studies of laser-produced In_2O_3 and Sn cluster-contained plasmas allowed both the efficient generation of lower-order harmonics of ultrashort pulses and the resonance enhancement of single (13th and 17th) harmonics. The comparison of the harmonic spectra obtained using the plasmas produced on bulk

and clustered materials showed that similar enhancement of single harmonics occurs in the case of the strong excitation of nanoparticle-contained targets, while weaker excitation causes generation of featureless lower-order harmonic spectra.

We also analyze the method of the measurements of electron density in the low-dense, low-ionized laser-produced plasmas using the nonlinear optical process of high-order harmonic generation of ultrashort pulses at the conditions of the quasi-phase-matching of driving and harmonic waves. N_e was defined using the relations of QPM. We discuss the results of N_e measurements in the region of 10^{16} cm^{-3} using the multi-jet silver plasma produced for the HHG.

6.1 Third and Fourth Harmonics Generation in Laser-Induced Periodic Plasmas

In this section, we analyze the first demonstration of the enhanced low-order harmonics of picosecond laser radiation in the perforated plasmas compared with the imperforated extended plasmas [1]. We discuss the properties of the multiple plasma jets produced by three different methods for the low-order harmonic generation. Particularly, we analyze the third (3H) and fourth (4H) harmonic generation using the single-color and two-color pumps of the plasmas of different periodicity produced on the surfaces of various targets. It was shown in [1] that, while a shortening of the plasma produced on the homogeneous surfaces causes a considerable decrease of plasma harmonic intensity, the application of short-period plasmas leads to the enhancement of low-order harmonics.

A single pulse from the Nd:YAG laser (wavelength 1064 nm, pulse duration 38 ps) was divided on two parts, one (heating pulse) with the energy of up to $E_{\text{hp}} = 28 \text{ mJ}$, which was used for the plasma formation on the targets, and another (fundamental pulse) with the energy of up to $E_{\text{fp}} = 15 \text{ mJ}$, which was used for the harmonic generation in the plasmas. The heating pulse was focused using a 30 cm focal length cylindrical lens inside the vacuum chamber contained the target to create the extended plasma plume (Fig. 6.1). The fundamental pulse, after some delay from the beginning of ablation, was focused onto the prepared plasma from the orthogonal direction, parallel to the target surface. The intensity of fundamental pulse at the focus area was $2 \times 10^{13} \text{ W cm}^{-2}$. The confocal parameter of this focused radiation (8 mm) was longer than the length of extended plasma plumes (5 mm). The delay between these two pulses during most of experiments was maintained at 30 ns, which was optimal for the efficient 3H ($\lambda = 355 \text{ nm}$) generation in laser-produced plasmas.

The two-color pump scheme was used to analyze the 4H ($\lambda = 266 \text{ nm}$) generation. Part of the fundamental pulse was converted to the second harmonic in the nonlinear crystal (KDP, type I). Conversion efficiency of second harmonic was 6%. The fundamental and second harmonic beams were then focused inside the plasma

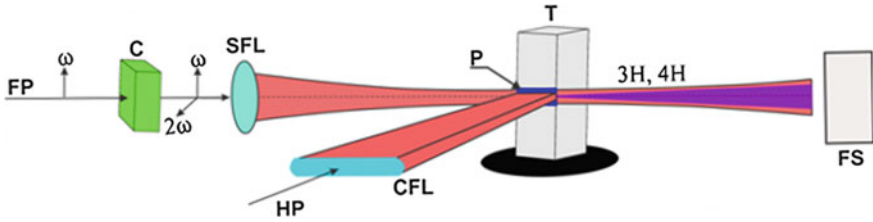
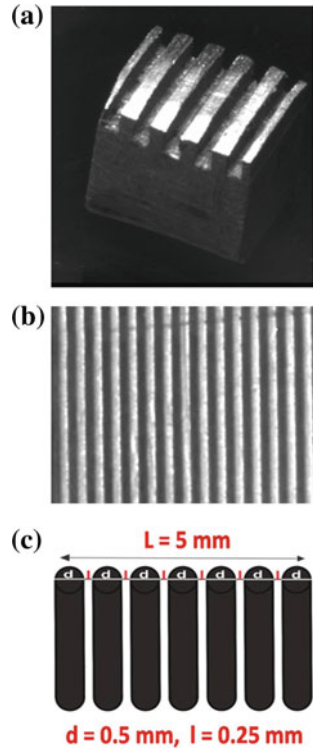


Fig. 6.1 Experimental scheme. *FP* fundamental pulse; *HP* heating pulse; *C* nonlinear crystal (KDP); *SFL* spherical focusing lens; *CFL* cylindrical focusing lens; *T* target; *P* plasma; *FS* fiber spectrometer (HR4000). Reproduced from [1] with permission from Elsevier

plume. The polarizations of these two pumps were orthogonal to each other (Fig. 6.1). The 3H and 4H radiations were analyzed using the spectrometer.

The targets were made of various materials (aluminum, copper, and pencil lead). The sizes of targets where the laser ablation occurred were 5 mm. A three-coordinate manipulator made it possible to move the targets and control a zone of interaction of the fundamental radiation with the plasma relative to the target surface. The shapes of these targets allowed the formation of the periodic plasma jets. The example of aluminum target is shown in Fig. 6.2a. The periods

Fig. 6.2 Periodically perforated targets used in these experiments.
a Perforated aluminum target.
b Microlithographic copper strips.
c Bunch of pencil leads. Reproduced from [1] with permission from Elsevier



between the perforated areas of Al targets were chosen to be 0.5, 0.3 and 0.15 mm. The corresponding widths of plasma jets were 0.5, 0.3 and 0.15 mm respectively. Another target was a microlithographic periodic surface of the copper strips (Fig. 6.2b), with their width of 0.15 mm and the distance between strips of 0.15 mm. Third target comprised a bunch of pencil leads placed parallel to each other. The leads were polished so that their width was 0.5 mm and the distance between these rods was 0.25 mm (Fig. 6.2c). The plain Al, Cu, and C targets of the widths of 5 mm were also used for the comparison with above described perforated targets.

The application of periodic targets assumes a decrease of a whole length of medium compared with the ablation of plain, imperforated target. In the case of aluminum, copper, and carbon targets, the perforation of plasma leads to a decrease of effective lengths of plasma plumes from ~ 5 mm (plain targets) to 2.5 mm (perforated aluminum targets with different widths of single plasma jet), 2.5 mm (microlithographic periodic surface of 0.15 mm wide copper strips separated by 0.15 mm of dielectric), and 3.5 mm (bunch of pencil lead targets).

The sizes of ablated area were restricted by the length of targets and focusing conditions using cylindrical lens. The focusing of heating pulse on the plain target surface produced the line plasma with the thickness of 40 μm (FWHM). The ablated area represented a parallelepiped with the sizes $5 \times 0.04 \text{ mm}^2$. The intensity of 2.1 mJ, 38 ps heating pulses on the plain target surface was $3 \times 10^{10} \text{ W cm}^{-2}$. The intensities of heating radiation in the cases of 8.2 and 5 mJ pulses were $\sim 1.2 \times 10^{11}$ and $\sim 2.2 \times 10^{11} \text{ W cm}^{-2}$.

Once one assumes that only micro-processes (i.e. single particle response) rather than macro-processes (related with collective propagation effects, etc.) govern the yield of harmonic emission then the 3H intensity should follow the quadratic dependence on the length (L) of nonlinear medium ($I_{3\text{H}} \propto L^2$, where $l = 2$ [2]). These dependences were analyzed, for both 3H and 4H, in a few plasma plumes produced on the plain surfaces of Al and Cu targets by changing the length of plasmas using the slit placed after the cylindrical lens. These $I_{3\text{H},4\text{H}}(L)$ studies are shown here for the comparison of the nonlinear optical response of short and long media to emphasize the involvement of macro-processes in the cases when the extended plasma was shortened and modified to be a perforated one.

The experiments were carried out at $E_{\text{hp}} = 2$ mJ when the free electron concentration in the plasma did not affect the phase relations between the interacting waves. At these conditions, the coherence length of 3H and 4H was larger than the width of the targets due to small concentration of free electrons. The absorption of 355- and 266-nm pulses in the plasma plumes was insignificant, due to small concentration of plasma ($\sim 2 \times 10^{17} \text{ cm}^{-3}$). Figure 6.3 presents the dependences of the 3H and 4H intensities on the length of Al plasma. In the case of 3H generation (Fig. 6.3a), this dependence had a slope l close to 2.2 up to the $L \sim 2.5$ mm, with further insignificant decrease of the slope ($l = 1.8$). The harmonics were assumed to be generated from the ablated aluminum atoms and singly-charged ions. The spectroscopy studies of Al plasma showed the neutral and singly charged ionic lines. In the meantime, the involvement of clusters in harmonic generation is also

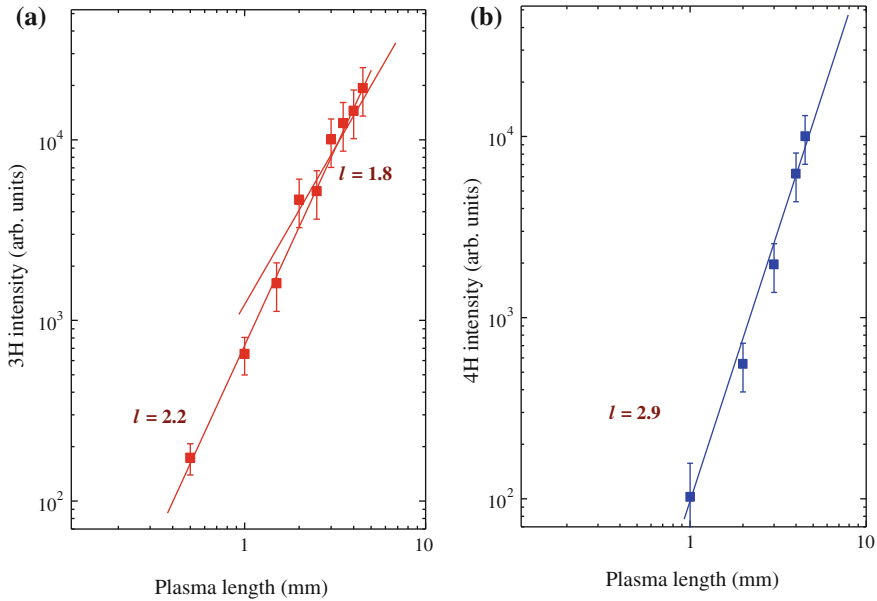


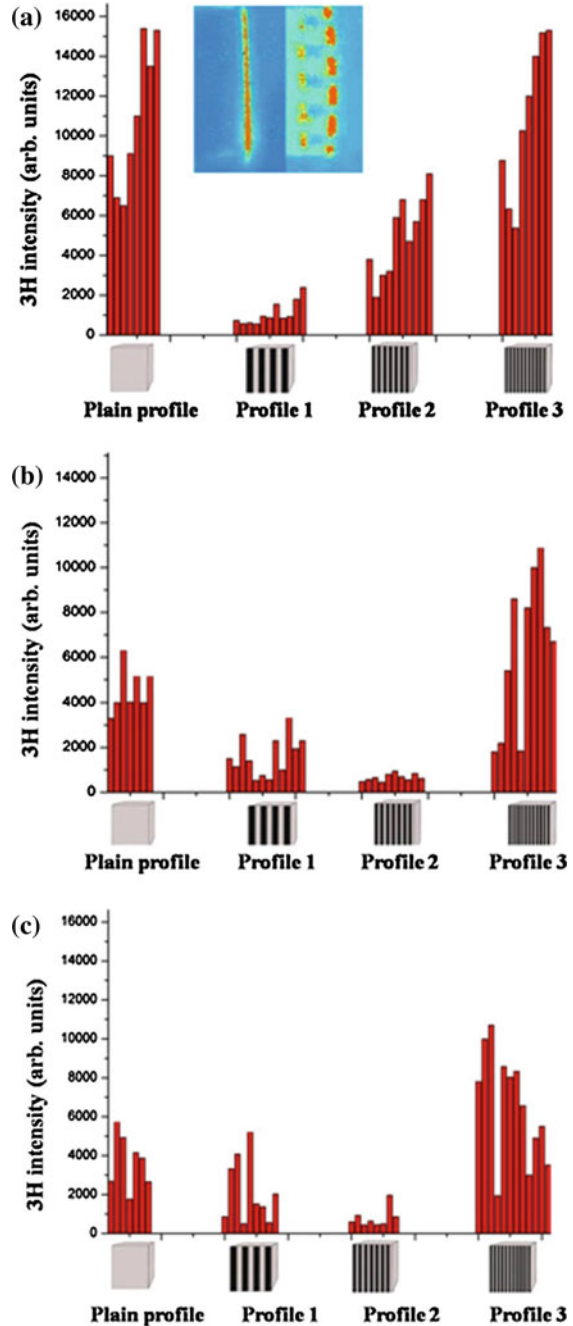
Fig. 6.3 Dependences of the **a** 3H and **b** 4H intensities on the length of Al plasma. Reproduced from [1] with permission from Elsevier

possible. Similar dependences were observed in the cases of plain copper and carbon plasmas.

The 4H was stronger than the 3H, though the ratio between the intensities of these harmonics was unstable, due to some instability of laser intensity and plasma formation. The conversion efficiencies of 3H and 4H were measured to be 3×10^{-5} and 5×10^{-5} using the technique described in Sect. 2.3.2. The nonlinear dependence of the 4H yield on the length of plasma medium was analyzed using the Al plasma plume (Fig. 6.3b). The slope of $I_{4H}(L)$ dependence ($l = 2.9$) was steeper compared with the 3H case. The reasons of the increase of a slope of this dependence are not clear, since both 3H and 4H generation are related with the four-photon micro-processes. The possible assumption for explanation of this difference of slopes is the involvement of macro-processes in overall yield of 4H, or imperfect overlapping of the two pump beams. Another option is the involvement of the laser ablation-produced nanoparticles in the enhancement of harmonic yield in the case of longer plasmas [3].

The growth of heating pulse energy above 3 mJ led to a decrease of the 3H yield from long (5 mm) plain plasma (Fig. 6.4), which is a sign of the influence of free electrons on the phase relation between the harmonic and fundamental waves during propagation through the extended plasma. To overcome this decrease of harmonic yield one has to implement the perforated plasma medium. Below we describe the results of studies of the periodic modulation of plasma length at different heating pulse energies.

Fig. 6.4 Dependences of the 3H intensity on the profile of Al targets at different energies of heating pulse. The plasma widths and distances between plasma jets were 0.5 mm (profile 1), 0.3 mm (profile 2), and 0.15 mm (profile 3). Thick red lines show a statistic distribution of 3H yield from shot to shot. These dependences were taken at the heating pulse energies of **a** 2.1 mJ, **b** 8.2 mJ and **c** 15 mJ. *Inset* in Fig. 6.4a shows the plasma images obtained from the plain aluminum target (*left panel*) and perforated target (profile 1, *right panel*). Reproduced from [1] with permission from Elsevier



The measurements (Fig. 6.3a) showing a significant decrease of harmonic yield with shortening of plasma area may predict a fall of 3H efficiency for the periodic plasmas, using the effective lengths two times shorter than the length of the plasma produced on the plain target. Actually, one can expect a four-fold decrease of 3H yield in the cases of periodic Al and Cu plasmas and a 2.4-fold decrease of 3H yield in the case of a bunch of pencil leads, once we assume a decisive role of micro-processes and ignore the role of macro-processes, such as the phase matching of fundamental and harmonic waves. This was true for the aluminum targets with relatively large sizes of plasma jets (0.5 and 0.3 mm; see the 3H yields in the cases of perforated Al targets with the profiles 1 and 2 shown in Fig. 6.4). Notice a change of the relative intensities of 3H in the case of these two targets with the increase of heating pulse energy. Particularly, the formation of 0.5-mm-long jets led to a $\sim 3\text{--}5$ fold decrease of the 3H yield at different energies of heating pulse, which follows from the $I_{3H} \propto L^2$ rule.

Another pattern was observed in the case of the aluminum target producing plasma jets of shortest period (target with profile 3, with the thickness of plasma jets of 0.15 mm). Starting from smallest energies of heating pulse, no significant decrease of 3H yield was observed from the plasma produced on this perforated target compared with the plain target. Moreover, with the increase of heating pulse energy, the 3H yield from this periodic target became stronger compared with the one from the plain target. In particular, at the 15 mJ energy of heating pulse, the harmonic yield from these plasma jets was two times stronger than the one from the plain target. The length of perforated nonlinear medium was two times less than the length of extended plasma. The expected quadratic dependence of the harmonic yield on the length of medium should lead to the four-fold decrease of the harmonics from the shorter plasma rather than the two-fold increase observed in those studies. One can obtain from this assumption an eight-fold growth of 3H yield from the used perforated target assuming the comparison with the plain target of the same length of plasma (as it is a practice accepted during harmonic generation in the perforated gaseous media [4, 5]), contrary to the expected decrease of conversion efficiency related with the involvement of single-particle response.

The inset in Fig. 6.4a shows the plasma images obtained from the plain Al target (left panel) and periodic target (right panel, profile 1). In the case of periodic Al samples, the excitation of target by the heating radiation focused using the cylindrical lens led to formation of plasma on the upper and bottom surfaces (see the plasma jets on the right side of inset in Fig. 6.4a). These images were taken from the top of vacuum chamber to show the profiles of plasmas used in those experiments (the driving pulse was propagated through these plasmas from the bottom to the top). The plasma formation in the deeps of target profile (0.5 mm below the surface) causes longer time for those particles to propagate toward the axis of driving pulse propagation. They reach this area after $(0.5 + 0.1 \text{ mm})/5 \times 10^5 \text{ cm s}^{-1} = 120 \text{ ns}$, i.e. long time after the propagation of 38 ps driving pulse, and thus do not participate in harmonic generation. Thus the driving pulse propagates only through the periodically shaped plasma jets produced on the upper surface area.

In the case of plain plasma, the 3H radiation saturates over the length of L_{coh} and then down-converts back to the 1064 nm radiation due to the change of the phase difference between the two pulses. This destructive interference may restrict the harmonic generation efficiency for longer length media, thus cancelling the advantages of using the extended plasmas. To overcome this obstacle, one can create the conditions when, after propagation of the path equal to the L_{coh} for this nonlinear optical process, the driving and converted radiations propagate in a free space, thus preventing the down conversion (see also Chap. 3). The “optimal” length of plasma jet depends on a few parameters, such as harmonic order and concentration of the free electrons in the plasma. The variation of heating pulse energy directly influences the change of free electron concentration and correspondingly modulates the refractive index of plasma and phase matching conditions.

At stronger heating pulses, the yield of 3H from the plain plasma becomes less than at $E_{\text{hp}} = 2.4$ mJ (see Fig. 6.4; the plots (a–c) have the same scale, which allows comparison of the harmonic yields for different targets and pumps). One can expect various scenarios in the case of presence of the free electrons in long plain plasma, which can change the phase matching conditions between the driving and harmonic waves. The exceeding of the length of plasma over the coherence length of 3H generation should lead to a decrease of harmonic yield. This was achieved during over-excitation of plain plasma. The observation of stronger harmonic yield from the short-period plasma (profile 3) manifests the first demonstration of the prevention of destructive interference between the long-wavelength waves propagating through the plasma medium.

Analogous comparative studies of 4H generation in the plain and periodic plasmas have also revealed the growing influence of plasma sizes in the case of periodic jets. Stronger (compared with the 3H generation) $I_{4\text{H}}(L)$ dependence (Fig. 6.3b) should cause a steeper decrease of harmonic yield in the periodic plasmas. However, experiments with the aluminum targets perforated with 0.15 mm period showed that the 4H yield was at least the same as the one from the bulk long plasma.

The effect of perforated plasma was also observed in the case of microlithographic copper strips. During ablation of these targets, the plasma formation occurred predominantly on the metallic parts of microlithographic target. The ablation of intermediate parts of this target containing organic material was inefficient for the plasma formation and 3H generation, which was confirmed during the experiments using same targets without copper strips. At 8 mJ heating pulse energy, the 3H yield from plain copper plasma clearly exceeded the one from ablated microlithographic target. However, with the growth of pumping energy ($E_{\text{hp}} = 15$ mJ), the pattern of this dependence was considerably changed, and the 3H yields from these plasmas became approximately equal. Further growth of heating pulse energy caused a significant decrease of harmonic conversion efficiency for both targets. No 3H was observed at the heating pulse energy of 25 mJ.

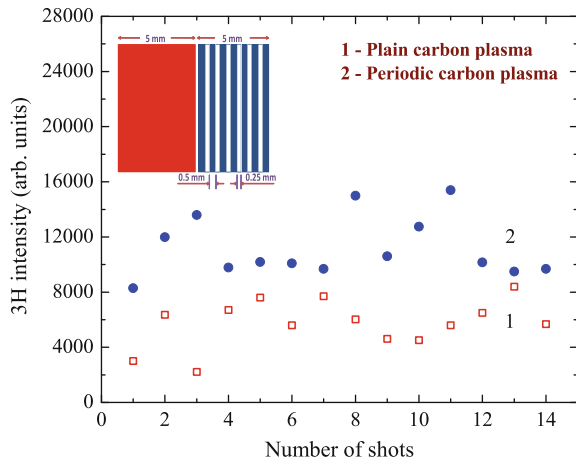
Final set of those studies was related with the comparison of the 3H harmonic yields from the plasmas produced on the plain carbon target (Fig. 6.5, red empty

squares) and periodic strips of the pencil leads (blue filled circles). The whole lengths of these targets were 5 mm, while the length of plasma area in the latter case was 3.5 mm. The energies of heating and fundamental pulses in both these cases were 8.2 and 15 mJ. The harmonic yield from periodic target exceeded the one from plain target (Fig. 6.5), while it should be decreased almost 2.5 times due to shorter length of plasma (5 and 3.5 mm for the plain carbon target and periodic target respectively).

The plasma and electron concentrations of the Al plasma produced using the 38-ps heating pulses at the fluence of 0.7 J cm^{-2} were calculated using the code ITAP IMD [6]. The calculated N_p and N_e at this fluence were 2×10^{17} and $3 \times 10^{16} \text{ cm}^{-3}$. To maintain the QPM conditions, one has to realize a modulation of the coupling between the driving and converted waves, which is periodic along the generation path. For a given size of single plasma jet, the QPM for the q th harmonic could be fulfilled at a fixed product $q \times N_e$ (since $L_{\text{coh}} \approx 1.5 \times 10^{18} (q \times N_e)^{-1}$ [7] for the 1064 nm radiation). An increase of N_e (at higher excitation of target) should lead to the optimization of the QPM for the lowest harmonic to keep the product $q \times N_e$ unchanged at the fixed spatial characteristics of plasma jets. This feature is demonstrated in Fig. 6.4c for the shortest (0.15 mm) plasma jets.

The relation between the optimal thickness of the plasma jets (L_{coh}), which corresponded to the coherence length of specific harmonic, and the maximally enhanced harmonic order (q) is given by the above formula. As it is seen, it depends on the product $q \times N_e$. One can assume that, for lowest orders, the over-excited plasma could be a good choice. At a reasonable excitation of targets (i.e. at a fluence of $\sim 1\text{--}2 \text{ J cm}^{-2}$), the maximally enhanced harmonics from the multi-jet plasmas should be in the range of twenties orders at the used thickness of single plasma jet. In the meantime, the weak dispersion of such plasma would lead to the conditions when some lesser enhancement will also be seen for a large number of neighboring harmonic orders, particularly lower-order ones.

Fig. 6.5 Comparison of 3H yields from the plasmas produced on the plain carbon target (red empty squares) and periodic strips of pencil leads (blue filled circles). Inset shapes and sizes of plain and periodic carbon targets. Reproduced from [1] with permission from Elsevier



The main goal of those studies was to show that the modification of plasma from being extended to being perforated leads to the enhancement of lowest-order harmonics, even though the length of perforated plasmas becomes twice shorter, which should lead to the four-fold decrease of harmonic yield. Those observations point out the involvement of the QPM on the lower-order harmonic yield and allow predicting a significant growth of the higher-order harmonics in the case of generation in such periodic plasma structures. This growth of the nonlinear optical response of medium due to formation of the quasi-phase-matched conditions for high-order harmonics has been discussed in Chap. 4.

6.2 Resonance-Enhanced Harmonics Generated in Nanoparticle and Monomer Plasmas

Clustered media subject to intense laser pulses produce strong low-order nonlinear optical response (e.g., nonlinear refraction and nonlinear absorption), as well as can emit the coherent radiation through the low-order harmonic generation. The enhanced nonlinear optical properties of clusters may cause the improvement of the high-order harmonic efficiency as well. Initially, studies of cluster-induced harmonic generation were limited to exotic nanoparticles of gases. The physical origin of this process in the gas clusters was mostly related with standard atomic harmonic generation, modified by the fact that in clusters the atoms are disposed to each other [8–16]. The increase of HHG conversion efficiency in those studies was attributed to the growth of the concentration of emitters and the specific properties of clusters. Particularly, the cross-section of recombination of the accelerated electron with the parent particle in the case of clusters is higher compared with the atoms. In the meantime, the uncertainty in the exact mechanism of the HHG from clusters has previously been underlined in a few studies [17–19]. Among additional mechanisms the ionization and recombination to the same ion, to the neighboring ions, and to the whole nanoparticle have been proposed. The experiments with gas clusters have revealed some difficulties in disentangling the harmonics produced by different species (monomers and clusters of different sizes).

Similar studies of the HHG in the laser-produced plasmas consisted of clusters or monomers showed that, at equal experimental conditions, the former emitters provide considerably stronger lower-order harmonic yield, thus pointing out the advanced properties of the clustered emitters of harmonics in the longer-wavelength range of extreme ultraviolet [20]. Recently, it became possible to generate the laser plasmas containing different nanoparticles due to availability of various metal-based clusters. The enhancement of harmonics in the metal nanoparticle plasmas has been achieved in various laboratories [21–24]. In the meantime, additional option could be a resonance enhancement of single harmonic in the cluster-contained plasmas. First attempts to analyze this process were reported in [25]. Those studies have revealed that, though the single harmonics were strongly enhanced in the plasmas

produced on the surfaces of bulk Sn and In targets, the harmonic spectra from the In and Sn nanoparticle-contained plasmas showed featureless plateau-like spectra with low cut-offs.

However, there are no fundamental restrictions in the resonance enhancement independently on the sizes of harmonic emitters. To achieve the resonance-induced growth of harmonics from large particles one has to find the conditions of optimal plasma formation during cluster ablation. In that case one can simultaneously analyze two mechanisms of the growth of harmonic yield (i.e. nanoparticle-induced enhancement and resonance-induced enhancement). First observation of this process has been reported in [26] where conditions of the optimal enhancement of single (29th) harmonic were achieved in the Cr_2O_3 cluster-contained plasma. However, no systematic comparative studies of this process were reported in the case of the HHG in nanoparticle- and monomer-contained plasmas.

Here, we analyze the results of studies of two cluster-contained plasmas (In_2O_3 and Sn) at the conditions of excitation of these species allowing both the efficient generation of lower-order harmonics and the resonance enhancement of single 13th and 17th harmonics, respectively [27]. The comparison of the harmonic spectra obtained using the bulk and cluster materials of the same origin showed that similar enhancement of single harmonics occurs in the case of strong excitation of nanoparticle-contained targets.

Experimental scheme for HHG was described in Sect. 4.1. The powders of In_2O_3 and Sn nanoparticles were glued on the 5-mm-long glass plates and then installed in the vacuum chamber for ablation. The harmonic spectra from the ablation of 5-mm-long In and Sn bulk targets were also studied for comparison with the powdered targets. The morphology of nanoparticles before and after ablation was analyzed using the transmission electron microscopy. The TEM images of nanoparticles before their ablation are shown in Fig. 6.6. The sizes of nanoparticles

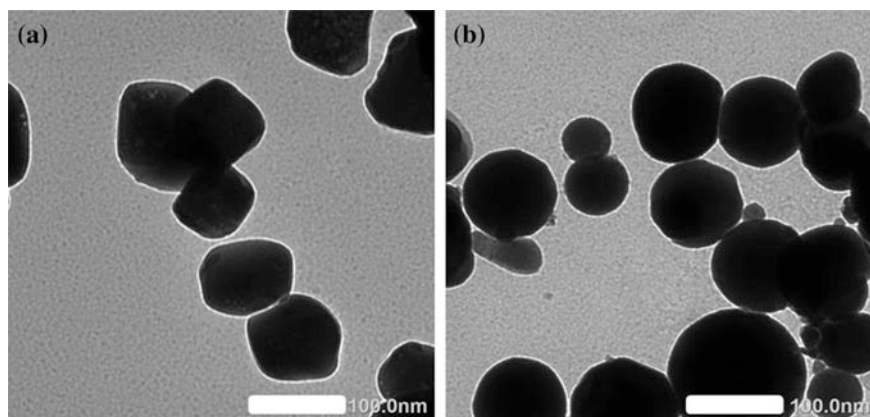


Fig. 6.6 TEM images of the **a** In_2O_3 and **b** Sn nanoparticles before their ablation. While lines on the images correspond to 100 nm. Adapted from [27] with permission from IOP Publishing. All rights reserved

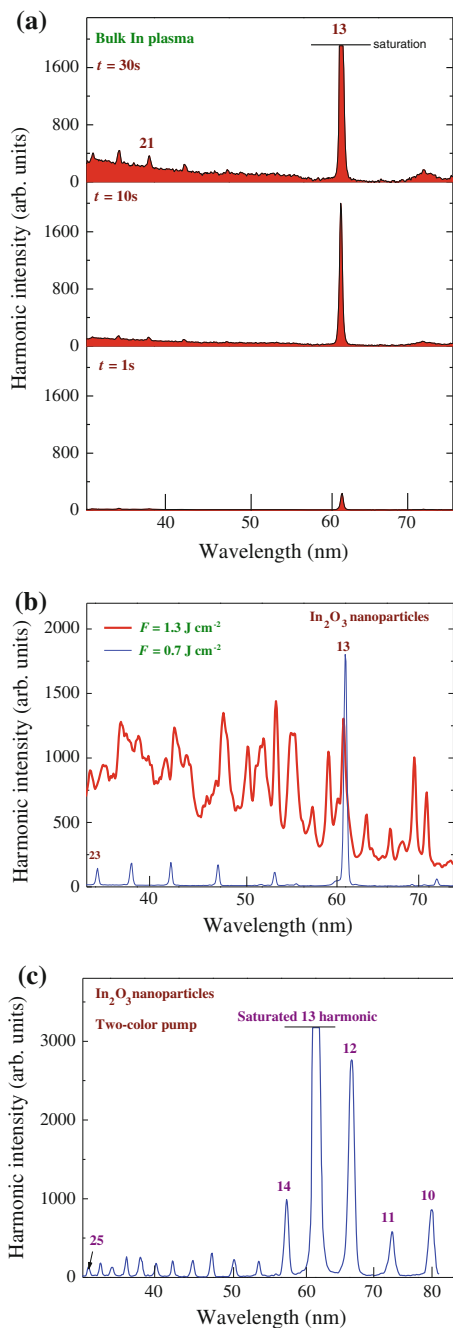
were in the range of 40–130 nm. The Sn nanoparticles were presented in the sphere-like shape, while the indium oxide nanoparticles showed the elliptical or squared shapes. The analysis of the ablated clusters, which were deposited on nearby glass plates, showed the nanoparticles similar to the original ones, which confirmed the presence of these species in the plasma plume. The morphology study of the debris deposited on the glass plates during ablation of bulk targets has shown that no nanoparticles were observed in that case at the heating pulse fluences up to 1.2 J cm^{-2} . This observation points out the presence of monomers in the plasma plumes at the conditions corresponding to the harmonic generation from the ablation of bulk metals.

The HHG spectra were measured from the plasmas produced on the surface of indium bulk target at a heating pulse fluence of 0.9 J cm^{-2} ($I_{\text{hp}} \approx 2.5 \times 10^9 \text{ W cm}^{-2}$). Figure 6.7a shows the harmonic spectra obtained during ablation of bulk indium and measured at different acquisition times (30, 10 and 1 s). One can see a significant enhancement of the 13th harmonic over other harmonics. Upper panel of Fig. 6.7a shows the spectrum of saturated 13th harmonic collected during 300 laser shots. These conditions of registration were chosen to show the spectral distribution of weak neighboring harmonics. The analysis of this emission during unsaturated regime of registration showed that the 13th harmonic was 60 times stronger than the 21st harmonic, which in turn exceeded other harmonics in the 30–75 nm spectral range. Harmonic cut-off in this plasma was extended up to the 45th order.

The ablation of indium oxide clusters at the fluence $F = 1.3 \text{ J cm}^{-2}$ led to generation of plasma spectrum, without the appearance of harmonic emission during propagation of the strong pulse through the plasma plume (Fig. 6.7b, thick curve). The gradual decrease of fluence (from 1.3 to 0.7 J cm^{-2}) allowed the formation of plasma conditions when the intense lower orders became visible in the spectrum, which did not contain the plasma emission (thin curve). Strong enhanced 13th harmonic was observed at these conditions, though the enhancement of this harmonic over neighboring ones ($10\times$) was not as high as in the case of bulk indium ablation. This nanoparticle-contained plasma allowed achieving the 27th harmonic cut-off. Further decrease of heating pulse fluence (0.3 J cm^{-2}) led to considerable decrease of 13th harmonic and appearance of featureless plateau-like spectrum along the whole range of harmonic generation. Polarization measurements of enhanced 13th harmonic yield from nanoparticle plasma showed the anticipated significant decrease of its intensity with the change of the polarization of driving radiation from linear to elliptical and circular, which is a characteristic feature of this nonlinear optical process.

Two pulses (802 and 401 nm) interacting in the indium oxide nanoparticle-contained plasma were used to analyze the influence of weak second field on the growth of harmonic yield. The additional motivation of these two-color studies of the HHG from clustered plasmas was related with the analysis of possible enhancement of the nearby even harmonics (12th and 14th orders) generating close to the resonance-enhanced odd (13th) harmonic. One can assume that the resonances, which were responsible for enhancement of 13th harmonic, could also influence the harmonic yield of the neighboring even orders. Part of the driving

Fig. 6.7 Harmonic spectra in the cases of **a** ablation of bulk indium (see text), **b** ablation of indium oxide nanoparticles using the fluences 0.7 J cm^{-2} (*thin curve*) and 1.3 J cm^{-2} (*thick curve*) on the target surface, and **c** application of two-color pump of the indium oxide nanoparticle-contained plasma (13th harmonic was collected at saturation level to demonstrate the odd and even harmonic distribution). Adapted from [27] with permission from IOP Publishing. All rights reserved



pulse was converted to the second harmonic in the BBO crystal placed inside the vacuum chamber on the path of the focused femtosecond beam at a distance of 150 mm from the plasma plume. The 0.5-mm-long crystal was used for second-harmonic generation, which allowed a sufficient overlapping of two pumps in the plasma medium despite the group velocity dispersion induced delay between the 802 and 401 nm pulses, while producing a sufficient amount of 401 nm photons. The second harmonic conversion efficiency in this crystal was 7 %. The driving and second harmonic beams were focused inside the plasma plume. The polarizations of these two pumps were orthogonal to each other. The application of the two-color pump of nanoparticle-contained plasma at the optimal fluence of heating radiation (0.7 J cm^{-2}) allowed achieving the growth of the 12th harmonic, which was close to the resonance transition of In II responsible for the enhancement of 13th harmonic (Fig. 6.7c). This spectrum is presented at the conditions of saturation of enhanced 13th harmonic for better visibility of relative intensities of other odd and even harmonics (particularly, compare the intensities of 10th and 12th orders).

The influence of strong ionic transition $4d^{10}5s^2 \ ^1S_0 \rightarrow 4d^9 5s^2 5p \ (^2D) \ ^1P_1$ or some other nearby transitions of In II on the 12th harmonic yield led to enhancement of this radiation compared to the lower-order (10th and 11th) harmonics even using the weakly overlapped leading and trailing parts of the two pulses in the extended plasma. The origin of such enhancement could be attributed to both the single ion response and propagation effect. Note the absence of 12th harmonic in the emission spectrum comprising only 10th, 14th, 18th, etc. orders in the case of using single-color 401 nm pump of cluster-contained plasma, which confirms the origin of this radiation in the former experiments as a result of interaction of the two waves in the plasma plume. In the case of two-color pump scheme, the range of enhanced harmonics was extended towards the shorter wavelength region (31st order), in spite of relatively small ratio of the 401 and 802 nm pump energies of the overlapped pulses inside the plasma (0.04). One can assume that the application of extended plasma allowed diminishing the delay between two pumps due to positive dispersion of this medium.

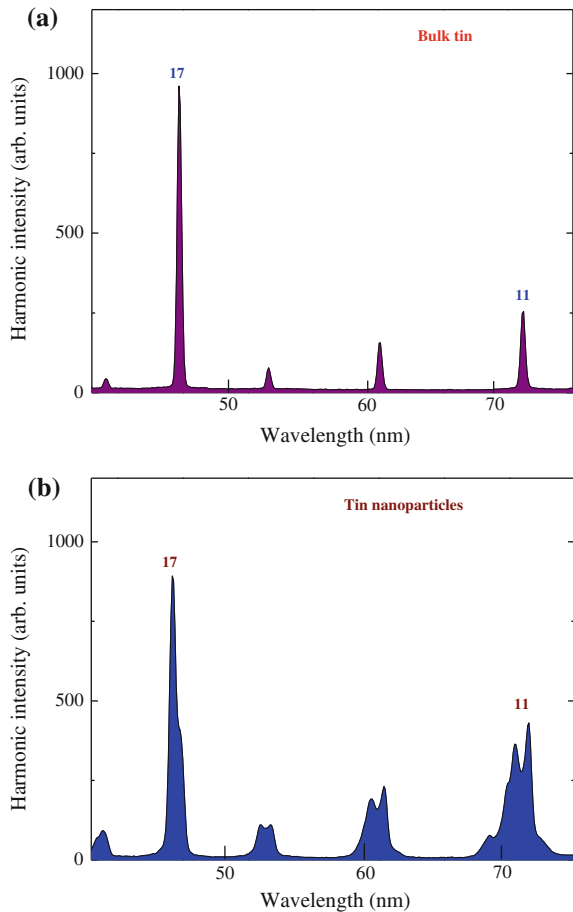
The 13th harmonic ($h\nu = 20.15 \text{ eV}$) of 802 nm radiation generated in an indium plasma is a strongest enhanced single harmonic ever reported in the plasma harmonic experiments, which has been confirmed in multiple studies of bulk indium ablation [28–31]. Particularly in [30], the properties of this harmonic were supported by hydrodynamic simulations of the plasma plume already suggesting that the optimized 13th harmonic yield can be essentially correlated with the In II density evolution. The enhancement of the 13th harmonic emission from the plasma containing indium ions is due to the influence of the radiative transitions between the $4d^{10}5s^2 \ ^1S_0$ state of In II and the low lying $4d^9 5s^2 \ np$ transition array of In II (see also Sects. 2.2 and 2.3).

These experiments have demonstrated that the resonance enhancement in clustered plasmas occurred only at the heating fluences allowing the formation of ionized species of nanoparticles, while further growth of target excitation led to deterioration of HHG conditions and strong plasma emission. Note that, in the case of bulk indium ablation, the enhanced 13th harmonic was observed in a broad range

of heating fluences, thus indicating the appearance of emitters of this harmonic at both weak and strong excitation of indium target.

Among a few laser-produced plasmas demonstrating enhanced harmonics, Sn shows an interesting sample of single harmonic generation, when strong transitions of singly and doubly charged ions can considerably influence this process depending on the experimental conditions (wavelength of driving radiation, laser chirp, single- or two-color pump, spectral width of driving radiation, pulse duration, etc.), which was confirmed during experimental and theoretical studies of the HHG in a tin plasma [32–36]. Here, we analyze the resonant enhancement of single harmonic in the tin-contained plasmas using the bulk target ablated at a fluence $F = 0.8 \text{ J cm}^{-2}$ (Fig. 6.8a). Strong 17th harmonic was observed with an enhancement factor of about $10\times$ compared with neighboring harmonic orders. In the case of Sn nanoparticle-contained target, similar enhancement of single harmonic was observed as well pointing out the appearance of ionized clusters at

Fig. 6.8 Harmonic spectra from the plasmas produced **a** on the Sn bulk target ($F = 0.8 \text{ J cm}^{-2}$) and **b** on the target contained Sn nanoparticles ($F = 0.6 \text{ J cm}^{-2}$). Adapted from [27] with permission from IOP Publishing. All rights reserved



relatively weak excitation of the target ($F = 0.6 \text{ J cm}^{-2}$, Fig. 6.8b). At lower fluences, the enhancement of 17th harmonic was significantly suppressed. Note that the spectral lines of harmonics from Sn nanoparticles were broadened at the shorter-wavelength side and showed additional peaks compared with the narrow lines of the harmonics generated in monomer-containing Sn plasma.

The Sn II resonances, which influence the enhancement of harmonics, correspond to the wavelengths in the region of 47 nm. It was found from the published data of the Sn II transitions in the studied spectral region [37] that the observed enhancement of the 17th harmonic of the 802 nm radiation (47.17 nm) can be attributed to the influence of the transitions $4d^{10}5s^25p^2P_{3/2} \rightarrow 4d^95s^25p^2$. Some of these transitions possess large oscillator strengths in the photon energy range of 24.9–27.3 eV.

An approach that suggests a HHG model describing enhancement of the generation efficiency for the harmonic resonant with the transition between the ground and the autoionizing state of the generating ion was developed in [34]. In this approach, the third (recombination) step of the three-step scenario of HHG [38–40] was partitioned into two steps: the capture of a laser-accelerated electron into an autoionising state of the parent ion followed with the radiative relaxation of this state to the ground state with emission of the harmonic photon. Probably, this scenario could be applied to the ionized large particles as well.

Among the factors responsible for the enhancement of individual harmonics, one has to mention the variation of the phase-matching conditions for different harmonic orders. The phase mismatch varies as the laser pulse propagates through the plasma plume due to further ionization of the nonlinear medium. For harmonics in the plateau region, the phase mismatch attributed to free electrons is one to two orders of magnitude larger than the mismatch due to neutrals and singly charged ions. However, under resonance conditions, when the frequency of a given harmonic becomes close to the frequency of inner-shell atomic or ionic transitions, the wave-number variation for this harmonic caused by atoms or ions might be significantly increased and the role of free electrons and dispersion effects may be diminished. The dispersion in the vicinity of a resonant transition can be considerably changed thus allowing coincidence of the refractive indices of the plasma at the wavelengths of the driving laser and the harmonic emission [31]. In these circumstances, it is possible to satisfy the optimal phase conditions for a single harmonic, with the consequent increase of conversion efficiency for this emission.

These two approaches in description of resonance-enhanced harmonics, which comprise micro- and macro-processes in monomer media, may also be applied for the analysis of the observed enhancement of single harmonic from the plasmas containing clusters. When clusters become ionized, the above-described mechanisms start to play important role. Probably, an insufficient amount of ionized clusters does not allow the cut-off extension. From other hand, further growth of excitation of nanoparticle targets may cause a significant growth of electron concentration in plasma followed with phase mismatch and strong plasma emission.

The powdered targets are difficult to keep intact for a long time during their continuous ablation. The studies of the decay of harmonic yield from the clustered

plasmas were performed at 10 Hz pulse repetition rate, without the movement of targets from shot to shot. The fixed position of target led to deterioration of the optimal plasma formation after a few hundred shots (or a few tens of seconds) on the same place of cluster-contained target. This effect was observed in previous studies of powdered target ablation and is attributed to the modification of target surface (i.e. evaporation of clustered powder, melting of heated area, modification of surface properties, etc.). To keep stable harmonic yield from this target, one has to drag the nanoparticle holder up and down, while in the case of bulk target ablation the stable harmonic generation was lasted for considerably longer time (a few thousand shots) without the movement of ablating sample. Previous method to hold the stable harmonic emission from cluster-contained plasmas was based on the rotation of target (cluster-contained cylindrical rod) and the ablation of its surface by narrow heating beam [41]. In the described case, this method cannot be applied since the plain targets were used to create the extended plasmas.

The feature specific to nanoparticle-produced harmonics compared to respective bulk targets is the appearance of blue shifted lobes and the broadening of the low-order harmonic. Below we address the experimental finding and origin of this spectral feature specific to nanoparticle targets. Figure 6.8b shows the appearance of blue-sided lobes and double peaks in the case of lower-order harmonics. Note that this modification of harmonic spectra was observed only in the case of nanoparticle-contained plasmas, similarly to those analyzed in [42]. Several investigations on variations of the width of the spectrum of harmonics due to the broadening of the spectrum of radiation to be converted have been reported in [43–45]. All of these investigations were performed under the conditions of broadening of the spectrum of laser radiation at a comparatively weak action of the self-phase-modulation on the spectral properties of harmonics. In the case of the pulse that underwent a significant phase self-modulation due to additional ionization of the medium through which it propagated a significant heterogeneous broadening of the spectral distribution can be observed. This effect can be explained by the wavelength change in the leading edge of the laser pulse due to self-phase modulation of the radiation propagating through the laser plasma. The initial lower intensity portion of the pulse creates harmonics. As the pulse intensity reaches its peak, the additional ionization can change the distribution of laser spectrum along the whole pulse. It has been shown in previous studies of gas and plasma HHG using the chirped pulses that the leading edge of the pulse mainly contributes to the HHG. Laser radiation becomes negatively chirped along the propagation through the extended plasma. The part of harmonics produced with negatively chirped laser pulses becomes blue-shifted because the harmonics produced in the leading edge of the laser pulse come from the blue part of the laser spectrum. Though this assumption qualitatively explains the blue-sided broadening of lower-order harmonics, the appearance of the peaks in the spectral distribution of individual harmonic requires additional consideration.

The growth of intensity of the femtosecond pulse did not lead to extension of the harmonics generated in the nanoparticle-containing plasma plumes, which is a sign of saturation of the HHG in these media. Moreover, at relatively high intensities of

driving femtosecond pulses, a decrease in harmonic conversion efficiency in cluster-contained plasma was observed due to some restricting factors (appearance of abundance of free electrons, self-defocusing, phase mismatch, etc.). The same can be said about the increase of heating pulse intensity on the surface of nanoparticle-containing targets over some optimal value. In that case the deterioration of harmonic generation was attributed to the increase of free electron concentration and phase mismatch.

6.3 Electron Density Measurements in Laser-Produced Plasma Using the Nonlinear Optical Method

The electron density of plasma governs various properties of this medium. Several diagnostic methods were developed for the measurements of N_e , which include Langmuir probe [46, 47], Thomson scattering [48], laser interferometry [49], and plasma spectroscopy [50–56]. Latter method is the most useful technique, which is based on the analysis of the Stark broadening of spectral lines [57, 58]. However, additional three broadening mechanisms (Doppler broadening, pressure broadening, and instrumental broadening) may contribute to line broadening during laser ablation. The difficulty in definition of the role of various factors increases the uncertainty in the accuracy of the measurements of N_e , in the region of low densities. Note that most of above methods were developed for the analysis of relatively dense (10^{18} cm⁻³ and above) and strongly ionized plasmas. As for the low-density, low-ionized plasmas with the N_e of a few units of 10^{16} cm⁻³, the Stark broadening of ionic lines will be of the order of 0.005 nm, which is hard to distinguish from other broadening mechanisms. In the meantime, such plasmas are of special interest, since they allow the efficient conversion of the long-wavelength laser sources towards the short-wavelength spectral region.

In this section, we discuss the method of electron density measurements using the nonlinear optical processes occurring in the low-ionized laser-produced plasmas. We analyze generation of the high-order harmonics of ultrashort pulses in the laser-produced plasmas at the conditions of the quasi-phase-matching of driving and harmonic waves and define the electron density of plasma through the relations of QPM (see also Chap. 4).

Below we analyze the method of the measurement of electron density based on the analysis of the coherence length of the group of enhanced harmonics generated in the plasmas at the conditions of QPM. QPM aims at canceling the out-of-phase emission, particularly, by modulating the medium density [59], which allows suppression of the phase mismatch between the interacting driving and harmonic waves. One can accomplish this suppression by dividing the whole extended plasma on a group of small plasma jets. Various methods could be used to divide the extended laser-produced plasmas. Among them are (i) the interference of two heating beams on the target surface with the variable angle between the interacting beams, (ii) tilting of the multi-slit shield placed on the path of heating pulse, and

(iii) installation of the multi-slit shield inside the telescope on the path of heating pulses. The most affordable methods are (ii) and (iii) since they allow the tuning of jet sizes by simple tilting or relocating the MSS.

As it was described in Chap. 4, there are four factors that contribute to the phase mismatch (Δk) between the driving and harmonic waves: atomic and ionic dispersion, Gouy phase shift, intensity-dependent dynamic phase shift, and electron-affected plasma dispersion [60, 61]. At the used conditions, the only factor influencing phase mismatch is related with the presence of electrons in the plasma.

The plasma dispersion-induced phase mismatch for the q th harmonic is defined by the relation

$$\Delta k_{\text{disp}} = qN_e e^2 \lambda / 4\pi m_e \varepsilon_0 c^2, \quad (6.1)$$

where λ is the wavelength of driving radiation, m_e and e are the mass and the charge of the electron, c is the light velocity, and ε_0 is the vacuum permittivity [62, 63]. The coherence length of this harmonic at the used conditions is

$$L_{\text{coh}} = \pi / \Delta k \approx \pi / \Delta k_{\text{disp}} \approx 4\pi^2 m_e \varepsilon_0 c^2 / qN_e e^2 \lambda. \quad (6.2)$$

From this expression, the coherence length (measured in millimeters) at the conditions of using the 800 nm driving laser could be presented as

$$L_{\text{coh}} \approx 1.4 \times 10^{18} / (N_e \times q_{\text{qpm}}). \quad (6.3)$$

Here q_{qpm} is the harmonic order in the QPM region showing the highest enhancement and N_e is the electron density in the plasma jets measured in cm^{-3} . This simple formula allows defining the electron density by knowing the coherence length (which is in fact the size of single plasma jet at the conditions of QPM) and the maximally enhanced harmonic order. The decrease of heating pulse fluence should lead to the decrease of electron density followed by the tuning of q_{qpm} towards the shorter-wavelength range. Similarly, one can anticipate that, for the plasma jets of different sizes, the maximally enhanced harmonics will also be moved along the XUV spectrum. These assumptions allow the comparison of electron density measurements using different multi-jet plasmas and different ablation conditions.

The proposed method of electron density measurements could be a useful tool for the diagnostic of the electrons appearing on the path of the driving pulses during laser ablation of targets [64]. The experimental setup (Fig. 6.9) was similar to the one described in Sect. 4.1. The modulation of the spatial shape of heating pulse was accomplished using the installation of the MSS on the path of propagation of this radiation. The image of MSS is shown in the inset in Fig. 6.9. The sizes of each slit of this shield were 0.3 mm, and the distance between the slits was 0.3 mm. The images of plasma formations were captured from the top of the vacuum chamber by a CCD camera. Figure 6.10a shows the line and multi-jet plasmas formed on the silver surface by the extended focused heating beam and by installation of the MSS

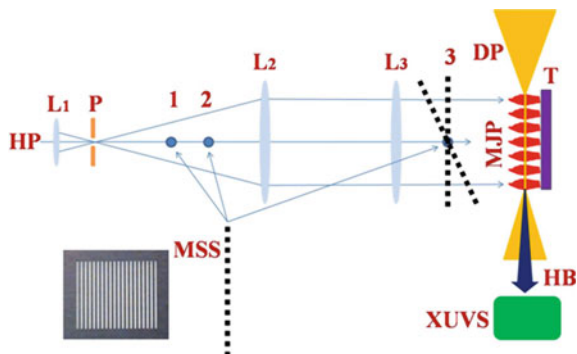
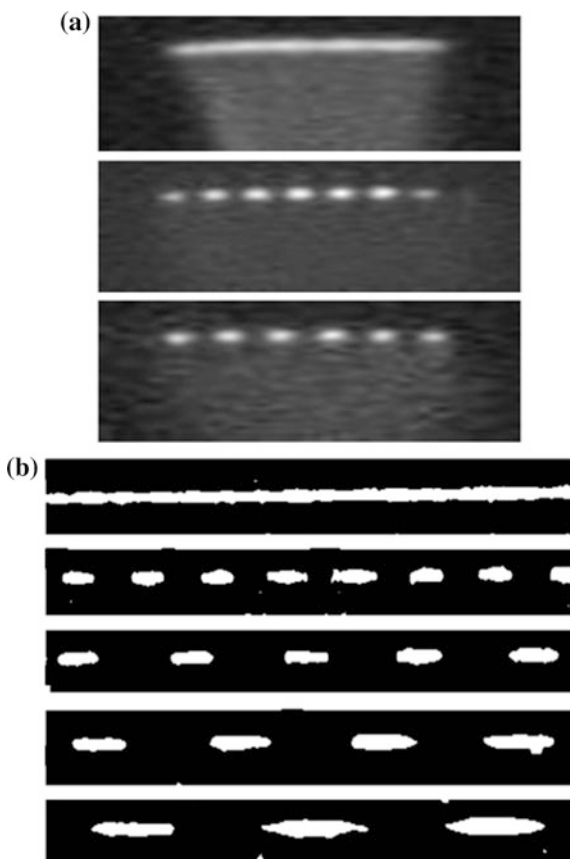


Fig. 6.9 Experimental setup for the HHG using the formation of variable multi-jet plasmas in the focal plane of cylindrical lens (L_3) at different positions (1–3) of the multi-slit mask. L_1 , L_2 lenses of telescope; P pinhole of telescope; T , silver target; HP heating pulse; MSS multi-slit shield; DP driving pulse; HB harmonic beam; MJP multi-jet plasma; $XUVS$ extreme ultraviolet spectrometer. *Inset* Image of multi-slit shield. Reproduced from [64] with permission from Springer Science +Business Media

Fig. 6.10 a Images (from *top to bottom*) of extended, seven-jet, and six-jet plasmas formed on the silver target.

b Images of the ablated surface of silver target during formation of (from *top to bottom*) extended line-shaped plasma produced without the use of MSS, and eight-jet, five-jet, four-jet, and three-jet plasmas produced by placing the MSS at different positions inside the telescope.

Reproduced from [64] with permission from Springer Science+Business Media



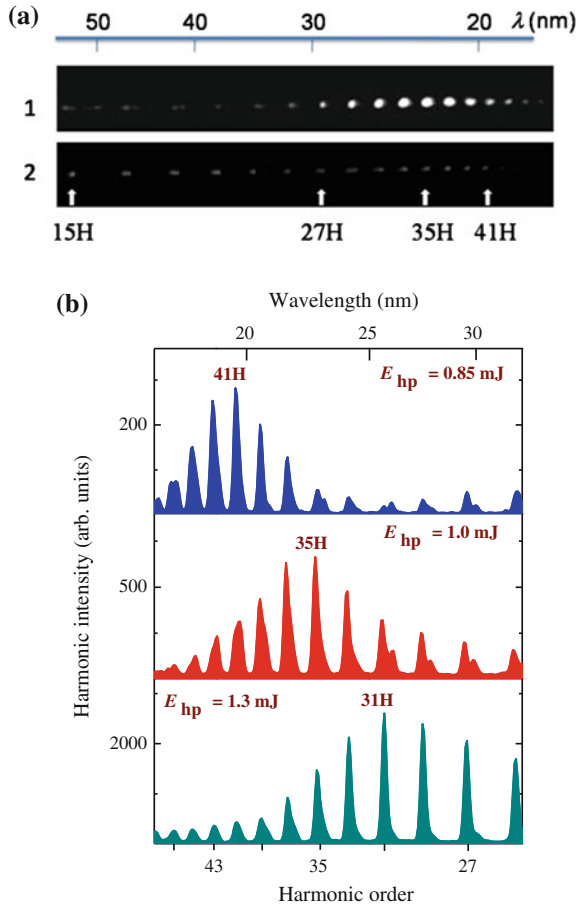
at different positions inside the telescope. One can see the extended plasma, as well as seven-, and six-jet structures. The sizes of plasma jets were defined by the measurement of the ablated areas of silver target (Fig. 6.10b), rather than by measuring the images of plasma emission. In the latter case, the registered emission of plasma does not accurately correspond to the actual sizes of jets. The jet sizes were also calculated from the geometrical characteristics of the radiation propagated through the MSS placed in different positions inside the telescope. The gradual tilting of the MSS placed in the position 3 (Fig. 6.9) allowed the steady growth of the number of jets up to 12.

The harmonic spectrum from the 5-mm-long Ag plasma in the case of removal of the MSS from the path of heating radiation showed a featureless plateau-like shape, with a gradual decrease of harmonic intensity in the shorter-wavelength region (Fig. 6.11a, panel 2). This featureless harmonic spectrum was drastically changed once the MSS was introduced inside the telescope (panel 1). One can see a significant enhancement of a group of harmonics in the 18–30 nm spectral range. The two raw images of harmonic spectra shown in Fig. 6.11a were taken by moving the MSS in and out of the path of heating pulse, without any other changes of experimental conditions and using the same collection time. Note that, in the latter case, the whole length of plasma was two times longer. The enhancement factor of the 35th harmonic from the five 0.5-mm-long plasma jets produced by the 1 mJ heating pulses was $\sim 20\times$ compared with the same harmonic generated in the extended plasma. These spectra demonstrate that the enhancement was observed for a group of five to seven harmonics, rather than for a single harmonic, due to small dispersion of the low-dense plasma.

The HHG spectra from the silver ablation using three different energies of heating pulses are shown in Fig. 6.11b in the case of the five 0.5-mm-long plasma jets produced on the ablating surface by inserting the MSS at the position 2 shown in Fig. 6.9. The energies shown in Fig. 6.11b (0.85, 1.0 and 1.3 mJ) account for the pulse energies measured after propagation of the heating radiation through the MSS. The energies of pulses before irradiation of MSS were two times larger. One can clearly see the QPM-induced enhancement of the groups of harmonics, which were tuned depending on the energy of heating pulses. This enhancement was observed at shorter wavelengths while using lesser excitation of target (Fig. 6.11b; compare the spectral maxima of QPM-enhanced harmonics at different energies of heating pulses). Indeed, as it was mentioned, a decrease of N_e at lesser excitation of target should lead to optimization of the QPM for the higher harmonic orders to keep the product $q_{\text{qpm}} \times N_e$ unchanged at the fixed sizes of plasma jets corresponding to the coherence lengths of those harmonics (see relation 6.3). The ablation of silver target using weaker and stronger beams led to the shift of the maximally enhanced harmonics from the 41st order towards the 31st order.

The use of relation (6.3) allows the definition of N_e in those three cases by measuring the q_{qpm} at the same sizes of plasma jets. The electron density was calculated to be $7 \times 10^{16} \text{ cm}^{-3}$ in the case of 0.5-mm-long jets and at the maximally enhanced harmonics centered near the 41st order (Fig. 6.11, heating pulse energy 0.85 mJ). The excitation of target using stronger heating pulses (1.0 and 1.3 mJ) led

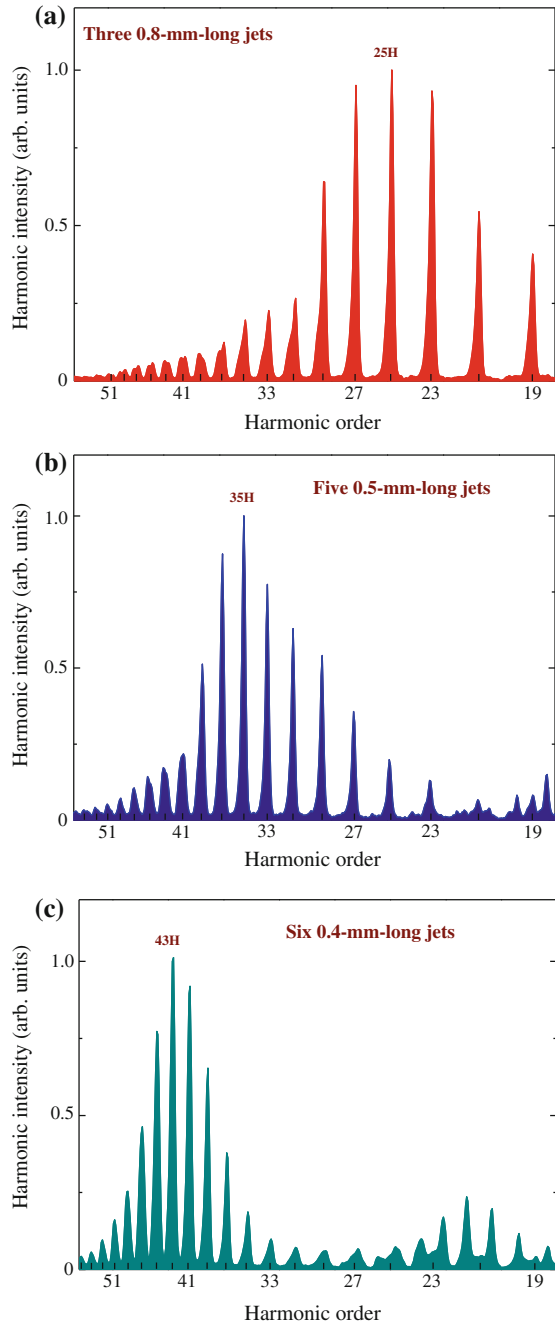
Fig. 6.11 a Raw images of harmonic spectra obtained from the five-jet plasma (panel 1) and extended (5-mm-long) homogeneous plasma (panel 2). These two images were taken by moving the MSS in and out of the path of heating pulse, without any other changes of experimental conditions. The enhancement factor of the 35th harmonic in the case of multi-jet plasma was $\sim 20\times$ compared with the same harmonic generated from the 5-mm-long plasma. **b** Harmonic spectra obtained from the five-jet plasma formed on the silver target at different energies of the heating pulses. Reproduced from [64] with permission from Springer Science +Business Media



to the plasma formation contained larger amount of electrons (with the N_e calculated to be 8×10^{16} and $9 \times 10^{16} \text{ cm}^{-3}$ respectively). These studies showed the dependence of the electron density on the heating pulse energy.

Below we analyze the QPM-based electron density studies using variable sizes of the jets formed on the target surface. Figure 6.12 shows three spectra of plasma harmonics obtained using six 0.4-mm-long, five 0.5-mm-long, and three 0.8-mm-long plasma jets. No any other changes were introduced during these experiments excluding the movement of the MSM along the telescope axis, thus maintaining a similar fluence of heating pulse on the target surface. In all these cases, only half of a whole energy of the heating beam was propagated through the shield. In each of these spectra, the enhancement of the groups of harmonics was observed in different spectral regions. The maximum enhancements were obtained for the 25th, 35th, and 43rd harmonics in the cases of the 0.8-, 0.5-, and 0.4-mm-long plasma jets, respectively. The electron density of plasma in these three cases was the same due to equal fluence of the heating pulse on the target surface.

Fig. 6.12 Normalized harmonic spectra in the cases of different multi-jet plasmas. The sizes of jets were **a** 0.8 mm, **b** 0.5 mm and **c** 0.4 mm. The variation of jet sizes was accomplished by installation of the MSS in different positions inside the telescope. The second group of emission shown in the *right side* of panel (c) corresponds to the second-order diffraction of the enhanced group of harmonics centered at the 43rd order. Reproduced from [64] with permission from Springer Science+Business Media



The calculation of N_e using relation (6.3) confirmed the equality of electron density in these three cases within the accuracy of measurements (7.0×10^{16} , 8.0×10^{16} and $8.1 \times 10^{16} \text{ cm}^{-3}$ respectively) assuming the experimentally measured parameters of L_{coh} and q_{qpm} in the cases of three different groups of jets with the size of single jet corresponding to the coherence lengths of maximally enhanced harmonic. The accuracy of these measurements will be discussed later.

Note that the electrons interacting with the driving and harmonic waves comprise those produced during the initial formation of plasma and those appeared during ionization of neutrals and singly charged ions by the propagating driving pulse. Independently on the role of these groups of electrons in the phase mismatch the proposed technique allows the measurement of the instant amount of the electrons influenced the dispersion of this medium during ablation and propagation of the driving pulse.

Earlier, we mentioned various methods for measuring the electron density of plasmas. Each of them has merits and demerits, since the accuracy of those methods depends on the experimental conditions. Particularly, we highlighted the uncertainty of Stark broadening method in the measurements of electron densities of the order of a few units of 10^{16} cm^{-3} . The accuracy of the proposed method using the nonlinear optical processes, which are extremely sensitive to the presence of the electrons in the medium, is defined by the uncertainty in definition of strongest harmonic order among the group of QPM-enhanced harmonics and by the uncertainty in the measurements of the plasma sizes. Shot to shot measurements of QPM-induced spectra from multi-jet plasmas showed that the highest yield was obtained for the same harmonic order. The maximal uncertainty in that case could not be larger than 2. The accuracy in the measurement of the spatial characteristics of plasma jets was mostly depended on the uncertainty in the relation between the sizes of the ablated spot on the target surface and the density distribution for each plasma jet. One can assume that, after propagation through the shield, each component of modulated ablating beam had a rectangular shape with the sizes equal to the sizes of the slit of MSS, which should lead to the rectangular shape of each jet in the case of installation of the shield between the cylindrical lens and target. The diffraction of heating beam after propagation of MSS may lead to some inclination of the spatial distribution from the rectangular shape for each component of modulated heating beam. This appeared to be true in the case when the MSS was placed far from the ablation area. To decrease the uncertainty of the measurements of plasma jet sizes one has to install the MSS as close as possible to the target surface. The experiments, when the MSS was placed inside the vacuum chamber and moved it in and out of the path of heating pulse, have confirmed this assumption. Summarizing, the accuracy of these measurements was mostly defined by the accuracy of the measurements of plasma jet sizes and by definition of the maximally enhanced harmonic. Based on above assumptions, the relative error of the measurements of electron density was estimated to be 20 %. It is difficult to compare the accuracy of this method with other reported methods due to different ranges of electron densities, which could be defined by those and discussed

methods. Note that all plasma and electron diagnostic methods have accuracy issues and none of them are perfect.

There are a few other uncertainties in the behavior of electron cloud during spreading out of surface. In particular, little is known about the relative distribution of electrons and other particles in the plasma plume. Whether the distribution of electron density along the plasma plume remains the same as the distribution of other components at the later stage of plasma movement remains unknown. However, this is not a necessary condition for the proposed method to derive the electron density. Note that the measurements show the influence of electrons on the nonlinear optical process in the plasma plume and define their density at the fixed spot inside the plume, while not defining their spatial distribution. To measure the spatial distribution of electrons one has to gradually move the driving pulse out of the ablating surface.

6.4 Concluding Comments

We have shown various approaches in the applications of the long plasmas for nonlinear optics. Particularly, we have analyzed three methods of multiple plasma jet formation from the point of view of their application for the lower-order harmonic generation of laser radiation. This allowed making some practical recommendations for further application of these techniques for generation of higher-order harmonics.

We demonstrated for some peculiar cases the advanced properties of the periodic plasma plumes over the plain long plasmas used for the low-order harmonic generation. Particularly, we analyzed the influence of the sizes of multiple plasma jets on the low-order harmonic intensity using single color and two color pumps of extended periodic plasmas, as well as discussed the role of heating pulse characteristics in the variation of harmonic yield from the periodically modulated plasmas. The discussed studies have shown that, for particular spacing and harmonic order, a clear suppression of destructive interference can be achieved that may be attributed to a partial QPM effect, though the additional studies are required for confirmation of the involvement of QPM in the observed enhancement of harmonics. While a shortening of the plasma length produced on the plain targets led to a considerable decrease of plasma harmonic intensity, the application of perforated targets led to the enhancement of the low-order harmonics using strong excitation of targets. The 8-fold enhancement of third harmonic yield from the set of 0.15 mm thick plasma jets was observed compared with the plain target of the same width of plasma.

This first demonstration of harmonic enhancement in laser produced periodic plasmas in the case of low (third and fourth) order harmonic generation of picosecond laser radiation has shown that this advanced approach could be used for the higher-order harmonics as well, where the effect of QPM could be significantly emphasized (as it was shown in Chap. 4).

The analyzed studies have shown that, for any nanoparticle-containing plume, no improvements in the extension of the harmonic cut-off were observed. At the same time, an enhancement of the harmonic yield in the low-energy plateau range in the case of nanoparticle-contained extended plasmas compared with monomer plasmas was achieved. Moreover, those experiments have shown the conditions when some additional enhancement was obtained for the single harmonics generating in the clustered plasmas at the conditions of the closeness of the wavelengths of these harmonics with the ionic transitions. Particularly, the enhancement of single (13th and 17th) harmonics was demonstrated in the nanoparticle-contained plasmas (In_2O_3 , Sn), together with the enhancement of lower-order harmonics compared with those generated in the monomer-contained plasmas. The comparison of the harmonic spectra obtained using the clustered and bulk materials of the same origin showed that similar enhancement of single harmonics occurs in the case of strong excitation of nanoparticle-contained targets. The feature specific to nanoparticles-produced harmonics versus respective bulk targets is the variation of the spectrum of individual enhanced harmonic. The discussed study has analyzed the difference with previously published data on harmonic generation from clusters and demonstrated the peculiarity of nanoparticle targets showing strong blue-sided lobes of harmonics. The origin of this spectral feature specific to the HHG in nanoparticle targets was discussed.

These studies showed that, at weak excitation of the targets contained similar elements the harmonics are mainly produced by ionized monomers from ablated bulk targets and by neutral clusters from ablated nanoparticle-covered targets. However, with the growth of fluence on the target surfaces, the most prominent feature, a single harmonic enhancement, can be straightforwardly interpreted by resonances in ions. Whether those ions are monomers or clustered ionized particles remains unknown. To reasonably associate the characteristics of the harmonic spectra with the presence of some specific species at the time of generation in the interaction volume one has to study the consistence of plasma at the moment of propagation of the driving pulse through the plasma.

Finally, we discussed the application of quasi-phase-matching concept for the definition of plasma characteristics. Among the advantages of the QPM of plasma harmonics are the simplicity in regulation of the electron density in the multi-jet plasmas, the high enhancement factors of harmonics, and the availability of the express analysis of N_e . The reported conversion efficiency for the enhanced 33rd harmonic of Ti:sapphire laser ($\lambda \approx 24$ nm) generated in the extended Ag plasma jets ($\sim 2 \times 10^{-5}$, [65]) is among the highest values achieved so far in this spectral region during the HHG in both gases and plasmas. As for the latter advantage, the definition of maximally enhanced harmonics at the fixed sizes of separated plasma jets allows the calculation of N_e , which was demonstrated during discussed studies. The N_e was defined using the relations of QPM. The proposed method allows the analysis of the variations of electron density in the low-ionized plasmas. Particularly, the variation of the distance from ablating target and the delay between heating and driving pulses will allow analyzing the distribution of electron density along the low-ionized medium.

References

1. R.A. Ganeev, G.S. Boltaev, T. Usmanov, *Opt. Commun.* **324**, 114 (2014)
2. J.F. Reintjes, *Nonlinear Optical Parametric Processes in Liquids and Gases* (Academic Press, New York, 1984)
3. R.A. Ganeev, G.S. Boltaev, N.K. Satlikov, R.I. Tugushev, T. Usmanov, *J. Photon. Optoelectron.* **2**, 96 (2013)
4. J. Seres, V.S. Yakovlev, E. Seres, C.H. Strelly, P. Wobrauschek, C.H. Spielmann, F. Krausz, *Nat. Phys.* **3**, 878 (2007)
5. A. Pirri, C. Corsi, M. Bellini, *Phys. Rev. A* **78**, 011801 (2008)
6. J. Stadler, R. Mikulla, H.-R. Trebin, *Int. J. Mod. Phys. B*, **8**, 1131 (1997)
7. C. Kan, N.H. Burnett, C. Capiack, R. Rankin, *Phys. Rev. Lett.* **79**, 2971 (1997)
8. T.D. Donnelly, T. Ditmire, K. Neuman, M.D. Pery, R.W. Falcone, *Phys. Rev. Lett.* **76**, 2472 (1996)
9. J.W.G. Tisch, T. Ditmire, D.J. Fraser, N. Hay, M.B. Mason, E. Springate, J.P. Marangos, M.H.R. Hutchinson, *J. Phys. B: At. Mol. Opt. Phys.* **30**, L709 (1997)
10. S.X. Hu, Z.Z. Xu, *Appl. Phys. Lett.* **71**, 2605 (1997)
11. T. Tajima, Y. Kishimoto, M.C. Downer, *Phys. Plasmas* **6**, 3759 (1999)
12. D.F. Zaretsky, P. Korneev, W. Becker, *J. Phys. B: At. Mol. Opt. Phys.* **43**, 105402 (2010)
13. C. Vozzi, M. Nisoli, J.-P. Caumes, G. Sansone, S. Stagira, S. De Silvestri, M. Vecchiocattivi, D. Bassi, M. Pascolini, L. Poletto, P. Villorresi, G. Tondello, *Appl. Phys. Lett.* **86**, 111121 (2005)
14. S.V. Fomichev, D.F. Zaretsky, D. Bauer, W. Becker, *Phys. Rev. A* **71**, 013201 (2005)
15. C.-H. Pai, C.C. Kuo, M.-W. Lin, J. Wang, S.-Y. Chen, J.-Y. Lin, *Opt. Lett.* **31**, 984 (2006)
16. M. Kundu, S.V. Popruzhenko, D. Bauer, *Phys. Rev. A* **76**, 033201 (2007)
17. P. Moreno, L. Plaja, L. Roso, *Europhys. Lett.* **28**, 629 (1994)
18. V. Véniard, R. Taïeb, A. Maquet, *Phys. Rev. A* **65**, 013202 (2001)
19. H. Ruf, C. Handschin, R. Cireasa, N. Thiré, A. Ferré, S. Petit, D. Descamps, E. Mével, E. Constant, V. Blanchet, B. Fabre, Y. Mairesse, *Phys. Rev. Lett.* **110**, 083902 (2013)
20. R.A. Ganeev, *J. Modern Opt.* **59**, 409 (2012)
21. R.A. Ganeev, M. Suzuki, M. Baba, M. Ichihara, H. Kuroda, *J. Appl. Phys.* **103**, 063102 (2008)
22. R.A. Ganeev, L.B.E. Bom, *J. Phys. B: At. Mol. Opt. Phys.* **42**, 055402 (2009)
23. H. Singhal, R.A. Ganeev, P.A. Naik, A.K. Srivastava, A. Singh, R. Chari, R.A. Khan, J.A. Chakera, P.D. Gupta, *J. Phys. B: At. Mol. Opt. Phys.* **43**, 025603 (2010)
24. R.A. Ganeev, C. Hutchison, M. Castillejo, I. Lopez-Quintas, F. McGrath, D.Y. Lei, J.P. Marangos, *Phys. Rev. A* **88**, 033803 (2013)
25. L.B.E. Bom, R.A. Ganeev, J. Abdul-Hadi, F. Vidal, T. Ozaki, *Appl. Phys. Lett.* **94**, 111108 (2009)
26. R.A. Ganeev, L.B.E. Bom, *J. Appl. Phys.* **106**, 023104 (2009)
27. R.A. Ganeev, M. Suzuki, S. Yoneya, H. Kuroda, *J. Phys. B: At. Mol. Opt. Phys.* **48**, 165401 (2015)
28. R.A. Ganeev, M. Suzuki, T. Ozaki, M. Baba, H. Kuroda, *Opt. Lett.* **31**, 1699 (2006)
29. R.A. Ganeev, H. Singhal, P.A. Naik, V. Arora, U. Chakravarty, J.A. Chakera, R.A. Khan, I.A. Kulagin, P.V. Redkin, M. Raghuramaiah, P.D. Gupta, *Phys. Rev. A* **74**, 063824 (2006)
30. L.B.E. Bom, F. Bouzid, F. Vidal, J.-C. Kieffer, T. Ozaki, *J. Phys. B: At. Mol. Opt. Phys.* **41**, 215401 (2008)
31. R.A. Ganeev, T. Witting, C. Hutchison, V.V. Strelkov, F. Frank, M. Castillejo, I. Lopez-Quintas, Z. Abdelrahman, J.W.G. Tisch, J.P. Marangos, *Phys. Rev. A* **88**, 033838 (2013)
32. M. Suzuki, M. Baba, R. Ganeev, H. Kuroda, T. Ozaki, *Opt. Lett.* **31**, 3306 (2006)
33. R.A. Ganeev, L.B.E. Bom, J.C. Kieffer, T. Ozaki, *Phys. Rev. A* **75**, 063806 (2007)
34. V. Strelkov, *Phys. Rev. Lett.* **104**, 123901 (2010)

35. R.A. Ganeev, J.A. Chakera, P.A. Naik, H. Singhal, R.A. Khan, P.D. Gupta, J. Opt. Soc. Am. B **28**, 1055 (2011)
36. R.A. Ganeev, V.V. Strelkov, C. Hutchison, A. Zaïr, D. Kilbane, M.A. Khokhlova, J.P. Marangos, Phys. Rev. A **85**, 023832 (2012)
37. G. Duffy, P. van Kampen, P. Dunne, J. Phys. B **34**, 3171 (2001)
38. J.L. Krause, K.J. Schafer, K.C. Kulander, Phys. Rev. Lett. **68**, 3535 (1992)
39. P.B. Corkum, Phys. Rev. Lett. **71**, 1994 (1993)
40. M. Lewenstein, Ph Balcou, M.Y. Ivanov, A. L'Huillier, P.B. Corkum, Phys. Rev. A **49**, 2117 (1994)
41. C. Hutchison, R.A. Ganeev, T. Witting, F. Frank, W.A. Okell, J.W.G. Tisch, J.P. Marangos, Opt. Lett. **37**, 2064 (2012)
42. R.A. Ganeev, H. Singhal, P.A. Naik, J.A. Chakera, A.K. Srivastava, T.S. Dhama, M.P. Joshi, P.D. Gupta, J. Appl. Phys. **106**, 103103 (2009)
43. V. Tosa, H.T. Kim, I.J. Kim, C.H. Nam, Phys. Rev. A **71**, 063 808 (2005)
44. C.A. Froud, E.T. Rogers, D.C. Hanna, W.S. Brocklesby, M. Praeger, A.M. de Paula, J.J. Baumberg, J.G. Frey, Opt. Lett. **31**, 374 (2006)
45. R.A. Ganeev, H. Singhal, P.A. Naik, J.A. Chakera, M. Tayyab, M. Baba, H. Kuroda, P.D. Gupta, J. Opt. Soc. Am. B **26**, 2143 (2009)
46. D.H. Lowndes, D.B. Geohegan, A.A. Puretzky, D.P. Norton, C.M. Rouleau, Science **273**, 898 (1996)
47. E. de Posada, J.G. Lunney, M.A. Arronte, L. Ponce, E. Rodríguez, T. Flores, J. Phys.: Conf. Series **274**, 012079 (2011)
48. S.B. Cameron, M.D. Tracy, J.P. Camacho, I.E.E.E. Trans, Plasma Sci. **24**, 45 (1996)
49. T. Mochizuki, K. Hirata, H. Ninomiya, K. Nakamura, K. Maeda, S. Horiguchi, Y. Fujiwara, Opt. Commun. **72**, 302 (1989)
50. S.S. Harilal, C.V. Bindhu, R.C. Issac, V.P.N. Nampoori, C.P.G. Vallabhan, J. Appl. Phys. **82**, 2140 (1997)
51. F.J. Gordillo-Vázquez, A. Perea, J.A. Chaos, J. Gonzalo, C.N. Afonso, Appl. Phys. Lett. **78**, 7 (2001)
52. S.S. Harilal, B. O'Shay, M.S. Tillack, J. Appl. Phys. **98**, 013306 (2005)
53. R. Sanginés, C.S. Aké, H. Sobral, M. Villagrán-Muniz, Phys. Lett. A **367**, 351 (2007)
54. B. Verhoff, S.S. Harilal, J.R. Freeman, P.K. Diwakar, A. Hassanein, J. Appl. Phys. **112**, 093303 (2012)
55. N. Smijesh, R. Philip, J. Appl. Phys. **114**, 093301 (2013)
56. M. Ruiz, F. Guzmán, M. Favre, S. Hevia, N. Correa, H. Bhuyan, E.S. Wynham, H. Chuaqui, J. Phys.: Conf. Series **511**, 012064 (2014)
57. H.R. Griem, *Plasma Spectroscopy* (McGraw-Hill, New York, 1964)
58. H.R. Griem, *Spectral Line Broadening by Plasmas* (Academic Press, New York, 1974)
59. P.L. Shkolnikov, A. Lago, A.E. Kaplan, Phys. Rev. A **50**, R4461 (1994)
60. H. Singhal, V. Arora, B.S. Rao, P.A. Naik, U. Chakravarty, R.A. Khan, P.D. Gupta, Phys. Rev. A **79**, 023807 (2009)
61. H. Singhal, R.A. Ganeev, P.A. Naik, V. Arora, U. Chakravarty, P.D. Gupta, J. Appl. Phys. **103**, 013107 (2008)
62. A. Paul, R.A. Bartels, R. Tobey, H. Green, S. Weiman, I.P. Christov, M.M. Murnane, H.C. Kapteyn, S. Backus, Nature **421**, 51 (2003)
63. L. Zheng, X. Chen, S. Tang, R. Li, Opt. Express **15**, 17985 (2007)
64. R.A. Ganeev, M. Suzuki, S. Yoneya, H. Kuroda, Appl. Phys. B **121**, 307 (2015)
65. R.A. Ganeev, M. Suzuki, H. Kuroda, Phys. Rev. A **89**, 033821 (2014)

Chapter 7

Harmonic Characterization Using Different HHG Schemes in the Extended Plasmas

Among the achievements of extended plasma approach for HHG are (i) the high efficiencies obtained using several plasma formations and the resonance-induced enhancement of individual harmonics; (ii) the growth of harmonic yield from the plasma plumes containing clusters of different materials; (iii) enhanced yield of harmonics compared with narrow plasma; (iv) demonstration of quasi-phase-matching concept during plasma harmonic generation; efficient application of extended non-metal targets for plasma formation; etc. The conversion efficiencies of plasma harmonics became in some cases comparable with those reported during gas HHG studies. One can expect that the use of extended plasmas can further improve the nonlinear optical response of such a medium. Among the important tasks of this approach is the characterization of harmonics and the analysis of different methods of extended plasma formation.

In this chapter, we analyze the systematic studies of the harmonic generation of ultrashort laser pulses in the 5-mm-long Zn and Mn plasmas (i.e., application of nanosecond, picosecond, and femtosecond pulses for ablation, comparison of harmonic generation from atomic, ionic, and cluster-contained species of plasma, variation of plasma length, two-color pump of plasmas, etc.). We show the physical restrictions and pave the way in a search for other options, notably plasma HHG spectroscopy allowing the material study through the analysis of the high-order nonlinear optical processes during material ablation.

We also discuss the harmonic generation using the femtosecond pulses propagating in the vicinity of extended solid targets. The harmonics were observed in the case of double-pulse scheme while using different solids (metals, nanoparticles, and microparticles). We address the usefulness of the application of proposed double-pulse method for the harmonic generation in extended media. This method allows the simplified analysis of the high-order nonlinear optical properties of the media. At the same time, this technique could be applied for the direct observation of the HHG from the solids.

7.1 Low- and High-Order Harmonic Generation in the Extended Plasmas Produced by Laser Ablation of Zinc and Manganese Targets

Approximately half of the solid elements of periodic table have been probed for the plasma HHG (Fig. 2.1). Search for the “old” and “new” plasma formations allows the achievement of the extremes in the plasma harmonics (i.e., most extended cut-off and highest harmonic yield in the longer wavelength range of XUV), which however requires the systematic studies of these species. The choice of zinc [1] and manganese [2] plasmas was motivated by a search of these extremes. A superiority of manganese plasma from the point of view of highest harmonic cut-off was reported in [2], though the reasons of this peculiarity yet clearly explained. Note that the harmonic yield from this plasma was not as strong as from some other plasma species. For example, silver plasma showed strongest harmonics in the range of 30s–50s orders with weaker harmonics in the longer wavelength range [3]. Why it happens in the case of Ag plasma also remains unclear. Another puzzle is why some elements demonstrate the enhancement of single harmonics near ionic resonances [4], whereas other elements with similar closeness of harmonics and ionic transitions do not show this enhancement [5]. One can admit that there are many puzzles in this field of nonlinear optics.

There no published studies of harmonic generation in the Zn plasma excluding [1] where this medium was used, along with other plasmas, for the analysis of the coherence properties of the harmonics generated by a few-cycle pulses. The analysis of Zn plasma has clarified the issue of the influence of free electrons on the coherence properties of harmonics in the cases of their static and dynamic appearance in the nonlinear medium. The analysis presented in this section is mostly aimed in finding the best conditions for the strongest low-order harmonic generation of Ti:sapphire laser in the plasma plumes. Zn plasma has proven to be the right choice for these purposes.

In the past, manganese plasma, as a medium for HHG, has been studied in [2, 6]. Previous studies have shown the advanced properties of this plasma from the point of view of generation of the “second” plateau of harmonic distribution. Moreover, the use of a few-cycle pulses (3.5 fs [6]) has allowed the observation of single (33rd) broadband harmonic. Meanwhile, in the discussed studies of Mn ablation, the limits of harmonic cut-off in the case of plasma media are demonstrated [7].

As it was mentioned earlier, the majority of plasma harmonic studies were carried out using the narrow plasma plumes (~ 0.5 mm). It was shown in Chap. 3 that application of longer plasmas can further enhance the harmonic conversion efficiency. Long plasma allows the use of the quasi-phase-matching concept for enhancement of a group of harmonics. To create an extended area of ablation on the target surface, one has to carefully choose the conditions of plasma formation.

The absorption of harmonics in the extended plasma and the phase mismatch can prevent the enhancement of harmonic yield.

The harmonic generation scheme is described in Sect. 3.1. The ablation of Zn and Mn extended bulk targets was studied and, in some cases, compared them with the plasmas produced on other metals. The sizes of targets where the ablation occurred were 5 mm. The harmonic yield from the manganese oxide to zinc oxide nanoparticles was also analyzed. The nanoparticles were glued on the 5-mm-long glass plates and used as the targets for plasma formation.

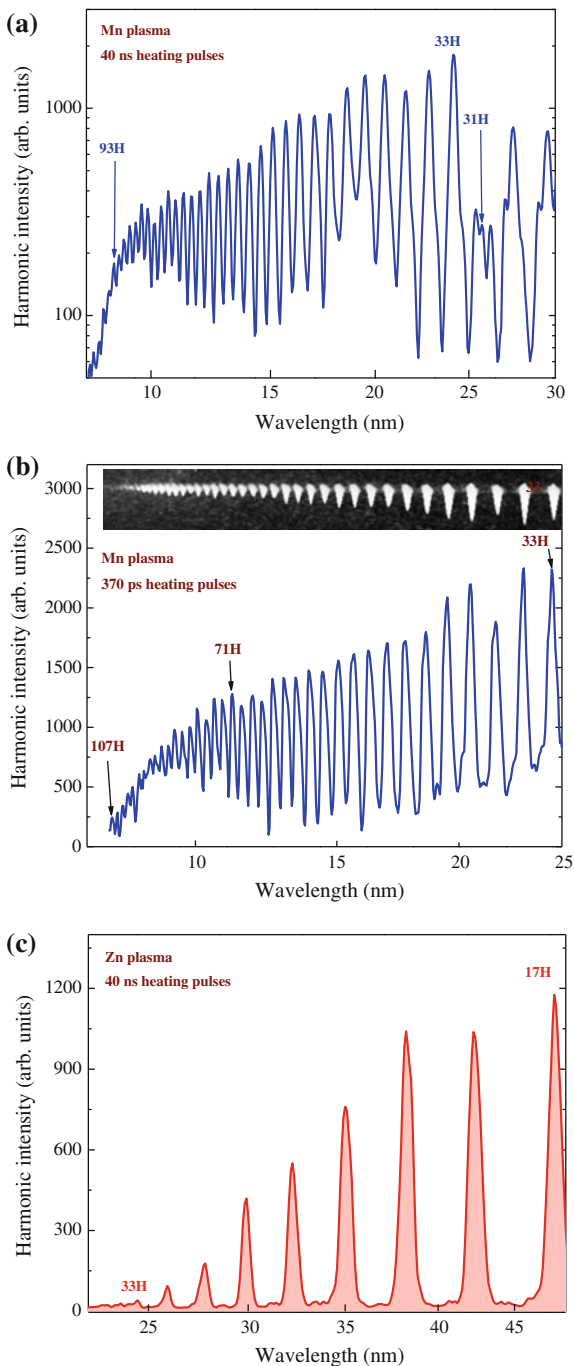
Different pulses were used for the formation of the plasma plumes to optimize the HHG during ablation of Mn and Zn targets. The Mn plasma produced by 40 ns pulses allowed generation of harmonics up to the 93rd order (Fig. 7.1a). The studies showed that the harmonic yield and cut-off at these conditions were less than in the case of the 370 ps heating pulses. In the latter case, harmonics above the 100th order were observed (Fig. 7.1b). The application of ultrashort pulses (80 fs, 802 nm) allowed the formation of the plasma plumes suitable for harmonic generation as well. However, the strong plasma emission from ablated area and the high electron concentration prevented the achievement of the enhanced yield of coherent emission in the XUV range compared with two other cases.

The same tendency was observed in the case of zinc ablation. The harmonics up to the 33rd order were generated in the case of ablation using the 40 ns pulses (Fig. 7.1c). The use of 80 fs pulses led to similar results. As in the case of Mn ablation, the application of 370 ps pulses for ablation has demonstrated better properties of the Zn plasma for the harmonic generation. The 39th harmonic cut-off was achieved in the case of Zn plasma at the optimal conditions of ablation by the 370 ps pulses. During following studies, the 370 ps pulses were used for ablation and plasma formation.

The analysis and optimization of plasma and harmonic emission from the ablation of Mn and Zn targets was based on the studies of various factors responsible for the HHG in those extended media. The length of plasma, delay between heating and driving pulses, heating pulse energy, and distance between the targets and propagating femtosecond pulses can be considered as the most important factors. One can estimate the beginning of restricting factors by analyzing the $I_H(L)$ dependence. Figure 7.2a shows the variation of 17th harmonic at different lengths of Mn plasma at the fluence of 370 ps heating pulse of 0.3 J cm^{-2} . This figure demonstrates the quadratic growth of harmonic yield with the increase of plasma length up to $\sim 3\text{--}4$ mm, with some saturation at longer plasma lengths.

Figure 7.2b, c show similar dependences for different harmonics generated in the Zn plasma at the heating pulse intensity of $I_{\text{hp}} = 1.5 \times 10^9 \text{ W cm}^{-2}$ and the fluence of $F_{\text{hp}} = 0.5 \text{ J cm}^{-2}$. In the case of 11th harmonic (Fig. 7.2b), this dependence had a slope $m \approx 2.2$ up to the $L = 1.5$ mm, with further insignificant decrease of the slope ($m \approx 1.9$). One can see a gradual and almost unsaturated growth of 11th harmonic with the increase of plasma length along the whole range of variations of this parameter. Those studies showed that the free electrons, absorption of plasma,

Fig. 7.1 a Harmonic spectrum from the Mn plasma produced by 40 ns heating pulses ($I_{dp} = 1 \times 10^{15} \text{ W cm}^{-2}$). **b** Harmonic spectrum from the Mn plasma produced by 370 ps heating pulses ($I_{dp} = 1 \times 10^{15} \text{ W cm}^{-2}$). *Inset* Raw image of harmonic spectrum. **c** Harmonic spectrum in the cut-off region produced from the Zn target ablated by 40 ns heating pulses ($I_{dp} = 8 \times 10^{14} \text{ W cm}^{-2}$). Reprinted with permission from [7]. Copyright 2014. AIP Publishing LLC



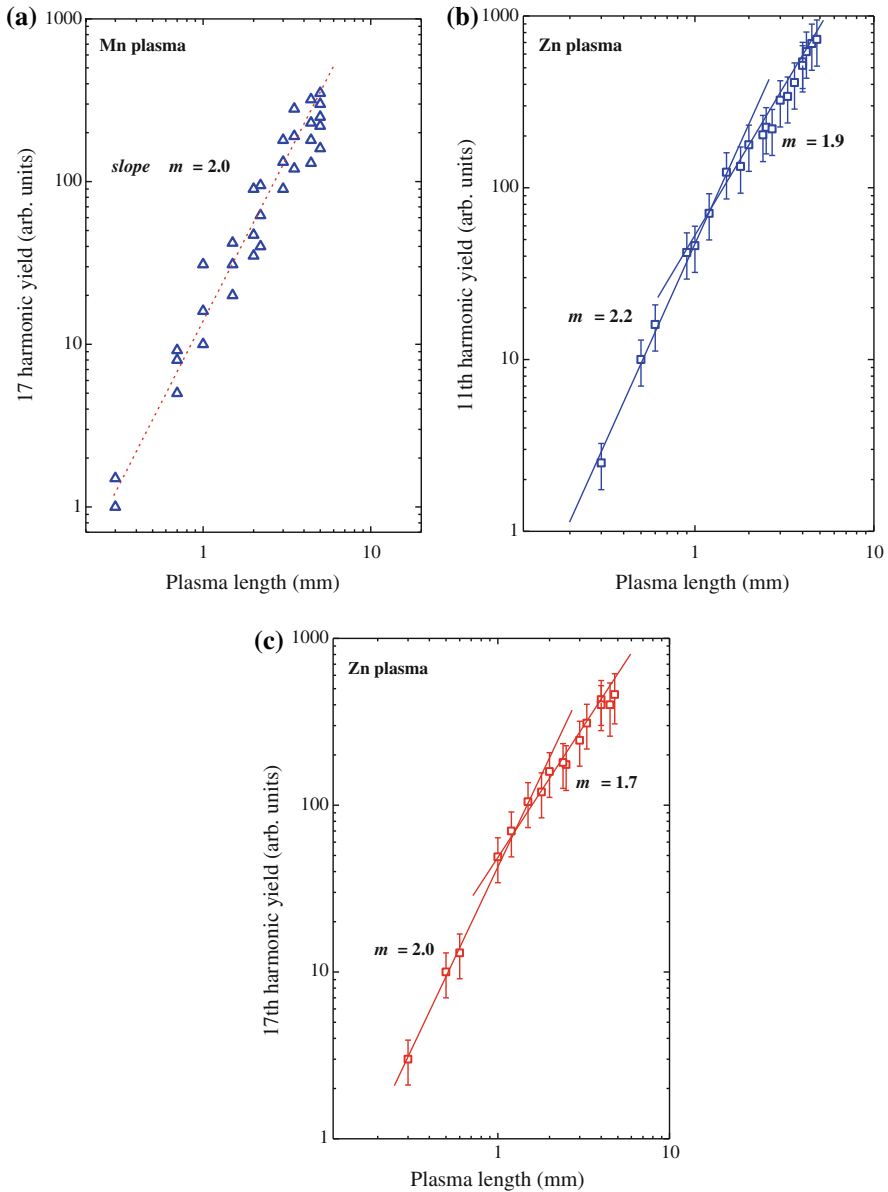


Fig. 7.2 **a** Dependence of the 17th harmonic yield on the length of Mn plasma at weak excitation of the target. **b, c** Dependences of the **b** 11th and **c** 17th harmonic yields on the length of Zn plasma. These data were obtained using the 370 ps heating pulses and heating fluence $F = 0.6 \text{ J cm}^{-2}$. Reprinted with permission from [7]. Copyright 2014. AIP Publishing LLC

phase mismatch, Kerr effect, etc. did not play a significant role in the variation of this dependence at weak excitation of the target. Similar dependences were observed for other lower-order harmonics (see, for example, the $I_H(L)$ dependence for the 17th harmonic, Fig. 7.2c).

The growth of target excitation by 370 ps pulses increases the plasma concentration, which in turn should lead to the growth of the harmonic yield. The $I_H(F_{hp})$ dependence for the 47th harmonic generated in the Mn plasma showed a maximum at $F_{hp} = 0.7 \text{ J cm}^{-2}$ with the following gradual decrease of harmonic yield during irradiation of the target using stronger heating pulses. The over-excitation of target led to appearance of the abundance of free electrons in the extended plasma plume and to the growth of the phase mismatch between the interacting waves.

The long plasma plumes obtained at optimal excitation conditions allowed the generation of the maximally extended cut-off. A weak excitation of target by 370 ps pulses ($F_{hp} = 0.2 \text{ J cm}^{-2}$) led to the plateau-like harmonic generation up to the cut-off (27th harmonic) similar to the one defined from the three-step model of HHG [8–10] for the singly changed Mn ions. At higher fluence ($F_{hp} = 0.7 \text{ J cm}^{-2}$), the second plateau appeared starting from the enhanced 33rd harmonic. In the case of 5-mm-long Mn plasma, the harmonics up to the 107th order were achieved (Fig. 7.1b). Further growth of fluence ($F_{hp} > 1.2 \text{ J cm}^{-2}$) caused the disruption of harmonic generation. In the case of 0.5-mm-long Mn plasma, the harmonic cut-off was extended up to the 95th order.

The important parameter of plasma harmonic studies is the incoherent plasma emission in the XUV range. The analysis of plasma emission spectra allows defining the ionic transitions, which could be responsible for the enhancement of harmonics. Below we present the analysis of the Zn plasma emission appearing at the optimal ablation near the harmonic wavelengths in the range of 40–100 nm. For better visual comparison of the lowest-order harmonic spectra, plasma spectra, and spectra obtained using two-color pump, we show them as the raw images appeared on the phosphor screen of MCP. A strong emission of 9th harmonic ($\lambda = 89.1 \text{ nm}$) was observed, which considerably exceeded the neighboring orders (Fig. 7.3, upper panel). The ratio of the intensities of this and neighboring higher-order harmonics ($\sim 8\times$) analyzed at unsaturated conditions of registration was considerably larger compared with other plasmas (C, Au, Cu). This observation points out that the mechanism of the enhancement of 89.1 nm radiation was other than the prevalence of the lower orders over the higher ones at the beginning of the plateau-like range of harmonic distribution. The analysis of plasma emission during excitation of the Zn target, without the propagation of the driving pulse through the plasma, showed the presence of some ionic lines attributed to the Zn II and Zn III transitions (Fig. 7.3, middle panel). Note the closeness of two $3d^{10}4s-3d^94s4p$ transitions (Zn II, $\lambda = 88.1$ and 89.3 nm) with the wavelength of 9th harmonic. There is some possibility in the influence of these transitions on the nonlinear optical response of the medium during propagation of the strong ultrashort laser pulse through the ionized medium. The strong emission of 9th harmonic could be originated from the

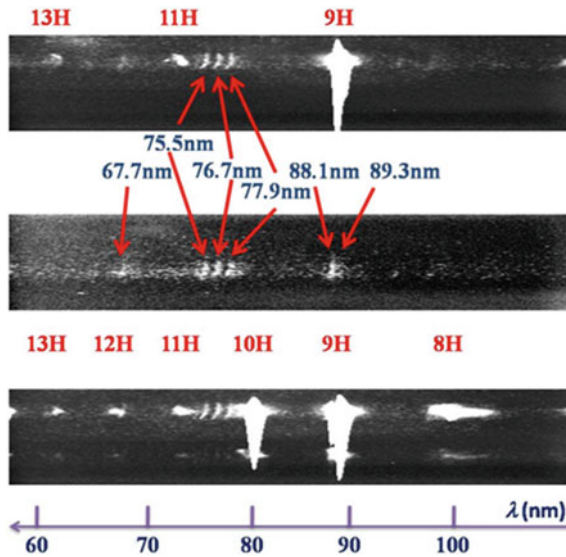


Fig. 7.3 Raw images of harmonic and plasma spectra obtained from the zinc ablation by 370 ps pulses. *Upper panel* Harmonic spectrum generated using the 802 nm driving pulses. *Middle panel* Plasma emission measured in the absence of driving radiation. *Bottom panel* Two-color pump induced harmonic spectrum. The wavelengths of ionic transitions are shown in the top of middle panel. The images are presented at the saturated conditions of registration for better visibility of the peculiarities of plasma and harmonic emission. Reprinted with permission from [7]. Copyright 2014. AIP Publishing LLC

resonance-induced enhancement of the HHG conversion efficiency in the Zn plasma. The studies of Zn plasma emission in the XUV for a long time have been related with the identification of the terms responsible for the observed ionic lines [11, 12]. However, no information about the oscillator strengths of those ionic transitions presented in Fig. 7.3 has been reported. Similar observations reported previously in other plasmas (In, GaAs, Sb, etc. [13]) point out the correlation between the presence of the ionic transitions possessing strong oscillator strengths in the vicinity of some harmonics and the strong yields of those harmonics.

The same can be said about the observation, in the case of two-color pump (401 and 802 nm), of a strong 10th harmonic ($\lambda = 80.2$ nm; Fig. 7.3, bottom panel) close to some other ionic transitions (particularly, $4s-7p$ transition of Zn II, $\lambda = 77.9$ nm [14]). It is unclear whether their influence on the 10th harmonic yield causes the growth of efficiency of this radiation. However, once we compare the intensities of 8th and 10th harmonics, the prevalence of the latter radiation becomes obvious. To check the assumption of resonance enhancement, one has to tune the wavelength of 10th harmonic close to and out of these transitions, which was not possible in those experiments.

The strong emission of some ionic transitions does not necessarily point out that they possess the high oscillator strengths. Particularly, the observation of the strong emission of 18.3 eV transition ($3d^{10}-3d^9(^2D)4p$) of Zn III at the conditions of plasma excitation by a few-cycle broadband pulses centered at 770 nm was attributed to the enhancement of the part of 11th harmonic of this radiation, though the wavelength of this harmonic ($\lambda = 70$ nm) did not exactly match with the wavelength of $3d^{10}-3d^9(^2D)4p$ transition ($\lambda = 67.7$ nm) [1]. The enhancement of some particular harmonic could also be related with the modification of the refractive index of plasma in the area of anomalous dispersion near the ionic transitions, which can create the phase matching conditions between the waves of this specific harmonic and driving pulse. There are also other explanations of the resonance enhancement of harmonics, which are mostly based on the analysis of the micro-processes [6, 13].

Below we analyze studies of the harmonics generated in the plasma produced on the glass substrates contained the manganese oxide and zinc oxide nanoparticles. The aim of those studies was to show the difference in the harmonic spectra from the Mn- and Zn-contained plasmas in the cases when different species of nonlinear medium become responsible for the harmonic generation.

The shapes of nanoparticles before their ablation were analyzed using the transmission electron microscope. The sizes of Mn_2O_3 nanoparticles were in the range of 80–130 nm (Fig. 7.4a). The Zn_2O_3 nanoparticles had the sizes of 40–80 nm (Fig. 7.4b). The TEM analysis of the debris of nanoparticle ablation has shown the similarity of the deposited material with the one glued on the glass substrates before the ablation. Thus, the presence of nanoparticles in the laser-produced plasmas during these HHG experiments was confirmed.

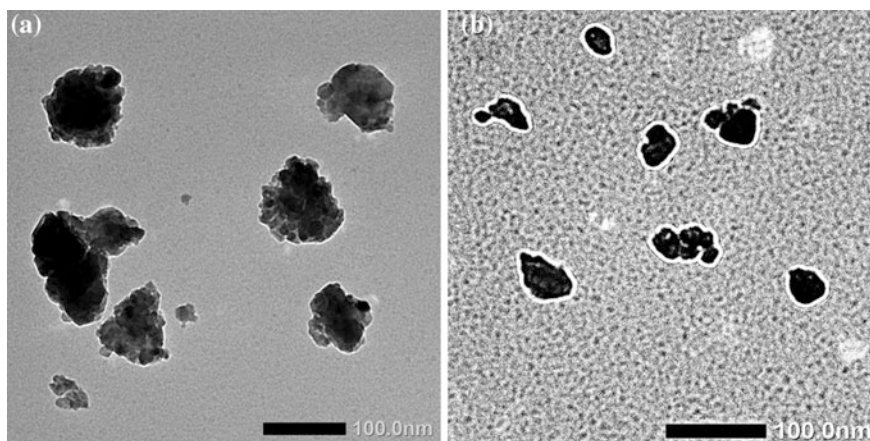
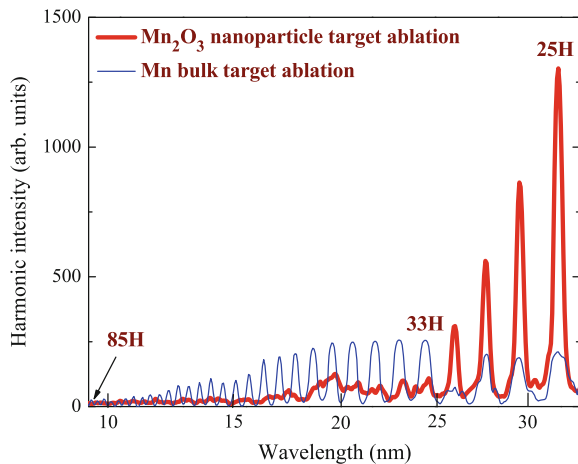


Fig. 7.4 TEM images of the **a** manganese oxide and **b** zinc oxide nanoparticles used in the HHG experiments. The *black lines* in the images correspond to 100 nm. Reprinted with permission from [7]. Copyright 2014. AIP Publishing LLC

The harmonic spectrum generated from the Mn_2O_3 nanoparticle-contained plasma at optimal excitation of target ($F_{\text{hp}} = 0.4 \text{ J cm}^{-2}$) is shown in Fig. 7.5 (thick curve). The growth of the excitation of nanoparticle target led to generation of weak harmonics and strong plasma emission. Here, we also present the harmonic spectrum obtained from the plasma produced on the Mn bulk target at similar conditions (Fig. 7.5, thin curve). It was shown that the intensity of the lower-order harmonics generated in the nanoparticle-contained plasma was six times stronger compared with the same harmonics generated in the plasma produced on the Mn bulk target. In the meantime, the harmonic cut-off from the nanoparticle-contained plasma was considerably lower comparing with the one from the plasma produced on the solid target (37th and 107th harmonics, respectively). Note that the low-order harmonics generated from the Zn_2O_3 nanoparticle-contained plasmas at optimal excitation of target ($F_{\text{hp}} = 0.3 \text{ J cm}^{-2}$) were weaker compared with the same harmonics generated from the ablation of Zn bulk target.

Here, we discuss the source of intense harmonics from nanoparticle-contained plasma, which could be revealed from the two experimental observations. The first one is related with the harmonic spectra produced from the nanoparticle plasma. The harmonic cut-off typically scales with the second ionization potential of the target material when one uses the plasma from solid target for the HHG. When nanoparticles were used for ablation and plasma formation, the intense harmonics were generated at relatively low heating fluences, while showing the low cut-off. At higher fluences of heating radiation, the harmonic cut-off could be extended similarly to those obtained from the plasma produced on the solid targets. However, the harmonic intensity becomes weaker compared with the harmonics generated from the ablated solids. Those observations suggest that there are two regimes of harmonic generation in the presence of nanoparticles: the weakly excited plasma allowing relatively strong harmonic intensities and low cut-offs and the highly excited plasma allowing relatively weak harmonic intensity and higher cut-off. The

Fig. 7.5 Harmonic spectra between the 25th and 85th orders obtained from the plasmas contained Mn_2O_3 nanoparticles (*thick curve*) and monomers of manganese (*thin curve*). Reprinted with permission from [7]. Copyright 2014. AIP Publishing LLC



low cut-off observed in the case of nanoparticle plasma in the first regime suggests that harmonic generation in that case occurs with the involvement of the neutral atoms of nanoparticles. Stronger excitation of nanoparticles caused their disintegration and appearance of singly and doubly charged ions of Mn, Zn, and their oxides, which led to higher cut-offs using these species (see also Sect. 6.2).

The second important peculiarity of the emission spectra from manganese oxide nanoparticles is the absence, at moderate intensity of heating pulse ($E_{\text{hp}} = 1.5 \times 10^9 \text{ W cm}^{-2}$), of the enhanced 33rd harmonic (Figs. 7.1a and 7.5, thick curve), contrary to the case of ablation of the solid Mn target, where the enhanced 33rd harmonic was stronger than the nearest lower-order harmonic (Fig. 7.5, thin curve). The enhancement of a group of harmonics starting with the 33rd order, compared with nearest lower-order harmonics, is clearly seen in Fig. 7.5 (thin curve) and is attributed to the influence of the resonance transitions of Mn II in this spectral region. This observation shows that the ionic transitions of manganese oxide nanoparticles do not play a significant role in the modification of the harmonic spectrum from this medium. It also confirms the prevailing role of neutrals, rather than ions, as the emitters of lower-order harmonics from the cluster-contained plasma, while some small amount of singly charged clusters could be responsible for the generation of weak higher-order (H17–H27) harmonics.

Below, we analyze the equally enhanced even and odd harmonics generated in the extended manganese and zinc plasmas using relatively weak second field in the two-color pump scheme. Those studies have shown a considerable growth of single even harmonic near the giant $3p-3d$ resonances of manganese ions. Figure 7.6a shows the harmonic spectra generated after propagation of the extended manganese plasma in the case of pumping by single-color (802 nm) and two-color (802 and 401 nm) pulses at the equal conditions of plasma formation. One can distinguish the similarity of the odd and even harmonic intensities along almost whole range of generation (bottom curve). The advanced properties of extended plasmas were also emphasized, while comparing with the odd and even harmonics generating in the 0.5-mm-long manganese plasma plume. In latter case, the cut-off of even harmonics was considerably lower comparing with the one of odd harmonics. Moreover, the intensity of former harmonics was a few times weaker comparing with the odd harmonics, contrary to the case of extended plasma.

Contrary to the case of the 0.7-mm-long BBO used for the two-color experiments in the zinc plasma [14], the application of the 0.5-mm-long BBO crystal allowing 7 % second harmonic conversion efficiency led to the generation of strong odd and even harmonics along a whole spectrum of generation (Fig. 7.6b). Two spectra presented in this figure were collected at similar conditions when the BBO crystal placed in vacuum chamber was moved in and out of the path of driving radiation. The measurements of harmonic yield have shown the $3\times-4\times$ enhancement achieved for lower-order odd harmonics in the case of the two-color pump (thick curve) compared with the single-color pump (thin curve). One can see that the odd harmonics were improved in the case of two-color pump, though in that case the intensity of 802 nm pulse in the plasma area was smaller compared with the single-color case. This observation demonstrates the evidence of significant

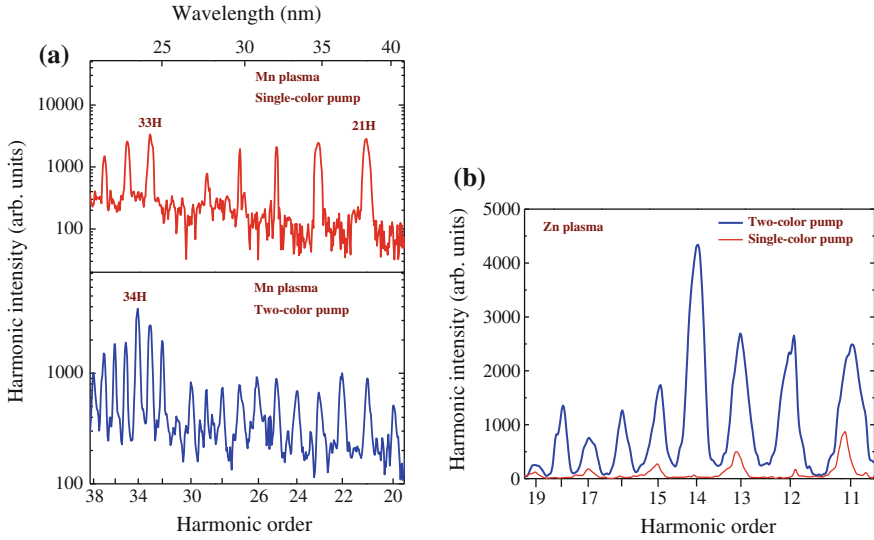


Fig. 7.6 **a** Harmonic spectra in the 20–40 nm range obtained using the single-color (*upper panel*) and two-color (*bottom panel*) pumps of Mn plasma. **b** Single-color pump (*thin curve*) and two-color pump (*thick curve*) induced HHG in the extended Zn plasma. These data were obtained using the 370 ps heating pulses. Reprinted with permission from [7]. Copyright 2014. AIP Publishing LLC

influence of the second wave on the harmonic generation efficiency in the extended plasma. The application of narrow (~ 0.5 mm) Zn plasma did not allow obtaining similar enhancement induced by the two-color pump.

The discussed study combined various milestones of previous achievements of the plasma harmonics. The joint influence of various mechanisms of harmonic enhancement was applied to the two plasma samples with the aim of practical achievement of the best results of plasma-based HHG (i.e., most extended cut-off and strongest harmonic yield in the longer wavelength range). The use of clusters, two-color pump, extended plasma, and ionic resonances allowed the demonstration of most advanced characteristics of plasma harmonics reported so far. Here we notice the limits of most extended harmonic cut-off in the plasma media. Though yet clearly explainable, these limits in highest photon energy show the physical restrictions and pave the way in a search for other options, notably plasma HHG spectroscopy allowing the material study through the analysis of the high-order nonlinear optical processes during material ablation. Whilst not competing with gas HHG in the extension of highest harmonic order, we demonstrate that plasma approach may provide the excellent source of lower-order harmonics in the 40–100 nm spectral range, which would be useful for various applications.

The comparison of the zinc plasma with the carbon plasma, which showed strongest low-order harmonics so far [15, 16], have confirmed that the former medium possesses the advanced properties with regard to the latter one. No absolute

measurements of conversion efficiency in Zn plasma were carried out in the range of 11th–19th harmonics. However, the comparison of the harmonic yields obtained at best conditions of generation from the zinc and carbon ablations, which was carried out during those studies, showed stronger conversion efficiency of the Ti:sapphire laser radiation in the former plasma with a factor of two to three. From the reported data on the lower-order harmonic yield from carbon plasma [15], one can estimate the $\sim 5 \times 10^{-5}$ conversion efficiency for the 11th–19th harmonics generated in the zinc plasma. Other plasmas (Mn, as well as Au, Ag, and Cu) used during these comparative studies showed 4–6 times weaker yields of the lower-order harmonics. Thus, the Zn plasma could be a best choice ones one needs the strongest coherent emission in the longer-wavelength range of XUV.

7.2 Application of Double Femtosecond Pulses for Plasma Harmonic Generation

The high-order harmonic generation of ultrafast laser pulses in the solids took the attention relatively recently after the demonstration of this process in the mid-infrared range using the ZnO crystal [17]. Those studies have shown for the first time the perspective of using the dense medium for the HHG contrary to the commonly accepted techniques of the harmonic generation in gaseous [18, 19] and plasma [13] media, as well as of the specularly reflected harmonics from the surfaces [20].

The attractiveness of HHG in the use of solids is related with considerably higher amount of harmonic emitters compared with the gases and plasmas. The main obstacle of this approach is a strong absorption of the generated radiation in the dense materials. A search of new methods of the HHG in solid targets led to the theoretical studies [21, 22], which defined the main principles of this technique. The principles of solid target HHG was mostly based on the same approach, which has been used in the case of gas and plasma HHG. The three-step model [8–10] allowed the explanation of main experimental findings of the HHG by different means. In the meantime, other methods were also examined during recent time. Among them is the consideration of the small-sized dense species as the media for harmonic generation.

The application of dense media was first examined during the pioneering experiments with gas clusters [23–25], microdroplets [26, 27], and nanoparticle ablation plumes [28, 29]. The basics of cluster-induced enhancement of the high-order nonlinear optical processes are still debated in literature [25]. The increase of the cross-section of recombination of the accelerated electron and parent nanoparticle and the surface plasmon induced growth of the nonlinear optical response of cluster-contained medium were among the explanations offered during last time to define the origin of the observed enhancement of harmonic yield from the clusters. However, with the growth of the sizes of particles, the self-absorption, large amount of free electrons, and phase-mismatch between the interacting waves

can play a major role in the suppression of HHG. It is obvious that the dense species can increase the conversion efficiency of HHG once the absorption of the driving and harmonic radiation will be minimized.

Below we analyze the harmonic generation of the femtosecond pulses propagated in the vicinity of solid targets [30]. The harmonics were observed in the case of double-pulse beams while using different solids (metals, nanoparticle powders, and organic materials). We discuss the perspectives of the application of proposed method. We also compare this double-pulse method and commonly used method of plasma formation using picosecond pulses and delayed propagation of a single femtosecond pulse through the preformed plasma.

The radiation of Ti:sapphire laser (central wavelength 802 nm, pulse duration 64 fs, pulse energy $E_{fp} = 4$ mJ, 10 Hz repetition rate) was used in these experiments. This radiation was focused using the 400 mm focal length spherical lens in the vicinity of the solid targets placed in the vacuum chamber (Fig. 7.7a). The intensity of driving pulse at the focus area was varied up to 4×10^{14} W cm⁻². The targets (various metals, nanoparticle powders, and organic materials) were moved to and out of the optical axis of ultrashort radiation using the translation stage to create the conditions when this radiation “touches” the targets. The optimization of the distance between the target and driving beam allowed choosing the conditions when the generating harmonics prevail over the plasma emission induced during ablation of these samples by the wing of the spatial distribution of focused radiation.

The optimization of this process was accomplished by producing the variable output radiation using the manipulation of the triggering signal on the Pockels cell in the regenerative amplifier of Ti:sapphire laser. The variation of the delay signal on the driver of Pockels cell allowed the separation of either single pulse or double pulses with the time interval between pulses of 8 ns. It became possible to produce two driving pulses for harmonic generation (double-pulse method) with variable ratio between the intensities of these pulses. The temporal tuning of the triggering signal allowed the variation of the intensities of these two pulses, as shown in the oscilloscope traces of output radiation presented in Fig. 7.7c.

The harmonics generated using double-pulse method were compared with the commonly used method of plasma formation by the picosecond pulse and propagation of the single femtosecond driving pulse, after the optimal delay, through the preformed plasma plume (ps+fs method, Fig. 7.7b). The application of different extended targets allowed the optimization of HHG. The conditions of plasma formation and harmonic generation using the double-pulse method in most cases were less favorable compared with the commonly used ps+fs method. One can expect that less suitable conditions of HHG in the case of double-pulse scheme can decrease the efficiency of this process. This assumption was proved in the case of solid metals, while in the case of non-metal materials and powdered targets the efficient HHG was achieved using the double-pulse scheme. Below we analyze the studies of the HHG in the cases of interaction of the wing of spatial distribution of femtosecond beam in the focal area with the metal and nonmetal targets and then compare with the cluster contained extended powdered targets.

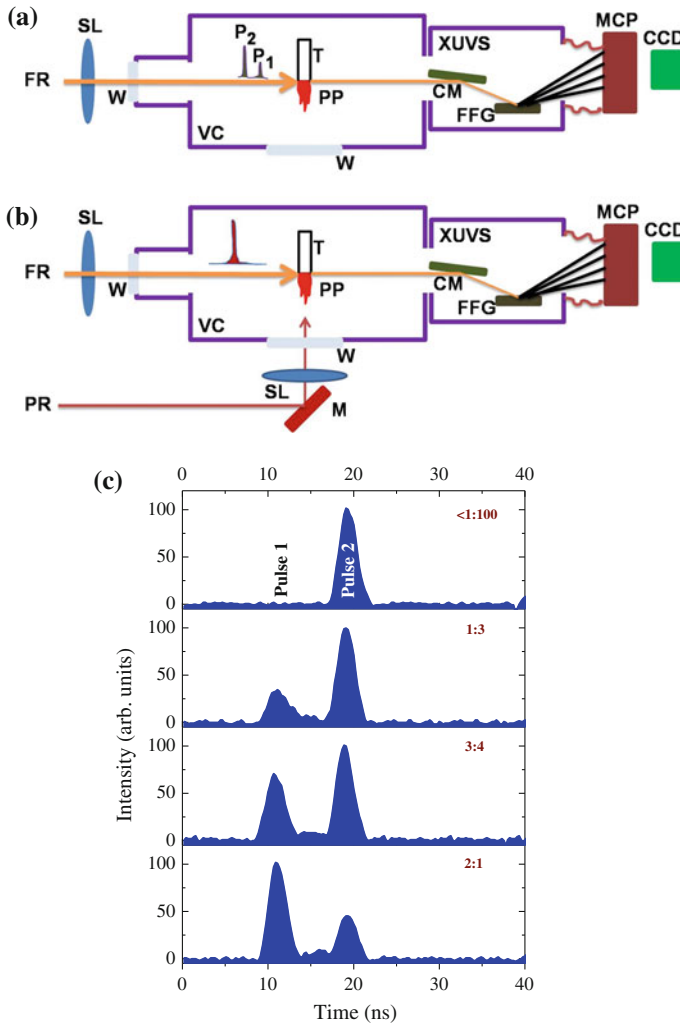


Fig. 7.7 **a** Experimental scheme for harmonic generation during interaction of the double femtosecond pulses and targets. *FR* femtosecond radiation; *SL* spherical lens; *VC* vacuum chamber; *W* windows of vacuum chamber; *P₁* first pulse; *P₂* second pulse; *T* target; *PP* plasma plume; *XUVS* extreme ultraviolet spectrometer; *CM* cylindrical mirror; *FFG* flat field grating; *MCP* micro-channel plate; *CCD* charge coupled device camera. **b** Commonly used scheme for plasma formation using the heating picosecond pulse followed with the propagation of delayed single femtosecond pulse through the optimally preformed plasma. *PR* picosecond radiation; *M* mirror. **c** Oscilloscope traces of the output radiation of Ti:sapphire laser at different ratios of the first and second pulses (the ratios are shown on the plots). Reprinted with permission from [30]. Copyright 2014. AIP Publishing LLC

Metal bulk targets allowed the weak harmonics generation in the case of double-pulse method. Both harmonic yield and cut-off were decreased compared with the ps+fs method. Particularly, the cut-off in the case of silver plasma was smaller compared with the case of conventional plasma HHG (49th and 59th harmonics respectively), while the harmonic yield in the former case was almost 10 times weaker.

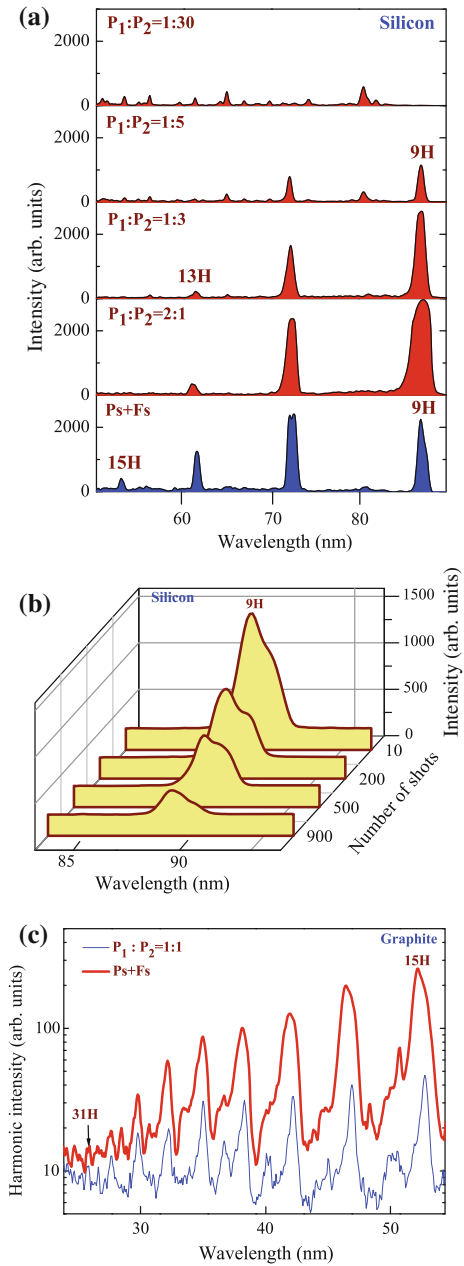
Similar pattern was observed in the case of Cr target, with the resonantly enhanced 29th harmonic dominated in the spectra produced using two methods. No harmonics using the double-pulse method were observed in the cases of Zn and In targets. One can assume the difficulty in the formation of a sufficient amount of particles in the plasma plume produced during the excitation of the target by the part of the first pulse in the double-pulse scheme. Small delay between the first (P_1) and second (P_2) pulses (8 ns) also prevented the appearance of the large amount of plasma particles along the axis of propagation of the second pulse. No harmonics were observed in the case of single pulse and low $P_1:P_2$ ratios ($<1:5$) of the double-pulse scheme applied to any metal.

The best conditions of the HHG using double-pulse scheme for extended bulk targets were observed in the case of silicon (Fig. 7.8a). The conditions were defined when the double-pulse method (at the ratio of the intensities of the first and second pulses $P_1:P_2 = 1:2$) allowed the generation of stronger lower-order harmonics compared with the ps+fs method (panels 4 and 5). The stability of double-pulse technique was insufficient for the practical application of generating harmonics in the case when the targets were maintained at the same position during these experiments. Figure 7.8b shows the decay of the 9th harmonic with the growth of the number of shots at the same position of silicon target. The three-fold decrease of the intensity of 9th harmonic was observed after 900 shots, which was induced by the modification of target surface.

The graphite target allowed harmonic generation and similar cut-offs using both methods (Fig. 7.8c). In that case, the blue sided lobes were observed along the harmonic spectra. The clear evidence of the variation of harmonic spectra was also observed in the case of polyvinyl alcohol target (Fig. 7.9). Upper and bottom images show the relatively weak and strong interactions of the wing of femtosecond beam with the target surface. These conditions were accomplished by moving the target farther or closer with respect to the femtosecond beam axis. The strong short-wavelength components of each harmonic are clearly seen in the bottom panel of this figure, which were corresponded to the stronger interaction of the pulse and target. Previously, the appearance of short-wavelength lobes has been reported in a few studies of plasma harmonics. Particularly, the origin of the broader width of harmonics and the short-wavelength lobes have been discussed in [31], and they were attributed to the influence of the self-phase modulation of the driving femtosecond pulse during propagation through the plasma plume.

The application of the powdered targets glued on the glass substrate in the double-pulse scheme allowed the achievement of better conditions for the HHG. Various powders were used as the targets for the studies of the HHG using the double-pulse scheme. Figure 7.10a shows the harmonic spectrum from the carbon

Fig. 7.8 **a** Dependences of plasma and harmonic spectra at different ratios of the first and second femtosecond pulses propagated close to the silicon target (*four upper plots*). *Bottom plot* shows the harmonic spectrum generated during the formation of silicon plasma by 370-ps pulses and delayed propagation of the femtosecond pulse through the preformed “optimal” plasma plume (ps+fs scheme). **b** Decay of 9th harmonic with the growing number of the femtosecond pulses propagated near the same spot of silicon target. Ratio of the first and second femtosecond pulses was 3:2. **c** Harmonic spectra from the graphite target. *Thick red curve* shows the harmonics generated from the plasma produced by the 370-ps pulses. *Thin blue curve* shows the harmonic spectra generated during propagation of the double femtosecond pulses close to the graphite target at the ratio of first and second pulse intensities of 1:1. Reprinted with permission from [30]. Copyright 2014. AIP Publishing LLC



nanofiber powder (diameter 40 nm, length of fibers 400 nm–10 μ m) glued on the glass substrate. The ratio $P_1:P_2$ was varied in a broad range (between 1:100 and 3:1), which allowed finding the optimum conditions ($P_1:P_2 = 1:3$, middle panel)

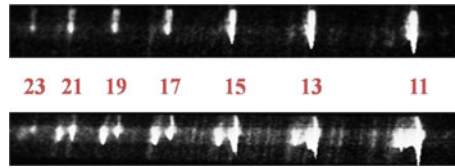


Fig. 7.9 Raw images of the harmonic spectra generated during propagation of the double femtosecond pulses close to the polyvinyl alcohol target at the ratio of first and second pulses of 1:2. The strong *blue-sided* lobes of harmonics alongside with plasma emission was appeared at the conditions when the target was moved close to the driving beam (*bottom panel*). Reprinted with permission from [30]. Copyright 2014. AIP Publishing LLC

when the strong lower-order (H11–H17) harmonics were generated while the plasma emission was insignificant. Similar studies were carried out using the silver nanoparticle powder (diameter of 10 nm), with the ratios $P_1:P_2$ varying between 1:4 and 5:4, which corresponded to the highest harmonic yields (Fig. 7.10b, three middle panels). The comparison of double-pulse and ps+fs schemes in that case showed higher conversion efficiency in the latter case (see bottom panel of Fig. 7.10b). Notice that the practical application of the powdered targets for the HHG is limited due to short-lasting stability of generating harmonics. The melting of cluster-contained target and the modification of ablated surface cause a decrease of harmonic yield after a few hundred shots. The cluster-contained targets were gradually moved up and down to keep the stable harmonic yield. The application of narrow targets ($L \sim 0.5$ mm) did not allow generation of harmonics using the double-pulse scheme excluding the case of nanoparticle targets. However, in the latter case, the efficiency of harmonics was weaker compared with the case of extended targets.

The NaCl microparticle (~ 100 μm) powder was also used to analyze the difference of the harmonic yields from the species of different consistency and dimensions. These studies were also carried out at different ratios of the first and second pulses of the driving radiation (Fig. 7.10c). Some advantages of the microparticles over nanoparticles were observed with the stronger harmonic yield in the former case, though the tendency remained similar to the previous case.

The proposed double-pulse method allows the simplified analysis of the high-order nonlinear optical properties of the media. At the same time, this technique could be applied for the direct observation of the HHG from the solids. Particularly, the ultrathin species, such as graphene sheets, could be directly probed by the femtosecond pulses taking the advantage of small absorption in this medium. The prevalence of harmonic over plasma emission could also be observed in other media. In the meantime, the conversion efficiency using the conventional scheme of plasma formation by the picosecond pulse followed with the propagation of the optimally delayed ultrashort pulse through the preformed plasma plume showed in most cases the stronger harmonic yield. Each of these two methods can find their own niche in the field of coherent XUV sources and nonlinear spectroscopy.

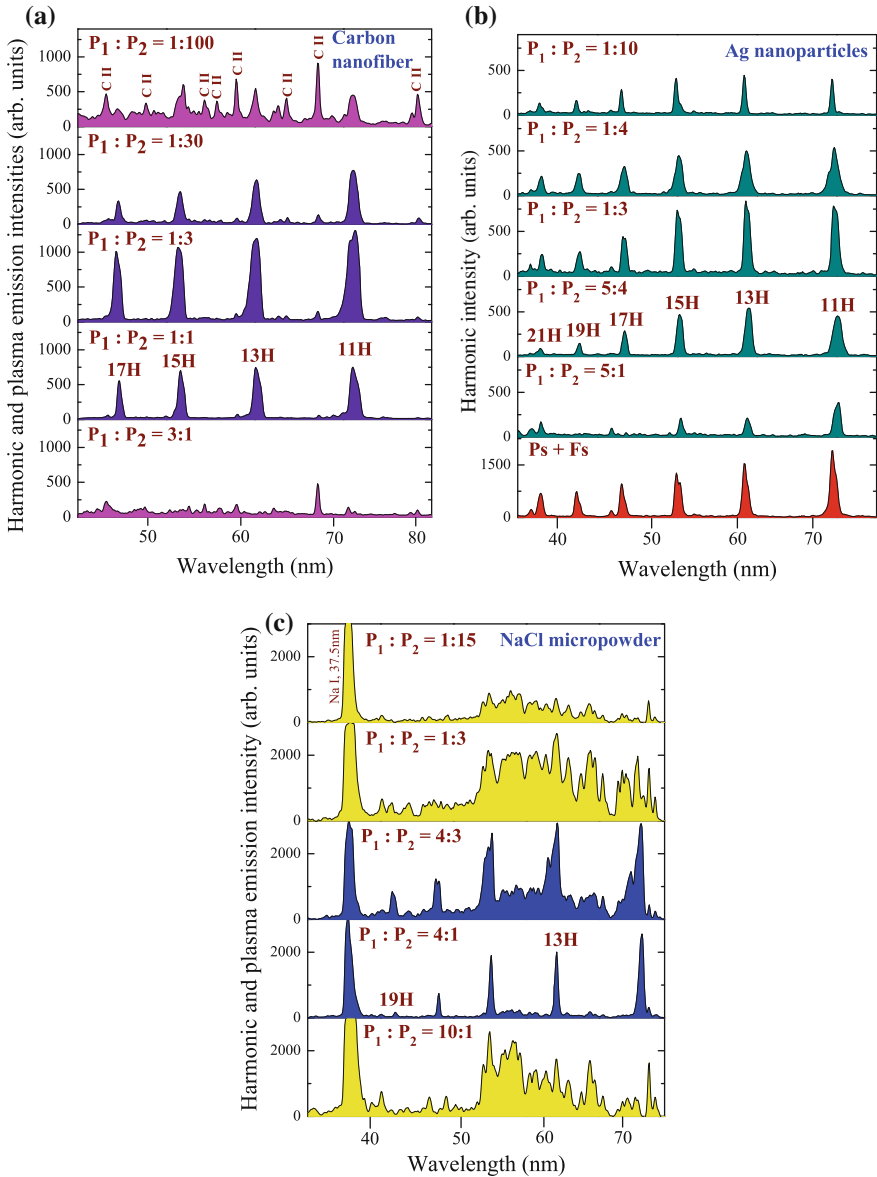


Fig. 7.10 Harmonic spectra at different ratios of the first and second pulses of driving beam in the cases of **a** carbon nanofiber, **b** silver nanoparticle, and **c** NaCl microparticles targets. *Bottom plot* in Fig. 7.4b shows the harmonic spectrum generated from the Ag nanoparticle plasma produced during ablation by 370-ps pulses and propagation of delayed (43 ns) femtosecond single pulse. Reprinted with permission from [30]. Copyright 2014. AIP Publishing LLC

7.3 Concluding Comments

We have demonstrated the advanced properties of extended manganese and zinc plasma plumes for the harmonic generation in the shorter and longer wavelength regions of XUV compared with the short-length plasmas used in previous studies. The range of energy fluence of $\sim 0.3\text{--}1\text{ J cm}^{-2}$ satisfied the requirement for the formation of the optimal plasma. The 370 ps pulses were found to be most suitable for plasma formation due to creation of the weakly ionized medium allowing generation of strongest harmonics and extended cut-off. During those systematic studies the harmonic generation in the manganese plasma up to the 107th order was demonstrated. We have shown the advanced properties of extended zinc plasma plumes for the harmonic generation in the longer wavelength region of XUV compared with other plasmas used in previous studies. The conversion efficiency of the 11th–19th orders at these conditions was estimated to be 5×10^{-5} . Those studies have demonstrated the limits of most extended harmonic cutoff in the plasma media. These limits in highest photon energy show the physical restrictions and pave the way in a search for other options, notably plasma HHG spectroscopy allowing the material study through the analysis of the high-order nonlinear optical processes during material ablation.

We have also discussed the harmonic generation using the two femtosecond pulses propagated in the vicinity of solid and powdered targets. The harmonics were observed in the case of double-pulse beams while using various materials (bulk metals and nonmetals, nano- and microparticle powders). The efficiency and cut-off of harmonic generation using the double-pulse method in most cases were lower compared with the ps+fs method. However, the simplicity, absence of additional source of heating radiation, and artificial optimization of the HHG using the adjustment of the double pulses and targets have shown the advantages of this technique. This method allows the simplified analysis of the high-order nonlinear optical properties of the media. It could be useful for the laser ablation induced HHG spectroscopy.

References

1. R.A. Ganeev, Z. Abdelrahman, F. Frank, T. Witting, W.A. Okell, D. Fabris, C. Hutchison, J.P. Marangos, J.W.G. Tisch, *Appl. Phys. Lett.* **104**, 021122 (2014)
2. R.A. Ganeev, L.B. Elouga Bom, J.-C. Kieffer, T. Ozaki, *Phys. Rev. A* **76**, 023831 (2007)
3. R.A. Ganeev, M. Baba, M. Suzuki, H. Kuroda, *Phys. Lett. A* **339**, 103 (2005)
4. R.A. Ganeev, *Open Spectrosc. J.* **3**, 1 (2009)
5. R.A. Ganeev, M. Suzuki, S. Yoneya, H. Kuroda, *J. Opt. Soc. Am. B* **31**, 3105 (2014)
6. R.A. Ganeev, T. Witting, C. Hutchison, F. Frank, M. Tudorovskaya, M. Lein, W.A. Okell, A. Zair, J.P. Marangos, J.W.G. Tisch, *Opt. Express* **20**, 25239 (2012)
7. R.A. Ganeev, M. Baba, M. Suzuki, S. Yoneya, H. Kuroda, *J. Appl. Phys.* **116**, 243102 (2014)
8. J.L. Krause, K.J. Schafer, K.C. Kulander, *Phys. Rev. Lett.* **68**, 3535 (1992)
9. P.B. Corkum, *Phys. Rev. Lett.* **71**, 1994 (1993)

10. M. Lewenstein, P. Balcou, M.Y. Ivanov, A. L'Huillier, P.B. Corkum, *Phys. Rev. A* **49**, 2117 (1994)
11. A.M. Crooker, K.A. Dick, *Can. J. Phys.* **46**, 1241 (1968)
12. K.A. Dick, *Can. J. Phys.* **46**, 1291 (1968)
13. R.A. Ganeev, *High-Order Harmonic Generation in Laser Plasma Plumes* (Imperial College Press, 2012)
14. R.A. Ganeev, M. Suzuki, H. Kuroda, *J. Opt. Soc. Am. B* **31**, 911 (2014)
15. L.B. Elouga Bom, Y. Pertot, V.R. Bhardwaj, T. Ozaki, *Opt. Express* **19**, 3077 (2011)
16. R.A. Ganeev, C. Hutchison, T. Witting, F. Frank, W.A. Okell, A. Zair, S. Weber, P.V. Redkin, D.Y. Lei, T. Roschuk, S.A. Maier, I. López-Quintás, M. Martín, M. Castillejo, J.W.G. Tisch, J.P. Marangos, *J. Phys. B: At. Mol. Opt. Phys.* **45**, 165402 (2012)
17. S. Ghimire, A.D. DiChiara, E. Sistrunk, P. Agostini, L.F. DiMauro, D.A. Reis, *Nature Phys.* **7**, 138 (2011)
18. M. Ferray, A. L'Huillier, X.F. Li, L.A. Lompré, G. Mainfray, G. Manus, *J. Phys. B: At. Mol. Opt. Phys.* **21**, L31 (1988)
19. A. McPherson, G. Ginson, H. Jara, N. Johann, I.A. McIntyre, K. Boyer, C.K. Rhodes, *J. Opt. Soc. Am. B* **4**, 595 (1987)
20. B. Dromey, M. Zepf, A. Gopal, K. Lancaster, M.S. Wei, K. Krushelnick, M. Tatarakis, N. Vakakis, S. Moustazis, R. Kodama, M. Tampo, C. Stoeckl, R. Clarke, H. Habara, D. Neely, S. Karsch, P. Norreys, *Nature Phys.* **2**, 456 (2006)
21. S. Ghimire, A.D. DiChiara, E. Sistrunk, G. Ndabashimiye, U.B. Szafruga, A. Mohammad, P. Agostini, L.F. DiMauro, D.A. Reis, *Phys. Rev. A* **85**, 043836 (2012)
22. F. Kemper, B. Moritz, J.K. Freericks, T.P. Devereaux, *New J. Phys.* **15**, 023003 (2013)
23. T.D. Donnelly, T. Ditmire, K. Neuman, M.D. Pery, R.W. Falcone, *Phys. Rev. Lett.* **76**, 2472 (1996)
24. J.W.G. Tisch, T. Ditmire, D.J. Fraser, N. Hay, M.B. Mason, E. Springate, J.P. Marangos, M.H.R. Hutchinson, *J. Phys. B: At. Mol. Opt. Phys.* **30**, L709 (1997)
25. H. Ruf, C. Handschin, R. Cireasa, N. Thiré, A. Ferré, S. Petit, D. Descamps, E. Mével, E. Constant, V. Blanchet, B. Fabre, Y. Mairesse, *Phys. Rev. Lett.* **110**, 083902 (2013)
26. A.D. DiChiara, E. Sistrunk, T. Miller, P. Agostini, L.F. DiMauro, *Opt. Express* **17**, 20959 (2009)
27. H.G. Kurz, D.S. Steingrube, D. Ristau, M. Lein, U. Morgner, M. Kovačev, *Phys. Rev. A* **87**, 063811 (2013)
28. R.A. Ganeev, M. Suzuki, M. Baba, M. Ichihara, H. Kuroda, *J. Appl. Phys.* **103**, 063102 (2008)
29. R.A. Ganeev, C. Hutchison, M. Castillejo, I. López-Quintás, F. McGrath, D.Y. Lei, J.P. Marangos, *Phys. Rev. A* **88**, 033803 (2013)
30. R.A. Ganeev, M. Suzuki, S. Yoneya, H. Kuroda, *Appl. Phys. Lett.* **105**, 041111 (2014)
31. R.A. Ganeev, P.A. Naik, H. Singhal, J.A. Chakera, M. Kumar, M.P. Joshi, A.K. Srivastava, P.D. Gupta, *Phys. Rev. A* **83**, 013820 (2011)

Chapter 8

Summary: Achievements and Perspectives

This book is about the amendments of the nonlinear optical response of extended plasma medium in the field of intense laser radiation. Long plasmas have proven to be an interesting object of studies using the high-order nonlinear optical spectroscopy method. The book demonstrates how one can improve plasma HHG through the double excitation of laser-produced plasmas (i.e. double-pulse method), optimization of the longitudinal harmonic generation schemes in the laser plume, use of multi-component plasma plumes, optimization of the ablation of nanostructured targets, formation of QPM conditions in complex extended and perforated plasmas, provision of a regime of waveguide pump propagation through the plasma medium, use of non-metals as the ablating targets, etc.

The book follows the logic of developments of the emerging field of nonlinear optical studies of the extended plasma media. Below, I summarize the achievements of extended plasma HHG described in this book and discuss the future developments in this field.

The main goal of the description of HHG in narrow plasmas was to acquaint the reader with most advanced results of this technique achieved so far using the 0.3–0.5 mm long plasma plumes. While presenting the overview of previous results of plasma harmonic studies, we also showed recent developments in this field. Among them are (1) the measurements of the spatial coherence of the high-order harmonics generating in laser-produced narrow plasma plumes in the cases of resonant and non-resonant harmonics; (2) the application of femtosecond and picosecond laser pulses for plasma formation on the surfaces of metal targets for the high-order harmonic generation using the 1 kHz laser systems; (3) definitions of the concentrations of neutrals and ions of various plasma formations; (4) the analysis of the enhanced 11th harmonic (96.7 nm), which originated from the resonance-induced growth of the nonlinear optical response of lead plasma at the wavelength of the strong ionic transitions of this metal; (5) the superior harmonic intensity from an aluminum cluster containing plasma compared to atomic Al plumes.

The HHG in partially ionized narrow plasmas was actively developed during last few years in different laboratories worldwide. The developments in this area allow us to expect further amendments to this technique of coherent short-wavelength radiation generation. It follows from the overview of plasma harmonics that recent investigations in this area of nonlinear optics are making rapid strides and may

bring new success in the near future. The achievements in present-day plasma harmonic studies motivate further development of this technique. It has become obvious that plasma HHG is not simply another method for generation of coherent XUV light but is rather a new technique for the analysis of various features of the harmonic emitters appearing in the plasma plumes during laser ablation of solids. The extended plasma medium is the example of such a new formation for the amendments of the high-order nonlinear optical processes in the plasma plumes. To prove this assumption, we have shown how the extension of medium allows the improvements of the harmonics in the case of plasma.

Major part of this book deals with the extended plasma formations. We have analyzed the advanced properties of extended plasma plumes for the efficient harmonic generation compared with the short-length plasmas used in previous studies. We showed the dependences of the length of nonlinear medium on the harmonic yield and found some peculiarities in the cases of indium and carbon plasmas, which were related with the resonance and morphology properties of these media. The demonstration of plasma HHG has been shown along the whole XUV range, particularly including the resonantly enhanced conditions, as well as the single-color and two-color pumps of plasma for harmonic generation. The possibility of using such plasmas for quasi-phase-matching experiments was discussed.

We have discussed the technique allowing a fine tuning of the distance between the multiple laser-produced plasma plumes on the surfaces of ablating materials (Mn and Ag), as well as the variation of the sizes of these plumes. The multi-plume plasmas with the sizes of single plume ranging between 0.1 and 1 mm were produced. This method has proven to be useful for the tuning and extension of the QPM-enhanced harmonics of Ti:sapphire laser radiation.

The application of the heating pulses of different duration covering the range of a few tens of femtoseconds and a few tens of nanoseconds revealed the advanced nonlinear optical features of the extended plasmas produced by picosecond pulses. We have shown that the optimal extended plasma formation, which is crucial for achieving the efficient harmonic generation, mostly depends on the energy fluence rather than the intensity of heating pulse on the target surface. Various samples of harmonic emission spectra were analyzed to support this conclusion about the attractiveness of the subnanosecond pulses for extended plasma formation and HHG.

We have analyzed the spatial and coherence characteristics of the harmonics generated in the extended plasmas produced by 370 ps pulses. It was demonstrated that the divergence of plasma harmonics was seven times smaller than the divergence of the driving femtosecond pulses used for HHG. The visibilities of the lower-order harmonics were in the range of 0.54–0.73 depending on the harmonic order and plasma species. These studies confirmed that the harmonics from extended plasma ablation can be used for the applications requiring high spatial coherence and low divergence.

We have discussed the new approach in plasma HHG allowing the enhancement of a group of harmonics. The method of QPM of the high-order harmonics generating in the multiple plasma jets produced on the surfaces of perforated silver,

vanadium, and manganese targets allows the manipulation of the phase difference between the interacting waves in the laser produced plasmas and the enhancement of a group of harmonics in different spectral ranges.

We have also presented the analysis of the harmonic generation in the long (~ 5 mm) modulated plasma plumes divided onto a set of small jets using the modulation of the heating beam on the target surface. We have shown both the QPM induced enhancement of some groups of harmonics along the plateau range and the tuning of maximally enhanced harmonic order at different regimes of multi-jet plasma formation. The tuning of QPM enhanced harmonics was accomplished by changing the sizes of multiple plasma jets. The $40\times$ and $15\times$ enhancement factors for the QPM enhanced harmonics were achieved in the silver and manganese multi-jet plasmas. We have shown the potential of the proposed plasma harmonic QPM approach for the express analysis of the plasma characteristics. We have also analyzed the QPM induced variations of harmonic spectra in the case of the two-color pump of perforated plasma formations. During this analysis we discussed the influence of driving and heating pulse energies on the enhancement of the QPM harmonics, showed the spatial characteristics of a few harmonics in the region below 20 nm produced in the extended imperforated and multi-jet plasmas, showed the fine tuning of those enhanced harmonics by tilting the multi-slit shield placed in front of the ablating targets, analyzed the enhancement factors of harmonics in different regions of XUV, demonstrated the small divergence of QPM-enhanced harmonics compared with larger divergence and modulated shape of the “ordinary” harmonics generated in the extended plasmas, etc.

Further, we have discussed the peculiarities of the HHG in the extended non-metal plasmas (crystals, semiconductors, and carbon-based clusters). Summarizing the current vision of the generation process in the crystal ablations, one can consider the following scenario. Initially, the ablation of the unpolished surfaces of crystals causes the heating, melting, and further evaporation, ionization, and disintegration of the molecules comprising crystals. Thus the plasma under consideration is close to the gas-like medium rather than to the crystalline state. During propagation of ultrafast pulses through the mixed medium containing neutral molecules, singly ionized molecules and atoms, ionized components of disintegrated molecules, electrons, and probably clusters, the most suitable species start to emit harmonics. The analysis of the reported studies have revealed that, in the case of a group of F-containing crystals, the fluorine ions became responsible for the most efficient harmonic generation compared with other components of plasmas. The latter components may also contribute, to some extent, to the growth of lower-order harmonic yield. However, this contribution seems insignificant in the shorter-wavelength region. These assumptions of the generation process and sources of harmonics were supported by both spectroscopic and nonlinear optical studies. Though the O-containing crystals have shown some other peculiarities, the harmonic generation in the plasmas of these crystals can also be described by the same mechanism.

We have reviewed the studies of the high-order harmonics of ultrashort pulses generated in the plasma plumes produced during ablation of various elemental semiconductors (Te, Se, Si, As, Sb, and Ge). These plasma media were distinguished by the harmonic cut-offs ranging between the 27th and 51st orders. Application of two-color pump allowed the generation of both odd and even harmonics, with the intensities of latter harmonics stronger than those of former ones. Strong resonance-induced 35th harmonic, with the enhancement factor of $12\times$ compared with the neighboring harmonic orders, was reported in the case of the selenium plasma.

We have discussed the studies of the high-order harmonic generation in the extended carbon cluster contained plasmas (fullerenes, nanofibers, diamond nanoparticles, and nanotubes). Those studies have shown the usefulness in the application of the carbon cluster media for the HHG. The comparison with the harmonic generation from the ablated bulk graphite showed that the probable sources of efficient harmonics in the range of 15–33 eV ($\lambda = 80\text{--}40$ nm) are the low-sized nanoparticles produced during ablation and disintegration of the large clusters and agglomerates of carbon-contained materials. The reason for stronger harmonic yield from cluster ablation compared with the ablation of bulk material in the case of carbon-based species is the easiness in low-sized nanoparticles formation. The latter species can lead to the growth of lower-order harmonic yield due to enhanced probability of recombination of the accelerated electron with the whole cluster, while keeping the weak absorptive properties of the extended plasma medium.

Previously, it has been revealed in the case of the Al nanoparticles of different sizes, that the enhancement of the harmonic signal from large nanoparticles (~ 100 nm) was found to be insignificant with respect to that from the bulk target ablation. Ablation of the narrow targets constituted by larger nanoparticles most probably leads to the entrainment of larger clusters in the plume, which causes a reduction of the local field effect and contributes to a larger absorption probability of the generated short-wavelength radiation. This effect is probably exaggerated in the case of extended plasmas. The optimal sizes of the nanoparticles participating in most efficient harmonic generation is still an unresolved issue that should be investigated further due to the necessity of defining the relative role of different competitive mechanisms of the HHG in clustered plasmas. The large neutral clusters and agglomerates in the extended plasma (as in the case of CNF, CNT, C_{60} and DN, when the amount of carbon atoms exceeds a few tens of thousands of the carbon atoms) do not enhance the harmonic yield. The absence of large clusters in the graphite plasmas and the similar efficiency of lower-order harmonics in the case of the ablation of bulk graphite and clustered carbon species allow making a conclusion on the prevailing role of small carbon clusters over the large ones in the growth of HHG conversion efficiency from those plasmas.

We have reviewed the high-order harmonic generation studies in the extended plume containing the graphene nanoparticles. The harmonics up to the 33rd order were observed in the case of those emitters. The presence of graphene nanoparticles in the laser plasma was confirmed during the analysis of ablation debris.

The comparative studies of harmonic generation from the ablation of graphene, carbon nanotubes, and diamond nanoparticles showed the advanced properties of the latter medium. We have discussed the optimal extended plasma formation, which is crucial for achieving the efficient harmonic generation in the case of this clustered medium. The formation of such plasmas mostly depends on the energy fluence rather than the intensity of heating pulse on the surface of cluster-contained target.

The advanced properties of extended manganese and zinc plasma plumes for the harmonic generation in the shorter and longer wavelength regions of XUV were analyzed compared with the short-length plasmas used in previous studies. During those systematic studies, the harmonic generation in the manganese plasma up to the 107th order was achieved. We have analyzed the advanced properties of extended zinc plasma plumes for the harmonic generation in the longer wavelength region of XUV compared with other plasmas used in previous studies. The conversion efficiency of the 11th–19th orders at these conditions was estimated to be 5×10^{-5} . The joint influence of various mechanisms of harmonic enhancement was applied to those two plasma samples with the aim to achieve the best results of plasma HHG (i.e. most extended cut-off and strongest harmonic yield). We have discussed the limits of most extended harmonic cut-off in the plasma media. These limits in highest photon energy show the physical restrictions and pave the way in a search for other options, notably plasma HHG spectroscopy allowing the material study through the analysis of the high-order nonlinear optical processes during material ablation.

Finally, we have analyzed the new method of harmonic generation using the two femtosecond pulses propagated in the vicinity of the solid and powdered targets. The harmonics were observed in the case of double-pulse beams while using various solids (bulk metals and non-metals, nanoparticle and microparticle powders). The efficiency and cut-off of harmonic generation using the double-pulse method in most cases were lower compared with the commonly used method of plasma HHG. However, the simplicity, absence of additional sources of heating radiation, and artificial optimization of the HHG using the adjustment of the double pulses and targets demonstrate the advantages of this technique. This method allows the simplified analysis of the high-order nonlinear optical properties of the media and thus it could be useful for the laser ablation induced HHG spectroscopy. At the same time, this technique could be applied for the direct observation of the HHG from the solids.

One can expect that, in a nearest future, various approaches for further amendments of extended plasma HHG will be examined. Among them are: (i) harmonic generation in plasma using the two-color pump in the case of commensurate and noncommensurate wavelength sources in the mid-IR and ultraviolet ranges, (ii) application of mid-IR pulses for the studies of organic molecules through the HHG method, (iii) studies of HHG from various clusters appearing in situ during laser ablation of bulk targets, (iv) analysis of the influence of molecular orientation on the harmonic output from molecular plasma plumes, (v) use of various polarization schemes for HHG, (vi) development of

ablation-induced HHG spectroscopy of newly emerged complex organic and inorganic materials in the mid-IR region, (vii) analysis of the orientation-induced nonlinear optical response of large ablated molecules and clusters, (viii) time-resolved pump-probe analysis of the complex plasmas containing various molecular structures, to mention a few potential amendments of plasma harmonic approach.

The joint implementation of abovementioned new and old (i.e. resonance-induced harmonic enhancement, application of the clusters with controllable and variable sizes, two-color pump-induced enhancement of the odd and even harmonics, search for the influence of the multi-electron dynamics of complex clusters, such as fullerenes and nanotubes, on the plasmon resonance-induced growth of a few harmonics in the XUV range, etc. [1–14] techniques will allow further establishment of this method of material science using long plasmas. The development of the advanced QPM schemes in multi-jet plasma plumes, studies of the time-dependent dynamics of aggregation and disintegration of clusters through their nonlinear optical response, comparative analysis of gas and plasma HHG, joint application of gas and plasma HHG for the studies of the interacting gaseous and ablated species, application of extended multi-component plasma plumes for HHG, etc. are also among the potential goals of plasma harmonic studies. Particularly, as it was shown in this book, recent studies have proven that the application of spatially modulated heating beams [15–17], or perforated targets [18], could be an alternative to the multiple plasma jets formation on the surfaces of microlithographic targets for the QPM, which was proposed in [19].

It would be interesting to analyze the application of radiation in the range of 2000–5000 nm to study the dynamics of the nonlinear optical response of ablated molecular structures compared with commonly used Ti:sapphire lasers for plasma HHG, including the studies of extended harmonics at the conversion efficiency comparable with shorter-wavelength laser sources, and a search for new opportunities in the improvement of HHG conversion efficiency in the mid-IR range, such as the application of clustered molecules.

Future developments may also include the analysis of the plasmonic properties of clusters produced during laser ablation at the conditions of resonance-induced enhancement of harmonics, application of graphene- and ring-like structures, multicomponent molecules, nanofibers, and other recently emerged clusters for plasma HHG using longer-wavelength pump sources [20], the analysis of plasmonic properties of carbon nanoparticles in the XUV, and the studies of the indirect involvement of clusters in HHG, when they did not directly participate as the harmonic emitters, but rather enhance the local field, analogously to the experiments and calculations using the gold nanostructures enhancing gas HHG [21–23]. The applications of thin films may also reveal some new opportunities in the plasma HHG, particularly using the double-pulse schemes.

These ideas of plasma harmonic developments were partially borrowed from the gas harmonics. There are no fundamental restrictions in the implementation of gas HHG approaches in the plasma harmonic generation. Moreover, some peculiarities of the latter medium may offer the advantages in the new developments using such

sources. Particularly, QPM in periodically modulated gas structures led to the growth of conversion efficiency for some groups of harmonics [24–27]. Recent implementation of similar approach in the plasma harmonic studies has demonstrated even larger ratio between QPM-enhanced and conventional plateau-like harmonics [15, 17]. Further, such methods as two-color pump and use of long-wavelength lasers have recently been applied to various plasma samples using a few-cycle laser pulses [28–30], which led to enhancement of odd and even harmonics, as well as extension of harmonic cut-offs. Moreover, single harmonic generation from such sources was reported in the case of manganese plasma [31]. Finally, the developed method of plasma harmonic spectroscopy has already allowed the analysis of the structural properties of complex systems, such as DNA components (thymine and uracil) [32, 33]. The new ideas of plasma HHG are actively pursued in various laboratories.

It is worth noting that, currently, the nonlinear spectroscopy involving gas harmonics is trying to deal with such problems as (a) extension of the HHG spectroscopy based attosecond structural technique to image the nuclear re-arrangements induced by localized hole excitations, (b) application of strong-field ionization to create localized hole excitations and study their attosecond dynamics in polyatomic molecules, (c) search for the selective imaging of hole dynamics induced by the removal of e.g. inner-valence electrons using the XUV initiated HHG technique, and (d) development of multi-dimensional HHG spectroscopy capable of following energy flow between different molecular modes over femtosecond time-scale. Plasma harmonic spectroscopy allows adding some important impulse to those studies, by using the peculiarities of plasma HHG and much broader range of newly developed solids.

The important topics of future plasma HHG studies will be the applications of ablation plumes for attosecond science. Measurement of physical processes with a temporal resolution approaching 10^{-17} s has emerged in the last decade as one of the most exciting frontiers in physical science. Such studies make accessible the ultrafast dynamics of correlated electronic motion that underpin the first moments of a wide range of physical and chemical processes, such as photo-chemical reactions, radiation damage in biomolecules and conversion of light energy into chemical energy. This science demands the most advanced technology and in particular suitable light sources of exceptionally high bandwidth (>10 eV) to support the ultra-high temporal resolution. Presently, the primary technique to do this is a harmonic generation in gases. Nevertheless the capabilities for present-day attosecond measurements are severely limited by some factors including (a) low photon yield in the generation of isolated attosecond pulses, and (b) the limited range of molecules that can be obtained in gas phase at the densities sufficient for HHG.

Plasma harmonic spectroscopy can offer some valuable advances in this field, particularly by introducing the new approaches. First attempts to analyze the temporal characteristics of plasma harmonics were discussed in [34] where the pulse duration of 11th–17th harmonics generated from chromium plasma was measured to be ~ 300 as. The studies of plasma harmonic pulse duration were also

reported in [35, 36]. The goal of the future research of ultrashort pulse generation through plasma nonlinearities is to enable various groups to fully develop world-leading capabilities in attosecond sciences using the emerged plasma HHG spectroscopy methods. Though the studies are challenging, one can expect that present expertise in this field has the possibility to make a step-change advance in plasma harmonics induced attosecond science.

The main objectives of these studies are: (a) to test if, as expected from calculation, the resonance enhanced HHG in some ablation plumes leads to isolated sub-femtosecond pulses using the attosecond streaking technique, (b) to utilize the isolated sub-femtosecond pulses from those metal plasmas in the pump-probe measurements at surfaces and in molecules, and (c) to develop optimal conditions for ablation plumes of high density for HHG studies of various organics, such as intact ribonucleic acid and deoxyribonucleic acid bases, to allow the first steps for attosecond investigation of electron's dynamics in these molecules.

Among other possible developments in the application of plasma HHG technique one may anticipate such areas as seeding of plasma resonance harmonics in the XUV free-electron lasers, application and analysis of endohedral fullerenes using the plasma HHG, analysis of molecular structures through the study of harmonic spectra from oriented molecules in plasmas using the gating and pump-probe techniques, studies of ring-like structures using the nonlinear optical method, to mention a few of them. Some of most recent studies of plasma harmonics [32, 34, 37–41] are trying to partially address the abovementioned issues.

References

1. R.A. Ganeev, M. Suzuki, M. Baba, H. Kuroda, *J. Opt. Soc. Am. B* **22**, 1927 (2005)
2. R.A. Ganeev, M. Suzuki, M. Baba, H. Kuroda, *J. Opt. Soc. Am. B* **23**, 1332 (2006)
3. R.A. Ganeev, P.A. Naik, H. Singhal, J.A. Chakera, H. Kuroda, P.D. Gupta, *J. Opt. Soc. Am. B* **24**, 1138 (2007)
4. R.A. Ganeev, L.B. Elouga Bom, J.-C. Kieffer, T. Ozaki, *J. Opt. Soc. Am. B* **24**, 1319 (2007)
5. M. Suzuki, M. Baba, R.A. Ganeev, H. Kuroda, T. Ozaki, *J. Opt. Soc. Am. B* **24**, 2686 (2007)
6. R.A. Ganeev, L.B. Elouga Bom, T. Ozaki, P.V. Redkin, *J. Opt. Soc. Am. B* **24**, 2770 (2007)
7. M. Suzuki, R.A. Ganeev, L.B. Elouga Bom, M. Baba, T. Ozaki, H. Kuroda, *J. Opt. Soc. Am. B* **24**, 2847 (2007)
8. R.A. Ganeev, M. Suzuki, M. Baba, M. Ichihara, H. Kuroda, *J. Opt. Soc. Am. B* **25**, 325 (2008)
9. R.A. Ganeev, D.B. Milošević, *J. Opt. Soc. Am. B* **25**, 1127 (2008)
10. R.A. Ganeev, M. Suzuki, M. Baba, H. Kuroda, *J. Opt. Soc. Am. B* **25**, 2096 (2008)
11. R.A. Ganeev, H. Singhal, P.A. Naik, J.A. Chakera, M. Tayyab, M. Baba, H. Kuroda, P.D. Gupta, *J. Opt. Soc. Am. B* **26**, 2143 (2009)
12. R.A. Ganeev, J.A. Chakera, P.A. Naik, H. Singhal, R.A. Khan, P.D. Gupta, *J. Opt. Soc. Am. B* **28**, 1055 (2011)
13. R.A. Ganeev, P. A. Naik, J.A. Chakera, H. Singhal, N.C. Pramanik, P.A. Abraham, N. Rani Panicker, M. Kumar, P.D. Gupta, *J. Opt. Soc. Am. B* **28**, 360 (2011)
14. P.V. Redkin, M.K. Kodirov, R.A. Ganeev, *J. Opt. Soc. Am. B* **28**, 165 (2011)
15. R.A. Ganeev, M. Suzuki, H. Kuroda, *Phys. Rev. A* **89**, 033821 (2014)

16. R.A. Ganeev, M. Suzuki, P.V. Redkin, H. Kuroda, J. Nonlin. Opt. Phys. Mater. **23**, 1450013 (2014)
17. R.A. Ganeev, M. Suzuki, H. Kuroda, J. Phys. B: At. Mol. Opt. Phys. **47**, 105401 (2014)
18. R.A. Ganeev, M. Suzuki, H. Kuroda, JETP Lett. **99**, 368 (2014)
19. A.H. Sheinfux, Z. Henis, M. Levin, A. Zigler, Appl. Phys. Lett. **98**, 141110 (2011)
20. R. A. Ganeev, *Laser-Surface Interactions* (Springer, 2013)
21. S. Kim, J. Jin, Y.-J. Kim, I.-Y. Park, Y. Kim, S.-W. Kim, Nature **453**, 757 (2008)
22. T. Hanke, G. Krauss, D. Traütlein, B. Wild, R. Bratschitsch, A. Leitenstorfer, Phys. Rev. Lett. **103**, 257404 (2009)
23. K.D. Ko, A. Kumar, K.H. Fung, R. Ambekar, G.L. Liu, N.X. Fang, K.C. Toussaint, Nano Lett. **11**, 61 (2011)
24. J. Seres, V.S. Yakovlev, E. Seres, C.H. Strelti, P. Wobruschek, C.H. Spielmann, F. Krausz, Nat. Phys. **3**, 878 (2007)
25. A. Pirri, C. Corsi, M. Bellini, Phys. Rev. A **78**, 011801 (2008)
26. V. Tosa, V.S. Yakovlev, F. Krausz, New J. Phys. **10**, 025016 (2008)
27. A. Willner, F. Tavella, M. Yeung, T. Dzelzainis, C. Kamperidis, M. Bakarezos, D. Adams, M. Schulz, R. Riedel, M.C. Hoffmann, W. Hu, J. Rossbach, M. Drescher, N.A. Papadogiannis, M. Tatarakis, B. Dromey, M. Zepf, Phys. Rev. Lett. **107**, 175002 (2011)
28. R.A. Ganeev, C. Hutchison, T. Witting, F. Frank, S. Weber, W.A. Okell, E. Fiordilino, D. Cricchio, F. Persico, A. Zaïr, J.W.G. Tisch, J.P. Marangos, J. Opt. Soc. Am. B **30**, 7 (2013)
29. R.A. Ganeev, C. Hutchison, T. Witting, F. Frank, W.A. Okell, A. Zaïr, S. Weber, P.V. Redkin, D.Y. Lei, T. Roschuk, S.A. Maier, I. López-Quintás, M. Martín, M. Castillejo, J.W.G. Tisch, J.P. Marangos, J. Phys. B: At. Mol. Opt. Phys. **45**, 165402 (2012)
30. R.A. Ganeev, C. Hutchison, A. Zaïr, T. Witting, F. Frank, W.A. Okell, J.W.G. Tisch, J. P. Marangos, Opt. Exp. **20**, 90 (2012)
31. R.A. Ganeev, T. Witting, C. Hutchison, F. Frank, M. Tudorovskaya, M. Lein, W.A. Okell, A. Zaïr, J.P. Marangos, J.W.G. Tisch, Opt. Exp. **20**, 25239 (2012)
32. C. Hutchison, R.A. Ganeev, M. Castillejo, I. López-Quintás, A. Zaïr, S.J. Weber, F. McGrath, Z. Abdelrahman, M. Oppermann, M. Martín, D.Y. Lei, S.A. Maier, J.W. Tisch, J.P. Marangos, Phys. Chem. Chem. Phys. **15**, 12308 (2013)
33. I. López-Quintás, M. Oujja, M. Sanz, A. Benitez-Cañete, C. Hutchison, R. de Nalda, M. Martín, R.A. Ganeev, J.P. Marangos, M. Castillejo, Appl. Surf. Sci. **302**, 299 (2014)
34. L.B. Elouga Bom, S. Haessler, O. Gobert, M. Perdrix, F. Lepetit, J.-F. Hergott, B. Carré, T. Ozaki, P. Salières, Opt. Exp. **19**, 3677 (2011)
35. S. Haessler, L.B. Elouga Bom, O. Gobert, J.-F. Hergott, F. Lepetit, M. Perdrix, B. Carré, T. Ozaki, P. Salières, J. Phys. B: At. Mol. Opt. Phys. **45**, 074012 (2012)
36. S. Haessler, V. Strelkov, L.B. Elouga Bom, M. Khokhlova, O. Gobert, J.-F. Hergott, F. Lepetit, M. Perdrix, T. Ozaki, P. Salières, New J. Phys. **15**, 013051 (2013)
37. R.A. Ganeev, C. Hutchison, M. Castillejo, I. López-Quintás, F. McGrath, D.Y. Lei, J. P. Marangos, Phys. Rev. A **88**, 033803 (2013)
38. M. Wöstmann, P.V. Redkin, J. Zheng, H. Witte, R.A. Ganeev, H. Zacharias, Appl. Phys. B **120**, 17 (2015)
39. R.A. Ganeev, E. Fiordilino, D. Cricchio, P.P. Corso, M. Suzuki, S. Yoneya, H. Kuroda, Laser Phys. Lett. **12**, 065401 (2015)
40. R.A. Ganeev, M. Suzuki, S. Yoneya, H. Kuroda, Appl. Phys. A **119**, 1231 (2015)
41. R.A. Ganeev, V. Tosa, K. Kovács, M. Suzuki, S. Yoneya, H. Kuroda, Phys. Rev. A **91**, 043823 (2015)

Index

A

Ablation, 10
Ablated nanoparticles, 12
Ablation debris, 140
Aluminum, 77
Aluminum plasma, 103
Atoms, 19

B

Barrier suppression intensity, 74
BBO crystal, 58

C

Carbon, 14
C₆₀, 133
C₆₀ powder, 133
C₆₀ plasma, 145
Carbon-contained plasmas, 134
Carbon nanofiber, 133
Carbon nanoparticles, 140
Carbon nanotubes, 141
Carbon plasma, 17
Chromium, 54
Chromium plasma, 54
Cluster media, 154
Clusters, 2
CNT powder, 140
CNF powder, 140
Coherence length, 4
Coherence, 4
Confocal parameter, 4
Conversion efficiency, 5
Cutoff energy, 5

D

Debris, 25
Delay, 27
Density of plasma, 178
Destructive interference, 37

Detection system, 30
Dispersion, 5
Driving pulse, 21
Driving beam, 38

E

Electron, 31
Electron density, 57
Emission, 63
Emission spectra, 81
Energy, 16
Enhanced harmonics, 14
Even harmonic, 51
Excitation, 54
Excited ions, 52
Extended harmonics, 214
Extreme ultraviolet, 120
Extreme ultraviolet spectrometer, 22

F

Femtosecond laser, 19
Femtosecond pulses, 21
Flat-field grating, 95
Four-step model, 14
Fragmentation, 138
Free electrons, 25
Frequency conversion, 5
Fullerenes, 12
Fullerene powder, 133
Fundamental pulses, 130
Fundamental radiation, 4

G

Gas HHG, 10
Gas clusters, 5, 121
Gases, 170
Gas jets, 4
Graphite, 65
Graphite plasma, 66

Graphite ablation, 35
 Grating, 44
 Ground state, 176
 Group velocity dispersion, 59

H

Harmonics, 3
 Harmonic conversion efficiency, 11
 Harmonic cutoff, 62
 Harmonic generation, 66
 Harmonic generation in gases, 215
 Harmonic intensity, 30
 Harmonic orders, 71
 Harmonic pulses, 73
 Harmonic radiation, 14
 Harmonic spectra, 25
 Harmonic wavelength, 36
 Harmonic waves, 58
 Harmonic yield, 5
 Heating pulse, 21
 Heating pulse duration, 45
 HHG, 2
 HHG conversion efficiency, 11
 HHG spectra, 2
 High-order harmonic generation, 5

I

Indium, 12
 Indium plasma, 19
 Interaction, 27
 Interference, 26
 Ionization, 1

K

Kerr effect, 52

L

Laser, 15
 Laser ablation, 27
 Laser beam, 68
 Laser intensity, 76
 Laser-produced plasma, 9
 Laser pulses, 11
 Laser radiation, 33
 Lenses, 52
 Low-order harmonics, 2

M

Macroscopic processes, 2
 Materials, 10
 Measurements, 14
 Media, 25
 Metals, 119
 Metal nanoparticles, 139

Metal plasmas, 30
 Micro-channel plate, 15
 Mirrors, 16
 Manganese, 61
 Manganese plasma, 68
 Molecules, 124
 Monochromator, 28

N

Nanoparticles, 37
 Nanoparticle-containing plasma, 38
 Nanosecond pulses, 76
 Nd:YAG laser, 28
 Neutral atoms, 37
 Nonlinear optics, 73

O

Odd harmonics, 99
 Optimal plasma, 122
 Optimal plasma formation, 25
 Oscillator strength, 10

P

Phase-matching conditions, 36
 Phase mismatch, 37
 Picosecond pulse, 16
 Plasma, 2
 Plasma formation, 10
 Plasma HHG, 11
 Plasma jet, 71
 Plasma plume, 92
 Pulse compressor, 15
 Pulse energy, 23
 Pulse repetition rate, 52

Q

Quasi-phase matching, 57

R

Radiation, 17
 Resonance-enhanced harmonics, 34
 Resonance-induced enhancement, 56

S

Second plateau, 194
 Self-phase modulation, 203
 Semiconductor targets, 127
 Short-wavelength radiation, 155
 Silver, 140
 Silver plasma, 63
 Singly charged ions, 93

T

Target, 23

Target ablation, [24](#)

Third harmonic, [161](#)

Three-stage process, [1](#)

Temporal delay, [59](#)

Ti:sapphire laser, [14](#)

Two-color pump, [215](#)

U

Ultrashort pulses, [212](#)

Uncompressed radiation, [121](#)

V

Vacuum chamber, [104](#)

W

Wavelength, [16](#)

X

XUV, [21](#)

XUV spectrometer, [39](#)

Z

Zinc, [41](#)

Zinc plasma, [53](#)